Université de Strasbourg

École et observatoire des sciences de la Terre de l'Université de Strasbourg et du CNRS

Université de Strasbourg

École doctorale n°413 : Sciences de la Terre et Environnement
Institut Terre et Environnement de Strasbourg

THÈSE

présentée par

Luc Moutote

soutenue le:
16 Novembre 2023
pour obtenir le grade de :

Docteur de l'Université de Strasbourg

Discipline : **Sciences de la Terre et de l'Univers**
Spécialité : **Géophysique**

Foreshock earthquake sequences: Earthquake cascades or aseismic triggering?

Thèse dirigée par:

Olivier Lengliné,	Maître de conférences,	Université de Strasbourg
Zacharie Duputel,	Chargé de recherche CNRS,	Observatoire Volcanologique du Piton de la Fournaise

Rapporteurs:

Sebastian Hainzl,	Senior Scientist,	Deutsches GeoForschungsZentrum
Romain Jolivet,	Professeur,	École Normale Supérieure (Paris)

Autres membres du jury:

Agnès Helmstetter,	Chargée de recherche CNRS,	Université Grenoble Alpes
Virginie Durand,	Chargée de recherche IRD,	Université Côte d'Azur
Luis Rivera,	Professeur,	Université de Strasbourg

Présidente du jury:

Alessia Maggi,	Professeure,	Université de Strasbourg

Remerciements

Hé bien voilà, finito la Thèse !

Voilà..., voilà bientôt 4 années que je sévis dans le laboratoire de sismologie de l'ITES et un peu plus de sept années à hanter les couloirs de l'EOST. Avec cette Thèse de Doctorat s'achève aussi, et probablement pour un bout de temps, mes aventures à Strasbourg, à l'EOST et en Alsace. Puisque cette partie de ma vie n'aurait certainement pas pu se dérouler sans les personnes qui m'ont accompagné au quotidien, un verre de Picon à la main, je saisis ici l'occasion de leur rendre hommage.

Avant toute chose, et puisqu'ils sont probablement les premiers concernés par les travaux présentés dans la suite, je souhaite remercier mes deux Directeurs de thèse : Zacharie Duputel et Olivier Lengliné. Leur bienveillance et leur écoute m'ont permis de tirer pleinement parti de leur direction à travers le monde scientifique. Rien de ce qui a été écrit dans la suite n'aurait été possible sans leur encadrement soigné et attentif. En particulier merci de m'avoir permis de voyager aux quatre coins du monde, notamment plusieurs mois à La Réunion.

Merci à Luis, personnage incontournable de mes moments à l'EOST, mentor et ami qui m'a apporté énormément grâce à sa bonne humeur. Merci à Rémi, le co-bureau et poto du RU éternel, de m'avoir écouté et supporté au plus près pendant ces trois ans. Je prendrai grand soin de notre plante sauvage. Merci à Dimitri, pour nos discussions, ses conseils, sa bonne humeur et de m'avoir ouvert le monde de la sismologie à travers un stage de Master 1. Merci à Alessia et Jérôme d'avoir accompagné le suivi de cette thèse et de m'avoir rassuré et encouragé.

Merci à tous les copains de l'ITES, Mérédith, Emmanuel, Franck, Cédric, Hugo (x2), Émile, Weiwei, Lise, Lucille, Lou, Oscar, Jean-Yves et Armelle, Roxane, Joachim, Charlotte, Clément, Estelle et tous les autres qui se reconnaîtront...

Merci à tous les révoltés de l'ITES, mégaphone à la main, on continuera le combat !

Merci à tous les membres de l'OVPF de m'avoir accueilli chaleureusement et qui m'ont permis de découvrir en détail l'île Bourbon et son volcan. Vu que je l'ai raté, je reviendrais pour enfin voir une éruption.

Merci à la famille Vergé, Laura, Maxime, Éloïse et la Catoche, de m'avoir accueilli chaleureusement chez eux, dans le fin fond du Sundgau, plusieurs mois pendant le premier confinement. Votre accueil, qui ressemblait plus à un sauvetage d'urgence de mon isolement, a sûrement permis à mon cerveau de ne pas se transformer en pâte à spaetzles. Votre générosité désintéressée est une qualité rare. En particulier merci à Laura, ma coloc, pour sa grande compagnie et ses conseils francs qui m'ont permis de redescendre sur terre plus d'une fois.

Merci à toute ma famille, mes parents, le Moustik et la Suzon, mon frère Yvanmamoto, mes oncles, mes tantes, mes cousines et cousins, pour tous votre soutien et les moments que nous partageons à Bellevaux, au coin du feu, confiné ou non. Je vous aime fort <3.

Merci à tous les copains en général. (Hé oui, je commence à fatiguer...)

Pour terminer, merci à Aurélie ma petite amie, qui rassemble tous les compliments précédents et plus encore. Ma survie mentale de ces dernières années tient à son inépuisable soutien et amour qui me ferait gravir la sainte cathédrale Notre-Dame de Strasbourg. Les prochaines lignes que j'écrirais sur ma vie seront, je l'espère, avec toi. Love u <3

Luc

Contents

Abstract

Understanding how large earthquakes begin remains one of the major challenge in seismology. This question is central to our understanding of earthquakes, including the long controversial issue of their predictability. Many large earthquakes are preceded by foreshocks, which are sometime considered to be precursors, reflecting a nucleation process of the main rupture. However, we are still unable to fully understand under which circumstances they occur and if they have any predictive power. Contrasting views have been proposed to explain foreshock earthquakes: First, a model where successive foreshock stress changes contribute to a cascade of failures ultimately triggering the mainshock. Second, a model where foreshocks are passive tracers of an aseismic nucleation phase of the mainshock in which the fault slip slowly accelerates to a large dynamic rupture. Finally, a mixed model where a slow-slip events drives an enhanced cascade of failure, ultimately increasing the likelihood of triggering a large asperity.

The recent increase of near-fault seismic and geodetic observations, coupled with recent advances in earthquake detection, provides an unprecedented opportunity to study active faults in detail. In this Ph.D. thesis I use high resolution seismicity catalogs to study foreshock sequences, their connection with aseismic processes and the preparation phase of mainshocks.

First, based on a highly complete earthquake catalog, we study 53 foreshock sequences observed in Southern California. Using the same catalog, previous studies suggested that mainshocks are often preceded by anomalously elevated seismicity. We test the seismicity against the Epidemic Type Aftershock Sequence model that accounts for temporal clustering due to cascade of earthquake interactions. We find that 10 out of 53 mainshocks are preceded by a significantly elevated seismic activity compared with our model. This shows that anomalous foreshock activity in Southern California is relatively uncommon when tested against a model of earthquake interactions. Only 3 out of the 53 foreshock sequences present a mainshock-specific anomaly with a high predictive power, while the other 7 sequences are located in regions where other anomalies are observed without being linked to the occurrence of a mainshock.

We then investigate the 2017 Valparaiso $M_w = 6.9$ earthquake sequence, which was preceded by an intense seismicity likely associated with the occurrence of a transient aseismic slip. We analyze seismic and aseismic processes from the foreshock sequence to the post-mainshock phase. By building a high-resolution seismicity catalog and searching for anomalous seismicity rate increases compared to aftershock triggering models, we highlight an over-productive seismicity starting within the foreshock sequence and persisting several days after the mainshock. Using repeating earthquakes and high-rate GPS observations, we highlight a transient aseismic perturbation starting just before the first foreshock and extending after the mainshock. Rather than pointing to a possible nucleation phase of the 2017 Valparaiso mainshock, the identified slow-slip event seems to act as an aseismic loading of nearby fault areas, increasing the seismic activity before and after the $M_w = 6.9$ mainshock.

This work supports the use of long-term, high-resolution seismicity catalogs to study in detail fault processes that generate mainshocks. Studies are needed to properly assess the role of seismic and aseismic interplay over entire seismic sequences, with a joint analysis of seismic and geodetic data from the pre-mainshock to the post-mainshock time-periods.

Résumé étendu en français

Introduction

Comprendre comment les grands tremblements de terre se déclenchent reste de nos jours un des principaux défis de la sismologie moderne. Les mécanismes physiques qui précèdent ces grandes ruptures de la croûte terrestre sont encore assez mal compris : nos observations ne permettent toujours pas d'affirmer si les signaux mesurés avant ces grands séismes peuvent permettre de mieux les anticiper.

Par exemple, avant de nombreux tremblements de terre de forte magnitude, il est assez courant (mais pas systématique) d'observer des plus petits séismes, amassés en temps et en espace autour de la future rupture. Ces activités sismiques précoces, les séquences pré-chocs, sont souvent interprétées comme des séquences de séismes précurseurs. Ces séismes pré-chocs pourraient refléter un processus de nucléation de ces grandes magnitudes et aider à les prévenir. Toutefois, nous sommes encore incapables de détecter ces séquences pré-choc en temps réel, avant que le choc principal soit observé, remettant en question leur réelle capacité prédictive.

Plusieurs interprétations sont, à ce jour, proposées pour expliquer l'existence de ces séismes pré-chocs (Voir Figure 1). Dans un premier modèle, le "modèle cascade", les séismes pré-chocs sont générés par une cascade de déclenchement de séisme à séisme. Cette chaîne de déclenchement se propage grâce aux variations successives de contraintes induites par chaque séisme, chargeant des portions adjacentes sur la faille. Cette cascade de déclenchement peut finir par déclencher une grande portion bloquée de la faille, interprété a posteriori comme le choc principal. Ici, le déclenchement du choc principal est donc difficilement prévisible, car il dépend de l'état de contrainte de la faille à chaque instant de la cascade. Si la faille ne possède pas de grande portion bloquée prête à être déclenchée, la cascade ne déclenchera pas de forte magnitude. Dans le modèle cascade, l'activité des séismes pré-chocs n'est ainsi pas relié à la future magnitude du choc principal

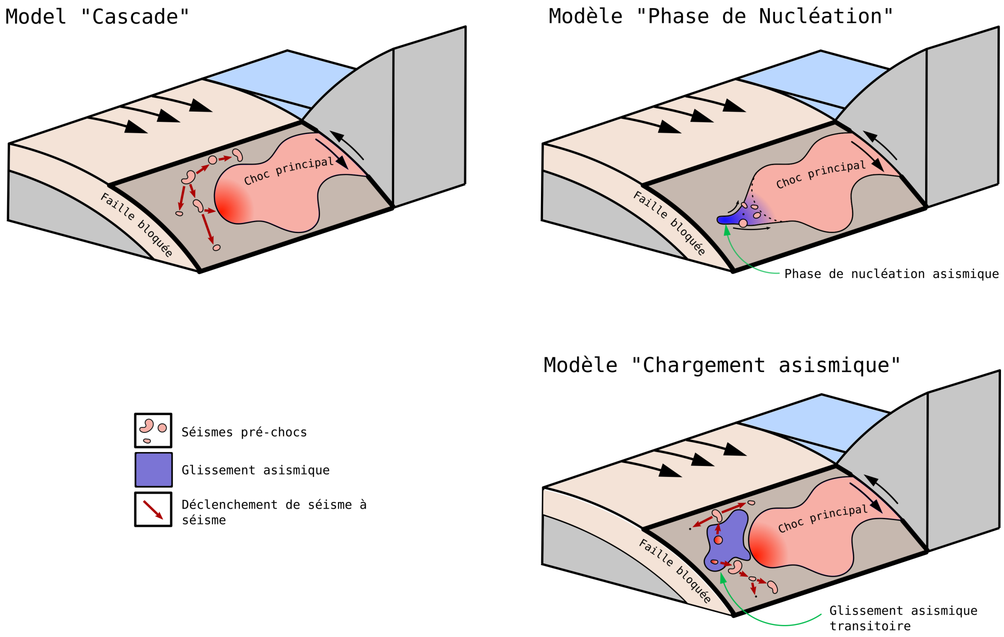

FIGURE 1: 3 Modèles conceptuels pour expliquer les séismes pré-chocs. Le modèle cascade : Les pré-chocs forment une cascade de déclenchement de séisme à séisme. Le modèle de nucléation asismique : une phase de nucléation asismique précède le choc principal et accélère vers la rupture, déclenchant de petites aspérités pré-chocs précurseures. Le modèle de chargement asismique : Les pré-chocs sont le fait d'une cascade de déclenchement et d'un chargement asismique "indépendant" du séisme principal

et ne permet pas de l'anticiper.

Dans un deuxième modèle, le "modèle nucléation", les séismes pré-chocs sont des traceurs passifs d'une phase de nucléation asismique du choc principal. Pendant cette phase de nucléation, la portion de faille du futur choc principal commence par glisser lentement et asismiquement (i.e.; Un glissement lent de la faille qui ne radie pas d'ondes sismiques majeures) avant d'accélérer vers une rupture dynamique (i.e.; Un glissement rapide qui radie des ondes sismiques). Cette lente nucléation asismique peut charger et déclencher de petites aspérités, entraînant une accélération de l'activité sismique pré-choc avant la rupture principale. Ici, l'activité de la séquence pré-chocs a un potentiel prédictif fort sur le choc-principal, car elle est intrinsèquement reliée aux prémices de la grande rupture.

Enfin, on peut également considérer un modèle mixte, le "modèle de chargement asismique", dans lequel glissement asismique et cascade de séismes coexistent. Ici, les cascades de séismes peuvent être complétées et excitées par un glissement asismique sur certaines portions de faille. Le glissement asismique induit des variations de contraintes et charge des portions adjacentes de la faille, pouvant déclencher certains séismes et accélérer les cascades de déclenchements. Dans ce modèle, le potentiel prédictif de l'activité pré-choc est un peu près équivalente au modèle cascade, sans lien causal avec l'arrivée d'un futur choc principal. Le déclenchement d'un grand séisme est possible seulement si la faille est suffisamment chargée pour observer une grande rupture. Néanmoins, l'observation d'un glissement asismique peut indiquer une perturbation supplémentaire de la faille, qui peut augmenter la probabilité de déclencher une grande rupture par rapport au modèle cascade.

D'une autre part, les efforts de la communauté sismologique ont permis depuis quelques années des améliorations significatives des réseaux d'observation sismologiques et géodésiques à proximité des failles. Ces améliorations ont principalement été portées par une densification des réseaux de détection et par des améliorations majeures des algorithmes de traitement des données sismologiques et de détection des séismes. Ces nouveaux grands volumes de données offrent une opportunité sans précédent pour étudier en détail les failles actives et les séismes pré-chocs. L'objectif de cette thèse de doctorat est d'explorer les possibles mécanismes de génération des séismes pré-chocs et leur lien possible avec les chocs principaux au regard des modèles présentés précédemment. Pour avancer sur cette question, j'ai utilisé des catalogues de sismicité haute définition, incluant de nombreux séismes de très faible magnitude, suspectés d'aider à la détection de précurseurs asismiques. Ces catalogues de sismicité couvrent de longues périodes de temps pour étudier en détail les séismes pré-chocs au regard des autres activités sismiques de la région, lorsqu'il n'y a pas de grands séismes. Dans cette thèse, j'ai étudié plusieurs séquences de séismes pré-chocs en Californie et au Chili. J'ai utilisé une approche statistique pour tester si les variations du taux de sismicité peuvent être expliquées par le modèle cascade ou si une activité inhabituelle existe dans les séquences pré-choc. Pour cela, j'ai choisi comme hypothèse nulle des modèles de sismicité temporelle décrivant le déclenchement entre séismes. J'ai également étudié en détails le lien entre sismicité et glissements asismiques en analysant les séismes répétitifs et des observations géodésiques.

Séquences pré-chocs en Californie du Sud: peu de différences avec des cascades de déclenchements

Dans un premier travail, j'ai analysé de manière systématique et à l'aide d'outils statistiques de nombreuses séquences pré-chocs observés en Californie du Sud. Cette analyse se base sur un récent catalogue de séismes haute définition construit par « template-matching », couvrant la période 2008-2018 (Ross et al., 2019b). Le template-matching est un algorithme qui permet la détection de petits séismes, cachés dans le bruit sismique enregistré par les sismomètres, en calculant la corrélation croisée entre un séisme déjà identifié et les enregistrements continus des stations. Ce catalogue très complet a permis de détecter énormément de nouveaux séismes de faible magnitude et d'augmenter la résolution de la sismicité de la région.

En utilisant le même catalogue, deux études précédentes (Trugman & Ross, 2019; Ende & Ampuero, 2020) ont suggéré que les choc-principaux étaient souvent (jusqu'à 70% des chocs principaux) précédés d'une sismicité anormalement élevée. Ces résultats suggèrent qu'un signal spécifique existe pendant les séquences pré-chocs, potentiellement lié à une phase de préparation de la rupture principale. Cependant, les modèles statistiques utilisées dans ces études ne prennent pas complètement en compte les variations de sismicité induites par les déclenchements de séisme à séisme, notamment au cours des séquences de répliques. Un certain nombre de séquences pourraient donc être expliqué par des cascades de déclenchement.

Pour compléter leurs observations, j'ai testé la sismicité pré-chocs de la Californie du Sud avec le modèle Epidemic Type Aftershock Sequence (ETAS). Ce modèle permet de mieux contraindre les augmentations du taux de sismicité pendant les séquences de répliques et de mieux modéliser le modèle cascade. Ce modèle statistique permet de décrire la sismicité au cours du temps comme une simple superposition de deux processus : un taux de fond stationnaire, décrivant un chargement tectonique constant et un taux de sismicité déclenché, représenté par la loi d'Omori-Utsu de chacun des séismes précédents. En d'autres termes chaque séisme a une probabilité d'être déclenché soit par le taux de fond stationnaire ou par un des séismes avant lui.

J'ai sélectionné 53 chocs principaux de magnitude $M > 4$ (Voir Figure 3) et j'ai extrait toute la sismicité sur 10 ans dans une fenêtre spatiale de 20x20 km^2. Pour chacun de ces sous-catalogues, j'ai inversé les paramètres ETAS qui représentent le mieux la sismicité observée sur 10 ans. Ensuite, j'ai estimé la probabilité que le modèle ETAS puisse expliquer les variations de sismicité observée dans une fenêtre glissante de 20 jours (Voir Figure 2).

Grâce à cette analyse, je montre que seulement 10 des 53 chocs principaux sont précédées d'une activité sismique significativement plus élevée que celle attendue par le modèle ETAS (Voir Figure 3). Donc, une activité anormale des séismes pré-choc en Californie du Sud est relativement rare lorsqu'on prend en compte les interactions et les déclenchements entre séismes. De plus, seules 3 des 10 séquences pré-chocs anormales présentent une anomalie uniquement spécifique à la séquence pré-choc. Les 7 autres séquences sont situées dans des régions où d'autres anomalies sont fréquemment observées sur les 10 ans sans être liées à l'occurrence d'un choc principal. Ces résultats suggèrent que les séismes pré-choc en Californie du Sud sont globalement bien expliqué par un modèle de déclenchement consistant avec le modèle cascade. D'autre part, même s'ils sont rares, les 3 cas anormaux sont néanmoins trop nombreux pour n'être qu'une anomalie statistique pour un échantillon de 53 chocs principaux. Ces séquences pré-chocs ont besoin d'un autre processus physique pour expliquer l'activité sismique et qui peut être lié à un forçage tectonique supplémentaire potentiellement relié au déclenchement du choc principal.

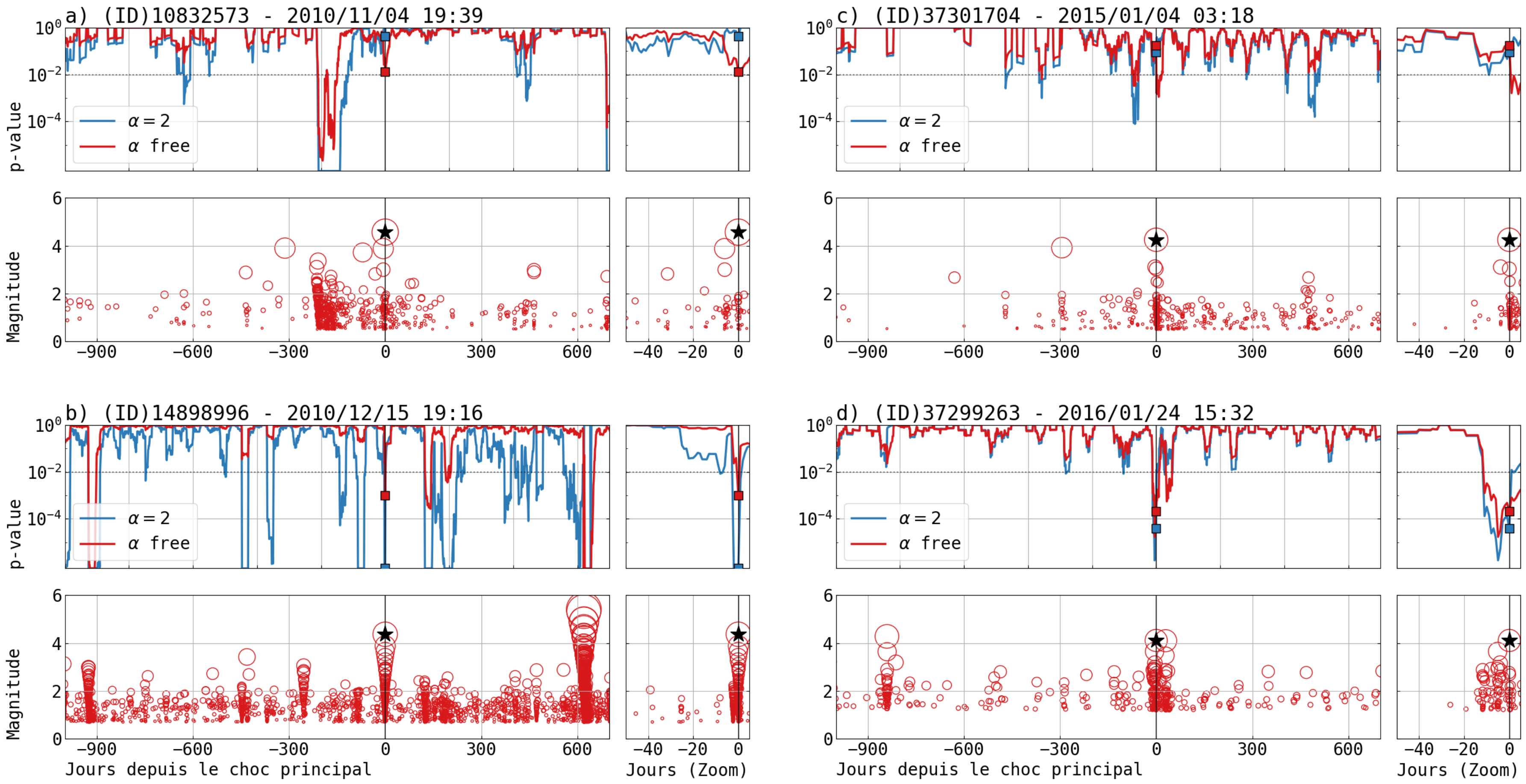

FIGURE 2: Analyse de la sismicité avec le modèle ETAS pour 4 des 53 chocs principaux en Californie du Sud (Étoile noire à t=0). La sismicité est testée à l'aide d'une fenêtre glissante de 20 jours, sur l'ensemble des 10 ans. Les chocs principaux correspondent à l'ID (a) 10832573, (b) 37301704, (c) 14898996 and (d) 37299263. (Graphique supérieur) La probabilité p que le modèle ETAS explique la sismicité sur les 20 derniers jours. Les deux courbes correspondent à des paramétrisations différentes du modèle ETAS (α=2 and α free). Les p-values de la fenêtre pré-choc (les 20 derniers jours avant le choc principal) sont présentée par les carrés de couleur. Le seuil de confiance du modèle ETAS est fixé à p=0.01 et est représenté par la ligne horizontale pointillée. Les p-values en dessous de ce seuil indique que le modèle ETAS ne peut pas expliquer la sismicité avec un seuil de confiance de 99%. (Graphique inférieur) Magnitudes au cours du temps de la sismicité observé autour du choc principal dans une fenêtre de $20 \times 20\,\mathrm{km}^2$. Les graphiques de droite sont un zoom sur la fenêtre pré-choc.

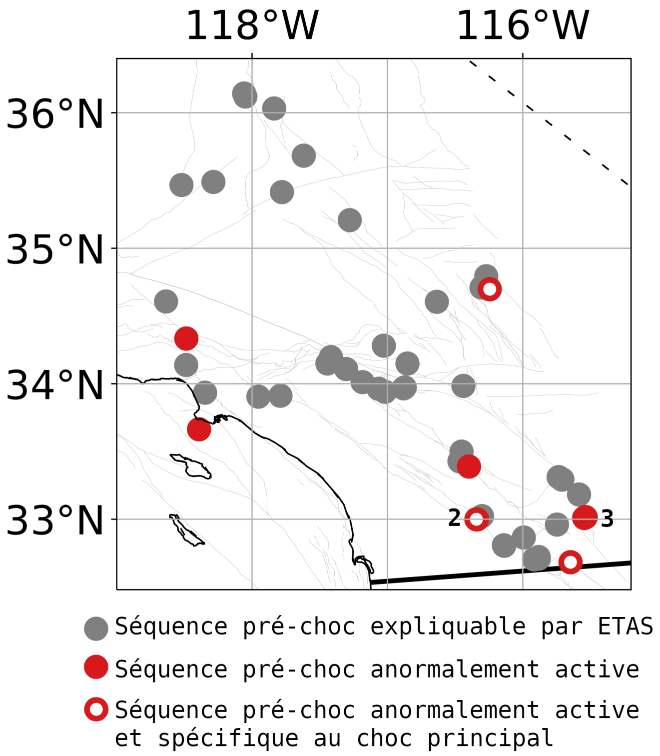

FIGURE 3: Carte de la Californie du Sud présentant la localisation des 53 chocs principaux et les résultats de l'analyse de leurs séquences pré-chocs. Les numéros en gras indiquent le nombre de chocs principaux situé dans la même zone.

Un glissement asismique transitoire à l'origine de la séquence sismique de 2017 à Valparaiso, depuis les séismes pré-chocs jusqu'aux répliques.

Après cette première étude statistique générale de plusieurs séquences pré-chocs en Californie, je me suis intéressé à une séquence pré-choc particulière au Chili. Ici, l'objectif est d'étudier plus en détail les possibles interactions entre la sismicité pré-choc et les glissements asismiques pour mieux comprendre leurs liens avec une possible phase de nucléation du choc principal. Dans ce chapitre, j'ai étudié une séquence de séismes observée en 2017 à Valparaiso (Chili). Cette séquence inclut un choc principal de magnitude $M_w = 6.9$ et a été précédé par une intense sismicité pré-choc de deux jours, avec de nombreux séismes de forte magnitude ($M > 5$). Le dernier élément surprenant de cette séquence est qu'un glissement asismique a été détecté par deux études précédentes (Ruiz et al., 2017; Caballero et al., 2021), avant et pendant la séquence pré-choc. La présence conjointe d'une intense activité sismique et d'un glissement asismique durant la séquence pré-choc est une bonne occasion pour comprendre comment les 2 processus interagissent, comment ils peuvent s'inscrire dans les différents modèles conceptuels présentés en introduction (Cascade, Phase de nucléation asismique ou chargement asismique) et s'ils sont reliés au déclenchement du choc principal de $M_w = 6.9$.

Pour cela, j'ai analysé en détails l'activité sismique et asismique pendant toute la séquence, depuis la séquence de pré-choc jusqu'à plusieurs jours après le choc principal, grâce à un catalogue de sismicité de haute résolution de 2016 à 2021. J'ai construit ce catalogue grâce à de récents outils de détection. Notamment, j'ai utilisé un récent réseau neuronal profond entraîné spécifiquement à détecter les phases sismiques P et S des séismes à partir des enregistrements continus des sismomètres (Mousavi et al., 2020). Les phases détectées ont ensuite été associées à un séisme et localisées. J'ai également mesuré pour chaque séisme une magnitude. Le grand nombre de détections automatiques permis par cet outil m'a permis de construire un catalogue très complet de la région avec plus de 10 000 détections autour du choc principal, augmentant la résolution de la sismicité de la région par rapport au catalogue officiel Chilien.

Dans ce catalogue, à l'instar des travaux de Californie, j'ai d'abord cherché les augmentations anormales du taux de sismicité par rapport à 2 modèles statistique

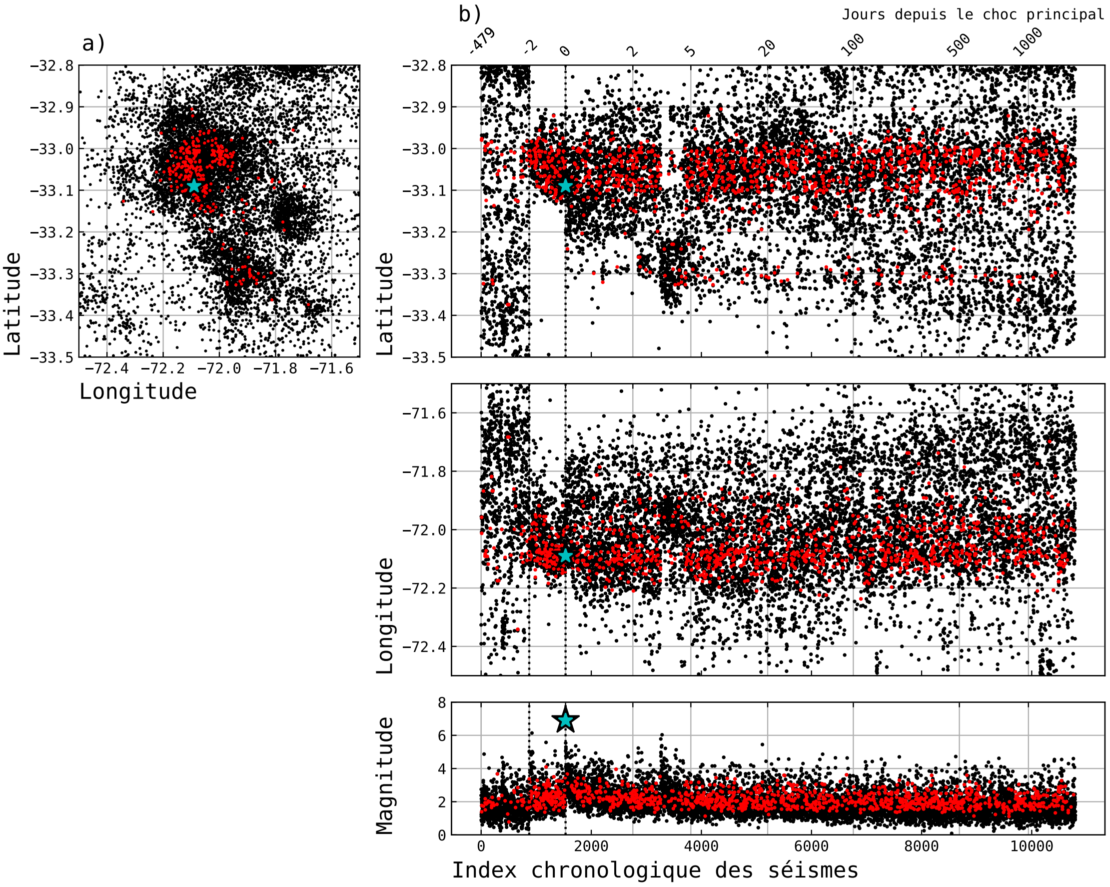

FIGURE 4: Évolution spatiale et temporelle de la sismicité du catalogue (Points noirs) et de ses séismes répétitifs (Points rouges). (a) Localisation horizontale. (b) Évolution de la Longitude, Latitude et des Magnitudes en fonction de l'index chronologique des séismes (i.e. ; L'ordre d'apparition depuis le début). L'équivalence en jours est graduée au sommet du graphe supérieur. Les deux lignes verticales pointillées montrent l'index/temps du premier séisme pré-choc et du choc principal.

de déclenchement de séisme à séisme : Le modèle Epidemique-Type-Aftershock Sequence (ETAS) et le modèle Model-Independent-Stocasting-Declustering (MISD). Le modèle MISD est très similaire au fonctionnement du modèle ETAS à la différence que la loi de déclenchement des répliques en fonction de la magnitude n'est pas explicite (i.e. ; au contraire de la loi d'Omori-Utsu pour ETAS), mais est inversée directement depuis les données. Ces deux modèles permettent donc de modéliser les variations de sismicité comme une superposition d'un taux de fond constant et d'une sismicité déclenché par les magnitudes précédentes.

Grâce à ces deux modèles, j'ai mis en évidence une activité sismique anormalement élevée depuis le début dans la séquence pré-choc et qui persiste plusieurs jours après le choc principal (Voir Figure 5.d pour ETAS et 5.e pour MISD). Cette anomalie montre que les variations de sismicité ne peuvent pas être complètement expliquées par un taux de fond stationnaire et le déclenchement de séismes. Un forçage sismique spécifique semble nécessaire pour expliquer l'activité sismique pré-choc et une partie de la séquence post- choc principal. Comme un glissement asismique transitoire a précédemment été observé dans la séquence pré-choc, il est probable qu'il soit responsable de ce forçage supplémentaire. Cependant, les précédentes études n'ont pas analysé ce glissement après le choc principal, ou notre anomalie sismique semble persister.

J'ai donc étudié en détails les signatures de ce glissement asismique depuis la séquence pré-choc jusqu'à plusieurs mois après le choc principal. D'abord, j'ai détecté et localisé les séismes répétitifs dans mon catalogue. Ces séismes répétitifs sont co-localisés et présentent des formes d'ondes quasi-identiques. Ils sont souvent interprétés comme originaire d'une même aspérité du plan de faille, successivement chargée et déclenchée par un glissement asismique encerclant l'aspérité. Traquer l'activité de ces séismes répétitifs permet alors d'estimer l'évolution du glissement asismique sur la faille. J'ai mis en évidence de nombreuses familles de séismes répétitifs pendant la séquence de 2017, depuis la séquence pré-choc jusqu'à plusieurs mois/années après le choc principal (Voir Figure 4). Ces séismes répétitifs permettent d'estimer que le glissement asismique commence dès le début de la séquence pré-choc, avec un fort taux de glissement et persiste en décélérant après le choc principal, sans être impacté par les autres grands séismes de la séquence. On ne distingue également pas d'accélération du glissement vers le choc principal (Voir Figure 5.c). Avec l'aide de Yuji Itoh et Anne Socquet du laboratoire grenoblois "ISTerre" nous avons pu confirmer ces observations à l'aide observations GPS à haute fréquence. Nous avons mis en évidence une déformation transitoire vers l'Est juste avant le premier pré-choc et qui persiste quasi continûment plusieurs jours après le choc principal (Voir Figure 5.a-b).

Ces observations montrent que les anomalies de sismicité et le glissement sont conjointement observés sur la même période, depuis les premiers pré-chocs jusqu'à plusieurs jours après le choc principal. De plus, le glissement et la sismicité n'accélèrent pas vers le choc principal, mais semblent au premier ordre continu pendant toute la séquence sismique. Il paraît donc peu probable que les signaux pré-chocs correspondent à une phase de nucléation accélérant vers le choc principale ou à une seule cascade de déclenchement. Ici, le glissement asismique semble agir comme un chargement asismique transitoire de la faille, depuis la période pré-choc jusqu'à la période post-choc. Ce forçage asismique a favorisé le chargement et la rupture de multiples portions bloquées du plan faille et a ainsi excité l'activité sismique. Ce forçage a fini par déclencher une grande portion bloquée de la faille, interprétée a posteriori comme le choc principal, mais sans que le forçage soit dirigé vers elle.

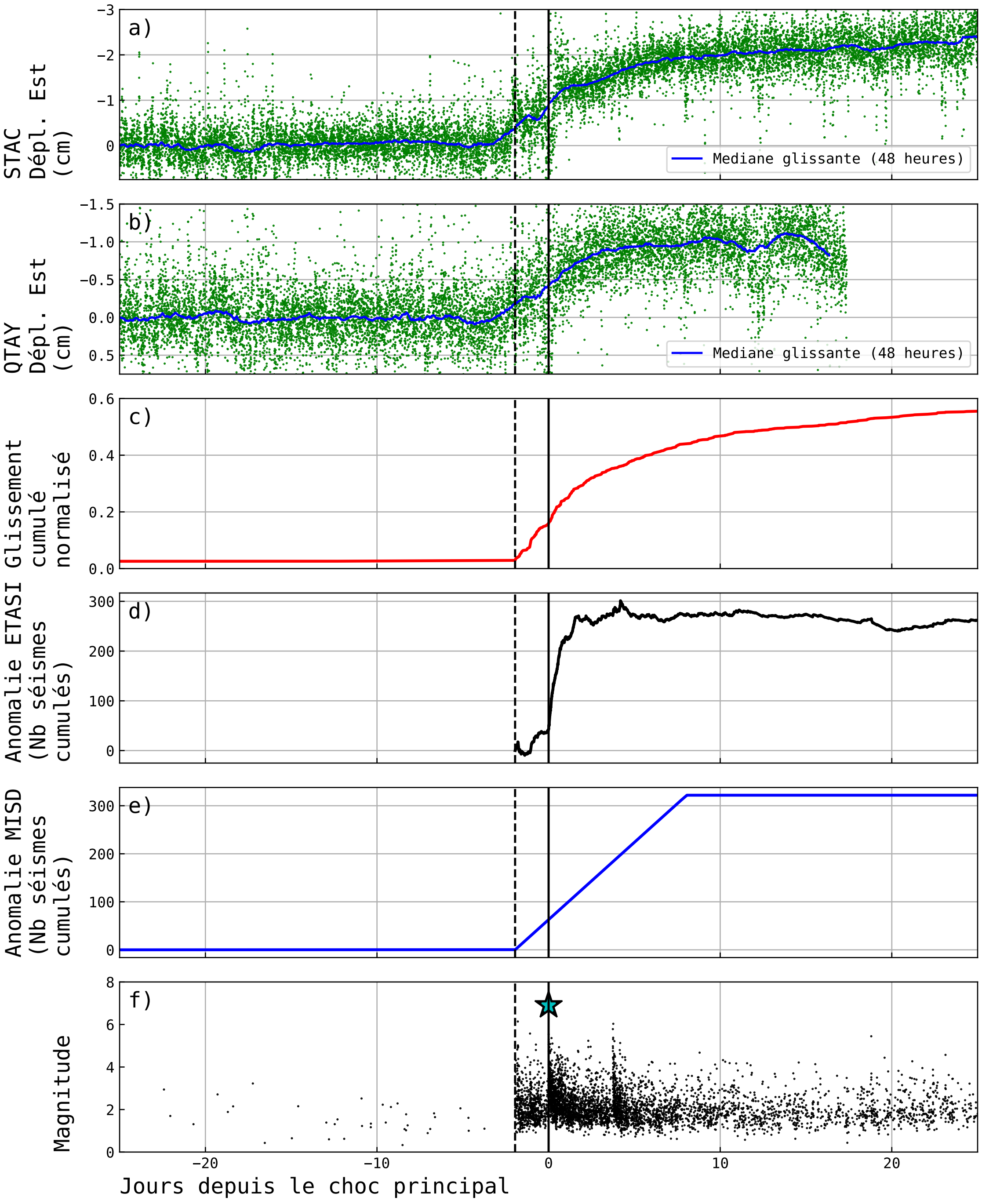

FIGURE 5: Résumé des analyses de l'activité sismique et du glissement asismique pendant la séquence de 2017 à Valparaiso (Chili). (a) Positions GPS haute-fréquence dans la direction est de la station STAC. Les données ont préalablement été filtrés et débruité puis retranchés des signaux co-sismique des séismes majeurs de la séquence. La ligne bleu est la médiane glissante des positions GPS calculée avec une fenêtre de 48 heures. (b) Pareil que (a) mais pour la station QTAY. (c) Glissement asismique cumulé et normalisé estimé à partir de l'analyse des séismes répétitifs. (d) Anomalie ETAS cumulée (i.e.; Nombre de séismes) observée depuis le début de la séquence pré-choc. (e) Anomalie MISD cumulée (i.e.; Nombre de séismes) observée depuis le début de la séquence pré-choc. (f) Temps et magnitudes du catalogue zoomé sur la séquence d'avril 2017. La ligne noire verticale correspond au temps du choc principal, celle en pointillé correspond au temps du premier séisme pré-choc.

Conclusion générale et perspectives

Les travaux présentés dans cette thèse montrent que l'utilisation de catalogues de sismicités haute résolution permettent d'avancer sur la compréhension des processus de faille qui précédent les chocs principaux. Les deux exemples analysés ici semblent contredire à la fois que : 1 - les pré-chocs sont la conséquence systématique d'une phase nucléation asismique du choc principal ; 2 - les pré-chocs sont le résultat seul d'une cascade de déclenchement de séismes à séismes. En effet, dans nos exemples, les signaux détectés avant les chocs principaux ne sont ni systématiquement anormaux ni ne semblent accélérer vers le choc principal. De plus, même si le modèle cascade explique la vaste majorité des variations sismiques, il ne suffit pas à expliquer certaines séquences pré-chocs anormalement actives. Plutôt, il semble que les glissements asismiques transitoires jouent un rôle important dans la génération, occasionnel, d'anomalies dans l'activité sismique. Les variations de contraintes induites par les glissements asismiques transitoires paraissent responsables de fortes perturbations de la faille et de l'activité sismique. Lors de ces forçages asismiques transitoires, la probabilité de charger et déclencher une grande rupture est augmentée, mais sans toutefois être garantie.

Les résultats de cette thèse suggèrent également qu'une meilleure compréhension des signaux pré-chocs implique d'analyser entièrement les séquences sismiques, comprenant à la fois l'activité des pré-chocs et celle post-choc principal. En effet, l'interprétation de signaux détectés dans une fenêtre qui s'arrête brusquement avec le choc principal est souvent fortement biaisé par la connaissance du futur déclenchement d'une forte magnitude. Par conséquent, la continuité des signaux avant et après l'occurrence du choc principal doit être étudiée avant de conclure sur la possible nature préparatoire d'un signal pré-choc.

Il est clair que des travaux supplémentaires restent nécessaires pour complètement comprendre les séquences pré-chocs et les processus de faille qui précèdent les chocs principaux. Des études supplémentaires restent nécessaires dans d'autres régions du monde pour évaluer en détail l'interaction entre sismicité, glissement asismique et un possible lien avec le déclenchement des fortes magnitudes. La récente disponibilité de vastes volumes de données sur une longue période de temps est un des points clef des futures recherches. Elle permettra à terme d'augmenter le nombre de chocs principaux à analyser et permettra de tirer des conclusions plus solides. En ce sens, les catalogues de sismicité haute définition et les mesures géodésiques couvrant plusieurs cycles sismiques (i.e.;

plusieurs chocs principaux) sont particulièrement nécessaires pour mieux contraindre une possible singularité dans les processus pré-chocs.

Chapter 1

Introduction

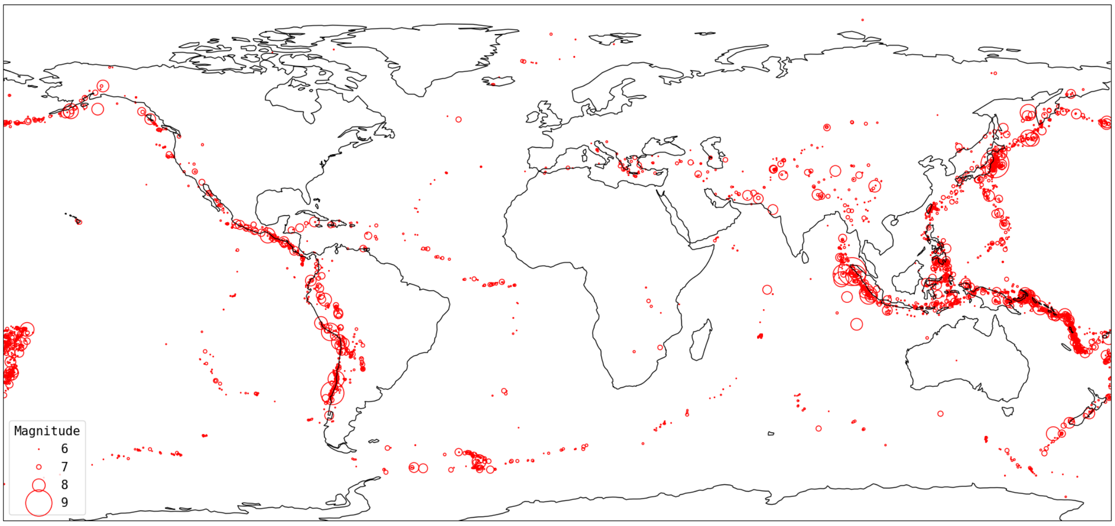

FIGURE 1.1: Worldwide earthquakes with magnitudes $M_w \geq 6$ from 2000 to 2020 (retrieved from USGS, the United States Geological Survey).

1.1 Large earthquakes and seismic activity

The Earth is a geodynamic system that slowly cools its hot core by mantle convection (Hanks & Anderson, 1969). At the Earth's surface, this cooling induces diverse movements of lithospheric blocks (i.e., upper mantle and crust). These moving blocks are known as tectonic plates (Le Pichon, 1968). At the edges of tectonic plates, the relative motion can create different plate boundaries with a convergent, divergent or a transform motion. At plate boundaries, we observe a dense network of crustal faults where stresses and strains are accumulated by friction, and sometimes suddenly released by large earthquakes. Such sudden releases of energy on faults radiate seismic waves that propagate through the Earth and can severely affect surrounding environments and infrastructures. Figure 1.1 shows the largest earthquakes recorded worldwide between 2000 and 2020. Most of them are concentrated at tectonic plate boundaries, mainly at continental coastal regions and mid-oceanic ridges but sometimes within continents. Largest earthquakes can be observed around the Pacific Ocean in Asia, Indonesia or the western coast of North and South America. These coastal regions are often densely populated and can be severely affected by large earthquakes.

1.1.1 A rapid slip on a fault

Tectonic earthquakes occur on faults, that are often idealized as planar structures within the Earth lithosphere. More specifically, an earthquake happens when one side of the fault is suddenly slipping with respect to the other side after an inter-seismic tectonic loading period (Stein & Wysession, 2008). During the interseismic period, friction resistance locks the two fault blocks. As the tectonic motion continue, stresses rise on locked asperities. A slip can occur when the tectonic loading has accumulated enough elastic strain energy on the locked fault to drive a rupture propagation. When the stress is sufficiently high to break locked asperities, the fault suddenly slips from a few seconds to a few minutes, releasing the stored strain energy. Energy is released mainly by heat and the fracture propagation process, but some is also radiated through the Earth as seismic waves, producing recordable evidences of the earthquake. This cyclic accumulation of strain and stress followed by a fault slip is known as the elastic rebound theory (Reid, 1910).

Figure 1.2 shows a sketch of the fault interface in a subduction zone during the tectonic loading and during an earthquake. Both radiated seismic waves and ground displacements induced by the fault slip can be recorded at the surface by seismometers and geodetic stations. Thanks to these remote observations, we are able to constrain certain source properties of the in-depth fault slip.

Depending on various factors such as the fault frictional properties, as well as the stress and strain conditions, a fault can sometimes slip smoothly without significantly radiating seismic waves (Shearer, 2019). When this occurs, it is referred to as aseismic slip. Over the last two decades, many studies have highlighted transient episodes of aseismic slip on faults known to lack any major earthquakes (Rogers & Dragert, 2003; Lohman & McGuire, 2007; Gomberg & the Cascadia 2007 and Beyond Working Group, 2010; Peng & Gomberg, 2010; Beroza & Ide, 2011). In these cases, the release of the strain energy accumulated during the tectonic loading phase is not sudden and rapid as for usual earthquakes, but is released over longer periods of time (a few minutes to a few months) with the slow slip of parts of the locked fault. Such transient aseismic fault slip is sometimes referred to as slow-slip events (SSE) or slow earthquakes. Figure 1.3, shows a sketch of an aseismically slipping section of a locked fault. The slow-slip event can be tracked down by geodetic measurements or with a detailed analysis of seismic signals such as tremors or repeating earthquakes (See section 1.4.2). During such a slow-slip event, displacement on either side of the fault occurs over a

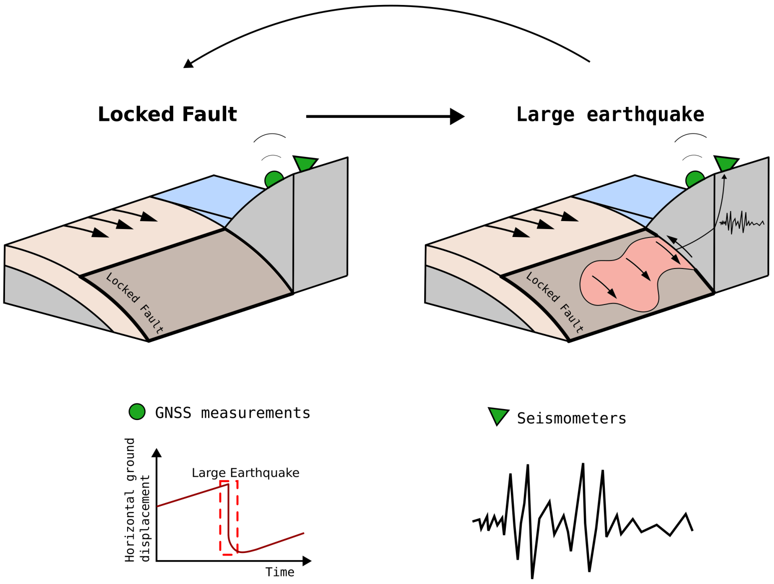

Figure 1.2: A schematic view of a tectonic earthquake on a subduction zone. The tectonic strain accumulates on a locked fault during the interseismic period. It induces a long-term ground displacement in the direction of the tectonic motion, which can be recorded by geodetic measurements. When the stress is sufficiently high, a rupture propagates along the fault, releasing the two blocks by slip and generating a large earthquake. The slip radiates seismic waves that can be recorded by seismometers. The relative motion of the fault blocks causes a sudden displacement of the ground in the opposite direction to the tectonic motion that can be recorded by geodetic measurements.

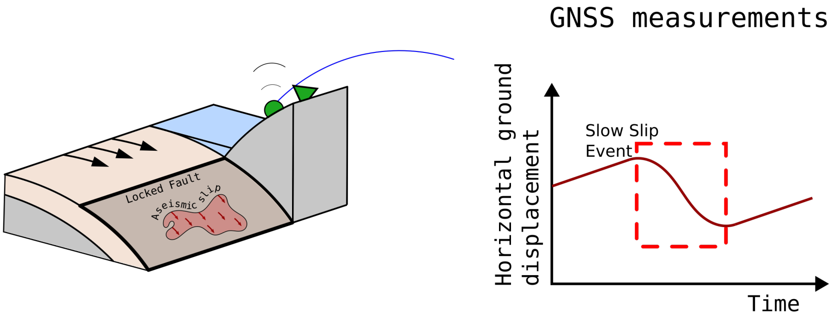

FIGURE 1.3: A schematic view of a slow-slip event. Parts of the locked fault slip slowly, releasing strain energy without producing a large earthquake. An episodic ground displacement, similar to an earthquake, can be recorded at the surface but over a longer period of time.

much longer period than during an earthquake. It is still unclear what ultimately mediates a seismic or aseismic regimes on a fault, but it likely relates to local stress conditions along with rocks properties, temperature and fluid circulations on the fault (Scholz, 1998).

1.1.2 Earthquake size and magnitude

The moment magnitude scale

A major source property to retrieve from an earthquake is an estimate of its size. We know that earthquakes produce static displacements and radiate seismic waves. Such static displacements and seismic waves can be interpreted as the consequence of a strain field change induced by the slip on the fault. The energy budget during an earthquake can be summarized as (Kanamori & Rivera, 2006):

$$E_T = E_R + E_{NR}, \tag{1.1}$$

where E_T is the total elastic strain energy released during the rupture. E_R is the radiated energy and E_{NR} the non-radiated energy. In practice the non-radiated energy E_{NR} can be decomposed in a frictional term (e.g., heat) and fracture energy. E_{NR} is difficult to measure because earthquakes occur at depth and we usually don't have near fault data. On the other hand, E_R can be estimated using seismological data (i.e., seismic waves).

With geodetic and seismological data we can estimate the static surface displacement induced by an earthquake. From this, we can estimate a seismic moment M_0 (Keiiti, 1966; Aki & Richards, 2009). According to Kanamori (1977), the seismic moment is at first order proportional to the available elastic strain energy released by the earthquake (that is E_T in equation 1.1 minus the energy dissipation as heat). The seismic moment can be defined as:

$$M_0 = \mu S D, \tag{1.2}$$

Where M_0 is the seismic moment (N.m) of the earthquake, μ is the shear modulus (Pa) of the surrounding rocks, S is the slip area (m^2) and D is the average slip (m) on the fault. In practice, M_0 can be estimated from the moment tensor inversion of long-period seismic data or using finite-fault models derived from seismic and geodetic data. With Equation 1.2, we see that the larger the slip area and the larger the amount of slip, the larger the seismic moment. More specifically, Kanamori & Anderson (1975) shows that, to first order, S scales with $M_0^{\frac{2}{3}}$, and D with $M_0^{\frac{1}{3}}$.

To link the seismic moment with an earthquake magnitude, Kanamori (1977) defined the moment magnitude scale (M_w) based on the measure of the seismic moment:

$$M_w = \frac{2}{3}(\log M_0 - 9.1), \tag{1.3}$$

The moment magnitude value is therefore directly related to the earthquake size (i.e., the fault size and amount of slip) and a good proxy for the elastic energy released. For example, the great 2011 Tohuku earthquake broke a fault surface of about 320 km by 100 km and has a seismic moment of $5.31 \times 10^{22}\ N \cdot m$ (GCMT). This value corresponds to a moment magnitude $M_w = 9.08$.

Other magnitude scales like the local Richter magnitude scale M_L (Richter, 1935) or the surface wave magnitude M_S (Gutenberg & Richter, 1956) have been historically used. While these magnitudes provide a good relative estimate of the earthquake size, they are only based on the measure of maximum amplitudes at higher-frequency seismic waves and no longer work properly for large earthquakes (Magnitude scale saturation) or for events with unusual radiation properties (e.g., low-frequency earthquakes, slow-slip events). The moment magnitude (M_w) naturally extend the concept of magnitude to larger earthquakes and to all types of events.

Frequency of magnitudes

As shown in Figure 1.1, we can see that large magnitude earthquake are less common than small events. From the same dataset, we can extract the frequency of each magnitude class and plot it in a log-linear plot (Figure 1.4). We observe a log-linear relation between the frequency of earthquake and their magnitude. Large magnitude earthquakes are far less frequent than lower magnitude earthquakes. This empirical relation is known as the Gutenberg-Richter law (Gutenberg & Richter, 1944) and can be written as follows:

$$\log N = a - bm \tag{1.4}$$

N is the number of earthquake with magnitude greater than m. a is a constant scaling the number of observed earthquakes and b (so-called b-value) is scaling the slope of the magnitude distribution. Using only earthquakes with magnitudes above a given threshold $m > m_c$, we can get rid of a and derive a probability density function of the Gutenberg-Richter law:

$$\begin{aligned} f(m) &= \beta e^{-\beta(m-m_c)} \quad ; m \geq m_c, & (1.5) \\ \beta &= b \ln 10, & (1.6) \end{aligned}$$

The threshold magnitude m_c is often referred to as the completeness magnitude. In fact, the detection capability of a network depends on many parameters, such as the density and distribution of seismic stations, the condition of the site or the level of seismic noise. Depending on these conditions, the detection of small magnitude earthquakes can be difficult and often incomplete. Therefore, the level of completeness m_c is defined as the lowest magnitude at which the vast majority of earthquakes can be detected with confidence.

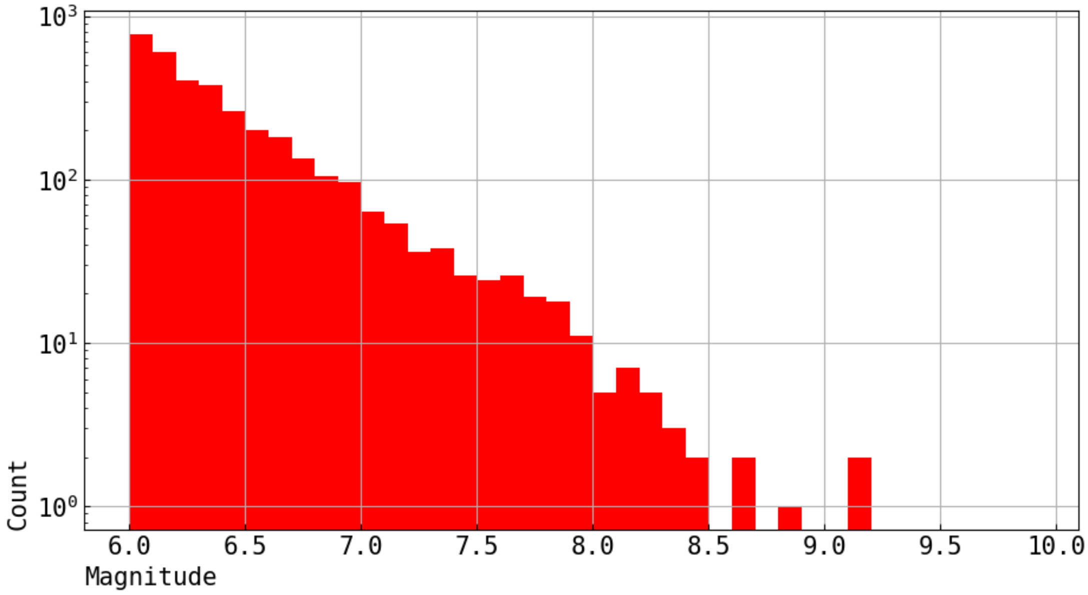

FIGURE 1.4: Magnitude-Frequency distribution of worldwide earthquakes with magnitude $M \geq 6$ from 2000 to 2020 (retrieved from USGS).

The Gutenberg-Richter law is an empirical property of earthquake magnitudes and is found to be scale invariant and observed for various range of magnitude values (if the earthquake detection is complete). The log-linear distribution holds for large magnitude earthquakes at global scales (Figure 1.4), for regional earthquakes at local scales (Utsu, 1971; Wiemer et al., 1998; Nishikawa & Ide, 2014), up to microscopic earthquakes within laboratory experiments (Scholz, 1968; Scholz, 2015). The b-value can however vary depending on the studied region. In most cases, b is found to be close to 1 as at global scale for example, but can be observed from $b = 0.3$ up to $b = 2.5$ (El-Isa & Eaton, 2014). Origin in the variations of the b-value is still debated but seems to take it sources with effective stress changes on faults (Scholz, 2015).

1.1.3 Mainshocks, aftershocks and foreshocks

The Gutenberg-Richter law points out that small earthquakes are much more common than large ones. This means that for every large earthquake breaking a large fault area, we observe many smaller earthquakes breaking smaller parts of the fault. The Gutenberg-Richter law therefore suggests that small earthquakes can be extremely frequent, as an almost continuous regime of small ruptures if m_c is very small. Such variety in size and frequency of earthquakes questions how the seismic activity can vary with space and time, if seismic events can interact and if there is a specific activity before and after large earthquakes. In a given region, the space and time evolution of the earthquake activity is referred to as seismicity. An example of the Japanese seismicity that included the occurrence of the great $M_w = 9.1$ Tohoku earthquake in 2011 is presented in Figure 1.5. We can see that the seismicity is intensely clustered just before and after the $M_w = 9.1$ earthquake. The largest earthquake seems to greatly impact the seismicity rate for months after its occurrence.

Mainshocks

Because of the amount of energy released and the impact of their destructive seismic waves on society, largest earthquakes often receive the most attention compared to the more frequent smaller earthquakes. Therefore, the largest earthquake within a seismic sequence in a given region of space and time is often referred to as the "mainshock".

It should be noted that this definition of a mainshock, although natural, is also quite arbitrary. This selection of a main earthquake within a seismic sequence tends to dismiss other significant earthquakes before and after the mainshock that can still have a major impact on the surrounding region. For example, in the Tohoku sequence (Figure 1.5), we see that earthquakes cluster around the time of the $M_w = 9.1$ mainshock, with other significant large earthquakes before and after the mainshock. These lower (but still large) magnitude earthquakes are often considered as secondary ruptures related to the occurrence of the larger $M_w = 9.1$ earthquake. However, if such earthquakes had occurred at a different time or in a different region or if the $Mw = 9.1$ mainshock was not observed , they would probably be considered a mainshock themselves. This reminds us that there is still no clear difference between mainshocks and other large earthquakes: We are still unable to define mainshocks in real time until the seismic sequence is over. It's only when the seismic activity is back to the background seismic activity of the region that we can retrospectively state which earthquake was the mainshock.

In addition, earthquake sequences doesn't necessarily have a clear mainshock. Sometimes, several earthquakes can be observed one after the other within a similar magnitude range (Dal Zilio & Ampuero, 2023, for a recent example). In that case the mainshock definition is even more arbitrary and is often attributed to the first large earthquake of the sequence.

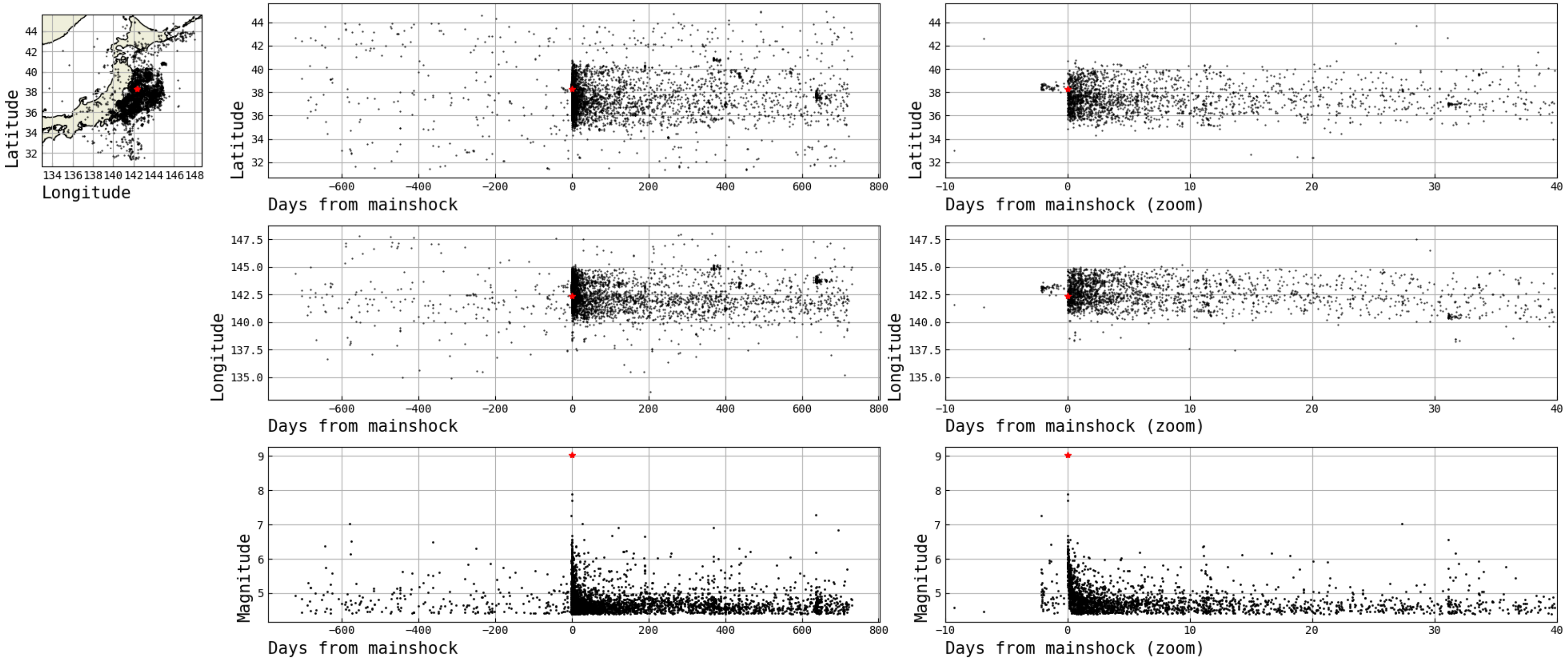

FIGURE 1.5: Seismicity of magnitudes $M \geq 4.5$ observed nearby the great $M_w = 9.1$ Tohoku earthquake (Red star), that occured on March 11, 2011 in Japan. The map shows the horizontal location of earthquake epicenters. The three left subplots show the time evolution of Latitudes, Longitudes and Magnitudes, respectively. The three right subplots are the same but zoomed close to the mainshock.

Foreshocks

The definition of foreshocks stems from the definition of a mainshock in a seismic sequence. Once a mainshock is defined, it seems natural to investigate the geophysical processes just before to decipher whether any precursor activity can be observed. In that way, any seismic activity clustered in space and time before a mainshock is often expected to be of great interest because it may reflect a possible preparatory process of the largest earthquake of the sequence. Such early seismic activity before a mainshock is often referred to as foreshock earthquakes or foreshock sequence.

With the example of the 2011 Tohoku sequence, we see that there is a distinct earthquake activity just before the mainshock (See zoom in Figure 1.5). We see an increase of the seismicity rate, quite distinct from the rate observed in the year before and close to the future mainshock epicenter. Here, the foreshock sequence is composed of large magnitude earthquakes up to $M_w \geq 7$. Such change in the seismic activity may reveal early geophysical processes driving the future earthquake sequence and its mainshock.

In practice, for the same reason that mainshocks are difficult to define, there is no clear definition of foreshock activity because we are still unable to detect earthquakes as foreshocks before we observe the mainshock, and thus before the seismic sequence is over. More generally, it refers to any seismic activity close enough to the mainshock epicenter and (but not necessarily) with an increased rate distinct from a previous quiet period.

Aftershocks

Referring again to the example of the Tohoku seismic sequence in Figure 1.5, we clearly see that earthquakes are clustered in time after the $M_w = 9.1$ mainshock. Such short-term increase of the seismicity rate after an earthquake is referred to as aftershock sequence. The first quantitative observations of aftershock sequences were reported by Omori (1895) after 3 large magnitude Japanese earthquakes in the late 19th century. He observed that the number of aftershocks tends to decrease with time after the mainshock and he derived an empirical power law decay, that can fit the aftershock rate $n(t)$ observed as a function of time, t, after mainshocks:

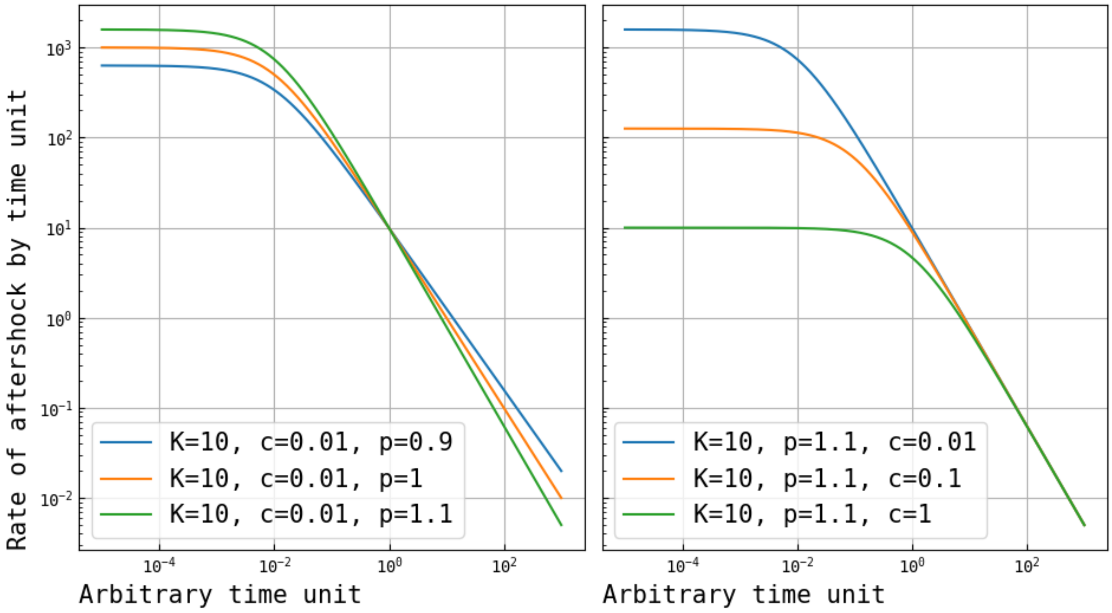

FIGURE 1.6: The Omori-Utsu law and the power law decay of aftershock rate. Left subplot shows variations of p value. Right subplot shows variations of the c value.

$$n(t) = \frac{K}{c+t}, \tag{1.7}$$

Here c and K are two constant parameters. Such power law decay has been found to fit well the seismicity rate observed after many large earthquakes over the world. However, to take into account some disparities in the power law decay of certain aftershock sequences, Utsu derived in 1957 a modification of the Omori law by including a new parameter p (Utsu, 1971; Utsu et al., 1995, and references therein) :

$$n(t) = \frac{K}{(c+t)^p}, \tag{1.8}$$

This modified version of the Omori law is referred to as the Omori-Utsu law and is a second major empirical relationship commonly used to characterize seismic activity. The Omori-Utsu law has been found to accurately describe the aftershock sequence of many earthquakes of different magnitudes, down to microearthquakes in laboratory experiments (Mogi, 1963b,a; Berg, 1968). Therefore, any large magnitude earthquake is expected to trigger its own aftershock sequence. We see from Figure 1.6 that the parameter p can control the power law decay with time. Usually, the p parameter is expected to be close to 1.1 but can occasionally take values from 0.6 up to 2.5 (Utsu et al., 1995). The parameter c imposes a constant rate for $t \leq c$ and also prevents the law to diverge at $t = 0$. Uncertainties persist on how to interpret c: It is sometimes though to be a consequence of an incomplete rate just after the mainshock because small earthquakes are often undetected when the rate is too high (Kagan, 2004). In that sense, the c value is sometimes believed to tend to $c = 0$ in complete catalogs, or at least to tend to the source duration of the triggering earthquake. Some studies also suggest that the c value rather reflects a source property of the aftershock process (Narteau et al., 2009; Davidsen et al., 2015).

The parameter K scales the global aftershock activity of the considered aftershock sequence. This value strongly depends on the magnitude of the triggering earthquake. The number of aftershocks triggered by an earthquake is expected to be log-linearly distributed with its magnitude when considering a common cutoff magnitude m_c (Ogata, 1988; Utsu et al., 1995; Hainzl & Marsan, 2008; Davidsen & Baiesi, 2016):

$$K(m) = Ae^{\alpha(m-m_c)}, \tag{1.9}$$

The main mechanism that is driving aftershock sequences is still debated, but it is likely because of the mainshock induced stress changes. Aftershocks are sometimes interpreted as the consequence of static or dynamic stress changes caused by the triggering earthquake (Harris, 1998), but can also be driven by an aseismic afterslip of the mainshock (Perfettini et al., 2018) or poro-elastic effects (Cocco & Rice, 2002).

Aftershock observations therefore indicate that earthquakes tend to increase the seismicity rate after them in a way that is well constrained empirically by the Omori-Utsu law. This implies that the seismicity rate is highly variable in space and time and is strongly dependent on the past distribution of magnitudes. Therefore, aftershock triggering must be taken into account when investigating space-time variations of the seismicity and linking it to any underlying geophysical process. Any seismicity rate increase associated with aftershock triggering can be interpreted as an expected increase and may not be indicative of any underlying driving process.

An increase in the seismicity rate that is not related to normal aftershock triggering or random fluctuations in a constant background rate is usually referred to as swarm-like seismicity. Swarm-like seismicity is therefore a deviation of seismic activity from its expected regime and is often interpreted as being driven by additional geophysical processes (e.g., transient aseismic slip, magma intrusion, fluid circulation, etc.).. The distinction between swarm-like seismicity and aftershocks is particularly important in this thesis for investigating the significance of foreshock seismicity rate increases and whether they reflect a preparatory process for mainshocks.

1.2 What is driving foreshock sequences?

Detecting and understanding a possible preparatory phase of large earthquakes remains one of the major challenge of modern seismology (Brodsky & Lay, 2014; Mignan, 2015). Foreshock earthquakes are often expected to reflect such preparatory process and many efforts have been made to assess their actual predictive power. In this Ph.D. thesis, I discuss the foreshock seismic activity often observed before mainshocks, its possible driving mechanisms and its link with mainshock occurrence. This section provides a quick review of the state of the art of foreshock knowledge and the major frameworks that may explain their occurrence before large earthquakes.

1.2.1 Foreshocks prevalence before mainshock

Seismologists have reported and studied foreshocks since the early development of seismology. One of the earliest formal descriptions of foreshocks was reported by Mallet (1862), before the Great Neapolitan Earthquake of 1857. Other foreshock observations were episodically reported around the world by various authors, and were already thought to help mitigate incoming large ruptures (see Richter, 1958, Chapter 6). However, the scarcity of foreshock observations in the early days of seismology, due to the poor ability to detect low-magnitude earthquakes, did not lead to a more systematic study of the foreshock phenomena until the early 1960s.

An early general study of foreshock sequences in Japan was presented by Mogi (1963a). He investigated more than 1500 mainshocks and found that at least 4% of them were preceded by foreshocks. Papazachos (1975) and Jones & Molnar (1976, 1979) later showed that at least half of the $M \geq 7$ mainshocks observed around the world were preceded by at least 1 foreshock earthquake in the vicinity of the future mainshock epicenter. Nowadays, with improvements in the detection of small earthquakes, detecting at least one foreshock earthquake is very likely because small earthquakes are expected to be extremely frequent (i.e., Gutenberg Richter law).

For this reason, a foreshock seismic activity is often considered significant only if its rates deviates from the 'usual' or 'background' seismic activity expected in the region. Because the seismicity rate strongly varies with time, defining the typical background seismic activity of a region is a challenging task. The choice of one background seismicity model over another may strongly impact the detection rate of an unusual foreshock activity. Nonetheless, one of the simplest null-hypothesis for the background activity is to consider earthquakes as a stationary Poisson process that can model random earthquake occurrences from a constant rate measured over previous years (Daley & Vere-Jones, 2003). Physically, a stationary background rate can model earthquakes driven by a constant inter-seismic tectonic loading. For example, following this approach using a catalog of Southern California with a low magnitude of completeness, Trugman & Ross (2019) estimated that about 72% of the mainshocks were preceded by a significantly high seismicity rate that deviates from the stationary Poisson process.

It is therefore quite common to observe foreshocks before a mainshock. The foreshock pattern appears to deviate from the stationary Poisson process and may be driven by more complex geophysical processes than a constant tectonic forcing. The question remains whether foreshocks can be interpreted as tracers of a preparatory process of mainshocks: Is their activity significantly different from other earthquakes that are not followed by a large earthquake? What is the actual physical mechanism driving their generation? Do they actually have predictive power for the upcoming mainshock? In the following section, I present several current models that attempt to explain foreshock generation.

1.2.2 The nucleation phase of a seismic rupture?

The spatial and temporal proximity of foreshocks to an impending large rupture is sometimes thought to highlight a fault process that is directly related to the nucleation of a mainshock. If foreshocks are driven by such a nucleation phase, tracking them could significantly help to mitigate the occurrence of future large earthquakes.

Theoretical and laboratory experiments

Friction theory and laboratory experiments shows that earthquake ruptures do not begin abruptly but are preceded by a slow slip phase accelerating over a finite nucleation zone (Das & Scholz, 1981; Dieterich, 1992; Ohnaka, 2000; Rubin & Ampuero, 2005; Latour et al., 2013; McLaskey, 2019). In these experiments, the nucleation zone is a slow-slipping region delimited by a growing rupture front. The nucleation zone grows up to a critical length before slipping dynamically and

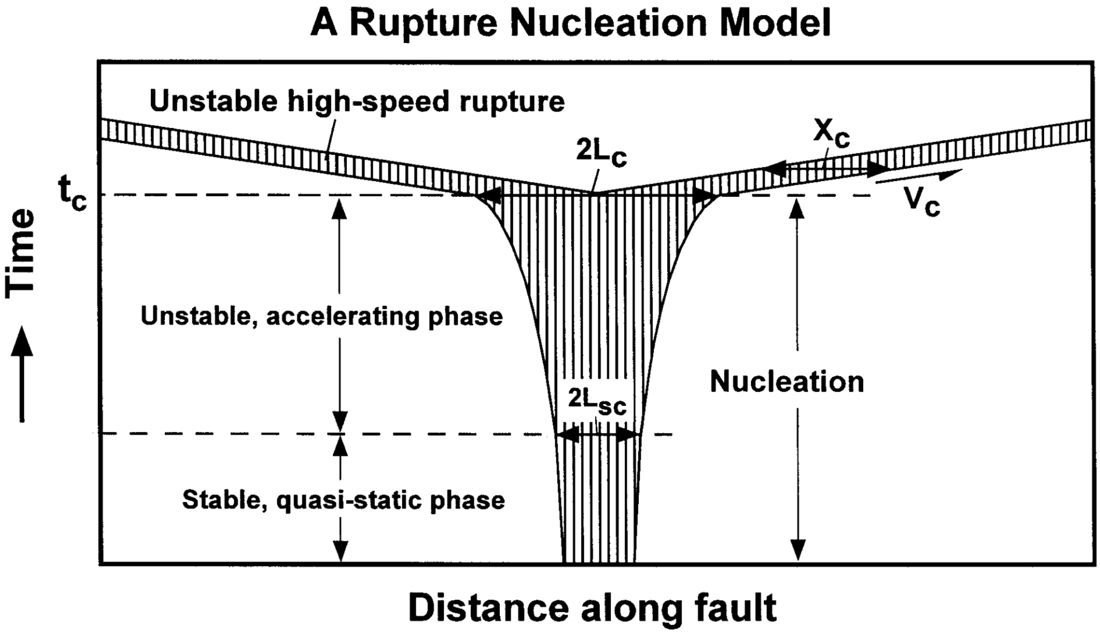

FIGURE 1.7: A rupture nucleation model. The rupture begins to propagate bidirectionally at a high-speed but constant velocity V_c and at the critical time t_c. The dynamic rupture is preceded by the nucleation phase with a slow acceleration of the slip. $2L_c$ denotes the critical size of the nucleation zone. Modified from Ohnaka (2000).

producing a seismic rupture. The nucleation is composed of three main phases: A stable quasi-static slip, followed by an unstable accelerating slip up to an unstable dynamic and high-speed slip (i.e., the earthquake). Figure 1.7 summarizes the different phases of the nucleation of a seismic rupture. The slow slipping phase before the rapid slip is called aseismic because the fault do not slip fast enough to radiate seismic waves.

Many laboratory stick-slip experiments achieved to image the rupture front of such nucleation phase by tracking stress changes produced by its propagation (Ohnaka, 2000; Latour et al., 2013). Figure 1.8, presents the nucleation phase of a rupture observed in a glass polymer (Latour et al., 2013) for different normal stresses. By tracking stress-induced light changes in the glass, it is possible to highlight the accelerating growth of the aseismic rupture front toward the dynamic mainshock. It clearly shows the quasi-static phase followed by the accelerating phase.

During the nucleation phase of laboratory earthquakes, small foreshock ruptures can also be observed by tracking down acoustic emissions (AE) of the rock

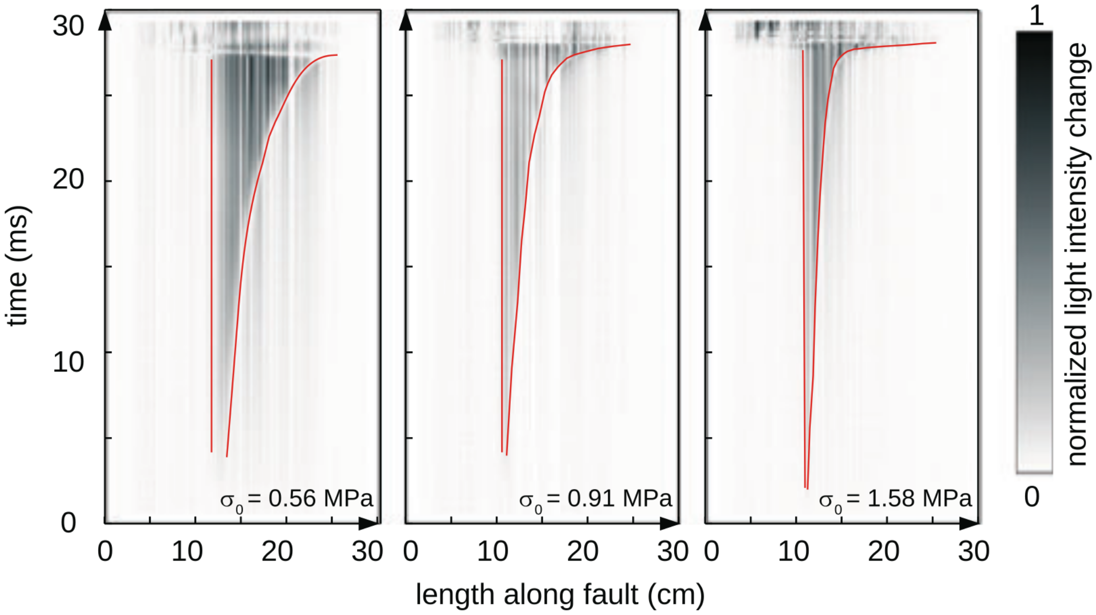

FIGURE 1.8: Three spontaneously nucleated laboratory earthquakes at increasingly higher normal stresses. The gray scale corresponds to the light intensity change since time t =0. The red curves highlight the position of rupture tips as a function of time. Modified from Latour et al. (2013)

sample. Such small precursory earthquakes are reported within the slow-slipping nucleation zone, as small embed asperities loaded by the aseismic slipping (McLaskey & Kilgore, 2013; Yamashita et al., 2021; Marty et al., 2023). The AE event rate is also found to accelerate towards the rupture time, as driven by the aseismic slip acceleration (Ojala et al., 2004; McLaskey & Lockner, 2014; Kwiatek et al., 2014; Marty et al., 2023). For example, after stacking slips and AE events measured before laboratory stick-slip, Marty et al. (2023) shows a slip displacement and velocity acceleration associated with an AE event rate acceleration (see Figure 1.9). Laboratory earthquakes are therefore preceded by an accelerating aseismic phase that can drive a foreshock activity interpreted as a nucleation phase of the rupture. Detecting such acceleration patterns may help to anticipate the dynamic rupture.

Even if the precursory nature of foreshocks and aseismic signals is well constrained in laboratory experiments, their observation on natural faults is still debated. It remains an open question to determine if the length and amount of slip of nucleation phases observed in laboratory conditions can scale with natural earthquakes that occur over kilometer-scale faults. If the nucleation phase

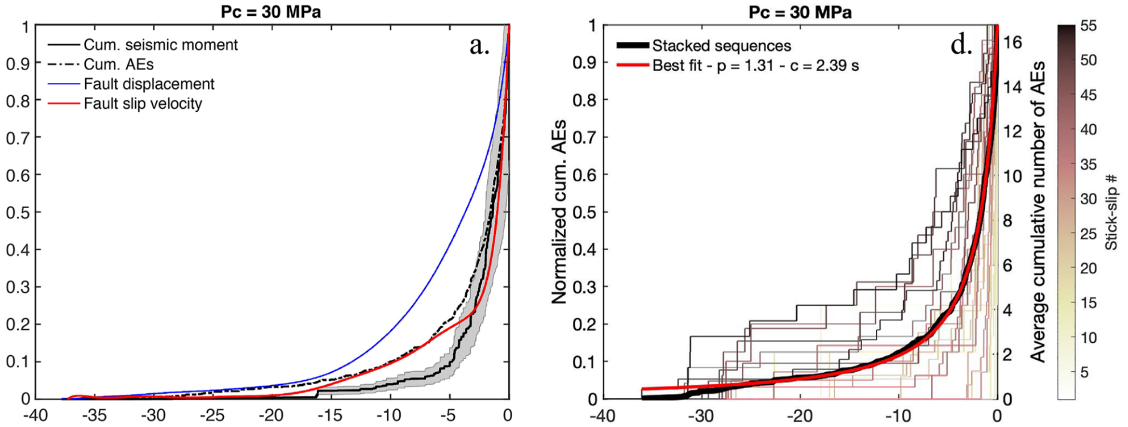

FIGURE 1.9: Normalized fault displacements, fault velocity, cumulative number of acoustic emissions (AEs) and cumulative AE moment release in the last 40 s prior to stick-slip failure at a confining pressure Pc = 30 MPa. Each curve represents stacking of all foreshock sequences before a stick-slip event. Right: Inverse Omori fit (red curve) of the stacked cumulative number of AEs (black curve) in the last 40 s prior to failure. The color curves display the individual precursory AE sequences, with the color-scale referring to the stick-slip event index Modified from Marty et al. (2023)

is scale independent, the amount of precursory slip and the magnitude of foreshocks would likely be undetectable at Earth surface, with an amount of slip below μm (Lapusta & Rice, 2003; Fang et al., 2010). However, if precursory slips and nucleation sizes are significantly larger on natural faults, it may be possible to detect the nucleation phase of mainshock ruptures, with meter-scale aseismic slip for large earthquakes (Ohnaka, 2003).

Field observations

Studies have reported unusual aseismic and seismic signals before mainshocks on natural faults. These observations are sometimes interpreted as evidences of a nucleation phase that is reported in theoretical and laboratory studies.

From the early 2000s, with the densification and improvements in GPS and satellite imagery, many observations of aseismically slipping faults have been reported, including just before the occurrence of a large earthquake. For example, Roeloffs (2006) reviewed precursory aseismic ground deformations reported before 10 major earthquakes up to 2005, based on leveling, tide gauge strain-meter and GPS observations. Overall, these signals were reported from a few days to years before the mainshock. Before the great 2011 Tohoku earthquake and using repeating earthquakes, Kato et al. (2012) highlighted an accelerating aseismic slip starting one month before the mainshock (see Figure 1.10.B). An observation confirmed by Ito et al. (2013) with ground deformations, using strain-meters and ocean-bottom pressure gauges. Mavrommatis et al. (2014, 2015) later suggested that aseismic slipping of the Tohoku fault plane may have even started several years before the earthquake (see Figure 1.10.D). In Chile, Ruiz et al. (2014) and Schurr et al. (2014) reported a precursory ground deformation from GPS time series one month before the 2014 $M_W = 8.1$ Iquique earthquake. Kato et al. (2016a) and Socquet et al. (2017) suggested that the aseismic slipping may have started up to 1 year before the mainshock (see Figure 1.10.A). Precursory aseismic slips are also reported before smaller magnitude earthquakes. For example, Tape et al. (2018) evidenced an unusual high-frequency seismic signal a few second before a $M_w = 3.7$ earthquake in Alaska in 2016 (see Figure 1.10.C). This precursory high-frequency signal is suspected to be generated by the accelerating nucleation phase of the earthquake.

On the other hand, many natural earthquakes are also preceded by an intense and/or accelerated foreshock sequence which may be additional evidence of a nucleation process as depicted in laboratory experiment. For example, at global scale, Papazachos (1975) highlighted that mainshocks were on average preceded by an accelerated seismicity, when stacking several foreshock sequences. Similarly, Bouchon et al. (2013) reported that many inter-plate earthquakes were preceded by accelerated seismicity and moment release, when averaging over many foreshock sequences at different timescales before mainshocks (see Figure 1.11). Dodge et al. (1995, 1996) reported that foreshock sequences observed before Californian mainshocks were likely driven by an underlying aseismic nucleation phase because of the large inter-event distances between foreshocks. Bouchon et al. (2011) reported a sequence of repetitive foreshocks just before the 1999 Izmit earthquake interpreted as tracer of an accelerating aseismic slip. In Chile, Ruiz et al. (2014) and Kato et al. (2016a) reported an intense and migrating foreshock sequence simultaneously with the precursory aseismic slip before the Iquique earthquake. Similar observation of a migrating foreshock sequence was also reported by Kato et al. (2012) before the 2011 Tohoku earthquake.

Therefore, field observations suggest that aseismic fault processes and accelerating foreshock activities do exist before mainshocks on natural faults. Such observations are often interpreted as evidences of a nucleation phase as depicted

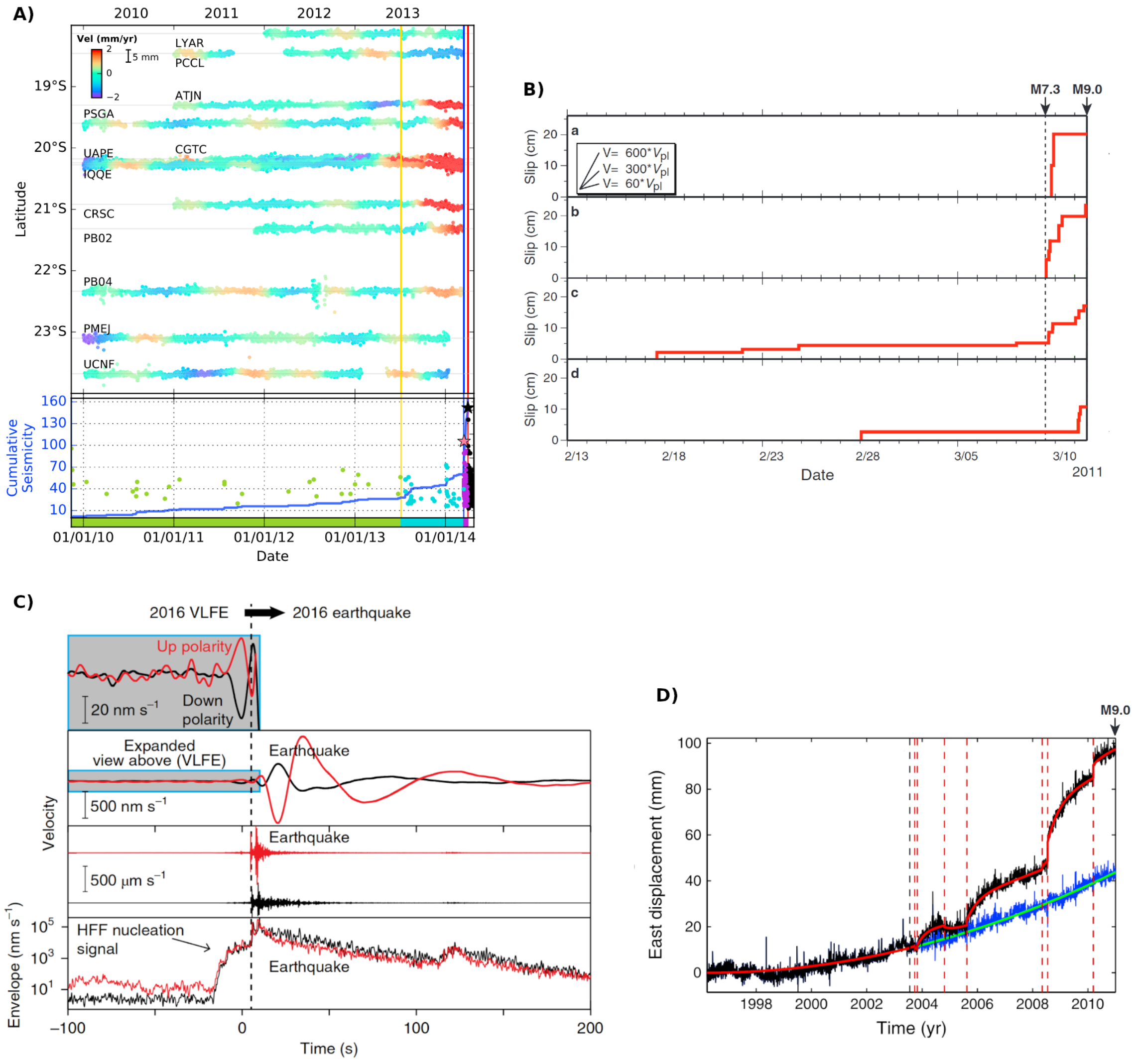

FIGURE 1.10: Four examples of precursory aseismic slip but with different time-scales. A) The top subplot show detrended GPS time series and velocities observed before the 2014 Iquique Earthquake (Socquet et al., 2017). Bottom subplot show the seismic activity observed before the mainshock. Yellow, blue and red vertical line show the onset of aseismic slip, the largest foreshock and the mainshock, respectively. B) Cumulative aseismic slip estimated from repeating earthquakes before the 2011 great Tohoku earthquake (Kato et al., 2012). Line segments in the inset denote slopes corresponding to 60, 300, and 600 times the plate convergence rate. The two arrows denote the largest foreshock and the mainshock. C) The 2016 Very Low Frequency Earthquake and Mw 3.7 Earthquake in Central Alaska, with high-frequency foreshock (HFF) nucleation signals (Tape et al., 2018). Top: seismogram causal-filtered 20–100 s. The grey box is cut at the earthquake S-wave time and is expanded above to show the waveforms for the precursory VLFE. Middle: seismogram filtered 2–8 Hz. Bottom: envelope of the high-frequency seismogram. Dashed line is the P-wave arrival for the Mw 3.7 earthquake. D) East GPS time serie from south-central Tohoku (stations 0203) (Mavrommatis et al., 2014). Black curve is GPS after removing common-mode errors and linear trends. Blue curve is GPS after removing offsets and postseismic transients. Red and green line are model fits. A decadal-scale deformation transient remains. Vertical dashed lines mark times of detected antenna offsets (black) and earthquakes (red).

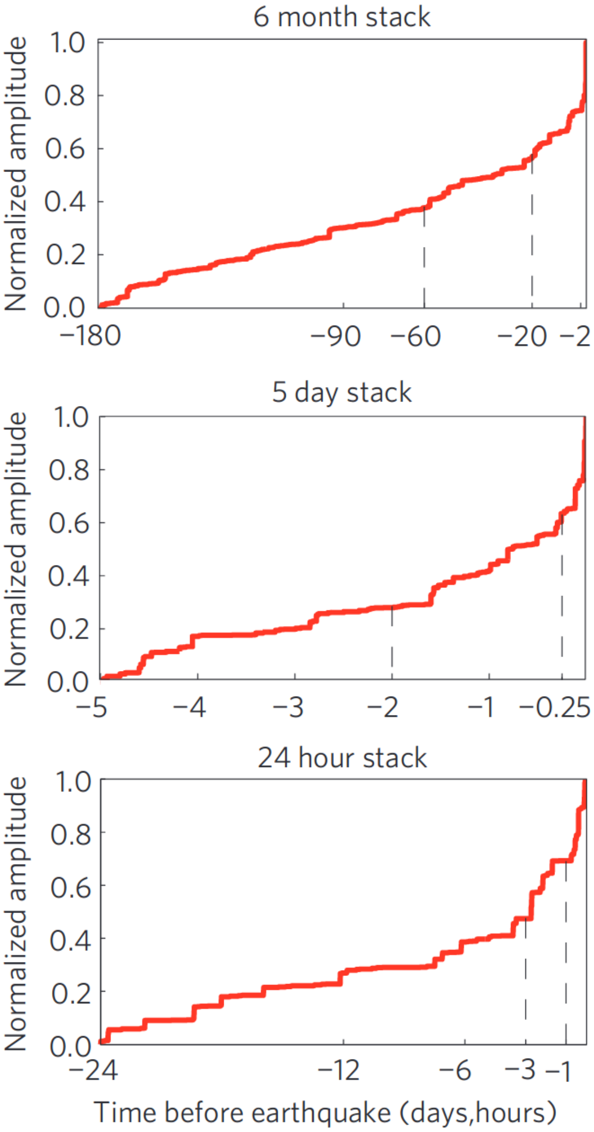

FIGURE 1.11: Stacked cumulative seismic moment observed before interplate mainshocks. Subplots show different time ranges before the mainshock. Modified from Bouchon et al. (2013)

by theoretical and laboratory experiments. If these observations actually reflect a nucleation phase of mainshock, tracking the foreshock activity may be informative on the future occurrence of a mainshock.

However, despite the densification of geodetic and seismic networks around active faults, such precursory observations still remain scarce in comparison with the number of instrumentally recorded large earthquakes. Moreover, the reported examples often have large uncertainties in both the location of aseismic slip and its temporal evolution, making it difficult to infer any acceleration trend as the mainshock approaches. In addition, we note that there are significant discrepancies in the duration of reported preparatory signals, ranging from a few tens of seconds to several years (see Figure 1.10). These scarce and multiple timescale observations of precursory aseismic slip and foreshock activity therefore raise doubt if they actually reflect the same nucleation process, possibly scaling in length with the incoming magnitude, or a different fault process that happen to be followed by a mainshock.

1.2.3 A cascade of earthquake interactions?

While the nucleation phase model suggests the possibility of anticipating large earthquakes using foreshock activity, we are currently still unable to label an increase in seismicity rate as a foreshock sequence before a mainshock has occurred. All the aforementioned examples are retrospective identifications of foreshocks after the seismic sequence has ended and its mainshock has been identified. In fact, the seismicity rate is expected to vary greatly with time, because of earthquake interactions (i.e., aftershocks). This makes it difficult to infer whether a rate increase simply reflects 'usual' seismicity rate variations of nested earthquake triggering or is actually driven by an additional process (possibly mediated by a nucleation phase of the mainshock). The current inability to identify in real time a seismicity rate increase as a foreshock sequence suggests that the process driving foreshocks may not be significantly different from other earthquakes. In this sense, another model proposes to explain the generation of foreshocks only with earthquake interactions, without any predictive power for the mainshock magnitude. This second model is referred to as the 'cascade model' (Ellsworth & Beroza, 1995; Helmstetter & Sornette, 2003; Mignan, 2015).

In the cascade model, foreshocks, mainshocks, aftershocks and any other earthquakes are considered to be driven by the same triggering mechanisms: Seismicity rate variations are the result of successive earthquake triggering, from one to another. A few earthquakes can also be triggered by a stationary background forcing, reflecting the constant tectonic loading of the region. As mentioned before, we know that earthquakes can trigger aftershocks on nearby fault areas, inducing a seismicity rate variation. This point out that earthquakes are a self-excited process, where the occurrence of an earthquake can impact the future occurrence of other nearby earthquakes. Physically, an earthquake releases stress on the fault that may load and trigger other ruptures on nearby locked asperities by stress transfer, possibly mediated by afterslip or other processes (Perfettini

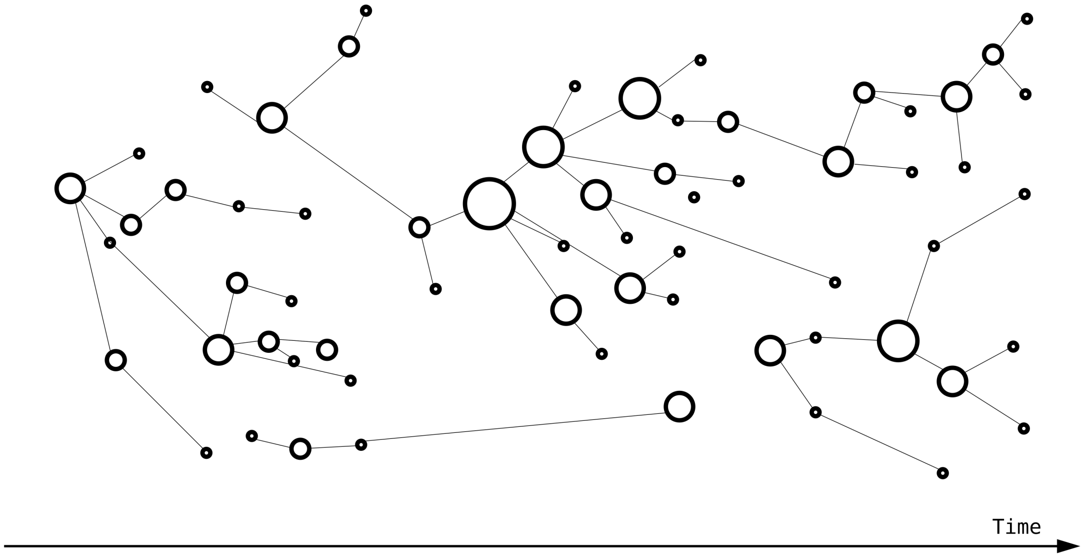

FIGURE 1.12: A schematic view of the cascade model and its triggering links. Black circle are earthquake. The circle radii increase with magnitude. Black lines are earthquake triggering links.

et al., 2018; Cocco & Rice, 2002). Successive occurrences of earthquake triggering may build up a self-excited cascade of fault ruptures. During such cascade, the future size of each patch is not predictable because they are rupturing the available locked portions of the faults. However, we assume that their global distribution follows the Gutenberg Richter law. The largest triggered asperity is retrospectively interpreted as the mainshock, and earthquakes before it are labeled as foreshocks. An illustration of cascade of earthquake triggering is presented in Figure 1.12. A cascade of earthquakes naturally build up the seismic sequence from a few background earthquakes. A large magnitude earthquake trigger more aftershocks than a small one but a small earthquake can trigger a large event. In other words, there is no distinction between the triggering mechanism of foreshocks and any other earthquakes.

Studies have presented convincing evidences that foreshock earthquakes may not behave differently than any other earthquakes, hence supporting the cascade model (Mogi, 1963a; Abercrombie & Mori, 1996; Helmstetter & Sornette, 2003; Felzer et al., 2004). For example, while investigating the Californian seismicity, Helmstetter & Sornette (2003) highlighted that foreshock precursory properties are independent of the mainshock magnitude and even shared with every earthquake, independently of being a mainshock, a foreshock or an aftershock. I

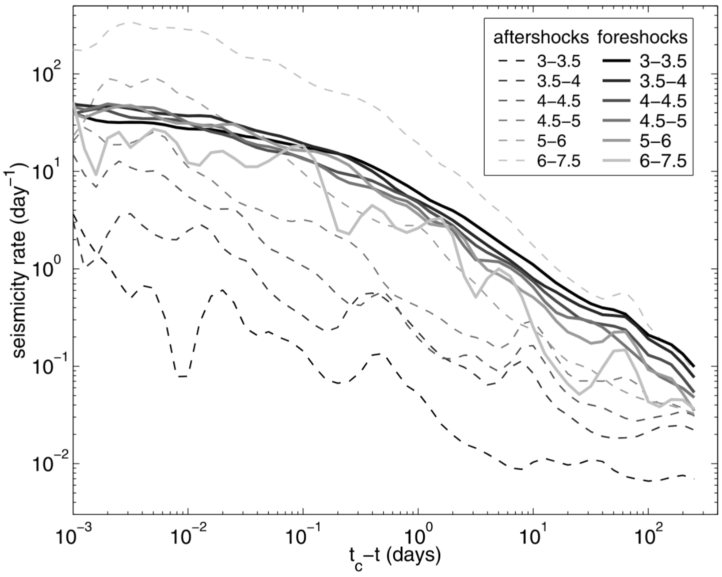

FIGURE 1.13: Foreshock and aftershock rate observed before and after earthquakes (t_c) in the Southern Californian Earthquake Center (SCEC) catalog. Modified from Helmstetter & Sornette (2003)

present part of their results on Figure 1.13 with the average seismicity rate measured before and after several classes of earthquake magnitude. First, it confirms that the aftershock rate scale with the magnitude (as described in Equation 1.9), supporting a causal triggering property of magnitude. Second, it shows that the precursory seismicity rate is accelerating toward impeding earthquakes but do not scale with the magnitude of the future seismic event. Large and small magnitude earthquakes are preceded by the same average increase in the precursory seismicity rate. This suggests that, independently of the future magnitude, the triggering mechanism between two earthquakes is expected to be the same (see also Christophersen & Smith, 2008). They also showed that these properties can be well reproduced by a seismicity model in which any earthquake can trigger another earthquake, simply by using the aftershock triggering property. From this observation, reports of foreshock accelerating rates before mainshocks can be interpreted as a direct consequence of the clustering property of earthquakes (i.e., due to aftershock triggering), and not necessarily as a tracer of a mainshock preparatory phase.

Many individual foreshock sequences have also been studied in the framework of the cascade model. For example, Felzer et al. (2002) investigated the triggering mechanism of the 1999 $M_w = 7.1$ Hector Mine earthquake. They showed that the triggering of the Lander mainshock may be explained by a long-term

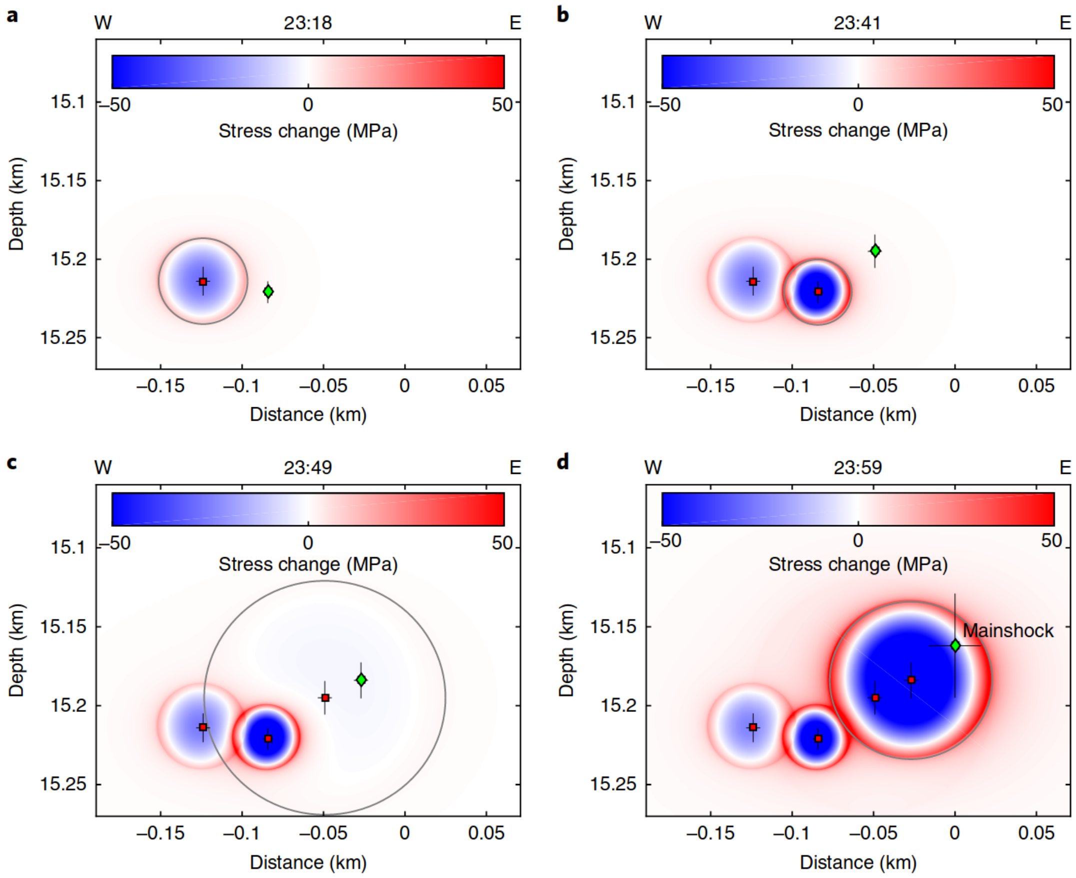

FIGURE 1.14: The 4 largest foreshocks observed before the 1999 Izmit mainshock and their induced stress changes. Modified from Ellsworth & Bulut (2018)

triggering chain of small earthquakes, initially triggered by the previous 1992 $M_w = 7.3$ Landers earthquakes. For the 2011 Tohoku earthquake, Marsan & Enescu (2012) suggested that a cascade of earthquake triggering was very likely to explain the foreshock sequence and the triggering of the mainshock.

In Figure 1.14, we present results of Ellsworth & Bulut (2018) that investigated static stress transfers induced by the 4 largest foreshocks of the 1999 Izmit mainshock. They show that foreshocks tend to occur at the edge of the stress change induced by previous foreshocks. This chain of static stress transfers seems to have ultimately triggered the mainshock. This result support with physical argument that the successive stress changes of foreshocks may lead to the triggering of a mainshock.

Therefore, a cascade of earthquake triggering is able to explain the generation of foreshocks. In this model the denomination foreshock lacks a physical definition because the foreshock seismic activity is independent on the impending mainshock magnitude. From that standpoint, foreshocks are like any other earthquakes, but that happen to occur before a large earthquake. In the cascade model, the predictive power of foreshocks for the mainshock occurrence is low and require a real-time knowledge of the state of stress on the fault.

1.2.4 Loading by a slow-slip event?

The nucleation phase model and the cascade model are two end members of a long-lasting debate on the predictive power of foreshocks (Ellsworth & Beroza, 1995; Mignan, 2015; Gomberg, 2018). Many authors have supported one of these two models, mainly depending on the method and geophysical data used, even for the same foreshock sequence (see for example the conflicting interpretations of Kato et al., 2012; Marsan & Enescu, 2012 or Bouchon et al., 2013; Felzer et al., 2015). Typically, studies tracking aseismic slip tend to favor the nucleation phase model, while statistical analyses of seismicity rate tend to rely more on the cascade model (Mignan, 2015). Still, no consensus has been reached in the last decade and both conceptual models shown their limitations when confronted with observational data. Such conflicting interpretations are pointing out that these two end member models may not describe foreshock activity accurately.

First, many studies have shown that aseismic slip can be observed on natural faults without a mainshock, as an independent fault process. For example, slow-slip events are historically detected without any significant seismic activity or only with small tremors of seismic radiations (Rogers & Dragert, 2003; Gomberg & the Cascadia 2007 and Beyond Working Group, 2010; Beroza & Ide, 2011). On the other hand, some slow-slip events can be associated with a moderate seismic activity, as a swarm-like sequence, but still without mainshocks (Lohman & McGuire, 2007; Vallée et al., 2013; Nishikawa et al., 2021). Other examples shows that slow-slip events can trigger a mainshock, not as nucleation phase but by static stress transfer, when aseismic slip is occurring near a large locked and seismogenic asperity. I present here in detail an interesting observation reported by Radiguet et al. (2016) near the Guerrero seismic gap, Mexico. The Guerrero Gap is a portion of the Central American subduction zone without major earthquakes compared to its neighborhood regions (see figure 1.15.D). Radiguet et al. (2012) highlighted that this part of the subduction zone is actually experiencing recurrent slow-slip events that episodically release the tectonic strain accumulation. From early 2000 to late 2010, at least 4 co-located slow-slip events were detected (Figure 1.15.A). During this period, slow-slip events release the short-term tectonic loading on a deep part of the subduction fault without significant large earthquakes (Figure 1.15.B and C). However, in 2014, a slow-slip event on the same part of the interface was followed by the $M_w = 7.3$ Papanoa earthquake on an upper part of the fault. This earthquake is thought to have been triggered by static stress transfer initiated by the slow-slip stress transfer. Similar observations of transient aseismic slip loading of a mainshock is also observed by Voss et al. (2018) before the 2012 $M_w = 7.6$ earthquake in Costa Rica, by Twardzik et al. (2022) before the 2017 $M_w = 8.1$ Iquique earthquake and by Klein et al. (2023) for the $M_w = 6.8$ 2020 Atacama sequence. Moreover, with numerical simulations, Meng & Duan (2022) shows that slow-slip events and dynamic rupture can theoretically interact: in their experiment, repetitive aseismic slip can be observed before a dynamic rupture, gradually loading the asperity. The triggering of the asperity by aseismic slip is sometimes observed but is not systematic, depending on the current state of stress in the locked asperity. Therefore, transient aseismic slips detected before large earthquakes are not necessarily an evidence of a nucleation phase. It may be an independent fault process that still can influence the occurrence of mainshock and trigger its own seismicity .

In the same way, foreshock sequences can sometimes show discrepancies with the cascade model. For example, Shearer (2012b) and Shearer (2012a) found some deviation from the earthquake triggering self-similarity between foreshocks and aftershocks in a high resolution catalog of Southern California. Some seismicity rate increases do not appear to be driven by earthquake triggering (as expected by the cascade model) but rather require underlying physical process. Lippiello et al. (2012) and Ogata & Katsura (2014) reported that spatial organization of foreshocks may not be independent of the mainshock magnitude and therefore may reflect a specific underlying process linked to the mainshock occurrence. Seif et al. (2019) and Lippiello et al. (2019) also reported that foreshock sequences in a high resolution catalog of Southern California and Italy presented higher rates than expected by statistical cascading models. We present in details with Figure 1.16 an interesting result of Marsan et al. (2014). With a worldwide selection of mainshocks, they investigated links between foreshock and aftershock rates. They show that mainshocks preceded by an accelerated foreshock seismicity (Population 1) were also associated with a very-productive aftershock activity compared to non-accelerating foreshock rates (Population 2). Moreover, they showed that

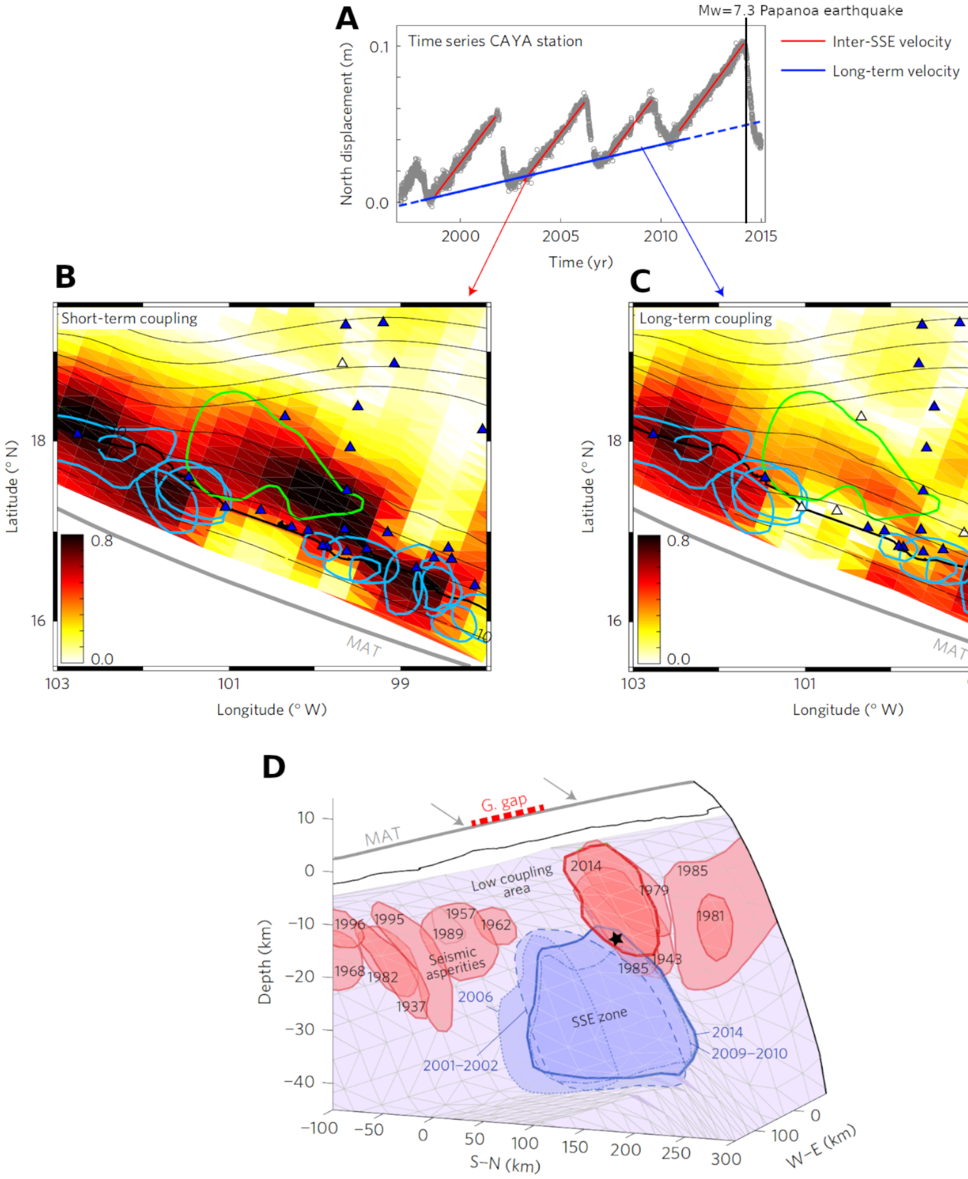

FIGURE 1.15: A. Inter-SSE (slow-slip events) and long-term velocities are extracted from the GPS time series. The example of the north displacement for the CAYA time series is shown. B. Coupling during the inter-SSE periods, computed by inversion of inter-SSE velocities. C. Long-term coupling, computed by inversion of long-term velocities. For B and C, the blue lines are large earthquake contours since 1940; the green line is the 2014 SSE slip contour. D. The red contours show recent (after 1940) large earthquake rupture areas, including the 2014 Papanoa earthquake (thicker contour), and the black star indicates its hypocenter location. The blue contours show SSE locations: The thick continuous blue line is the 2014 SSE; previous SSEs are shown with dotted lines. Modified from Radiguet et al. (2016)

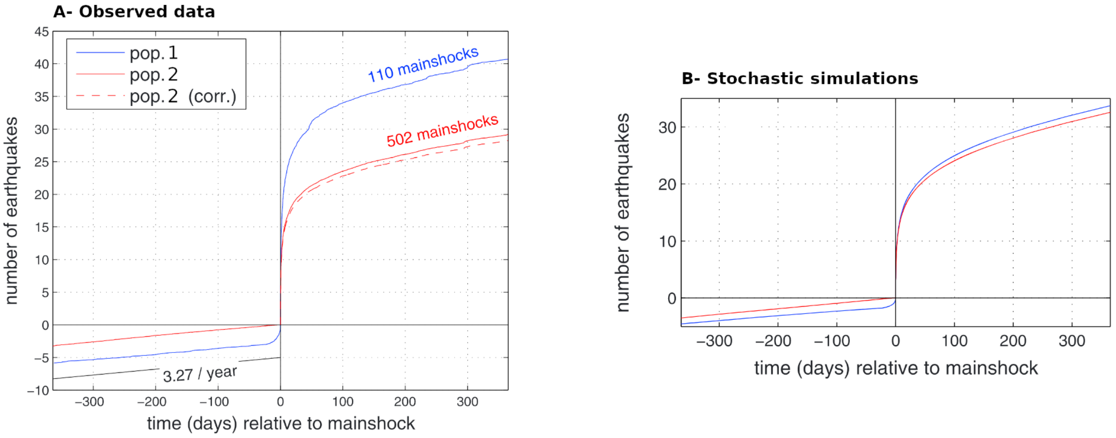

FIGURE 1.16: A. Stacked and averaged number of $M \geq 4$ earthquakes within 50 km of the mainshock epicenter, for the two populations 1 (accelerated foreshock seismicity) and 2 (non-accelerated). Red dashed line: aftershocks of population 2 after correcting for a difference in magnitude distribution for the two populations. B- Same as A. but with synthetic ETAS earthquake catalogs, modeling a cascading earthquake triggering process. Modified from Marsan et al. (2014)

this enhanced foreshock-aftershock activity cannot be reproduced using simulations of an earthquake triggering process (Figure 1.16. B). It suggests that enhanced foreshock activity may be part of a long-term seismicity perturbation, possibly mediated by transient aseismic slips and persisting even after the occurrence of the largest magnitude of the sequence. These examples show that, even if the earthquake triggering model can explain a vast majority of seismicity rates variations, some high rate anomaly still remains, including foreshocks sequences, specifically when taking into account small magnitude earthquakes (Mignan, 2015).

Therefore, beyond the nucleation phase and cascade model, efforts are still needed to understand the interplay of aseismic processes with the seismicity and with the triggering of large earthquakes. In a third conceptual model, earthquake sequences (foreshocks, mainshocks and aftershocks) can sometimes correspond to an enhanced seismicity regime driven by the stress loading of a nearby slow-slip event. Such transient aseismic slip enhance the triggering of locked asperities by static stress transfer and drive a seismic activity. This seismic activity, mediated by a slow-slip event, is enhanced and completed with cascade of earthquake triggering, building up a seismic sequence. Here, as for the cascade model, the triggering of a large earthquake is possible depending on the state of the fault.

In this model, foreshocks and slow-slip events are not deterministic of the mainshock but can still indicate a perturbed fault were the triggering of a large earthquake is more likely. We can think of this third model as a cascade model where the background tectonic forcing is not always constant but can observe transient changes, due to the occurrence of slow-slip events.

1.2.5 Further investigations of the foreshock activity in high resolution catalogs

The recent increase of near-fault seismic and geodetic observations, coupled with recent advances in earthquake detection, provides an unprecedented opportunity to study active faults in detail. As mentioned before, low magnitude earthquakes are suspected to be of great importance in the detection of unusual foreshock activities, and may help highlight additional underlying geophysical process. In a meta-analysis of foreshock studies, Mignan (2015) found that low magnitude-completeness catalogs were more likely to point an unusual foreshock activity compared to earthquake triggering models (see Figure 1.17). He suggested that studies with a difference of at least 3 magnitude units between the mainshock magnitude and the magnitude completeness of foreshocks were almost always pointing out toward an unusual foreshock activity, possibly mediated by aseismic slips.

In this Ph.D. thesis, I use and build long-term high-resolution catalogs of seismicity to further investigate the properties of foreshock sequences in California and Chile. I investigate their relation to earthquake triggering, aseismic processes and the possible preparation phase of mainshocks. I first test earthquake catalogs in Southern California against the cascade model using a statistical seismicity models. It allows identifying and quantifying the amount of foreshock activity that is unusually active compared to earthquake triggering. Such cases are the most likely to be mediated by an underlying aseismic process. In a second part, I examine in detail the role of an aseismic slip in a seismic sequence in Chile to better understand its possible interplay with unusual foreshock activity and whether it actually reflects a nucleation phase or a slow-slip event loading.

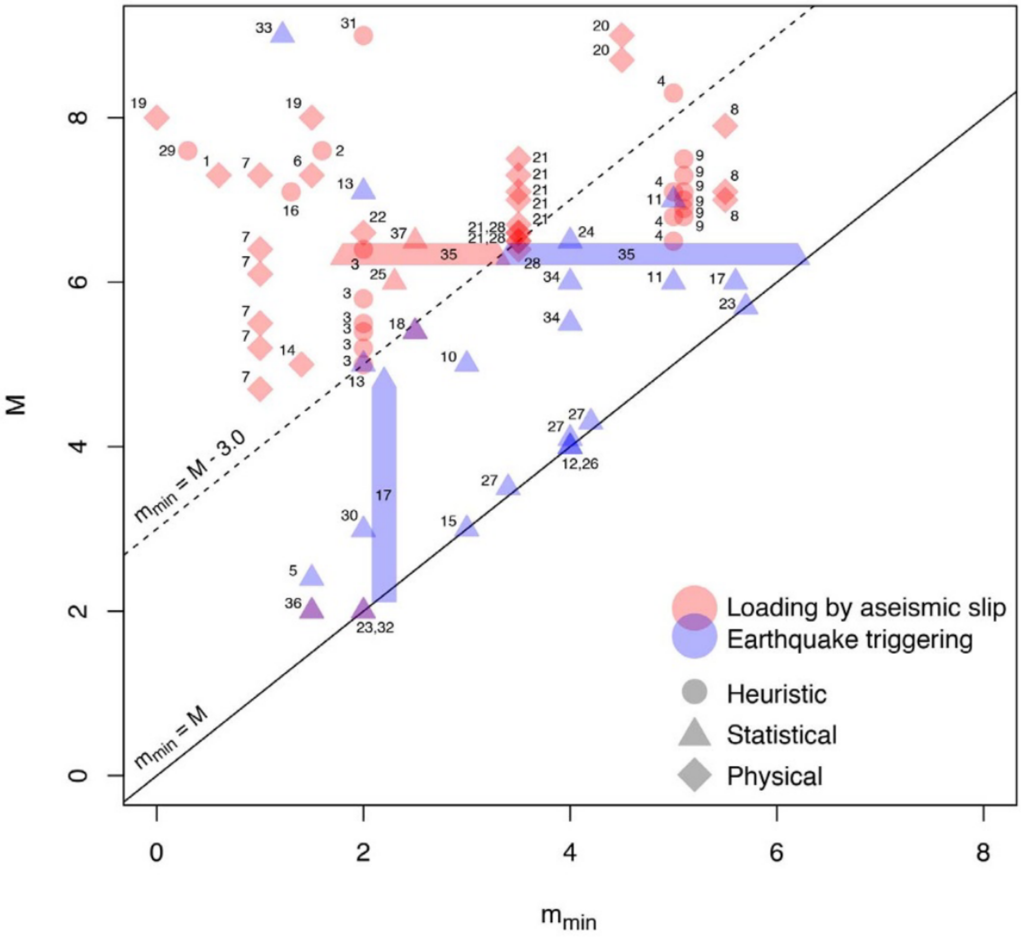

FIGURE 1.17: Meta-analysis of 37 published studies in which the origin of observed foreshocks is determined. Mainshock magnitude M versus minimum foreshock magnitude m_{min}. Arguments are based on heuristic, statistical or physical considerations. The emergence of an anomalous foreshock behavior (i.e., loading process due to aseismic slip) is observed once microseismicity is included in the analysis, otherwise foreshocks are best explained by the normal behavior of seismicity (i.e., earthquake triggering process). Modified from Mignan (2015)

1.3 Modeling the seismicity

When investigating foreshock seismicity, it is essential to evaluate whether foreshock activity is unusually large compared to the expected variations in seismicity rates in the studied region. It is well established that earthquakes naturally cluster in both space and time due to earthquake interactions (i.e., aftershocks triggering governed by the Omori-Utsu law). Therefore, as discussed above, an increase in seismicity rates during a foreshock sequence can be interpreted in two distinct ways. First, according to the cascade model described in section 1.2.3, a rise in seismic activity can naturally occur due to earthquake triggering, assuming a constant and stationary background seismicity rate. Second, in scenarios like a nucleation phase (section 1.2.2) and a loading by a slow-slip event (section 1.2.4), the activity increase (or at least part of it) cannot be attributed to basic earthquake interactions and is instead driven by a transient tectonic forcing. To decipher the origin of foreshocks, a possibility is to test if the foreshock activity can be explained by earthquake cascades over a stationary background seismicity rate. If such a cascade model is rejected, it suggests that the observed seismicity increase is not only the result of earthquake interactions but rather necessitates a transient increase in the background earthquake rate. Such deviation from standard earthquake clustering patterns can then be investigated with additional geophysical observations to decipher whether the transient background forcing is indeed driven by a transient tectonic forcing (e.g., nucleation phase, slow-slip event).

In this thesis I make extensive use of stochastic seismicity models to test whether foreshock sequences can be explained by cascades of earthquakes. These stochastic seismicity models serve as a null hypothesis to easily test foreshock patterns against the usual earthquake interactions observed in the region. Stochastic seismicity models are convenient because they don't require knowledge of the physical properties of the fault (i.e., stress state, fault geometries, etc.). While modeling the evolution of such physical properties is numerically possible (Dieterich, 1994; Im & Avouac, 2023), it is in reality very difficult because the fault geometry and the initial state of stress are usually unknown in natural seismicity catalogs. I focus specifically on the temporal evolution of foreshocks-mainshock-aftershocks sequences within regions unaffected by other nearby large earthquakes. These catalogs are assumed to reflect isolated fault systems in which earthquakes can interact with each other. Although ignoring earthquake locations appears to be a main drawback, the studied sequences generally occur on small spatial scales relative to location uncertainties and relative to the distances at which earthquakes can interact. The quality of earthquake locations is highly dependent on the spatial density of the seismological network, which is often sparse compared to the possible location volume. Therefore, inter-event times between earthquakes are generally more reliable than their inter-event distances (Moradpour et al., 2014).

1.3.1 The Poisson point process and background seismic activity

Before modeling earthquake cascades, we need a seismicity model that can reflect background seismic activity. In its simplest form, background seismicity is expected to be driven by a slow constant tectonic loading. Therefore, the background rate is expected to be stationary in time and background earthquakes independent of each other (without interactions). Because of its properties, the stationary Poisson process is often used to model such background activity (Zhuang et al., 2012). The stationary Poisson process can model complete randomness in a point pattern (Daley & Vere-Jones, 2003, p 27) and thus naturally serves as the null model in many hypothesis tests to investigate whether a systematic structure is included in the observations. Applied to earthquake occurrence, it can serve as a Null-hypothesis to test if an earthquake pattern have a deviation from a stationary random background activity. Such deviation may then be investigated and interpreted. For example, it may highlight additional geophysical processes (i.e., aftershocks, transient aseismic slip, etc) or detection flaws (e.g., due to changes in the seismic network).

Let's say that we observe N earthquakes (i.e., points) at times $t_i \in [T_1, T_2]$. This point pattern is a stationary Poisson point process only if:

1. The number of earthquakes observed in two distinct time period are independent of each other.
2. The probability distribution of the number of earthquakes observed in a time interval only depends on its length.
3. Two or more earthquakes cannot occur simultaneously.

If these properties are verified, the number of earthquakes observed in any time interval S follows a Poisson distribution (Daley & Vere-Jones, 2003; Zhuang et al., 2012):

$$Pr(N(t, t+S) = n) = \frac{\mu^n S^n}{n!} \mathrm{e}^{-\mu S}, \tag{1.10}$$

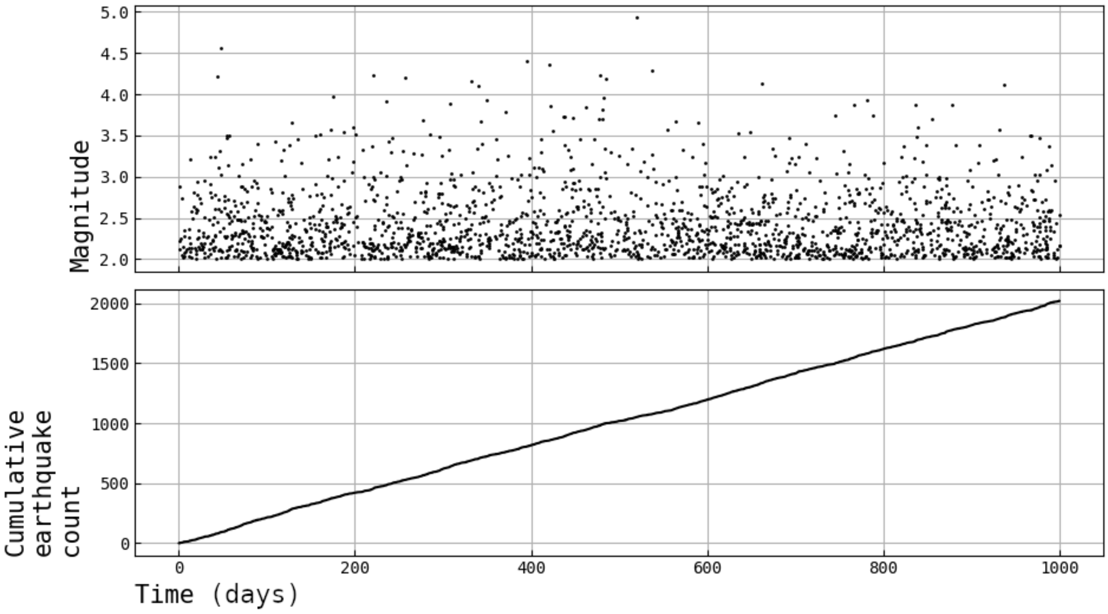

FIGURE 1.18: An example synthetic background earthquake catalog modeled as a stationary Poisson point process over time, with $\mu = 2$ (event/days). Earthquake occurrences are independent and randomly distributed over $T = 1000$ days. Magnitudes are independent and randomly sampled from the Gutenberg-Richter distribution with $b = 1$

where μ is the long-term average of the number of points per unit of time. The stationary Poisson process can also be described by a conditional intensity $\lambda_0(t)$, which is the expected rate at t depending on the past history of the point process. Since points are independently distributed at a constant rate over time, we can write the conditional intensity (i.e., the expected seismicity rate) of a Poisson process as:

$$\lambda_0(t) = \mu \tag{1.11}$$

Finally, for a given point process with time, we can estimate the maximum likelihood rate $\hat{\mu}$ of a Poisson Process using:

$$\hat{\mu} = N/(T_2 - T_1) \tag{1.12}$$

From a stationary Poisson point process, it is possible to model a simple background earthquake catalog, with a constant rate over time and random time of occurrences. Since earthquake magnitudes generally follow the Gutenberg-Richter

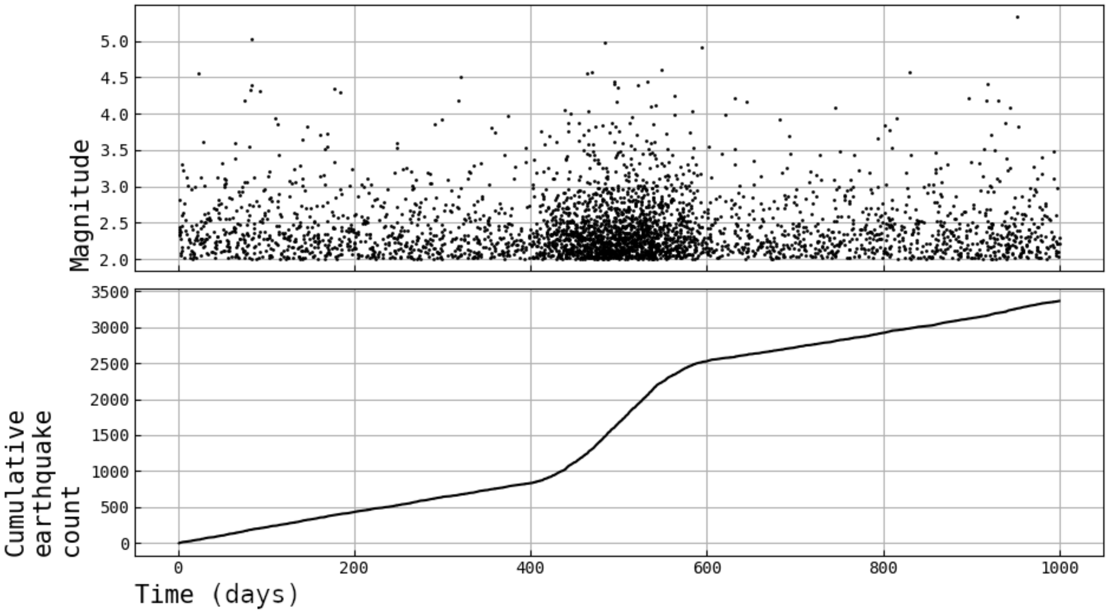

FIGURE 1.19: A synthetic background earthquake catalog modeled as a non-stationary Poisson point process. The long term background rate is $\mu = 2$ (event/days) but observe a transient acceleration between $400 \leq t \leq 600$. Magnitudes are independent and randomly sampled from the Gutenberg-Richter distribution with $b = 1$. If this simulation model background earthquake driven by a tectonic forcing, the rate change could model a transient aseismic slip.

distribution, magnitudes values are usually assumed to be independent and are randomly sampled from equation 1.6 (Zhuang & Touati, 2015). An example of a background catalog following a Poisson process is shown in Figure 1.18. We can clearly see that the earthquake rate is constant over time, but with random local fluctuations. No temporal pattern in the earthquake catalog can be detected.

In most cases, the stationary Poisson process is appropriate to model a constant background seismicity that is generated by constant forcing (e.g., a locked or continuously creeping fault). However, if this tectonic forcing is perturbed by an additional process; let's say a nearby slow-slip event; the background earthquake rate may deviate from stationarity (see Figure 1.19). In such case, background earthquakes can be modeled by a non-stationary Poisson process, where $\lambda_0(t) = \mu(t)$. The stationary Poisson process can be used as a null hypothesis to highlight such a change in a given background rate, and possibly point out a transient forcing phenomena (e.g., slow-slip event, magma intrusion, etc.).

1.3.2 ETAS: A self-exiting point process

While the stationary Poisson process can model the background earthquake rate, it does not account for changes in the seismicity rate due to earthquake interactions. As mentioned before, we know from aftershocks that earthquakes are neither independent nor random. Aftershocks can temporarily increase the seismicity rate, producing deviations from the background seismicity without any change in tectonic forcing. Therefore, aftershock clustering must be taken into account before studying variations in seismicity rates. Advanced seismicity models build on the stationary Poisson process as a fundamental basis for background seismicity and include an additional term to model aftershock triggering (Gardner & Knopoff, 1974; Ogata, 1988; Hainzl et al., 2006).

The aftershock rate is well described by the Omori-Utsu law (equation 1.8) and scales in productivity with the magnitude of the triggering earthquake (equation 1.9). Even if the underlying physical process driving aftershocks is still discussed today, the Omori-Utsu law empirically reflects an earthquake triggering process, where an earthquake impact the following seismic activity. It therefore mimics the increase in seismic activity due to various processes such as static stress transfer and afterslip. The aftershock triggering property can be easily modeled stochastically as a self-exiting point processes (Kagan & Knopoff, 1981, 1987; Ogata, 1988). One of the most used aftershock model is the Epidemic Type Aftershock Sequence model; ETAS (Kagan & Knopoff, 1981; Ogata, 1988; Zhuang et al., 2012). The ETAS model is a superposition of a stationary background seismicity term and an aftershock triggering term scaled in intensity by the magnitude of the triggering event. For a given time-magnitude earthquake catalog (t_i, m_i) with $i = 1...N$, the conditional intensity $\lambda(t)$ (i.e., the expected seismicity rate at t) given by the ETAS model can be written as:

$$\lambda(t) = \mu + \sum_{(t_i,m_i)<t} A\mathrm{e}^{\alpha(m_i - m_c)}(t - t_i + c)^{-p}, \tag{1.13}$$

where μ is the stationary background seismicity rate. The sum on the right hand side of this equation describes the expected aftershock seismicity rate at time t, triggered by all preceding events. Aftershocks are modeled using a combination of Equations 1.8 and 1.9. The parameters c and p describe the time-decay in the aftershock seismicity rate (Omori, 1895; Utsu et al., 1995). The intensity of the triggering is scaled by A and α, the global aftershock productivity of the region and the magnitude dependency in the number of triggered events, respectively.

The ETAS model is only defined for magnitude $m_i \geq m_c$, the magnitude of completeness of the catalog. Magnitudes are assumed to be independent and are usually distributed according to Gutenberg-Richter's law (G-R) and its b-value (cf., Equation 1.6) [1].

The ETAS model is described by 6 parameters $\theta = (A, c, p, \alpha, \mu, b)$, describing the background and aftershock properties of the seismicity, as well as the magnitudes distribution. For N observed earthquakes at times $t_i \in [T_1, T_2]$ with magnitude $m_i > m_c$ (i=1...N), we can estimate the maximum likelihood estimate of ETAS parameters $\hat{\theta}$ by maximizing the following log-likelihood function:

$$\begin{aligned} \mathcal{LL} &= \sum_{i=1}^{N} \ln[f(m_i)] + \left[\sum_{i=1}^{N} \ln[\lambda(t_i)] - \int_{T_1}^{T_2} \lambda(t)\, \mathrm{d}t \right], \\ \mathcal{LL} &= \mathcal{LL}_{GR} + \mathcal{LL}_{ETAS}, \end{aligned} \qquad (1.14)$$

where f is the probability density function of the Gutenberg-Richter law (Equation 1.6) and λ the ETAS conditional intensity (Equation 1.13). In practice the b-value and the other ETAS parameter are independent and can be maximized separately. An explicit solution exists for $\mathcal{LL}_{GR}$. It corresponds to the Aki-estimator of the b-value $b = \log(e)/(\bar{m} - m_c)$, where $\bar{m}$ is the mean magnitude above the magnitude of completeness (Aki, 1965). $\mathcal{LL}_{ETAS}$ needs to be maximized numerically, usually with classic optimization routines or with an Expectation-Maximization algorithm (Veen & Schoenberg, 2008).

A sketch description of the ETAS modeling is presented in Figure 1.20. In the ETAS model, the seismicity is driven by two mechanisms: stationary background earthquakes and triggered aftershocks. Background earthquakes are driven by a stationary Poisson process. Aftershocks are triggered by previous earthquakes according to the Omori-Utsu law. Any earthquake (i.e., backgrounds and aftershocks) can trigger aftershocks, with a productivity depending on the magnitude. The seismicity rate expected at time, t, is simply the sum of the background rate plus the Omori-Utsu aftershock rate of every previous earthquakes, evaluated in t. In other words, every earthquake has a chance to be triggered by a previous earthquake, depending on the distribution of past magnitudes. Therefore, one earthquake can be explained by a cascade of triggering through aftershocks

---

[1] We note here that the ETAS model can in pratice be used with any type of magnitude distribution but that G-R is usually the expected distribution of magnitudes for a general seismic activity.

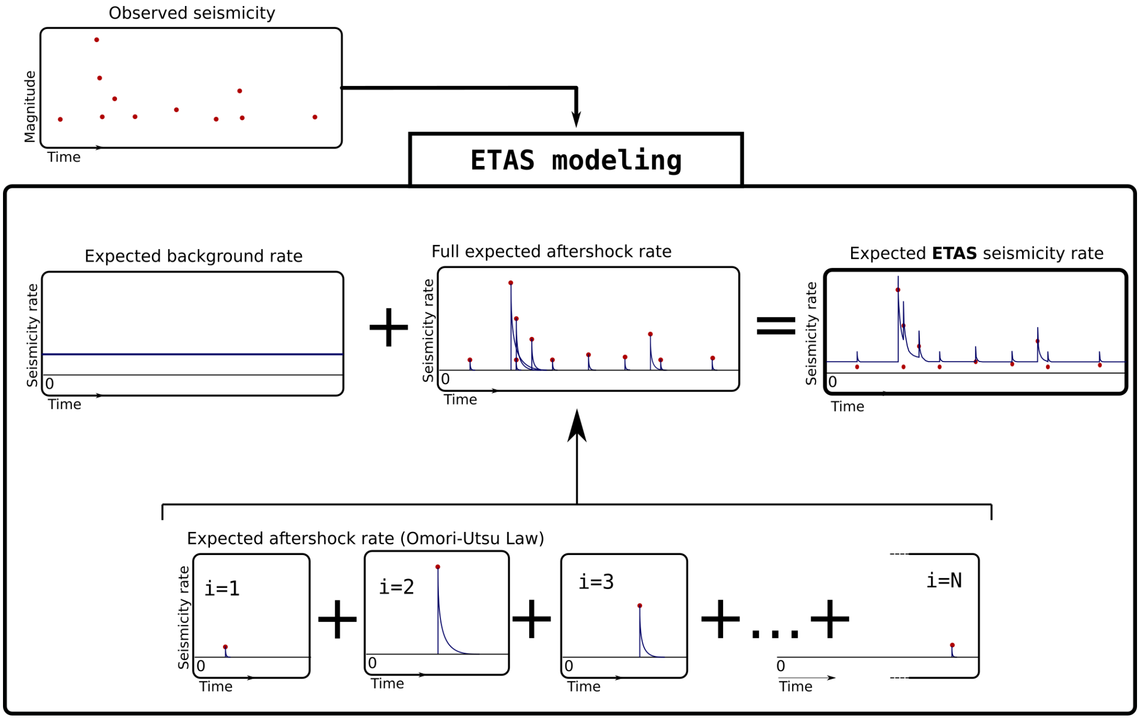

FIGURE 1.20: An illustration of the ETAS modeling of a seismicity with time. The expected ETAS seismicity rate at time, t, is a superposition of a stationary background rate and the aftershock rate of triggered by every earthquake before t. Individual aftershock rate are modeled by the Omori-Utsu law with an intensity scaled with the magnitude value. The label i in bottom insets refers to the index of the earthquake

interactions or by a stationary background forcing. Because magnitudes are independently sampled, every earthquake as the same chance to be a mainshock. However, there is a larger probability to observe large earthquakes during time-periods with enhanced seismicity rates (i.e., during aftershock sequences).

With the ETAS model, we can generate synthetic earthquake catalogs (Zhuang & Touati, 2015). An example of an ETAS simulation is presented in Figure 1.21. Background earthquakes used for this simulation are the same as the Poisson catalog presented in Figure 1.18. We can see that the aftershock triggering has built up strong seismicity rate variations and triggered a magnitude 7 earthquake. From the cumulative count we clearly see that the seismicity rate is not constant and is modulated by the occurrence of large magnitude earthquakes.

The ETAS model is able to naturally generate cascade of earthquake interactions that mimics well the property of natural catalogs, simply by using aftershocks (Helmstetter & Sornette, 2003; Felzer et al., 2004; Christophersen & Smith,

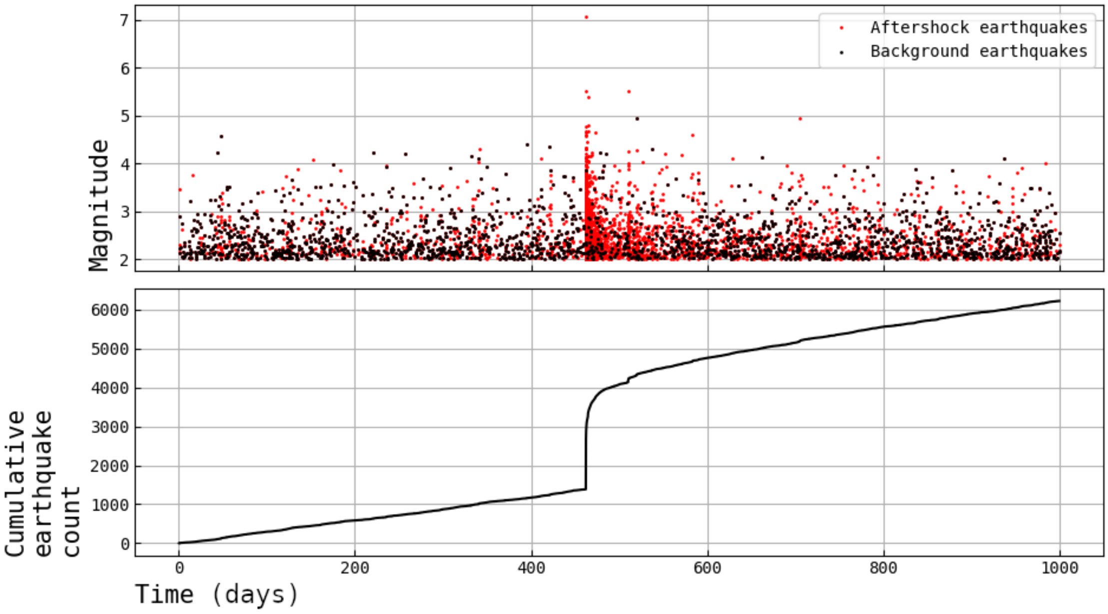

FIGURE 1.21: An example of a synthetic earthquake catalog generated with the ETAS model. Black dots are background earthquakes of rate $\mu = 2$ (event/days). Red dots are aftershocks of previous earthquakes. The ETAS parameters used to generate aftershock are $A = 0.005, c = 0.001, p = 1.1$ and $\alpha = 2$. Magnitude are drawn from the Gutenberg Richter law with $b = 1$.

2008). For this reason, it serves as a basis for establishing reference synthetic earthquake catalogs and testing any deviation from it (Ogata, 1989, 1992; Marsan et al., 2014; Seif et al., 2019). The ETAS model is also often used to forecast seismicity (Zhuang, 2012; Taroni et al., 2018; Mizrahi et al., 2021).

1.3.3 Detection of foreshock anomalies

Because ETAS can model earthquake triggering properties, it is widely used to test the significance of seismicity rate increases. As mentioned before, many studies have investigated foreshock seismicity rates and found that they were well explained by the ETAS model. These observations support that a cascade model may be enough to explain foreshock generation, without requiring an additional forcing (i.e., nucleation phase, slow-slip event; Helmstetter & Sornette, 2003; Felzer et al., 2004; Marzocchi & Zhuang, 2011). On the other hand, using a lower magnitude of completeness, Seif et al. (2019) re-evaluated foreshock sequences of California and Italy and highlighted some deviations from the ETAS model. Lippiello et al. (2019) obtained similar conclusions and proposed a slight modification of the ETAS model by including a foreshock specific triggering kernel to better constrain their natural activity. Such deviation suggests that foreshocks may not fully behave as the cascade model and are requiring an additional triggering process.

Studies investigating foreshock activities often average multiple foreshock sequences at once and compare them with the average activity observed within ETAS simulated catalogs. Averaging many seismic sequences has the disadvantage of potentially mixing different foreshock signatures. The average foreshock activity can be significantly biased by a small subset of unusually active foreshock sequences. Moreover, as suggested by Mignan (2015), deviations from an earthquake triggering process appears more frequently when including low magnitude earthquakes in the analysis. In this Ph.D thesis, I use the ETAS model as a null hypothesis for the cascade model and test how likely it can explain individual foreshock sequences, including low magnitude earthquakes. For that, we follow an approach similar to the original ETAS analysis procedure of Ogata (1988, 1989, 1992) for individual seismic sequences. It basically consists of the following steps :

1. I extract the best-fitting ETAS parameters $\hat{\theta}$ from a long-term seismicity catalog in the study area, ideally with a duration significantly longer than the length of the analyzed foreshock sequence.
2. I test the Null-hypothesis that the observed foreshock seismicity can be explained by the ETAS model estimated from the long-term catalog.
3. Any deviation from the ETAS model can later be interpreted as a tracer of an additional process, likely different from a cascade of earthquake interactions.

For example, from M observed earthquakes at times $t_i \in [T_1, T_2]$ with magnitude $m_i > m_c$ (i=1...M), we can extract the best-fitting ETAS parameters $\hat{\theta}$. Using $\hat{\theta}$ and Equation 1.13 we can compute the expected ETAS seismicity rate $\lambda(t)$ at any time t of the catalog. Let's say that we observe a foreshock sequence of N_{obs} earthquakes at time $t_j \in [T_{start}, T_{end}]$. The number of foreshock earthquakes in $[T_{start}, T_{end}]$ expected by the ETAS model is then:

$$N_{ETAS} = \int_{T_{start}}^{T_{end}} \lambda(u)\, \mathrm{d}u, \tag{1.15}$$

It can be shown that N_{ETAS} is Poisson distributed (Daley & Vere-Jones, 2003; Ogata, 1988; Zhuang et al., 2012). Therefore, we can compute the probability that the ETAS model explain N_{obs} with:

$$\begin{aligned} p &= P(N_{ETAS} \geq N_{OBS}), && (1.16) \\ &= 1 - \sum_{n=0}^{N_{OBS}-1} \frac{N_{ETAS}^{n}}{n!} \mathrm{e}^{-N_{ETAS}} && (1.17) \end{aligned}$$

We can then reject the null hypothesis with a significance level of p, that the foreshock seismicity is explained by an ETAS process. Such deviation may indicate that a cascade of earthquake triggering is not sufficient to explain the foreshock seismicity rate.

We note here that the rejection of the ETAS null hypothesis is not strictly a rejection of the cascade model. Indeed, even if the ETAS model parametrizes an earthquake triggering process by aftershocks, it is only based on a statistical description of the average aftershock behavior (Omori-Utsu). In principle, actual physical earthquake interactions within complex fault geometries can result in singular variations in seismicity rates that may not be captured by ETAS but still be a cascading process. For example, numerical simulation of cascading static stress transfer over a discrete fault network was recently found to produce slight deviations from ETAS (Im & Avouac, 2023). However, in reality, the deep fault geometry and stress state are very difficult to access. Therefore, in natural earthquake catalogs, the statistical description of aftershock triggering is one of the best proxy available to investigate deviations from the cascade model. Such deviations can later be completed with additional analyses to strengthen the existence of a transient forcing. Furthermore, if the null hypothesis is not rejected, we can't strictly conclude that the seismicity is actually driven by earthquake cascading. A stochastic seismicity analysis do not access the actual physical mechanism that took place. It simply shows that the seismicity rate variations are not significantly different from what would be expected from aftershock triggering.

Testing the seismicity against the ETAS model allows to take into account seismicity rate increases driven by aftershock interactions and a stationary background rate, modeling a constant tectonic forcing. The rejection of the ETAS null hypothesis suggests that the model requires an additional triggering term to explain the increase. One of the simplest interpretations and modifications is to attribute the seismicity deviation to a change in background seismic activity. Such variation can be associated to a change in tectonic forcing (e.g., a slow-slip event, a nucleation phase, etc.) or another phenomena (e.g., volcanic process, geothermal activity, etc.). To capture such change in seismic activity, the constant background term μ in the ETAS conditional intensity (Eq. 1.13) can be transformed to be time-dependent with $\mu(t)$. Such an ETAS model with a non-stationary background rate is called a non-stationary ETAS model (see Figure 1.22). During the transient background forcing, we observe enhanced earthquake interactions compared to stationary times, increasing the chance to draw a large magnitude. The deviation can also theoretically be attributed to a change in the aftershock triggering term, but it is very unlikely that it can occur independently of a physical change in fault conditions. If such a change does exist, the reasons for it are likely to lead to interpretations similar to those for a change in the background term (i.e., it is also a change in the stationarity of the seismic activity).

Unfortunately, extracting non-stationary ETAS parameters from seismicity is difficult because the background term $\mu(t)$ is likely to over-fit all variations in seismicity rate, including aftershocks, leading to $\lambda(t) = \mu(t)$. Therefore, to properly interpret the earthquake interaction term from the tectonic forcing term, bounds must be conditioned on the non-stationary background rate. For example, temporal smoothing of $\mu(t)$ is sometimes used to suppress high-frequency rate variations (Hainzl & Ogata, 2005; Marsan et al., 2013; Hainzl et al., 2013; Kattamanchi et al., 2017). It is also possible to fix an additional background forcing for μ with a simple shape, based on other available geophysical evidences of transient variations (e.g., aseismic slip from GPS; see Chapter 3). If this updated null hypothesis is not rejected, we can interpret the additional forcing as possibly driven by such a transient phenomena.

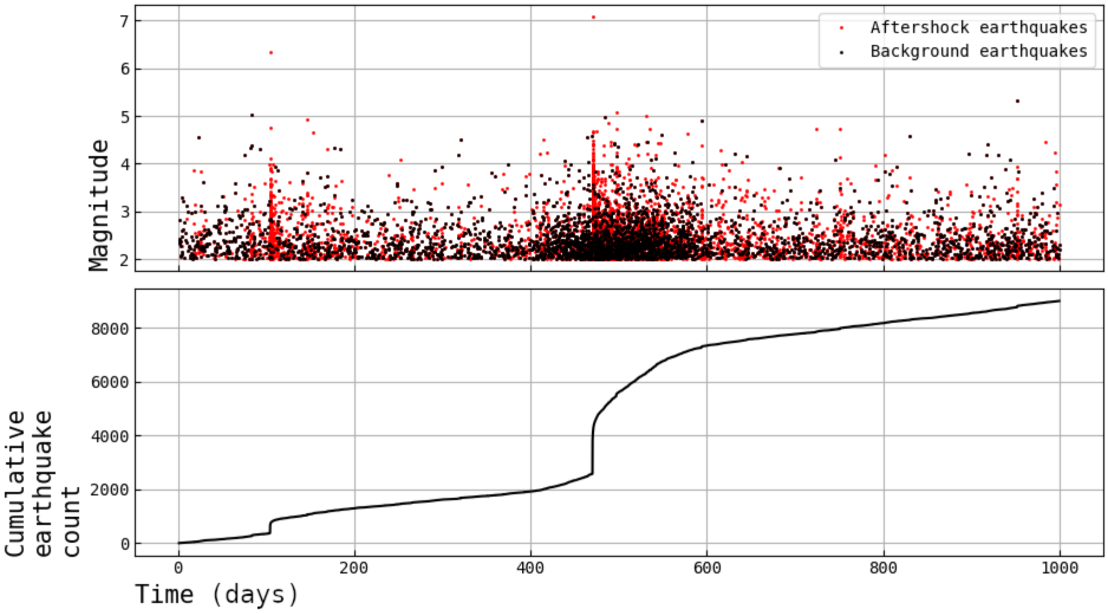

FIGURE 1.22: An example of a synthetic earthquake catalog generated with the non-stationary ETAS model. Black dots are the non-stationary background earthquakes from Figure 1.19. Red dots are aftershocks. The ETAS parameters used to generate aftershock are $A = 0.005, c = 0.001, p = 1.1$ and $\alpha = 2$. Magnitude are drawn from the Gutenberg Richter law with $b = 1$. The non-stationary background rate is generating a seismicity increase that is not explained by aftershocks. It can model a transient tectonic forcing hidden in earthquake interactions.

1.4 Improving earthquake catalogs

As mentioned above, numerous studies have demonstrated that deviations of foreshock seismicity from earthquake triggering models tend to be more pronounced when low-magnitude earthquakes are considered in the analysis. As proposed by Mignan (2015), anomalous foreshock activities seem to arise when the magnitude of completeness is at least 3 magnitude units below the mainshock magnitude. The last decade has witnessed a significant increase in near-fault seismological observations, providing a large amount of high-resolution data (Arrowsmith et al., 2022). There is therefore an unprecedented opportunity to exploit this wealth of data to incorporate as many low-magnitude earthquakes as possible and conduct a thorough investigation of foreshock processes.

On the other hand, the detection of transient background forcing with statistical seismicity analysis does not provide sufficient physical evidence to highlight an actual aseismic slip forcing. Therefore, statistical seismicity analysis need to be coupled with independent evidences of transient aseismic slip to properly interpret the results. The detection of aseismic slip relies on dense geodetic observations and/or meticulous analysis of seismic sources, including repeating earthquakes and low-frequency earthquakes (Beroza & Ide, 2011; Uchida, 2019). Such joint analysis can significantly enhance our understanding by offering deeper insights into the underlying fault physics that may be driving unusual foreshock activities.

In this Ph.D. thesis I take advantage of high-resolution seismicity catalogs, that include many low magnitude earthquakes. Such extensive datasets allow me to conduct a comprehensive exploration of foreshock sequences and their relation to aseismic processes. In this section, I introduce the state-of-the-art tools and methods directly or indirectly employed in this work to detect of low magnitude earthquakes and identify aseismic fault slip.

1.4.1 Detecting low magnitude earthquakes

In an ideal scenario, the statistical analysis of earthquake triggering patterns would be performed using flawless earthquake catalogs, including all earthquakes within a region, regardless of their magnitude. However, in reality, our ability to detect earthquakes depends on factors like network density and the level of seismic noise, making it impossible to capture every seismic events, particularly those of small amplitude. Therefore, earthquake catalogs only include the largest magnitude earthquakes that can be reliably detected. Usually, we estimate a level of completeness above which all earthquakes can be confidently detected by the network, using the minimum magnitude at which the Gutenberg-Richter law holds (i.e., the magnitude of completeness m_c in eq. 1.6). The lower this magnitude of completeness (m_c), the greater the number of low magnitude earthquakes that can be added to the catalog, significantly enhancing its quality. Given that the b value of the Gutenberg-Richter law is typically close to 1, reducing m_c by one magnitude unit results in a tenfold increase in the number of newly detected low-magnitude earthquakes.

Large magnitude earthquakes are easily detected by worldwide network because they radiate a lot of energy through high-amplitude seismic waves. For example, $M \geq 4$ earthquakes are routinely detected by global seismological networks (Ekström et al., 2012) and often reviewed by visual inspection of continuous seismic traces (possibly tool-assisted) by a trained seismologist. While manually reviewing large magnitude earthquakes is possible, it becomes an monumental task for low magnitude earthquakes given their large number, the amount of local stations to process and the low signal-to-noise ratio associated with these events. Therefore, improving the completeness of an earthquake catalog necessarily depend on reliable automatic detection algorithms (Arrowsmith et al., 2022).

A variety of earthquake detection tools have been proposed with different efficiencies and drawbacks (Allen, 1978; Baer & Kradolfer, 1987; Sleeman & van Eck, 1999; Saragiotis et al., 2002; Ross et al., 2016) but presenting an exhaustive list is beyond the scope of this thesis. I choose to present below two recent and efficient detection techniques that allow the automatic detection of many small earthquakes in order to lower the magnitude of completeness. These two techniques form the basis of the high resolution catalogs analyzed in this thesis.

Deep-learning phase pickers

Earthquake radiates two distinct seismic body wave fields, the P and S waves, each traveling at two different velocities (Aki & Richards, 2009). These wavefronts form the basis of many earthquake detection tools because they can be easily picked on continuous data and used for location. A recent and significant advance in earthquake detection techniques is the use of deep neural networks (DNN) to automatically detect and pick seismic phases of earthquakes. DNN are a type of artificial neural network consisting of successive layers of interconnected neurons that perform basic mathematical operations. These networks typically take a tensor of numerical values as input and process them through various layers and neurons, ultimately producing an output tensor containing the desired information extracted from the input data. The architecture of a DNN is often complex, with interconnected layers forming a chain of numerical operations. However, this complexity allows the network to perform highly complex tasks by carefully tuning the parameters of each neuron. After selecting a specific layer architecture, the utilization of DNN begins with a training phase. During this training phase, the network 'learns' to recognize features from a labeled dataset of inputs and outputs tensors. Basically, neuron parameters (that modulate the mathematical operations) are adjusted to optimize the network's ability to reproduce the correct output from a given input.

When properly trained, the DNN becomes a powerful predictive tool. When presented with an unknown input vector (e.g., seismic waveform here), the trained network can quickly process it using the fixed mathematical operations learned during training. The training phase of a DNN is computationally intensive and time-consuming, especially when dealing with many model parameters (i.e., layers and neurons). However, the prediction phase is very efficient because it only involves applying the pre-learned mathematical operations to the input vector.

Applied to seismic data, the DNN can accurately extract valuable information from waveforms, such as detecting earthquakes, and picking P-waves and S-waves. The automatic feature recognition capabilities of deep neural network offer a powerful advantage in efficiently picking many earthquake phases from continuous seismic waveforms. Several DNN models for the detection and phase picking have been presented in recent years (Mousavi et al., 2019a; Ross et al., 2018; Soto & Schurr, 2021; Woollam et al., 2019; Zhu & Beroza, 2018; Mousavi et al., 2020). In these cases, DNN models are trained over a database of known earthquake waveforms, phase picks and noise, which were meticulously reviewed by expert seismologists. For example, the EQTransformer model (Mousavi et al., 2020) was trained over the STanford EArthquake Dataset (STEAD; Mousavi et al., 2019b), a worldwide global dataset of labeled earthquake and non-earthquake waveforms. Subsequently, the trained model can be applied to continuous data streams in different regions to uncover previously undetected earthquakes.

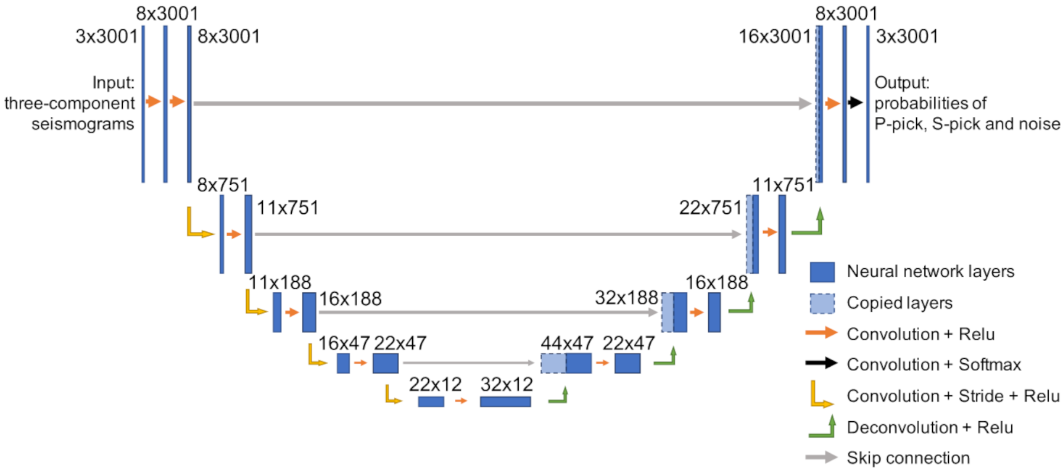

FIGURE 1.23: The Deep Neural Network architecture of the PhaseNet phase-picking algorithm. The input is the 30-s three-component seismograms sampled at 100 Hz. The output are three probabilities with the same length as input for P pick, S pick and noise. The blue rectangles represent layers inside the neural network. The numbers near them are the dimensions of each layer, which follow a format of "number of channels × length of each channel". The arrows are operations applied between layers. The input seismic data go through four down-sampling stages and four up-sampling stages. A skip connection at each stage directly concatenates the left output to the right layer without going through the deeper layers. Modified from Zhu & Beroza (2018)

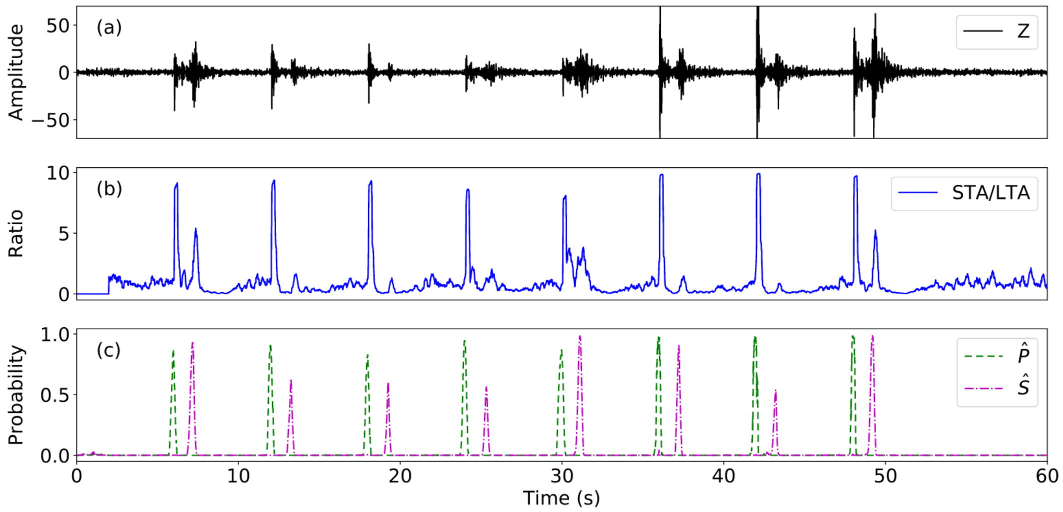

FIGURE 1.24: An example of a phase picking with Phase-net. (a) A waveform of vertical component. (b) Output of basic STA/LTA in Obspy. (c) Output of PhaseNet. Modified from Zhu & Beroza (2018)

An illustration of a deep neural network applied to earthquake phase picking Phase-Net (Zhu & Beroza, 2018) is presented in Figure 1.23. The model takes as input a three-component seismogram as a 2D tensor and output probability values to have a P phase, S phase or noise in the seismogram (a 2D tensor with dimension similar as input). The network consists of 18 intermediate layers of neuron that process the input data to generate the output. An example of the Phase-net results (Zhu & Beroza, 2018) is presented in Figure 1.24. It shows the P and S phase probabilities computed by the deep-neural model from a seismogram containing 8 earthquakes. These results are compared to a classic implementation of STA/LTA (Baer & Kradolfer, 1987), a phase picker based on waveform amplitude changes. Phase-Net effectively identifies both P and S phases and provides more accurate results compared to STA/LTA.

Following a comprehensive benchmark of their detection ability, Phase-Net (Zhu & Beroza, 2018) and EQTransformer (Mousavi et al., 2020) were found to outperform the other DNN models and classic detection techniques (Münchmeyer et al., 2022). These two models are now widely employed to produce high-resolution earthquake catalogs in various regions of the world because of their user-friendly use and reliability (Wang et al., 2020; Liu et al., 2020; Gong et al., 2022; Arrowsmith et al., 2022). In this Ph.D. thesis, I use the EQTransformer model to build a low magnitude of completeness catalog near Valparaiso in Chile (see Chapter 3).

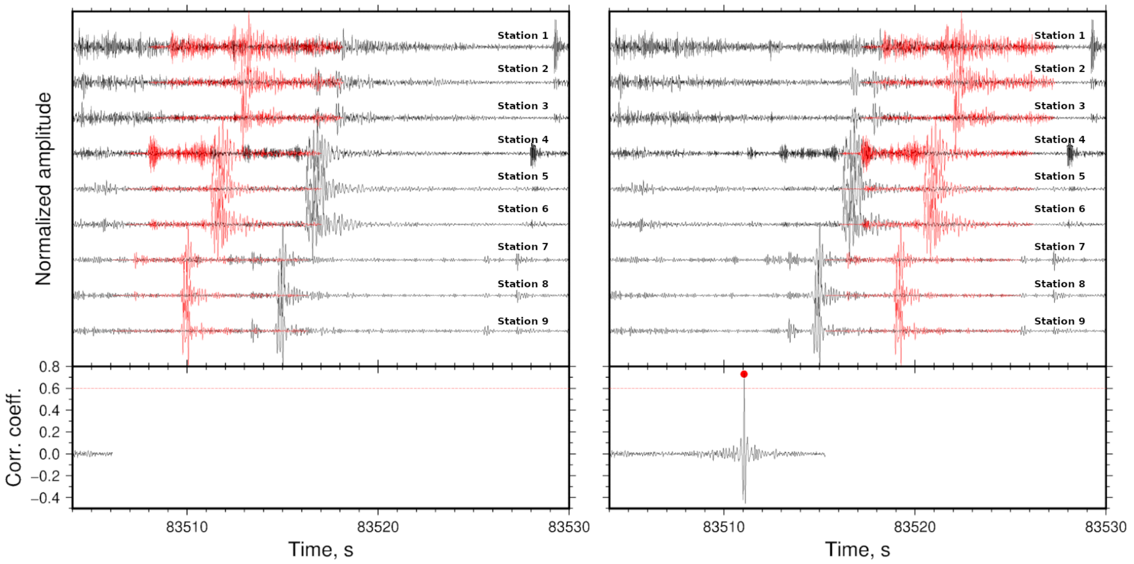

FIGURE 1.25: An illustration of the template matching technique at two different time steps. Black waveforms are continuous seismological record of a given network of stations. Red waveforms are a template earthquake detected within the same network. Bottom subplots are the corresponding cross-correlation coefficient with time. The template is scanning the continuous data by computing a cross-correlation coefficient over a sliding window. A new event (red dot) is detected when the cross-correlation coefficient exceeds a given threshold. Figure from courtesy of Z. Duputel

Template matching

Template matching is another signal processing technique frequently employed to enhance the detection of small earthquakes, particularly in scenarios where they are buried within noisy seismic data with unclear phase arrivals. This method involves comparing a known earthquake signature (referred to as the template) with continuous seismic data to identify new earthquakes (Kay, 1993; Gibbons & Ringdal, 2006; Peng & Zhao, 2009; Lengliné et al., 2012).

An illustration of the template matching technique is given in Figure 1.25. The process begins with the selection of a set of template earthquakes from a well-established catalog. These templates are subsequently used to scan continuous seismic data and detect new earthquakes. Each template consists of short segments of seismic waveforms including an earthquake at various seismic stations (in red in Figure 1.25). Using a sliding window, we then use template waveforms to scan continuous seismic records (black waveforms in Figure 1.25).

At each new position of the sliding window, the cross-correlation between the template waveforms and seismic data is computed. The cross-correlation measure the similarity between two discrete signals of n data samples $x = [x_1, .., x_n]$ and $y = [y_1, .., y_n]$. The normalized cross-correlation coefficient, ranging between -1 and 1, is given by (Gibbons & Ringdal, 2006):

$$\begin{aligned} C(x,y) &= \frac{\sum_{i=1}^{n}(x_i-\bar{x})(y_i-\bar{y})}{\sqrt{\sum_{i=1}^{n}(x_i-\bar{x})^2}\sqrt{\sum_{i=1}^{n}(y_i-\bar{y})^2}} \\ \text{with,} \quad \bar{x} &= \frac{1}{n}\sum_{i=1}^{n} x_i, \quad \bar{y} = \frac{1}{n}\sum_{i=1}^{n} y_i \end{aligned} \tag{1.18}$$

When several stations are employed, the correlation coefficient $C(x,y)$ is calculated for each data channel, and the results are averaged.

A new earthquake can be identified when the correlation coefficient exceeds a certain detection threshold (such as $C(x,y) \geq 0.6$). Values above this threshold indicate a significant similarity between template waveforms and the continuous seismic data (red dot in Figure 1.25). The detection process is then repeated for the other templates to match different type of earthquake waveforms, depending on their locations and source mechanisms.

Template matching is used by many authors to detect small earthquakes that may be buried in seismic noise and to improve the magnitude of completeness in seismicity catalogs (Gibbons & Ringdal, 2006; Peng & Zhao, 2009; Skoumal et al., 2014; Lengliné et al., 2016; Ross et al., 2019a,b; Lee & Douilly, 2022). For example, Ross et al. (2019b) applied the template matching techniques to improve the detection of small magnitude earthquakes in Southern California during the period from 2008 to 2018 (see Figure 1.26). Their approach lowered the magnitude of completeness of the region down to $m_c = 0.3$, compared to $m_c = 1.7$ for the Southern California Seismic Network (SCNC) reference catalog. This template matching catalog includes a total 1.81 million earthquakes, which is 10 times larger than the SCNC catalog (see Figure 1.26). Their template matching catalog is used in Chapter 2 of this thesis to conduct an in-depth analysis of foreshock sequences in Southern California.

1.4.2 Aseismic slip and repeating earthquakes

In addition to the statistical analysis of earthquake catalogs, we can exploit the valuable information included in seismic waveforms to better capture ongoing geophysical processes. In the study of foreshocks, aseismic slip is often invoked to explain precursory patterns that are sometimes detected prior to mainshocks.

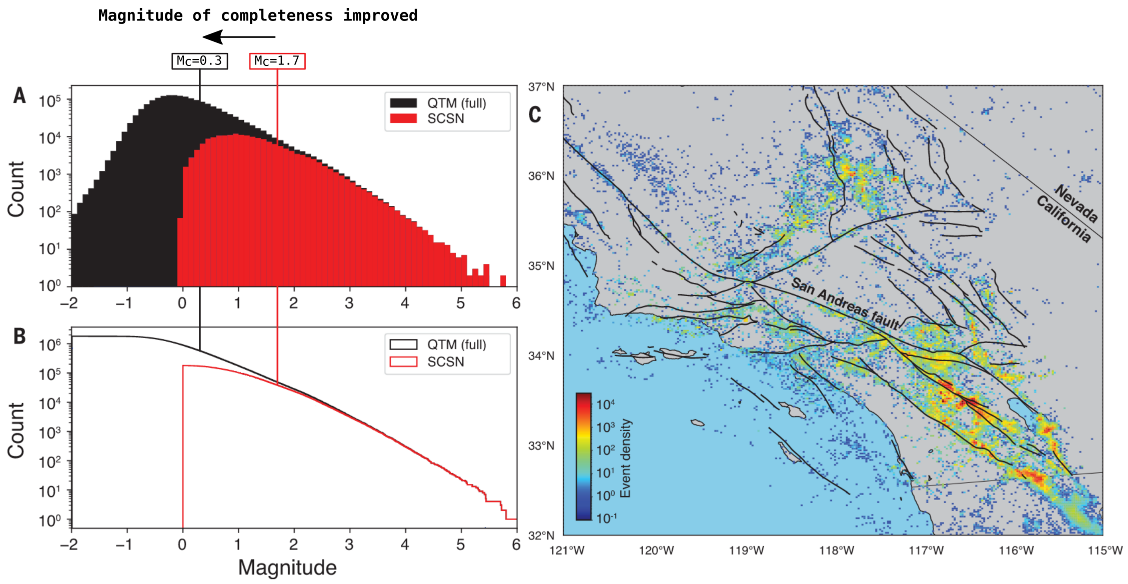

FIGURE 1.26: A low magnitude of completeness catalog of Southern California enhanced thanks to template matching: The Quake Template Matching (QTM) catalog. (A) Frequency-magnitude distribution of earthquakes listed in the Southern California Seismic Network (SCSN) catalog and the QTM catalog. (B) Corresponding cumulative frequency-magnitude distributions. (C) Map of earthquake density in the QTM catalog (bins: 2 km by 2 km). Modified from Ross et al. (2019b)

In this context, we present a method for tracking aseismic slip from earthquakes characterized by highly similar waveforms and source locations, commonly referred to as "repeating earthquakes". This approach can be used to assess the aseismic contribution to foreshock generation and its connection with the 3 conceptual models outlined in section 1.2 .

As pointed out above, repeating earthquakes, or "repeaters", are earthquakes that shares the same source location and exhibits high waveform similarity (Uchida, 2019; Uchida & Bürgmann, 2019, for a review). Such repeating earthquakes offer valuable information to track slow aseismic slip along faults (Nadeau & Johnson, 1998; Nadeau & McEvilly, 1999; Uchida, 2019; Uchida & Bürgmann, 2019).

Figure 1.27 illustrates the concept of a repeating earthquake. Within a slow-slip fault zone, small embedded and brittle asperities may exist. An ongoing aseismic slip can gradually load and rupture these asperities, producing small earthquakes. The amount of seismic slip on these asperities is expected to approximate the average aseismic slip on the surrounding fault area. If the ongoing aseismic slip is sufficiently long or rapid, the same asperity can be loaded and

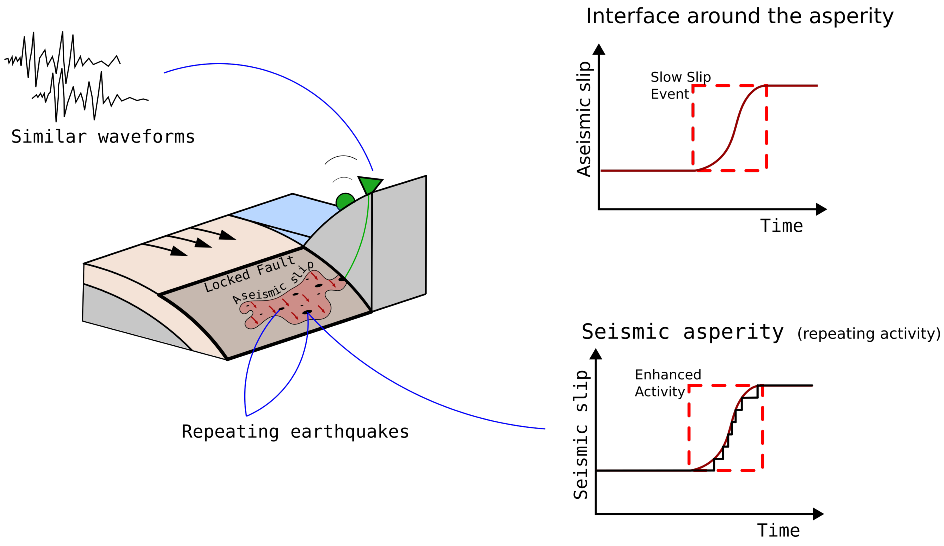

FIGURE 1.27: An illustration of repeating earthquakes driven by an slow-slip event. Repeating earthquakes are small seismic asperities (black ellipses) embedded in an aseismically slipping region (red patch). The top graph is the cumulative slip with time of the aseismic slip (arbitrary unit). Bottom graph is the cumulative seismic slip with time of an asperity (arbitrary unit). The aseismic slip successively loads and breaks the same seismic asperity producing repetitive earthquakes that can be recorded by seismological stations. Such repeating earthquakes are co-located on the fault and have similar waveforms. The rate and location of repeaters can help to track the evolution of aseismic slip.

broken several times, producing repeating earthquakes. By tracking repeating earthquakes from several asperities it is possible to have an estimate of the evolution of aseismic slip on the fault, both in time and space. Because the amount of seismic and aseismic slip is small (typically a few centimeters), the location of asperities on the fault does not change significantly with time, nor do their source characteristics. Therefore, repeating earthquakes exhibit very similar waveforms, a property can be exploited for analysis.

To identify repeating earthquakes from a seismicity, we can exploit the aforementioned properties of co-located sources and waveform similarity. As a first step, we gather earthquakes with similar waveforms by computing the cross-correlation coefficient (CC) between all pairs of earthquakes in the catalog, using equation 1.19. Instead of cross-correlation, some studies rather use waveform coherence, which also measures waveform similarity, but in the frequency domain

(Lengliné & Marsan, 2009; Uchida & Bürgmann, 2019). We then group earthquakes into clusters of high waveform similarity, for example using hierarchical clustering applied to the CC values. At this stage, only clusters of earthquakes with high waveform similarity are considered. Typically, it corresponds to an average cross-correlation value above 0.7 at several seismic stations (Uchida, 2019).

It should be noted that, waveform similarity alone is often not enough to reliably extract repeating earthquakes. The source time function of small earthquakes is often very short and their waveforms recorded at remote stations are dominated by the seismic response of the Earth structure. Therefore, two sufficiently close earthquakes can have very similar waveforms without necessarily being co-located (Gao et al., 2021), because they propagate in very similar medium. To ensure that repeaters are co-located, subsets of similar earthquakes must be accurately re-located. The relative distance between earthquakes can be well estimated with double-difference location algorithms using the differential travel-times of the P and S waves (e.g., Waldhauser & Ellsworth, 2000). After relocation, we can estimate the source area of each earthquake, either by detailed analysis of the earthquake's spectral characteristics, or by using magnitude estimates assuming a constant stress drop in circular crack (Kanamori & Anderson, 1975; Nadeau & Johnson, 1998; Hanks & Bakun, 2002). Then, only earthquakes with overlapping fault areas are considered as repeaters. I present on Figure 1.28 an example of a repeating earthquakes cluster detected near the epicenter of the 2017 Valparaiso mainshock (a seismic sequence that is analyzed in Chapter 3). Their waveforms are very similar with an average CC of 0.94 and their sources (Circular crack model) are collocated.

The repeating earthquake activity is often used to track aseismic slips in addition to geodetic measurements. Many transient aseismic slip detected before mainshocks were tracked down using repeaters (Uchida et al., 2004; Kato et al., 2012; Uchida & Matsuzawa, 2013; Meng et al., 2015; Kato et al., 2016a; Vuan et al., 2017; Ruiz et al., 2017). For example, repeating earthquakes were used by Kato et al. (2012) and Kato et al. (2016a) to track aseismic slip before the 2011 Tohoku earthquake and the 2014 Iquique earthquake. From the stack of many repeating earthquakes cumulative slips, they estimated the average amount of aseismic slip on the fault. They found that an aseismic slip was preceding and accelerating toward the mainshock and interpreted it as evidence of a mainshock nucleation phase.

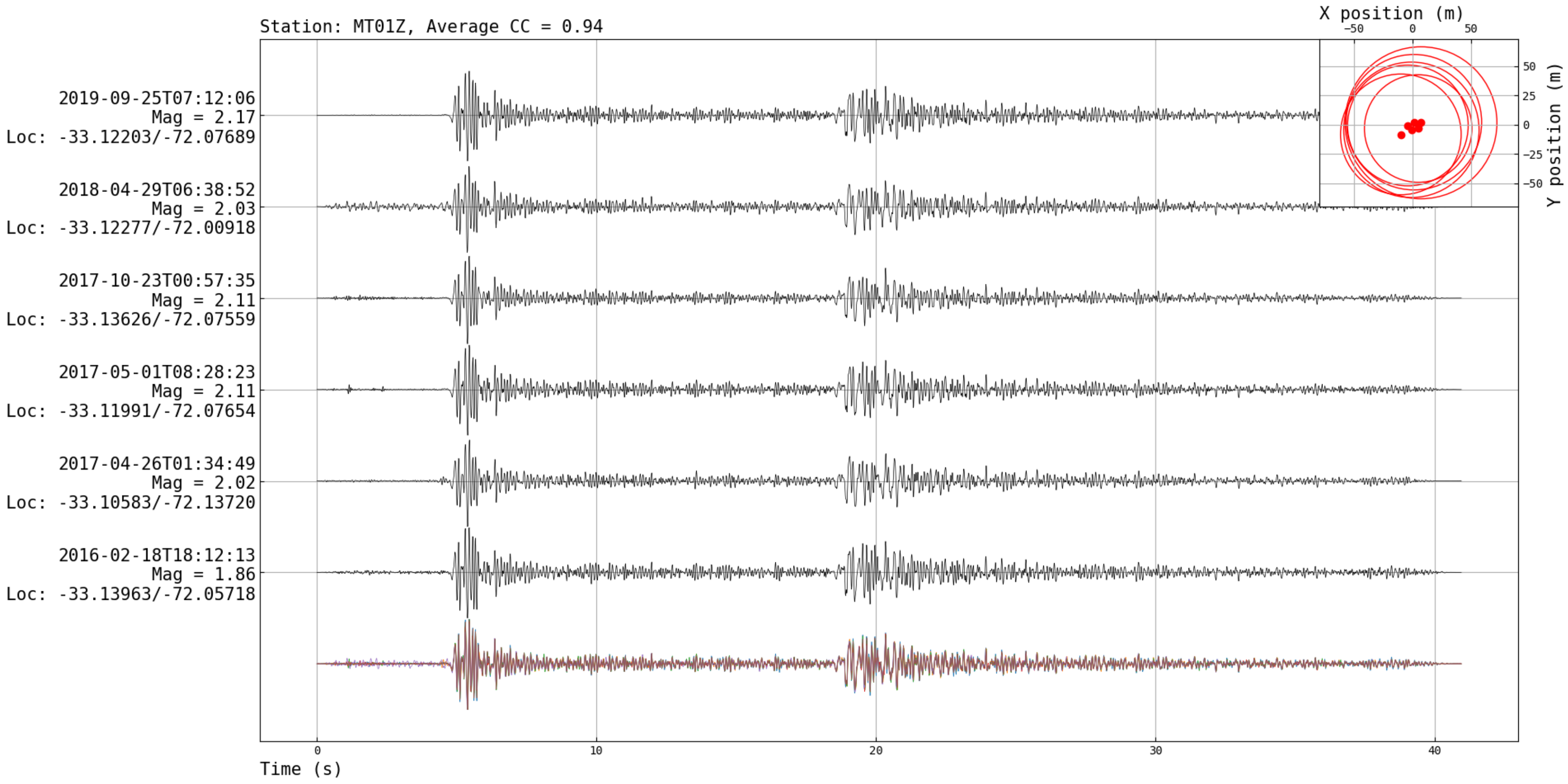

FIGURE 1.28: 6 Repeating earthquakes observed on the Chilean subduction zone near Valparaiso. Black lines show the normalized waveforms recorded on the vertical component of the Chilean broadband station MT01. Bottom colored lines show the same waveform superimposed for comparison. The labels on the left indicate the origin time, magnitude and horizontal absolute location of earthquakes. The top left inset shows their relative locations on the subduction fault and their estimated rupture areas. Earthquakes all show a high similarity in waveform and co-located sources.

The detection of repeating earthquakes offers a dual advantage by shedding light on aseismic fault processes while also establishing a link to seismic activity. The combination of a detailed statistical seismicity analysis, and the study of repeating earthquakes, can facilitate a better understanding of the foreshock generation process and its relationship with a possible nucleation phase, slow-slip event or earthquake cascade. In this thesis, repeating earthquakes are employed in the analysis of the 2017 Valparaiso seismic sequence in Chapter 3.

Chapter 2

Rare occurrences of non-cascading foreshock activity in Southern California

Preliminary words

As mentioned above, recent advances in earthquake detection motivate a re-evaluation of foreshock seismicity variations. The Southern California earthquake catalog has recently been enhanced using template matching from 2008 to 2018 (Ross et al., 2019b), improving the completeness level to $M_c = 0$ in the best-resolved regions. Based on this highly complete earthquake catalog, Trugman & Ross (2019) suggested that mainshocks in Southern California are more likely to be preceded by anomalously elevated seismicity when low-magnitude earthquakes are included in the analysis. 72% of mainshocks are found to be preceded by unusually active foreshocks, possibly highlighting the nucleation phase of the mainshock as depicted in theory and laboratory experiments. However, as pointed out by Ende & Ampuero (2020), their seismicity analysis did not take into account earthquake interactions. Taking into account long-term earthquake clustering properties, they pointed out that unusual foreshock rates are not as frequent as suggested. While Ende & Ampuero (2020) improves the significance of foreshock rate increase in the template matching catalog, their model still fails to completely reflect short-term seismicity rate variations caused by earthquake interactions.

In this first chapter, I re-evaluate the same catalog against the Epidemic Type Aftershock Sequence model, which accounts for complete temporal clustering due to aftershock triggering. I evaluate the significance of 53 foreshock sequences against the cascade model and estimate the fraction that may require additional tectonic forcing, possibly mediated by a nucleation phase.

This study was conceived with my 2 advisors Olivier Lengliné and Zacharie Duputel and in close collaboration with David Marsan from ISTerre. This work has been published in *Geophysical Research letter*.

2.1 Abstract

Earthquakes preceding large events are commonly referred to as foreshocks. They are often considered as precursory phenomena reflecting the nucleation process of the main rupture. Such foreshock sequences may also be explained by cascades of triggered events. Recent advances in earthquake detection motivates a reevaluation of seismicity variations prior to mainshocks. Based on a highly complete earthquake catalog, previous studies suggested that mainshocks in Southern California are often preceded by anomalously elevated seismicity. In this study, we test the same catalog against the Epidemic Type Aftershock Sequence model that accounts for temporal clustering due to earthquake interactions. We find that 10/53 mainshocks are preceded by a significantly elevated seismic activity compared with our model. This shows that anomalous foreshock activity are relatively uncommon when tested against a model of earthquake interactions. Accounting for the recurrence of anomalies over time, only 3/10 mainshocks present a mainshock-specific anomaly with a high predictive power.

2.2 Introduction

Large earthquakes are often preceded by an increase in seismic activity, which is then referred to as a foreshock sequence (Jones & Molnar, 1976; Bouchon et al., 2013; Marsan et al., 2014; Dodge et al., 1995, 1996; Reasenberg, 1999). Although these foreshock sequences are often referred to as precursors, a problem is the inherent difficulty to identify earthquakes as foreshocks before the mainshock occurs. In addition, we still do not fully understand the physical mechanisms that generate foreshocks and the reason why they occur. Two competing conceptual models have been proposed (Mignan, 2015). First, a "cascade model" where successive foreshock stress changes contribute to a slow cascade of random failures (possibly mediated by aseismic afterslip) ultimately leading to the mainshock (Helmstetter & Sornette, 2003; Marzocchi & Zhuang, 2011; Ellsworth & Bulut, 2018). Second, a "slow pre-slip model" where foreshocks are passive tracers of an evolving fault loading process preceding the mainshock rupture (Dodge et al., 1996; Bouchon et al., 2011; Kato et al., 2016a). The aseismic vs seismic contributions to the overall moment release during the precursory phase is ultimately what distinguishes these two models. Unfortunately, the aseismic part is generally difficult or merely impossible to estimate from the available observations, and one therefore needs to resort to indirect arguments, often pertaining to the spatial and temporal distribution of the foreshocks. Although recent observations of slow deformation transients lasting days to months before the mainshock favor the triggering of foreshocks by aseismic preslip (Socquet et al., 2017; Mavrommatis et al., 2014; Ito et al., 2013), the aseismic character of such precursory motion is vigorously debated (Ruiz et al., 2014; Bedford et al., 2015). In addition, foreshock sequences are not observed systematically before large earthquakes. However, this lack of systematic precursory observations might partly be due to the incompleteness of current seismicity catalogs (Mignan, 2015; Ross et al., 2019b)

The southern California catalog was recently enhanced thanks to the template matching analysis conducted by (Ross et al., 2019b). The resulting QTM (Quake Template Matching) catalog includes more than 850,000 earthquakes (for the higher choice of threshold, see Section 2.3.1) in a 10 year-long period from 2008 to 2017 and is complete down to magnitudes near or below zero for the best resolved regions. Such a high degree of completeness of the QTM catalog motivates the evaluation of the statistical significance of seismic activity preceding large earthquakes in southern California. By comparing seismic activity before $M \geq 4$ earthquakes to a constant and local background rate, Trugman & Ross (2019)[T&R from here on] estimated that 72% of mainshocks in the QTM catalog are preceded by a significantly elevated seismic activity. With the same approach using the SCSN catalog, which includes less earthquakes, only 46% of mainshocks were detected with a significantly elevated seismic activity. These results suggest that detailed earthquake detections could bear important information about an impending earthquake. The seismic activity observed in the 20-day window before $M \geq 4$ earthquakes was later re-evaluated by Ende & Ampuero (2020)[V&A from here on] to investigate in which cases these increases in seismicity were significant compared to the natural fluctuations of the seismicity rate. In their approach, V&A choose to test seismic activities smoothed at 20 days against a model that accounts for increases in seismicity. In this model, earthquake interevent times (IETs) are drawn independently from a gamma distribution. This approach is motivated by the fact that IETs in seismic catalog tends to follow a gamma, rather than an exponential distribution (i.e., T&R's background model) because the gamma distribution is more likely to fit the small IETs observed during clusters of earthquakes. Based on this analysis, V&A estimated that only 33% of mainshocks are preceded in the last 20 days by a significantly elevated seismic activity, coming down to 18% when accounting for temporal fluctuations of such anomalies, i.e., anomalies taking place at random and therefore not specifically related to mainshock occurrences.

For the sake of simplicity, we will now refer to as "foreshock activity" the seismic events observed in the 20 days immediately before $M \geq 4$ earthquakes. Although V&A further addressed the significance of elevated foreshock activity in the QTM catalog, we believe that their analysis still underestimates the effect of earthquake clustering. Namely, the random sampling approach of V&A assumes independent IETs, which is an over-simplification of the actual earthquake clustering observed during individual aftershock sequences. Indeed, during aftershock sequences, IETs are correlated rather than independent. We illustrate this concern in the supporting information (Text 2.S.4 and Figures 2.S.6) by applying the V&A approach on synthetic ETAS catalogs. In this study, we consider that local earthquake interactions needs to be fully accounted for in order to identify foreshock activity that stands out from simple cascades of triggered seismicity.

We extend the studies of T&R and V&A by testing the statistical significance of elevated foreshock seismicity in the QTM catalog, accounting for local earthquake interactions. In this work, we use the temporal Epidemic Type Aftershock Sequences (ETAS) model, in which the seismicity rate at each time is represented by the superposition of a background rate and a rate linked to the aftershock triggering from past events (Ogata, 1988). This model is the simplest that can reproduce both the gamma distribution of IETs (Saichev & Sornette, 2007) and their correlation during aftershock sequences. After selecting mainshocks using criteria similar to T&R and V&A, we extract ETAS parameters from the QTM catalog in the vicinity of each mainshock. We then compare the foreshock activity with ETAS predictions accounting for past seismicity. We find that the number of instances of anomalously elevated foreshock seismicity is significantly reduced when accounting for earthquake interactions (about 19% compared to 33% and 72% respectively in V&A and T&R). Moreover, out of these 10 cases, only 3 appear to be exclusively related to the subsequent occurrence of the mainshock.

2.3 Data and methods

2.3.1 Mainshock selection

We noticed that the full QTM catalog used by T&R and V&A suffers from episodic bursts of false detections, that occur due to too low a detection threshold (threshold fixed at 9.5 times the median absolute deviation (MAD) of the stacked correlation function). These bursts are easy to identify as they start or end at midnight, which is due to the MAD computation being performed over 24 hour long period starting at 00h00 UTC. To avoid any contamination of our analysis by such artifacts, we instead use the higher quality QTM catalog with a detection threshold at 12 times the MAD, for which these transients vanish or are strongly attenuated. In order to provide a fair comparison with previous results, we also present our analysis performed on the full catalog in the supporting information (Text 2.S.5 and Figures 2.S.7 and 2.S.8).

Using the higher quality QTM catalog, we then extract our own set of mainshocks with selection criteria similar to those used in T&R: A mainshock must have magnitude $M \geq 4$, and must occur from 2009/01/01 to 2016/12/31 within the geographic coordinates ranges [32.68°N, 36.2°N] and [118.80°W, 115.4°W]. To be selected, a mainshock must be preceded by at least 10 earthquakes with no larger magnitude event in the year before and within a 20×20 km^2 horizontal box around its epicenter. 53 earthquakes were selected as mainshock according to these criteria. For each selected mainshock, we extract a 10-year long local catalog that includes all the seismicity observed within the 20×20 km^2 box with no depth cutoff.

We evaluate for each local catalog the local magnitude of completeness M_c and remove all events with a magnitude $M < M_c$. We must acknowledge that removing all earthquakes of the QTM catalog below M_c may remove potentially interesting features, but we consider that such features cannot be properly interpreted because they might reflect variation of the detection capability of the network and not real fluctuations of the seismicity rate. Therefore, to achieve a trade-off between completeness and retaining as many earthquakes as possible, we estimated manually the local M_c as either the maximum of the local Gutenberg-Richter(G-R) frequency-magnitude distribution if this distribution decays smoothly for larger magnitudes, or the magnitude at which a notable break in slope is observed. Figure 2.S.1 of the supporting information shows the 53 local Gutenberg-Richter frequency-magnitude distributions and the corresponding estimated M_c values.

2.3.2 Inversion of ETAS parameters

The ETAS model has two main ingredients: first, a background term which is time-independent and follows a Poisson process; second, a triggered term that depends on the past earthquake activity. The conditional intensity of the ETAS model (Ogata, 1988; Zhuang et al., 2012) is :

$$\lambda(t) = \mu + \sum_{i|t_i<t} A e^{\alpha(M_i - M_c)}(t - t_i + c)^{-p} \tag{2.1}$$

where μ is the time-independent background seismicity rate. The sum in the right hand side of equation (2.1) describes the expected aftershock seismicity rate at time t triggered by all previous events. A and α are constant parameters describing respectively the global aftershock productivity of the region and the magnitude dependence in the number of triggered events. M_c is the magnitude of completeness whereas c and p are the parameters of the Omori-Utsu law describing the time-decay in the aftershock seismicity rate. Therefore, in ETAS-like catalogs, temporally clustered seismicity only emerges from cascades of aftershocks.

For local catalogs associated with each mainshock, we fit the temporal ETAS model by maximizing a likelihood function with an Expectation - Maximization (EM) algorithm (Veen & Schoenberg, 2008). We estimate parameters A, c, p, α and μ in equation (2.1) (all parameter values can be found in the supporting information). We run a first inversion where the ETAS parameters are constrained to be positive. We note that most α values are close to one. Larger α values are actually expected according to window-based methods (Helmstetter et al., 2005; Felzer et al., 2004), as well as following the argument that Bath's law, i.e., the fact that the difference in magnitude between the mainshock and its largest aftershock is independent of the mainshock's magnitude, requires that $\alpha = \beta = b \ln 10$ (Davidsen & Baiesi (2016) and references therein). Moreover, it has been shown that α estimates are particularly prone to model errors (e.g., Hainzl et al., 2008, 2013) and censoring effects (Sornette & Werner, 2005; Seif et al., 2017). Nandan et al. (2017) found that the α value is expected to vary between 1.7 and 2.2 when considering a larger portion of California and a longer period than the QTM catalog. A α value close to 2 may thus represent a more realistic value of the aftershock productivity for Californian earthquakes. Therefore, we perform a second inversion where we impose that $\alpha = 2$. We thus obtain two sets of ETAS parameters (referred to as "α free" and "$\alpha = 2$" sets) to model the seismicity of local catalogs around each mainshocks. We also evaluate in the supporting information the sensitivity of our results to the uncertainty in ETAS estimates for both sets of parameters (cf., Text 2.S.3 and Figures 2.S.4-2.S.5).

2.3.3 Detection of seismicity anomalies based on the ETAS model

We test the null hypothesis H_0 that the number of events observed in 20 days is smaller than or equal to the number of events predicted by the ETAS model for both sets of parameter estimates. If H_0 is rejected for both estimates, we assume that an anomalously high seismicity is detected in the window, suggesting that a mechanism other than simple ETAS cascading is required to explain the 20-day earthquake activity. The conditional intensity function in equation (2.1) allows to directly compute an expected seismicity rate at any time t from the set of ETAS parameters (A, c, p, α and μ) and the knowledge of past seismicity $(t_i < t, M_i)$. By integrating this modeled seismicity rate, we can compute the expected number of earthquakes $\overline{N}$ in a time interval T:

$$\overline{N}(t, T) = \int_{t-T}^{t} \lambda(u)\, \mathrm{d}u \tag{2.2}$$

Here we set $T = 20$ days similar to T&R, which choice was also adopted by V&A. We compute $\overline{N}$ over 20-day sliding windows, with a 1 day shift between two consecutive windows, and covering the full time range of the QTM catalog (i.e., 10 years). For all local catalogs around each mainshock, we then obtain two time-series of $\overline{N}$ generated using the two sets of inverted ETAS parameters (α free and $\alpha = 2$). Knowing $\overline{N}$, the probability of actually observing N_{obs} earthquakes in a given 20-day time-interval is given by the Poisson distribution with mean $\overline{N}$:

$$P(N_{obs}) = \frac{\overline{N}^{N_{obs}} \mathrm{e}^{-\overline{N}}}{N_{obs}!} \tag{2.3}$$

We then define the probability of observing at least N_{obs} events over 20 days for the null hypothesis as:

$$p = P(N \geq N_{obs}) = 1 - \sum_{n=0}^{N_{obs}-1} \frac{\overline{N}^{n} \mathrm{e}^{-\overline{N}}}{n!} \tag{2.4}$$

Following T&R and V&A, we use the probability threshold $p < 0.01$ to reject the hypothesis H_0 that N_{obs} is in agreement with the expected number of events

$\overline{N}$. A small p-value would therefore correspond to anomalously elevated seismicity rate compared with ETAS predictions.

2.4 Results

The detection of seismicity rate anomalies in a 20-day sliding window is illustrated in Figure 2.1 for the seismicity located in the vicinity of 4 mainshocks. For each mainshock, the top subplot shows the time-evolution of p-values measured for the two sets of ETAS parameters (α free and $\alpha = 2$) while the bottom subplot shows the observed seismicity (i.e., magnitude vs time). For the two examples on top (Mainshock IDs 10832573 and 37301704), we notice that the 20-day foreshock activity is consistent with at least one of the ETAS predictions (α free and $\alpha = 2$) with at least one p-value above 0.01 in the last 20-days window prior to the mainshock. In these cases, our null hypothesis H_0 cannot be rejected with a confidence of 99%. The two examples on the bottom (Mainshock IDs 14898996 and 37299263) show p-values that are below 0.01 before the mainshock for both ETAS estimates. In these cases, the observed foreshock seismicity is higher than the expected ETAS cascading seismicity with a confidence level of at least 99%.

In total, we find that 10 out of 53 mainshocks are preceded by an anomalously high 20-day activity with respect to ETAS predictions. Therefore, these mainshocks are likely preceded by complementary aseismic processes other than cascades of aftershocks. However, this result must be taken in perspective with the overall ability of the ETAS models to explain fluctuations in seismicity rates over the entire catalog. As pointed out by V&A, the predictive power of an anomalously high foreshock activity is reduced if seismicity anomalies are frequently detected without being followed by a large event. The significance of an anomalously high foreshock activity being predictive of future large events should therefore be assessed given the overall ability of ETAS predictions to explain the seismicity in the vicinity of the mainshock. For example, in the case of mainshock ID 14898996 in Figure 2.1c, ETAS predictions are unable to explain the observed seismicity at several occasions during the course of the catalog. Our null hypothesis H_0 is thus rejected for numerous 20-day windows with p-values smaller than the p-value of the foreshock window. On the other hand, Figure 2.1d shows that mainshock 37299263 presents an anomalously high seismicity rate almost exclusively in the 20 days preceding the mainshock. Such an elevated seismicity rate is thus highly correlated with the mainshock occurrence. We believe

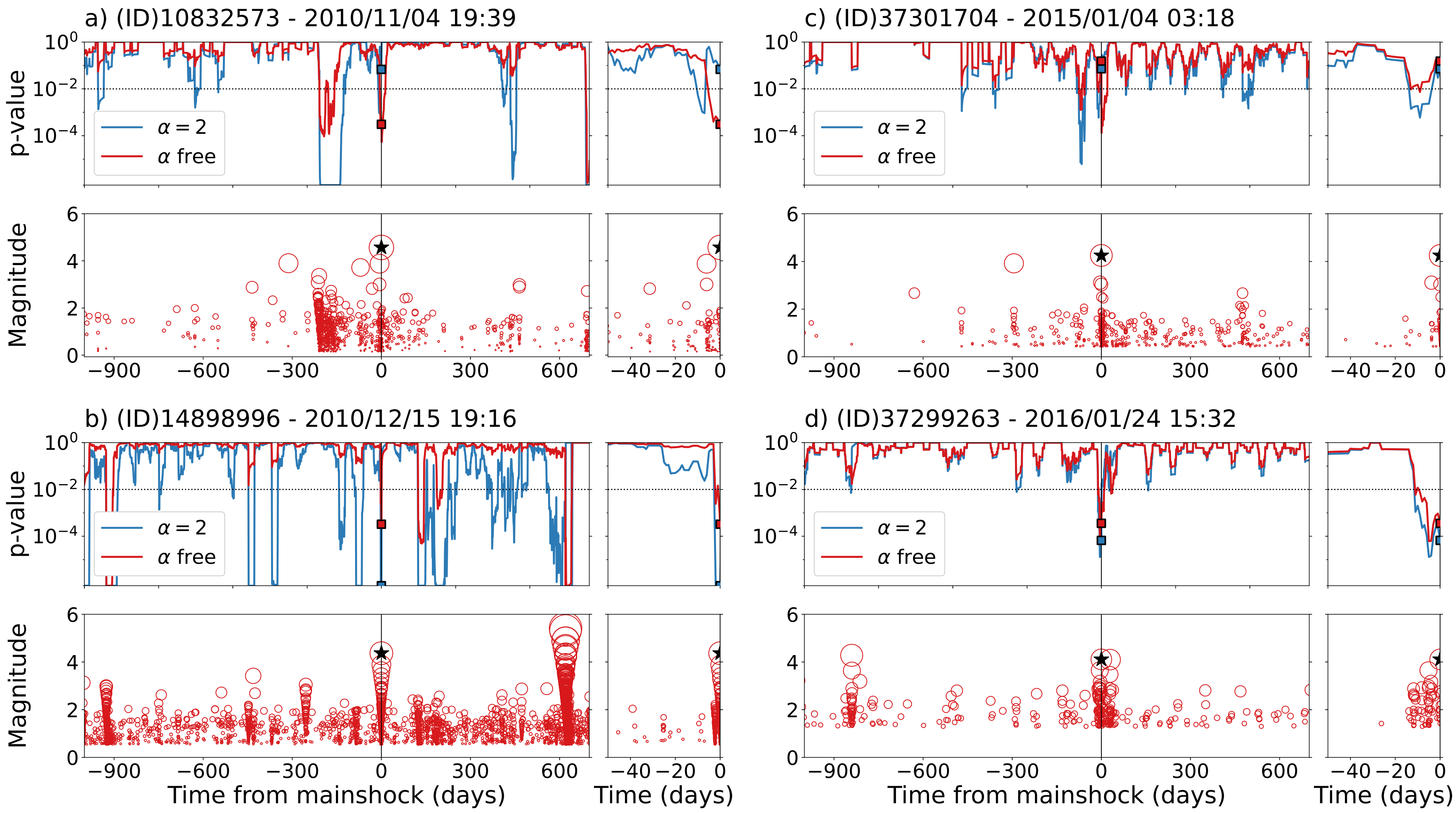

FIGURE 2.1: The 20-day sliding window analysis for 4 examples of mainshocks (black star at t=0) and their local catalog. Mainshocks IDs are (a) 10832573, (b) 37301704, (c) 14898996 and (d) 37299263. (Top graphs) probability p that ETAS explains the observed seismicity, computed for the two sets of ETAS parameters α=2 and α free. The p-value for the last 20-day window prior to the mainshock is shown with a thick square. The significance threshold of p=0.01 is shown with the horizontal dotted line. (Bottom graphs) magnitude vs time for the local catalogs in the 20×20 km^2 box around each mainshock. The right inset is a zoom around the foreshock window.

that the uniqueness of the anomaly observed before mainshock ID 37299263 is more likely to evidence predictive non-cascading mechanisms than mainshock ID 14898996.

Therefore, to quantify the significance of detected foreshock anomalies, we compare p-values in the foreshock window with the distribution of p-values over the entire 10-year catalog. For each mainshock, an anomalous foreshock activity is considered mainshock-specific if $\hat{p}$, the proportion of 10-year p-values lower or equal than the foreshock p-value, is less than 1%. This arbitrary threshold of 1% allows to discriminate between catalogs with frequent anomalous activities and those with foreshock activities that correspond to the strongest anomalies of their region. This is summarized in Figure 2.2b. Using such temporal specificity criterion, we identify that 7 out of the 10 anomalous foreshock activity already mentioned occur in regions with recurrent seismicity anomalies stronger than the foreshock one. Therefore, we argue that only 3 out of 53 mainshocks present a clear mainshock-specific anomalous activity. We note that this final selection is highly dependent on the choice of the $\hat{p}$ threshold. Figure 2.2b shows that all 10 selected sequences present less than 10% of 20-day windows over 10-years below the foreshock window p-value. The final selection of 3 out of 53 mainshock is therefore more like a refined selection of mainshocks with a local seismicity that best fit ETAS with a notable exception during foreshock time ranges.

We complement this analysis by declustering the local catalogs. The probability ω_i that earthquake i is a background earthquake is defined as $\omega_i = \frac{\mu}{\lambda(t_i)}$, and can be calculated once the ETAS parameters are estimated. We then simply count the numbers of background earthquakes as the sums of ω_i in 20 day long windows. We denote N_0 this count for the last 20 days prior to the mainshock, and by N all the counts for all the time windows before the mainshock (not just the last one). Following the same rationale that stimulated our previous analysis, we first compare N_0 to the Poisson distribution with a mean $\bar{N}$ equal to the mean of N, select the mainshocks for which $P(> N_0|\bar{N}) < 0.01$ for the two sets of ETAS parameters (1st test), and finally check whether these selected sequences display other anomalously strong bursts of background earthquakes by computing the probability that N can be greater than N_0 (2nd test). We finally select those short-listed mainshocks for which the latter probability is less than 0.01 (again, for the two sets of ETAS parameters). Figure 2.3 shows the results of this declustering approach. Only mainshocks 14598228 and 14600292 are preceded by an anomalously high foreshock activity (1st test) according to this declustering approach. According to our 2nd test, these two anomalies are also specific to the subsequent mainshock occurrences (i.e., p-value $\leq$ 0.01). These two foreshock sequences were also identified in our previous approach based on the predicted number of events according to the ETAS model. The difference in results between the declustering approach and the former method is due to the fact that declustering only leaves a small number of background earthquakes, and therefore has a strong tendency to lower the significance (i.e.; increase the p-values).

2.5 Discussion

We use the highly complete QTM catalog of Ross et al. (2019b) for southern California to further investigate the significance of anomalous high foreshock activity previously reported by T&R and V&A. As mentioned before, those studies did not fully address whether the temporal clustering of earthquakes observed during aftershock sequences is a possible explanation for the observed elevated foreshock activities. This clustering is considered as one of the possible origins of the high seismic activity observed before large earthquakes (Helmstetter & Sornette, 2003; Marzocchi & Zhuang, 2011; Ellsworth & Bulut, 2018). In practice, small $M < 4$ earthquakes trigger small aftershock sequences during which a larger $M > 4$ event is more likely to occur than at more quiet times. In this regard, high activity preceding a mainshock can naturally stem from such earthquake interactions and cascading without necessarily requiring an external preslip phenomenon. To address this concern, we use the ETAS model to discriminate which instances of QTM foreshock activities exhibit higher seismicity rates than expected from earthquake interactions.

We first assess the probability p that a given 20-day foreshock sequence can be explained by ETAS earthquake clustering. Using $p < 0.01$ as a threshold, our results indicate that $\sim$ 19% (10 out of 53) of mainshocks are preceded by increases in seismicity higher than 99% of the earthquake rates predicted by ETAS. The 20-day temporal evolution of these 10 anomalous foreshock sequences is detailed in Text 2.S.2 and Figure 2.S.9. In a second step, we further distinguish 3 out these 10 cases as being specific to the subsequent mainshock, i.e., the chance to see such a significant increase of activity occurring at random is less than 1%. The anomalously high seismicity of these 3 foreshock sequences is thus highly correlated with the $M \geq 4$ mainshock occurrences and likely to be controlled by aseismic

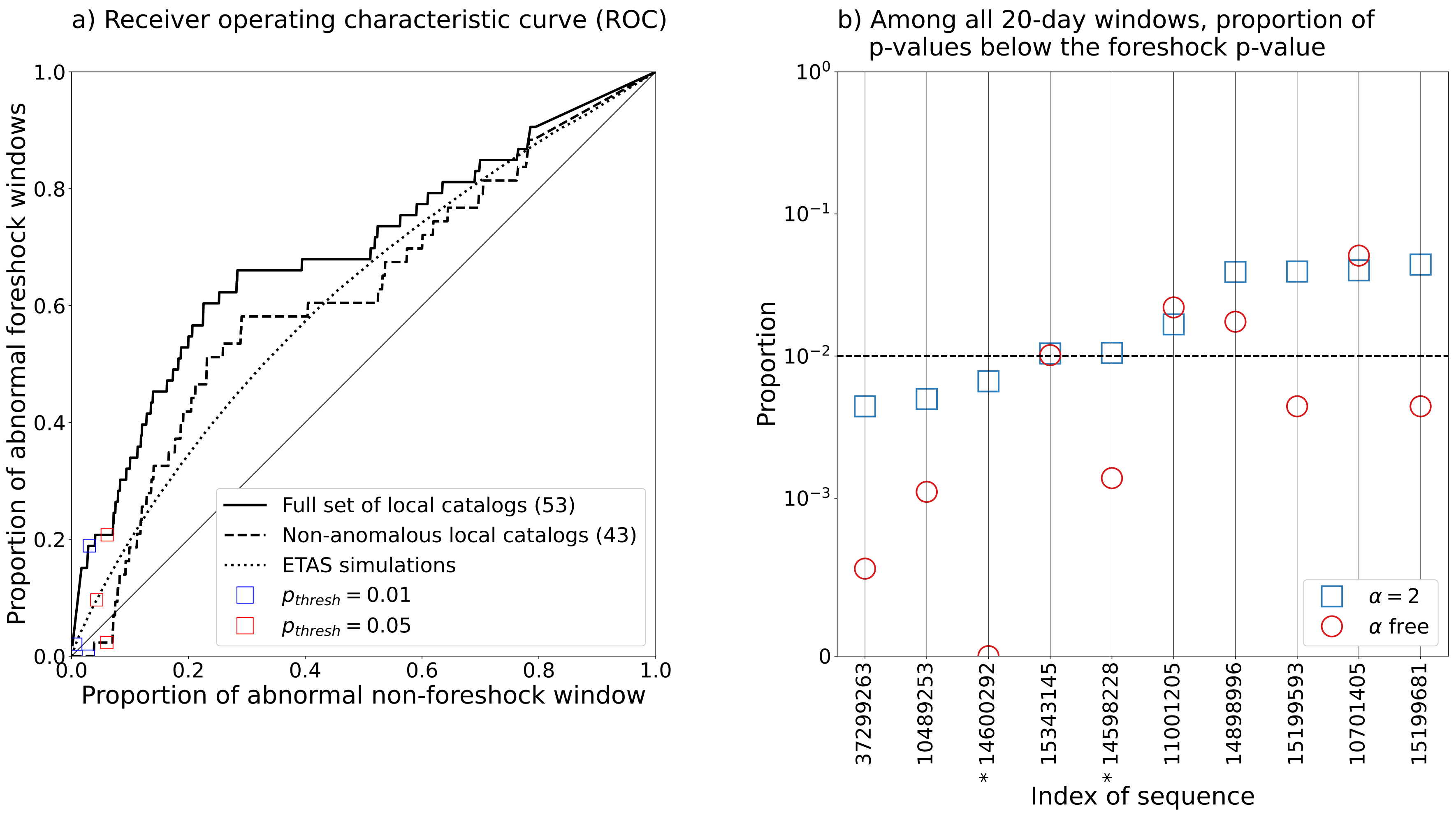

FIGURE 2.2: (a) Receiver Operating Characteristic (ROC) curves for our detection of anomalous foreshock windows. For a varying threshold p-value p_{thresh}, the curves show the proportion of foreshock windows below p_{thresh} against the proportion of non-foreshock windows below p_{thresh}. ROC curves are drawn for both the full set of 53 local catalogs and the set of 43 catalogs left after removing the 10 anomalous sequences of section 2.4 (with $p < 0.01$). We also include the ROC curve corresponding to the average of 53 sets of 1000 ETAS simulations computed using the α free ETAS parameters obtained in section 2.3.2. Note that ETAS simulations display a curved ROC, the departure from the "no-gain" line being particularly clear when considering large p_{thresh} values. This departure is weak for $p_{thresh} \leq 0.01$, with a gain of about 2 at maximum ($p_{thresh} = 0.01$). (b) Proportion $\hat{p}$ of windows with a p-value lower or equal to the 20-day foreshock window p-value, among all 20-day windows over 10 years. The proportion $\hat{p}$ is shown here for the 10 anomalously high foreshock activity and for the two ETAS estimates. We consider an anomalously high foreshock activity to be specifically related to a mainshock if $\hat{p}$ is below 0.01 for both ETAS estimates. Here, we identify 3 foreshock anomalies that are specific to subsequent mainshocks for both sets of ETAS parameters. Note that $\hat{p}$ is significantly sensitive to the value of α. Labels preceded by a star are mainshock IDs of the two anomalously high foreshock activity detected with the declustering approach.

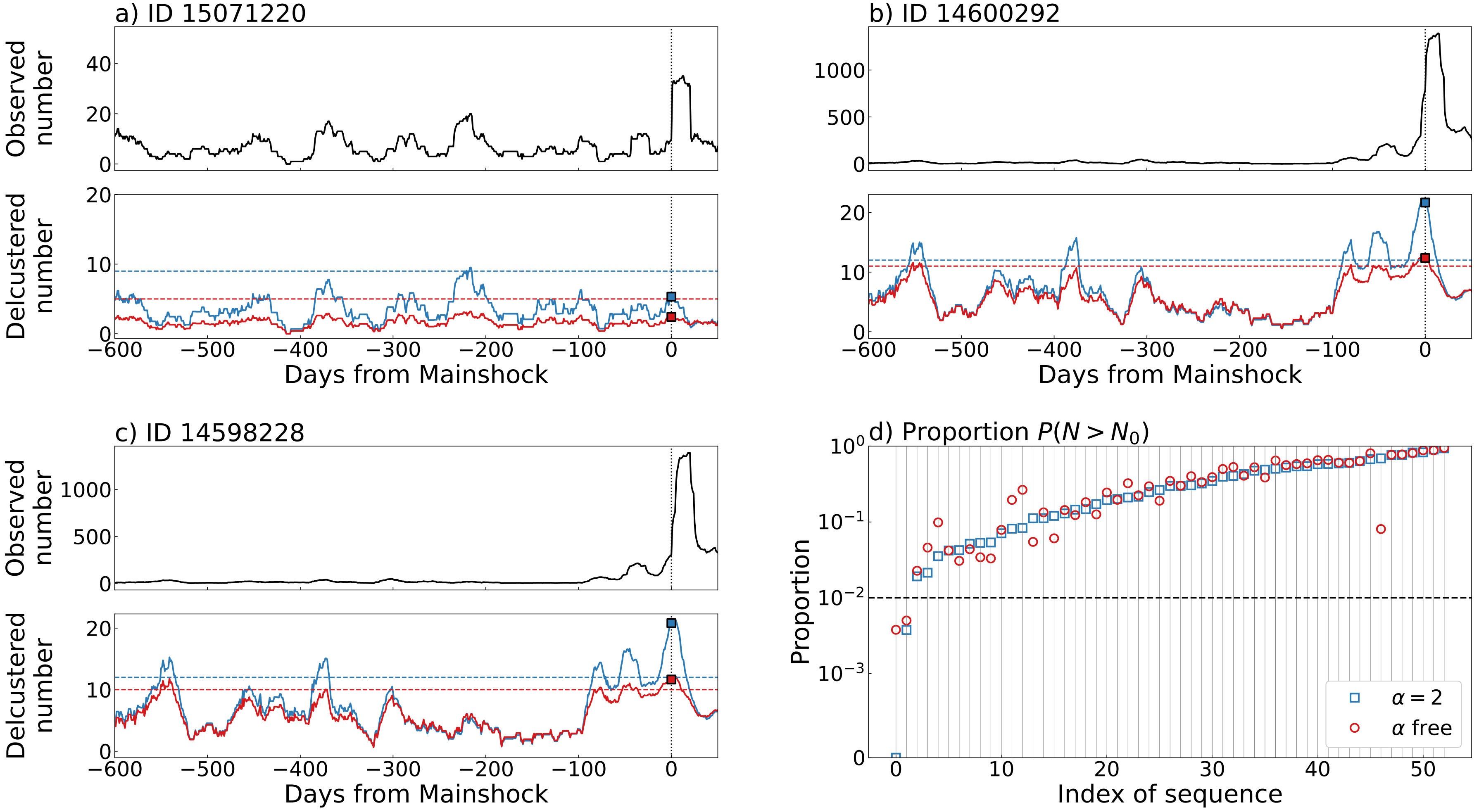

FIGURE 2.3: (a,b,c) Number of earthquakes in 20 day long windows counting (top) all earthquakes and (bottom) background earthquakes only, for 3 selected mainshocks. The number for the last window prior to the mainshock is shown with a thick square. The dashed lines show, for the two sets of ETAS parameters (free α in red, $\alpha = 2$ in blue) the limit over which the Poisson probability becomes less than 0.01. (d) Probability $P(N>N_0)$ that the last 20 days are anomalously active compared to the past, for the two sets of ETAS parameters; the sequence is selected as a mainshock-specific anomalous activity after declustering if this probability is less than 0.01 (2nd test) and if N_0 is above the dashed line (1st test). Mainshocks 14598228 and 14600292 correspond to indices 0 and 1 on this graph, and are the only mainshocks with both probabilities less than 0.01. All indices can be linked with their mainshock ID thanks to Table 2.S.2.

nucleation processes. We notice that this number (3 out of 10) would raise to 5 if accepting a threshold at 1.5% rather than 1%, cf. Figure 2.2b. The complementary declustering approach restricts the anomalously high foreshock activity to only two mainshock-specific sequences. A possible over-estimation of the background rate can be a cause for this more conservative selection. Even if the definitions of an anomalously elevated seismicity differ, Mainshock IDs related to the anomalously high foreshock activities detected in T&R, V&A and this study can be found in Table 2.S.1 of the supporting information. The Southern Californian location of these sequences are also compared in Figure 2.S.10.

We must emphasize that these results, along with those of T&R and V&A, likely depend on the initial choice of focusing on foreshocks in a 20 day period prior to each mainshock. Using a longer or shorter time-window may therefore provide different results. Moreover, the fixed 20×20 km^2 horizontal spatial window used in this study implies that all events in this box are evaluated with the same weight. This can artificially enhance the triggering role of foreshocks that are relatively far from the mainshock. The ETAS model used here would need to be extended to a space-time model in order to exploit the distance between earthquakes and to help to discriminate such cases (Zhuang et al., 2011)[for a review]. While this development does not appear over complicated, and was already investigated in Seif et al. (2019), the addition of several model parameters and the use of an isotropic spatial kernel for which no clear consensus exists (Moradpour et al., 2014) is likely to undermine the robustness and significance of the results.

The exact number of detected foreshock anomalies obviously depends on the significance threshold that we have fixed to $p < 0.01$ following T&R and V&A. To assess the impact of this arbitrary choice, we evaluate how the proportion of detected anomalous high foreshock activity changes as a function of the p-value threshold p_{thresh}. This result is compared with the proportion of windows that have $p < p_{thresh}$ without being followed by a mainshock (i.e., false positives). We thus compute the Receiver Operating Characteristic (ROC) curve as shown in Figure 2.2a. If the occurrence of anomalously elevated activity was not a sign of an incoming mainshock, then the ROC curve would follow a 1 to 1 straight line (hereafter referred to as the no-gain line). We find that there is positive correlation between preceding high activity and mainshock occurrence: the information gain is measured by the ratio of true positives over false positives, which is practically constant and close to 6 for $p_{thresh} \leq 0.05$. We however notice that significant departure from this no-gain line also exists in ETAS simulations computed with the same 53 sets of parameters as obtained for the local catalogs. Figure 2.2 shows that a large p_{thresh} (i.e., $p_{thresh} > 0.01$) allows to detect anomalous foreshock activities (i.e., a positive gain) in ETAS simulations, even though there is by definition no pre-slip in this model. This is caused by the clustering properties of the model: in the rare occasions where the observed number of earthquakes N_{obs} in a window largely exceeds the expected number $\overline{N}$, then the occurrence of earthquakes immediately after this window is more likely, including the occurrence of a mainshock. As an effect, the ROC curve departs from the no-gain line. We however notice that there is no information gain on the magnitude of the forthcoming earthquakes, as expected. We conclude that choosing too large a value of p_{thresh} may lead to the detection of "foreshock cascades" prior to mainshocks, which are not related to aseismic processes (e.g., preslip). According to our simulations, $p_{thresh} = 0.01$ appears as an acceptable threshold to discriminate a cascading-like seismicity from other processes that would also enhance the seismic activity: at $p_{thresh} = 0.01$, the information gain for ETAS is about 2, compared to about 6 for the observed seismicity (cf., $p_{thresh} = 0.01$ in Figure 2.2). This additional gain is mostly controlled by the 10 sequences we found to be anomalous: quite obviously, removing them from the calculations implies that the ROC curve is equal to zero at $p_{thresh} = 0.01$. Therefore, these 10 anomalous foreshock sequences suggest the existence of a precursory pattern before some $M \geq 4$ earthquakes stronger than expected from ETAS simulations.

Our results strengthen previous reports that earthquake activity precursory to mainshocks can sometimes deviate from simple clustering properties (as modeled by ETAS) (Lippiello et al., 2019; Seif et al., 2019). Our approach is however different. For example, compared to Seif et al. (2019), we seek to explain the last 20 days prior to mainshocks knowing all past seismicity (including activity in the last 20 days), by comparing what number of earthquakes would be "normally" expected (in the sense of ETAS) to the observed number. In contrast, Seif et al. (2019) compared observations to the number of foreshocks predicted by ETAS simulations not constrained by past seismicity. Our method is indeed close to the residual analyses of Ogata (1988, 1989, 1992) and Ogata et al. (2003), which is here performed individually on a set of 53 mainshocks thanks to the improved completeness of the QTM dataset.

2.6 Conclusions

According to our analyses, the low magnitude of completeness of the QTM catalog does not warrant the detection of aseismically-driven foreshock sequences in the 20-days window preceding isolated mainshocks. More than 80% of mainshocks are preceded in the last 20 days by activity exhibiting seismicity rates that are consistent with ETAS predicted rates, even when the magnitude of completeness is as low as $M_c = 0$. For these cases, earthquake interactions and local stress changes are a good candidate to explain all observed increases in seismicity rates prior to the mainshock. We find 10 mainshocks that are preceded in the last 20 days by a significantly high seismic activity. These cases show seismic activity that significantly differ from ETAS cascades, and are thus likely controlled by aseismic processes. Among those 10 cases, we distinguish 3 cases that exhibit non-ETAS like seismicity that is very likely specifically related to the mainshock; these 3 cases are the best evidences of a possible nucleation phase.

High quality earthquake datasets complete to low magnitudes are in any case required to pursue and develop efforts for understanding when and where aseismic pre-slip can lead to a large shock. Foreshocks remain the best observable to study preparatory processes, if they exist (Nakatani, 2020). First, increasing the location accuracy and the number of small earthquakes substantially improves the statistical significance of any test conducted to assess the reality of pre-slip processes, when comparing to the cascade (null) hypothesis. Second, the availability of large datasets allows to increase the number of potential mainshocks to be analyzed, hence offering more robust conclusions. Finally, we suggest that pre-slip seismicity analysis should be evaluated along other near-fault observables (such as GPS data Socquet et al., 2017, strainmeter data (Roeloffs, 2006), variations in groundwater level or flow rate (Roeloffs, 1988), radon emission rate (Ghosh et al., 2009), changes in seismic velocities as imaged by pairwise seismic station cross-correlation functions (von Seggern & Anderson, 2017)) whenever available, to independently assess any possible aseismic mechanisms at work during the preparation of large earthquakes.

2.S Supporting Information for "Rare occurrences of non-cascading foreshock activity in Southern California"

2.S.1 Overview of the p-value results for the 53 local catalogs

To evaluate the overall ability of the ETAS model to reproduce the observed 20-day seismicity and to isolate catalogs with an anomalously high foreshock activity, we computed p-value distributions over each entire local catalog (with a 20-day sliding window) and for the two ETAS parameter estimates. The 10-year p-value distributions of each selected local catalog are presented in Figure 2.S.2 (in red for α free and in blue for $\alpha = 2$). Square dots indicate the p-value observed in the foreshock window.

We use a probability threshold of 0.01 for both ETAS estimates to reject our null-hypothesis H_0 that 20-day foreshock window seismicity can be explained by an ETAS seismicity. We find that 10 out of the 53 mainshocks selected in this study present an anomalously high foreshock activity.

2.S.2 The 10 anomalously high 20-day foreshock clusters

Figure 2.S.9 shows the 10 anomalously high 20-day foreshock clusters detected in this study. We note that the 10 related mainshocks occur at different times but mainly in the South-Est of southern California. The foreshock activity is not really consistent between mainshocks but seems to follow 3 main spatio-temporal patterns, either: (1) a group of foreshocks less than 1 km away from the future mainshock position and homogeneous over the 20-day window (IDs: 14599228, 37299263, 11001205); (2) a sudden burst occurring just before the mainshock time and a few km from the mainshock position (IDs: 15199593, 14898996, 10489253, 15343145); (3) Mainshocks occur isolated by a few km from the foreshock locations (ID: 10701405, 14600292, 15199681). We note that 2 out of the 10 mainshocks with anomalous foreshock sequences occur close and less than 20 days after one of the 8 remaining "anomalous" mainshocks. As a consequence, the related 20-day windows are interlaced and may evidence similar anomalous activities. For example, the foreshock sequence related to Mainshock ID 14600292 occurs almost at the same location as Mainshock ID 14599228 but 4 days later. We note that

the two successive mainshocks respect our mainshock selection criterion since $M_{14600292} > M_{14599228} > 4$. The foreshock sequence of ID 14600292 is interlaced with the foreshock and aftershock activity of previous Mainshock ID 14599228. As a consequence, we observe seismic activity mainly clustered at the Mainshock ID 14599228 location, 2 km away from Mainshock ID 14600292. Even if these two mainshocks are studied independently in our approach, they both occur following the same burst of foreshock activity that therefore led to the production of two large magnitude events. Mainshocks ID 15199593 and 15199681 follow the same conclusions.

2.S.3 P-value sensitivity to uncertainties on ETAS estimates

We evaluate the ETAS estimate uncertainties obtained with the Expectation-Maximization algorithm for a few local catalogs to understand their influence on p-value results. For computational efficiency, we have only selected 14 mainshocks to perform the uncertainty analysis. This selection include 12 mainshocks with the lowest foreshock p-values (see Figure 2.S.2) and the 2 remaining mainshocks presented in Figure 1 of the main text. Note that we discarded Mainshock ID 37374687 because its local catalog is very large, making it very computationally expensive to run this Monte-Carlo approach. For each selected mainshock, we compute the ETAS estimates uncertainties as follow:

1. We generate between 100 and 200 10-year long synthetic ETAS catalogs using the initial sets of ETAS estimates (i.e., 200 simulations with the $\alpha = 2$ set and 200 simulations with the α free set).

2. We re-estimate new sets of ETAS parameters for each simulation with the Expectation-Maximization algorithm. Note that the 200 simulations computed with $\alpha = 2$ are re-inverted with the $\alpha = 2$ constrain. We thus obtain two distributions of synthetic ETAS estimates representing the initial ETAS estimate uncertainties.

3. We use each new synthetic ETAS estimate to compute the p-value curve for a sliding 20-day window. These p-values are therefore based on the actual QTM local catalogs but using the ETAS parameters deduced from the synthetic catalogs: we obtain twice 200 p-values for each time window, allowing us to infer uncertainties on the p-values.

The uncertainties of ETAS parameter estimates from 200 simulations are shown in Figure 2.S.3 for mainshock ID 37299263. The distribution is Gaussian shaped, centered around the initial value and with a moderate standard deviation. Foreshock window p-values computed with ETAS uncertainties are displayed in Figure 2.S.5 for the 14 selected mainshocks. Figure 1 of the main text is reproduced in Figure 2.S.4 with the corresponding foreshock p-value uncertainties. We note that the p-value sensitivity is moderate and does not change the selection of anomalously high foreshock activity when considering the 0.01 threshold.

2.S.4 V&A approach with synthetic ETAS catalogs

In this section, we illustrate how the V&A approach behaves on aftershock sequences by applying it to synthetic realizations of a temporal ETAS seismicity model (cf., Figure 2.S.6). Synthetic ETAS catalogs are able to reproduce a temporally clustered seismicity. In such model, clustering activity emerges spontaneously from random cascades of aftershocks. This is illustrated in Figure 2.S.6a with observable aftershock sequences initially triggered by several $M \sim 3$ events and a $M = 4$ earthquake. By construction, such a synthetic catalog does not contain any foreshock activity other than that due to earthquake interactions. As for natural seismicity, the distribution of inter-event times (IETs) of an ETAS catalog tends to a gamma distribution (cf., Figure 2.S.6b). Following V&A, if we independently resample the IETs of Figure 2.S.6b, we obtain for instance the catalog shown in Figure 2.S.6c in which the temporal clustering disappeared (even if IETs have the same distribution by construction). In particular, there is no visible aftershock sequences following $M \sim 3$ events contrary to catalog observations. To further quantify the limitations of such a random sampling approach, we generate 1000 realizations of 5-years duration synthetic ETAS catalogs and extract $M \geq 4$ mainshocks as in section 2.1 of the main article. Following V&A, we then sample a Probability Mass Function (PMF) of the expect number of event in 20 day windows assuming independent gamma realization of IETs (Figure 2.S.6d). We extract the probability p that independent IETs can explain foreshock seismicity by confronting this PMF with the "observed" number of events in the 20 days prior synthetic mainshocks (Figure 2.S.6e). Assuming the same significance threshold of $p < 0.01$ as in T&R and V&A, Figure 2.S.6e shows that more than 10% of mainshocks are preceded by an anomalously high seismic activity even though they are actually explained by cascades of aftershocks. The 1000 synthetic ETAS catalogs are also tested against the second approach of V&A. In this approach, the PMF is sampled empirically by counting the number of events in 20-days windows randomly distributed over the $[-380, -20[$ period with respect to the mainshock origin time (Figure2.S.6d). As for independent IETs sampled from a gamma distribution, the empirical approach of V&A shows that more than 10% of mainshocks are preceded by an anomalously high earthquake activity (Figure2.S.6f). Therefore, the two approaches of V&A struggle to properly consider causal earthquakes interactions and their corresponding seismicity rate increases.

2.S.5 Reproducing the ETAS analysis on Trugman & Ross, 2019 mainshock selection over the QTM 9.5 dev catalog

The Quake Template Matching catalog of Southern California provided by Ross et al., 2019b is presented as two separate catalogs with different confidence levels on the detection of events. The full QTM catalog (i.e., "QTM 9.5 dev" : detection threshold at 9.5 times the median absolute deviation (MAD) of the stacked correlation function) is used for foreshock analysis by Trugman & Ross, 2019 and Ende & Ampuero, 2020. We noticed that QTM 9.5 dev suffers from episodic bursts of false detections, that occur due to a too low threshold. To avoid any contamination of our analysis by such artifacts, we instead use the higher quality QTM catalog with a detection threshold at 12 times the MAD (i.e., QTM 12.5 dev), for which these transients vanish or are strongly attenuated. The use of the QTM 12.5 dev catalog implies that the mainshock selection is slightly different from the one used by T&R and V&A.

In order to provide a fair comparison with the results of T&R and V&A, we show in Figure 2.S.7 our ETAS analysis performed on the QTM 9.5 dev for the T&R mainshock selection (46 events). Apart from the mainshock selection, the method used is the same as the one presented in the main article.

Using the same criteria for the selection of anomalous high foreshock activity, we find that 9 out of 46 (20%) foreshock windows are anomalous. Only 2/46 of these anomalously high foreshock activity (5%) are considered mainshock specific when considering the 10-year variations of anomalies (Figure 2.S.8). We note that Mainshock IDs 37299263 and 14600292 are found as having mainshock-specific anomalous activity for both of QTM catalogs and mainshock selection criteria. Figure 2.S.10 summarizes the location of the detected anomalously high foreshock activity for the analysis mentioned in this study (T&R, V&A, ETAS QTM 9.5 dev and QTM 12.5 dev).

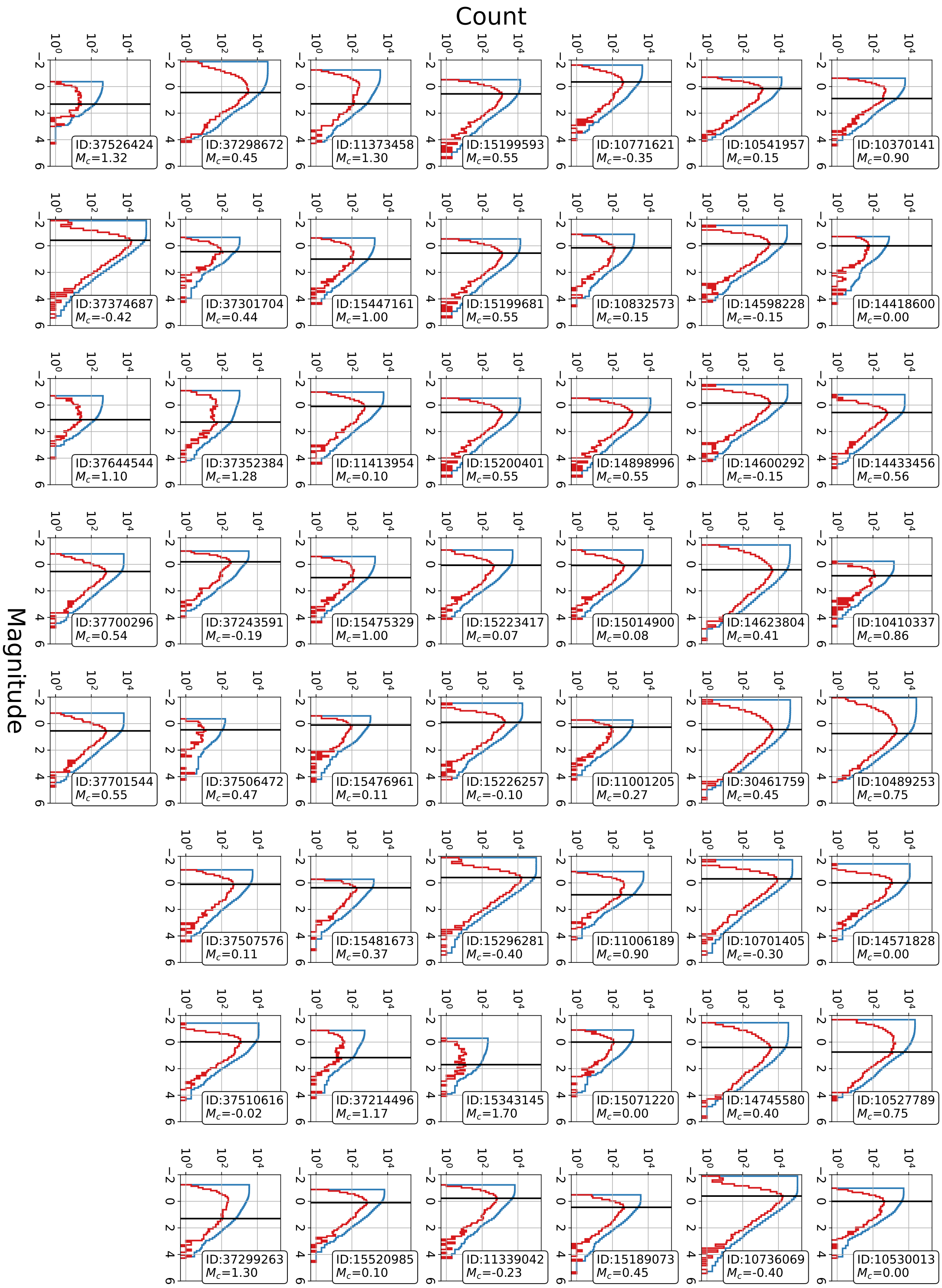

FIGURE 2.S.1: The magnitude of completeness M_c of local catalogs observed in a 20 by 20 km^2 box around the 53 mainshocks as selected in this study. *(red)* The frequency-magnitude distribution. *(blue)* The corresponding cumulative distribution. *(black)* The estimated magnitude of completeness.

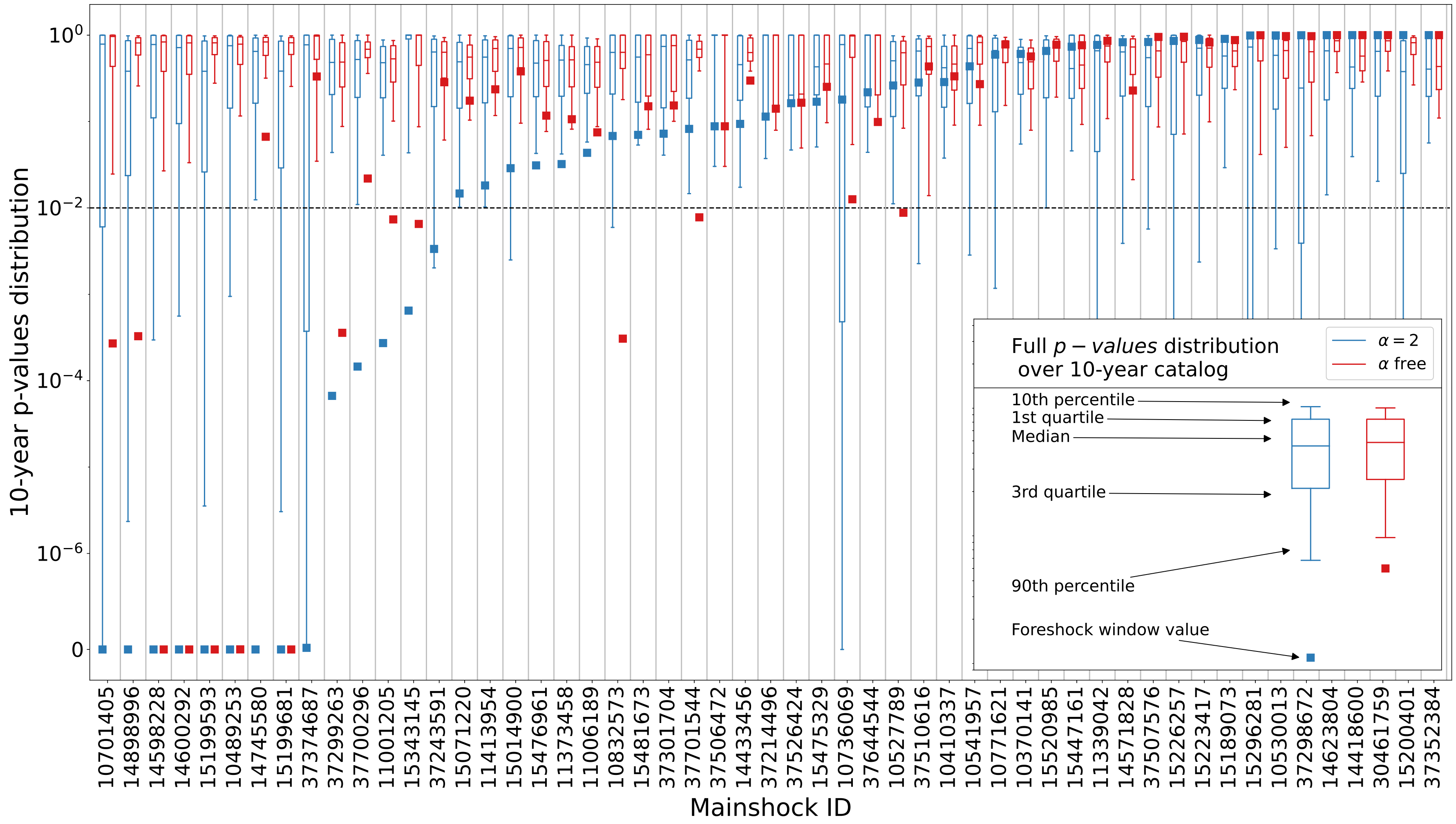

FIGURE 2.S.2: **[QTM 12.5 dev]** ETAS expected 20-day seismicity analysis over our mainshock selection from the QTM 12.5 dev catalog. For each selected mainshock, the boxplots give the p-value distribution computed with a 20-day sliding window over the 10-year for the two sets of ETAS parameter estimates. The squared dot is the p-value computed for the 20-day foreshock window. The black dashed line is the 0.01 p-value threshold. A foreshock window p-value is anomalous if it is below the threshold for both sets of ETAS parameter estimates. We here find 10 (among 46) anomalous foreshock windows.

a) (ID) 37299263: ETAS estimates from simulations with α free

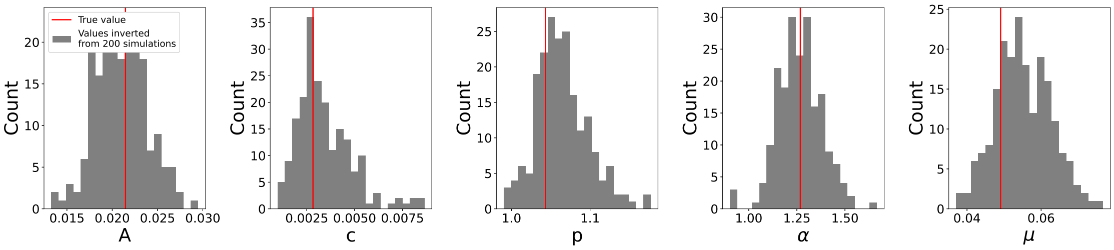

b) (ID) 37299263: ETAS estimates from simulations with $\alpha = 2$

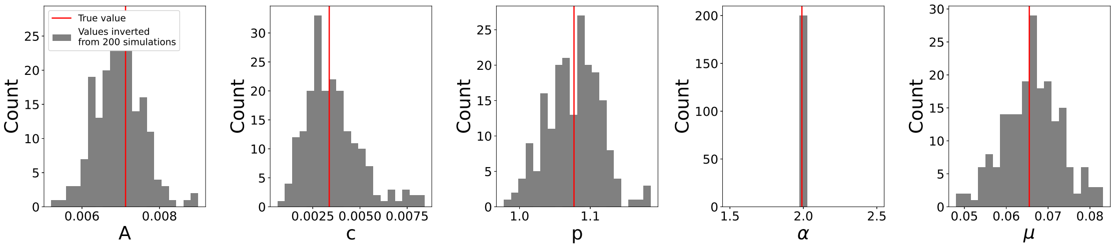

FIGURE 2.S.3: ETAS estimate uncertainties inverted from 200 synthetic ETAS catalogs, along with the 'real' ETAS estimates for the local catalog of mainshock ID 37299263. a) Uncertainties from 200 simulations computed with α free and re-inverted with no constrains on α. b) Uncertainties from 200 simulations computed with $\alpha = 2$ and re-inverted with α fixed to 2.

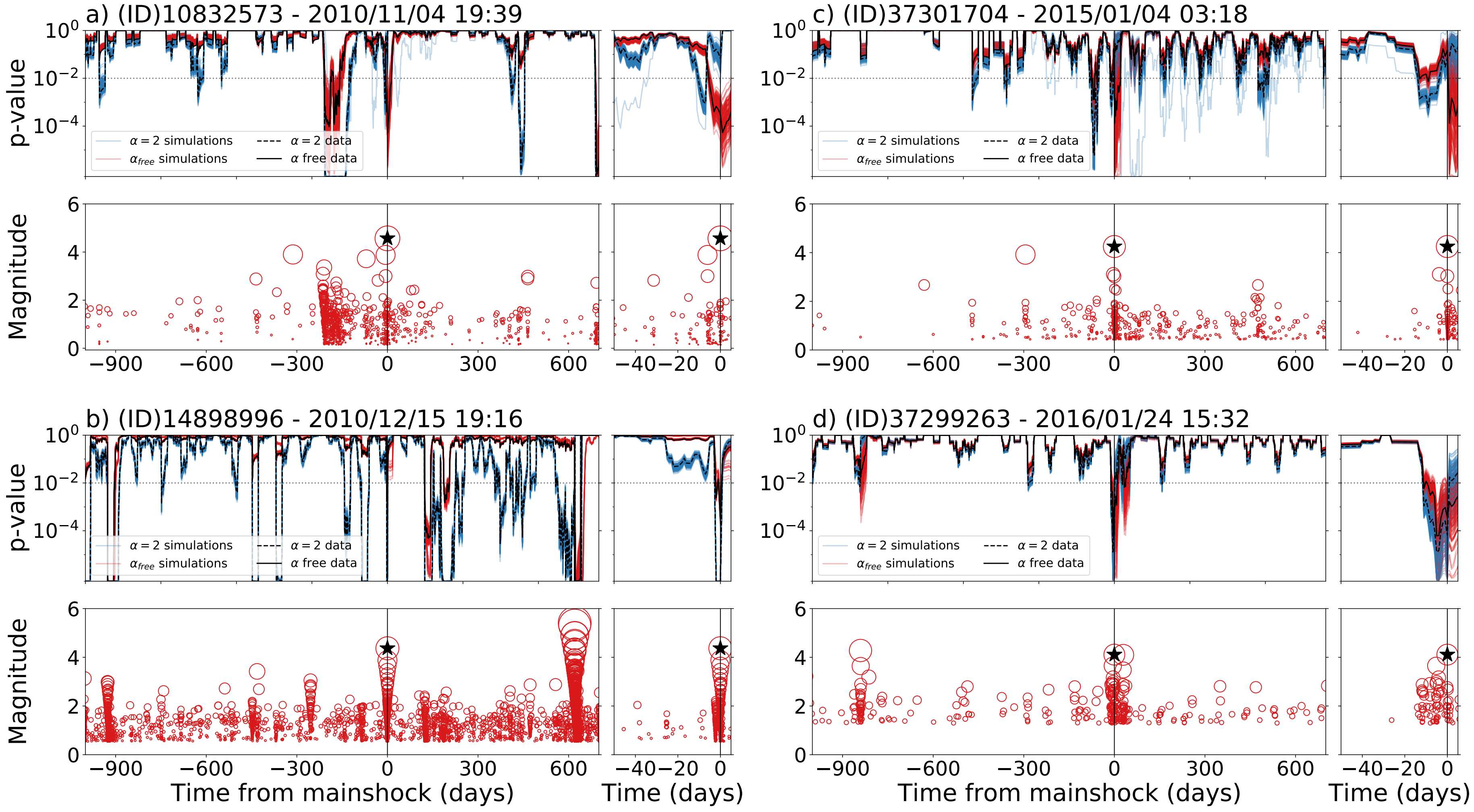

FIGURE 2.S.4: As in Figure 2.1 of the main text but including uncertainties: The 20-day sliding window analysis for 4 mainshocks (black star at t=0) and their local catalogs. (Top graphs) probability p that ETAS explains the observed seismicity, computed for the two sets of ETAS estimates inverted from the data (i.e., 'α=2 data' and 'α free data') and their uncertainties computed from simulations (i.e., 'α=2 simulations' and 'α simulations'). The significance threshold of p=0.01 is shown with the horizontal dotted line. (Bottom graphs) magnitude vs time for the local catalogs in the 20×20 km^2 box around each mainshock. The right inset is a zoom around the foreshock window.

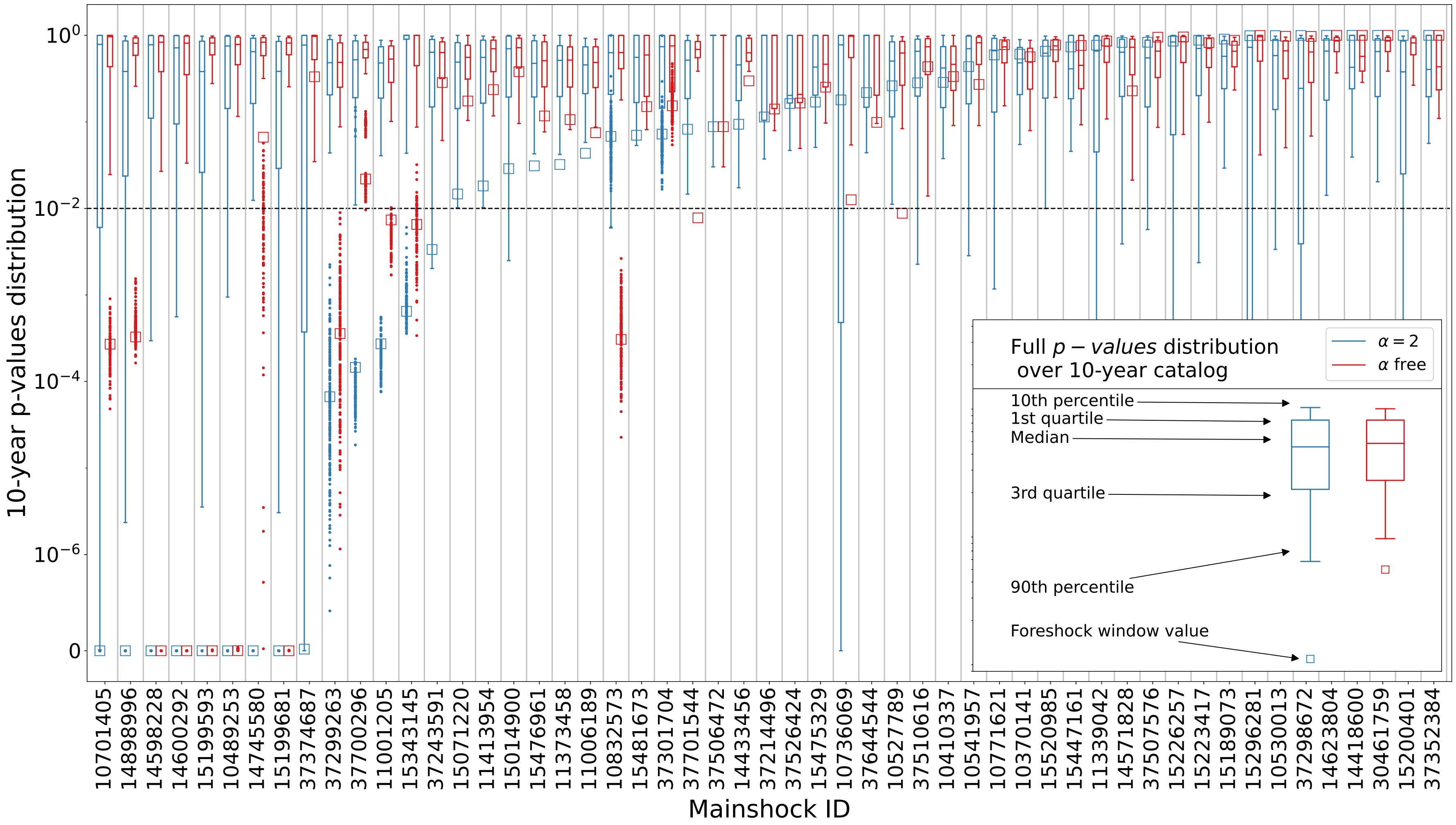

FIGURE 2.S.5: As in Figure 2.S.2 but including the p-value distribution obtained with our ETAS estimate uncertainties. Each dot is a foreshock p-value computed with one the set of ETAS parameter estimates inverted from the simulations.

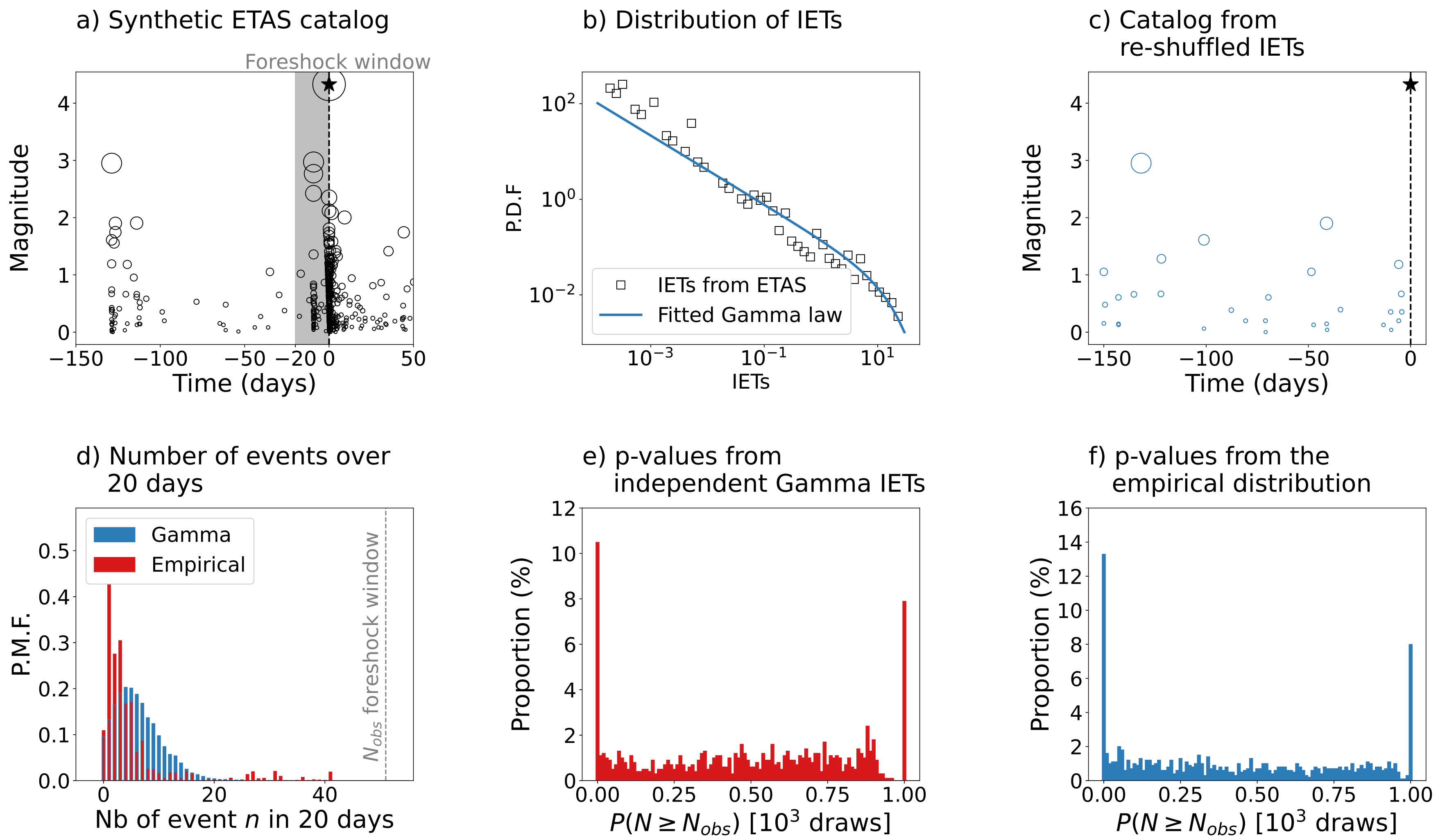

FIGURE 2.S.6: **(a)** A realization of a synthetic ETAS catalog (α=2, p=1.1, c=10^{-3}, μ=0.1, β=2.23 corresponding to a b-value of 1 for the Gutenberg-Richter law, M_c=0) and its 20-day foreshock window as defined by Ende & Ampuero, 2020. The $M \geq 4$ is considered here as the mainshock. **(b)** IETs distribution of this ETAS catalog observed in the $[-380, -20[$ window and its fitted gamma law. **(c)** IETs reshuffling of the $[-380, -20[$ days window. Note that clustered events are no longer related to the distribution of magnitude. **(d)** The sampled gamma/empirical probability mass functions (PMFs) of the number of events expected in the 20-day window according to the two approaches of V&A. The red vertical dashed line corresponds to the number of events N_{obs} actually observed in the ETAS 20-day foreshock window. **(e)** Distribution of the foreshock probability $p = P(N \geq N_{obs})$ using V&A first approach (drawing of independent, gamma-distributed IETs), for the 1000 synthetic ETAS catalogs. **(f)** Same as (e) but for the V&A second (empirical) approach (counting the number of earthquakes within random 20 day windows included in the $[-380, -20[$ period before the mainshock). More than 10% of the ETAS foreshock windows are detected with an anomalous seismicity ($p < 0.01$) although no anomaly is actually present. In (e) and (f), the p-value spike at 1 correspond to windows with $N_{obs} = 0$ or N_{obs} far from the minimum of the gamma/empirical PMF

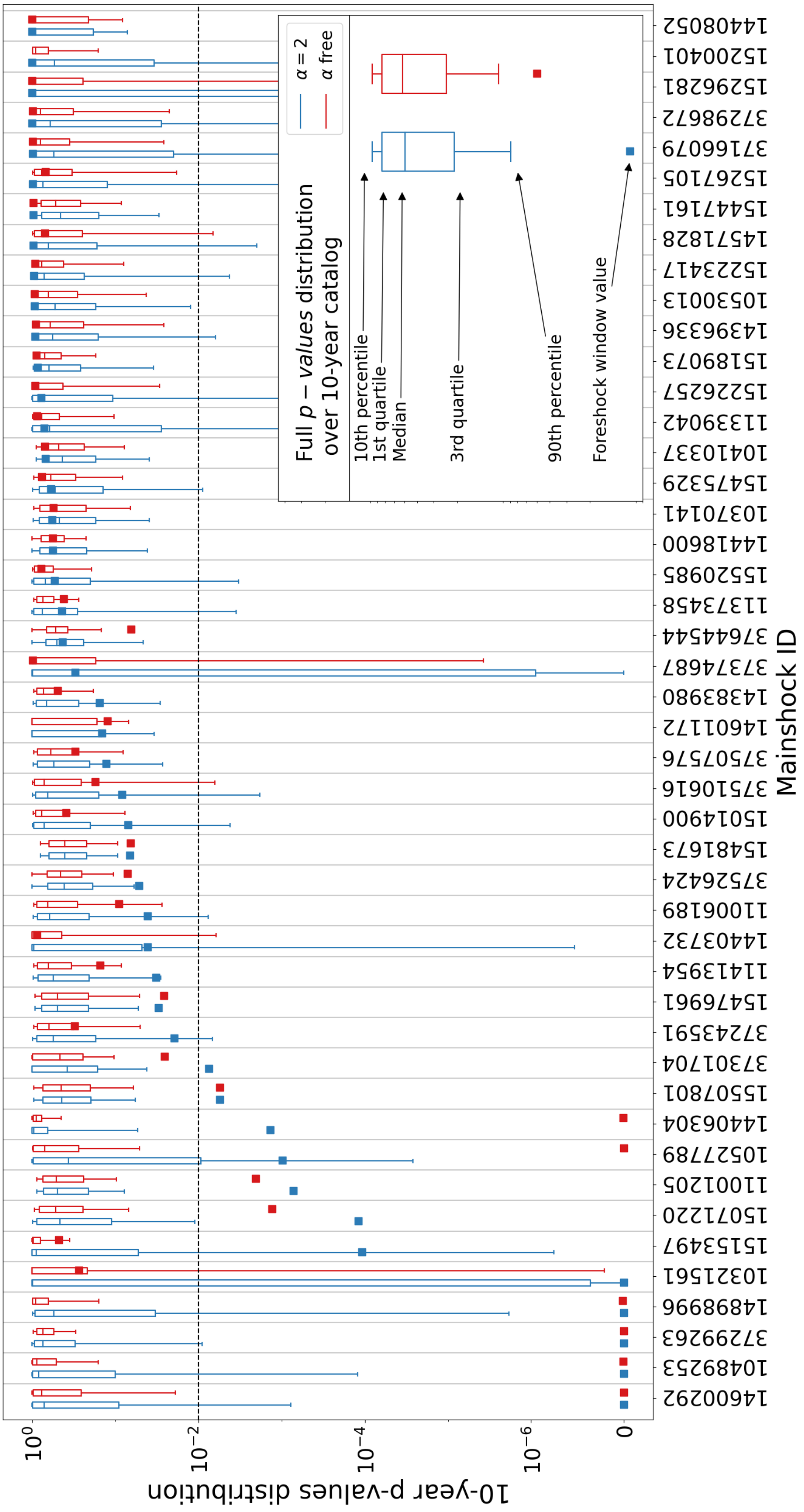

FIGURE 2.S.7: **[QTM 9.5 dev]** Same as 2.S.2 but this time using the Trugman & Ross, 2019 mainshock selection from the QTM 9.5 dev catalog. We here find that 9 out of 46 mainshocks have anomalously high foreshock activity.

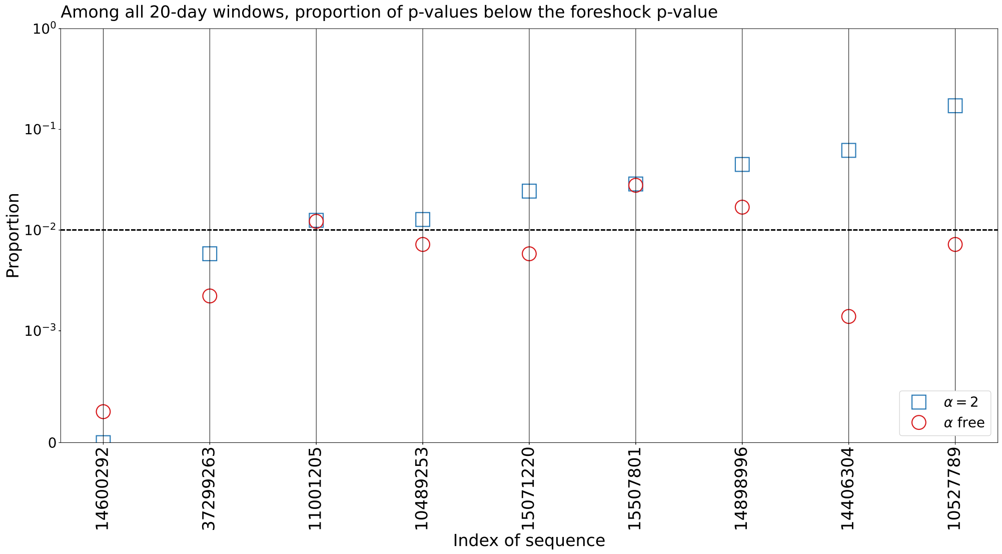

FIGURE 2.S.8: **[QTM 9.5 dev]** Among all 20-day windows over 10 years, proportion $\hat{p}$ of windows with a p-value lower or equal to the 20-day foreshock window p-value. The proportion $\hat{p}$ is computed for the 9 mainshocks with anomalously high foreshock activity and for the two ETAS estimates. We consider an anomalously high foreshock activity as mainshock-specific if $\hat{p}$ is below 0.01 for both estimates. Here, two foreshock anomalies are considered as mainshock-specific.

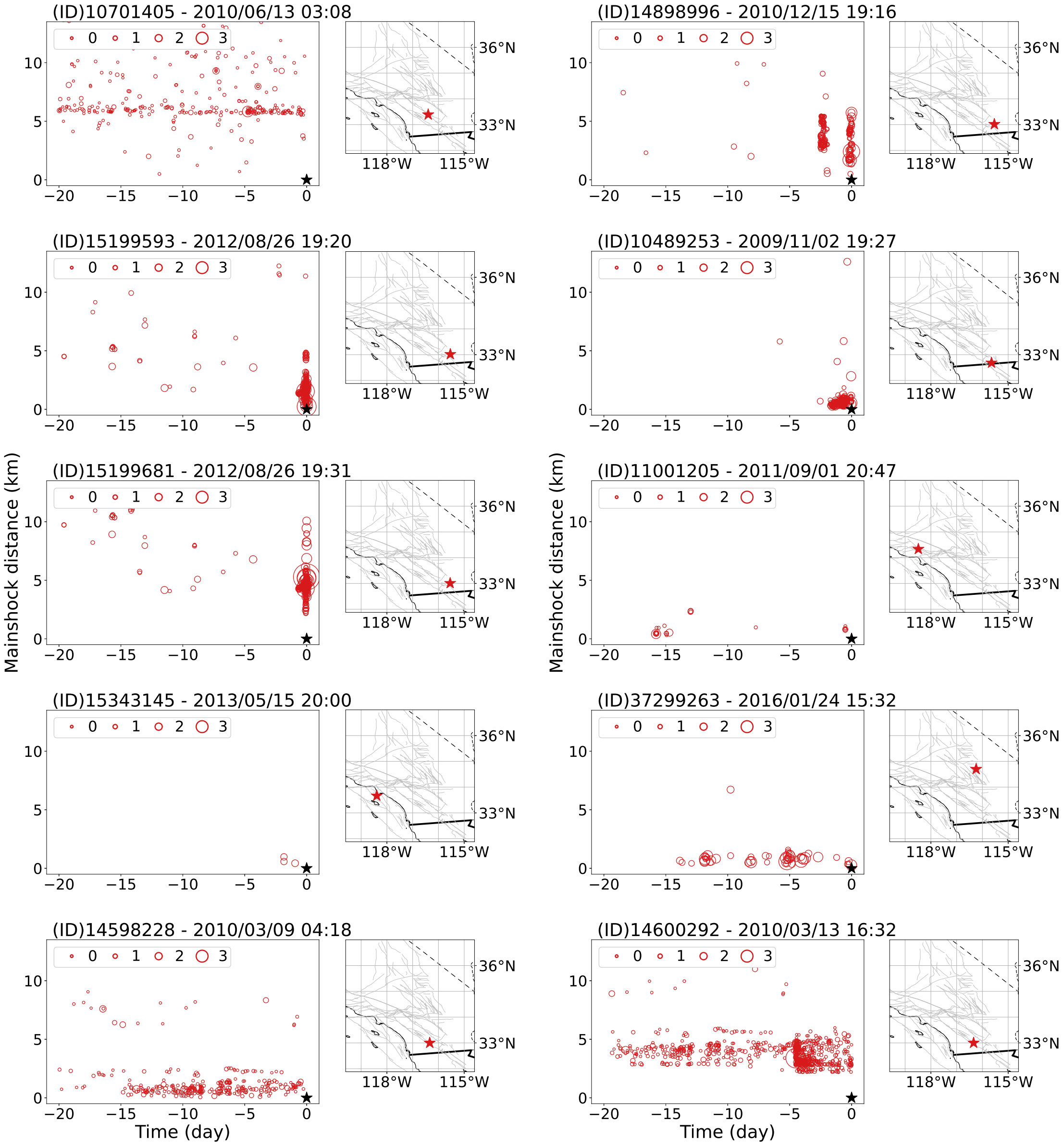

FIGURE 2.S.9: The 10 instances of anomalously high 20-day foreshock activity detected in this study. The mainshock distance correspond to the 3D distance in km (latitude, longitude and depth) between foreshocks and the mainshock (Black star) positions. The inset locate the mainshock position in Southern California.

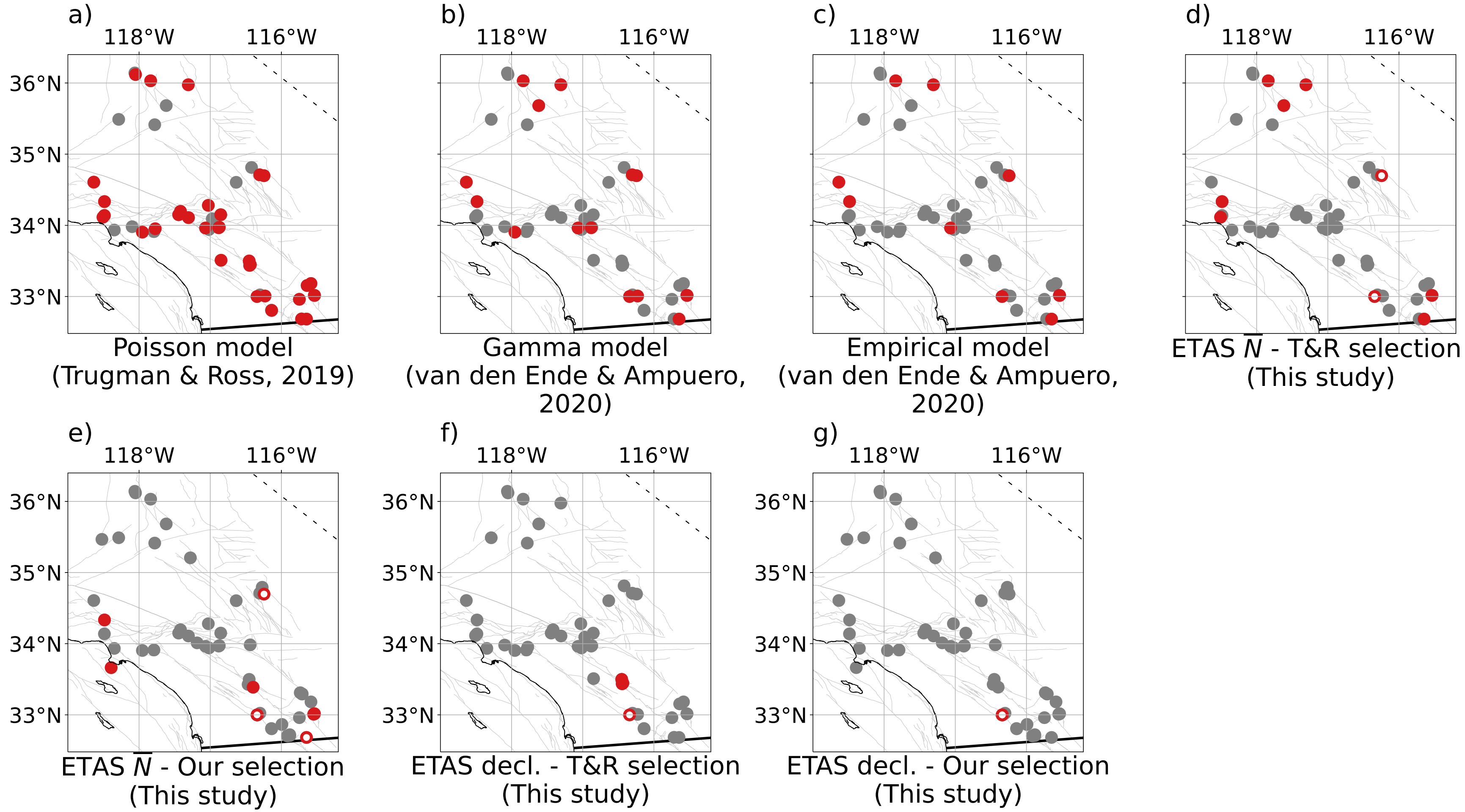

Poisson model (Trugman & Ross, 2019)

Gamma model (van den Ende & Ampuero, 2020)

Empirical model (van den Ende & Ampuero, 2020)

ETAS $\overline{N}$ - T&R selection (This study)

ETAS $\overline{N}$ - Our selection (This study)

ETAS decl. - T&R selection (This study)

ETAS decl. - Our selection (This study)

FIGURE 2.S.10: Location of the mainshocks for all the analyses discussed in this study. The red locations are the mainshocks detected with a anomalously high 20-day foreshock activity (p<0.01, according to the model used). Red markers with a white inner core correspond to the anomalously high activity considered as mainshock specific in this study. **(a)** Poisson analysis of Trugman & Ross (2019). **(b)** Gamma analysis of Ende & Ampuero (2020). **(c)** Empirical analysis of Ende & Ampuero (2020). **(d)** This study ETAS expected 20-day seismicity analysis on the Trugman & Ross, 2019 mainshock selection from the QTM 9.5 dev catalog. **(e)** This study ETAS expected 20-day seismicity analysis on our own mainshock selection from the QTM 12.5 dev catalog. **(f)** This study ETAS declustering analysis on the Trugman & Ross (2019) mainshock selection from the QTM 9.5 dev catalog. **(g)** This study ETAS declustering analysis on our own mainshock selection from the QTM 12.5 dev catalog. Note that mainshocks with similar locations may appear superimposed.

Table 2.S.1: QTM anomalous foreshock sequences

Approach	Mainshock selection	Anomalous high foreshock activity ($p<0.01$)	Mainshock specific anomalous activity
[a]Poisson	T&R (N=46)	14383980, 15200401, 37374687 15481673, 15296281, 15520985 10370141, 11413954, 10527789 15476961, 37507576, 15475329 37510616, 14898996, 11373458 14571828, 37301704, 11001205 14600292, 37298672, 10321561 15507801, 11006189, 10489253 37299263, 15014900, 14403732 37166079, 14406304, 37644544 15153497, 15267105, 37243591	NA
[b]Gamma	T&R (N=46)	15200401, 15481673, 10527789 37510616, 14898996, 11373458 37301704, 11001205, 14600292 11006189, 10489253, 37299263 15071220, 14406304, 15267105	NA
[b]Empirical	T&R (N=46)	15200401, 10527789 , 14898996 37301704, 11001205, 14600292 11006189, 10489253, 37299263 14406304	NA
[c]ETAS Expected $\overline{N}$	T&R (N=46)	15071220, 10527789, 14406304 15507801, 14898996, 10489253 14600292, 37299263, 11001205	14600292, 37299263
[c]ETAS Expected $\overline{N}$	This study (N=53)	37299263, 10489253, 14600292 15343145, 14598228, 11001205 14898996, 15199593, 10701405 15199681	37299263, 10489253 14600292
[c]ETAS Declustering	T&R (N=46)	10321561, 14600292, 15296281 37374687	14600292
[c]ETAS Declustering	This study (N=53)	14598228, 14600292	14598228, 14600292

[a]Trugman & Ross (2019), [b]Ende & Ampuero (2020), [c]This study

													ETAS inverted parameters (α=2)					Foreshock p-value (α=2)		ETAS inverted parameters (α free)					Foreshock p-value (α free)	
Mainshock ID	**Index Figure 3**	**Year**	**Month**	**Day**	**Hour**	**Minute**	**Second**	**Latitude**	**Longitude**	**Depth**	**Magnitude**	**Mc**	**A**	**c**	**p**	**α**	**μ**	**Expected Number $\bar{N}$**	**Declustering**	**A**	**c**	**p**	**α**	**μ**	**Expected Number $\bar{N}$**	**Declustering**
10370141	39	2009	1	9	3	49	45.938	34.10849	-117.30546	15.186	4.45	1.00	0.00240	3.85E-05	0.85168	1.99000	0.32342	3.25E-01	5.39E-01	0.00696	9.68E-05	0.86830	1.33267	0.30330	3.14E-01	6.44E-01
14418600	43	2009	1	31	21	9	22.192	35.41428	-117.77961	9.945	4.39	0.50	0.00266	1.16E-02	1.28530	1.99000	0.03291	1.00E+00	5.44E-01	0.01999	6.28E-03	1.25545	1.03850	0.02813	1.00E+00	4.92E-01
14433456	14	2009	3	24	11	55	43.491	33.31114	-115.73524	8.281	4.77	0.70	0.00597	3.24E-03	1.31963	1.99000	0.05055	1.05E-01	1.24E-01	0.02025	1.16E-03	1.32183	0.86466	0.04834	3.36E-01	1.08E-01
10410337	46	2009	5	18	3	39	35.759	33.93396	-118.34765	12.031	4.70	1.00	0.00461	3.93E-04	0.91128	1.99000	0.07188	5.13E-01	7.46E-01	0.01710	7.34E-04	0.93827	1.27732	0.05848	5.40E-01	6.72E-01
10489253	35	2009	11	2	19	27	31.491	32.68272	-115.64729	6.686	4.13	0.70	0.00959	1.98E-03	1.03098	1.99000	0.09329	0.00E+00	5.19E-01	0.04241	3.03E-03	1.12287	0.79876	0.08554	2.70E-09	3.68E-01
14571828	44	2010	1	12	2	36	8.138	33.97258	-116.87240	9.096	4.27	0.00	0.00316	3.92E-05	0.93720	1.99000	1.13493	8.28E-01	6.87E-01	0.01747	6.38E-05	0.94379	0.94132	0.88363	2.29E-01	6.33E-01
10527789	18	2010	1	15	8	23	27.294	36.03140	-117.83701	2.592	4.41	0.50	0.00569	5.26E-04	1.04625	1.99000	0.83557	1.33E-02	3.09E-02	0.02258	7.33E-04	1.05934	1.09606	0.60994	1.20E-05	1.70E-01
10530013	51	2010	1	16	12	3	25.334	33.94069	-117.01779	15.518	4.28	0.50	0.00253	6.88E-05	1.01485	1.99000	0.42602	9.50E-01	9.39E-01	0.01344	5.97E-05	0.94687	1.05198	0.32991	9.42E-01	9.07E-01
10541957	20	2010	2	13	21	39	6.276	34.01192	-117.18366	8.421	4.10	0.50	0.00663	3.55E-04	0.99007	1.99000	0.76937	1.19E-01	1.16E-01	0.02198	5.27E-04	1.01695	1.05101	0.66718	1.68E-01	1.79E-01
14598228	0	2010	3	9	4	18	21.534	32.99895	-116.33825	6.005	4.02	0.00	0.00823	7.76E-04	0.89178	1.99000	0.32610	0.00E+00	1.26E-06	0.03334	3.40E-03	1.01030	1.13565	0.29122	1.28E-14	3.58E-03
14600292	1	2010	3	13	16	32	31.980	32.99978	-116.34234	2.642	4.23	0.00	0.00827	7.15E-04	0.88227	1.99000	0.33251	0.00E+00	3.53E-07	0.03213	3.24E-03	0.99956	1.17707	0.29851	0.00E+00	1.24E-03
10701405	16	2010	6	13	3	8	57.139	33.38877	-116.39754	7.643	4.45	0.00	0.00406	3.53E-04	0.99155	1.99000	2.83928	1.91E-08	9.58E-03	0.01720	5.79E-04	1.05218	1.36097	2.09868	1.42E-02	9.89E-02
14745580	38	2010	6	15	4	26	58.140	32.70381	-115.91661	8.991	5.72	0.50	0.02071	2.43E-01	1.43167	1.99000	0.09312	2.66E-15	5.33E-01	0.03962	2.37E-02	1.34370	1.08907	0.08288	4.88E-02	6.68E-01
10736069	47	2010	7	7	23	53	33.371	33.42786	-116.46787	12.171	5.43	-0.30	0.00525	2.60E-04	0.98167	1.99000	6.32278	2.42E-01	8.50E-01	0.02253	6.56E-04	1.10313	1.14656	4.78588	2.28E-02	5.02E-02
10771621	33	2010	8	6	17	39	31.289	33.98402	-116.43848	8.699	4.05	0.00	0.00476	9.40E-04	1.05280	1.99000	0.12665	5.25E-01	4.03E-01	0.03889	1.41E-03	1.09460	0.52883	0.10250	7.03E-01	5.70E-01
10832573	21	2010	11	4	19	39	59.599	32.86551	-115.99244	11.257	4.57	0.50	0.00438	1.86E-03	0.96714	1.99000	0.02734	4.38E-01	1.73E-01	0.04213	5.83E-03	1.04989	0.75228	0.01979	1.36E-02	3.80E-01
14898996	26	2010	12	15	19	16	47.815	33.01552	-115.53741	7.773	4.37	0.70	0.00439	4.60E-03	1.29804	1.99000	0.31096	0.00E+00	2.76E-01	0.00606	1.29E-02	2.00000	0.80220	0.39296	1.01E-03	3.44E-01
15014900	12	2011	7	11	1	58	53.718	32.80423	-116.13689	9.111	4.11	0.30	0.00827	6.14E-03	0.99241	1.99000	0.03537	3.60E-02	1.45E-01	0.03993	1.16E-02	1.09009	1.02783	0.03395	3.55E-01	1.26E-01
11001205	30	2011	9	1	20	47	6.939	34.33383	-118.48573	4.977	4.24	0.50	0.00327	1.13E-03	1.12463	1.99000	0.13016	8.23E-04	2.99E-01	0.00828	9.72E-04	1.09511	1.55336	0.11388	6.06E-03	4.36E-01
11006189	8	2011	9	14	14	44	50.711	33.96296	-117.06606	16.525	4.14	0.20	0.00332	1.20E-04	0.95780	1.99000	0.54286	2.51E-04	2.20E-03	0.01921	2.09E-04	0.95415	0.93957	0.39332	8.66E-03	3.32E-02
15071220	19	2011	11	1	15	38	22.486	35.68315	-117.61833	9.008	4.10	0.00	0.00276	7.09E-04	0.97953	1.99000	0.11693	1.47E-02	1.73E-01	0.02985	1.59E-03	0.99771	0.78116	0.06172	1.74E-01	2.33E-01
15189073	50	2012	8	8	6	23	33.810	33.91169	-117.79032	9.266	4.46	0.50	0.00301	2.97E-03	0.96447	1.99000	0.13084	8.68E-01	8.31E-01	0.02546	7.08E-03	1.07852	1.19958	0.09357	8.42E-01	5.84E-01
15199593	7	2012	8	26	19	20	4.434	33.01531	-115.53862	7.829	4.59	0.70	0.00437	4.71E-03	1.30234	1.99000	0.31201	0.00E+00	9.94E-03	0.02154	2.05E-03	1.32885	0.82659	0.25749	1.32E-10	4.09E-02
15199681	6	2012	8	26	19	31	22.768	33.00956	-115.54596	13.016	5.32	0.70	0.00437	4.66E-03	1.30199	1.99000	0.31870	3.87E-14	1.21E-02	0.02219	1.95E-03	1.31500	0.83242	0.25432	1.03E-10	4.14E-02
15200401	5	2012	8	26	20	57	57.754	33.01499	-115.53377	8.166	5.41	0.70	0.00437	4.70E-03	1.30242	1.99000	0.31520	1.00E+00	1.05E-02	0.00603	1.29E-02	2.00000	0.80586	0.39606	5.02E-02	2.14E-02
15223417	49	2012	10	2	8	28	14.991	32.80795	-116.13970	9.229	4.13	0.30	0.00843	6.77E-03	0.99833	1.99000	0.03437	8.55E-01	4.99E-01	0.03876	1.16E-02	1.08959	1.05976	0.03302	8.21E-01	4.67E-01
15226257	41	2012	10	8	0	39	8.226	33.02293	-116.30118	10.635	4.16	0.00	0.00838	2.85E-03	0.96419	1.99000	0.10274	7.80E-01	6.14E-01	0.04701	6.57E-03	1.08752	0.84919	0.09068	9.42E-01	4.76E-01
15296281	48	2013	3	11	16	56	5.820	33.49917	-116.45238	10.545	4.70	-0.20	0.00545	1.96E-04	0.98444	1.99000	5.02673	8.79E-01	9.96E-01	0.02246	4.60E-04	1.08258	1.16805	3.73388	9.73E-01	9.45E-01
15343145	9	2013	5	15	20	0	5.875	33.66392	-118.39185	4.740	4.08	1.50	0.00359	8.59E-06	0.89060	1.99000	0.01265	1.37E-04	2.12E-02	0.01503	9.11E-06	0.88558	0.97366	0.01135	1.75E-03	1.65E-02
11339042	28	2013	7	24	16	46	2.261	35.48926	-118.28577	5.581	4.29	0.00	0.00480	5.11E-04	0.90753	1.99000	0.06105	4.81E-01	2.37E-01	0.04662	3.03E-03	1.03840	0.68915	0.04389	7.15E-01	5.05E-01
11373458	31	2013	10	6	2	6	21.837	34.70998	-116.30505	10.929	4.28	1.00	0.00576	2.91E-03	1.07313	1.99000	0.10473	7.94E-02	4.42E-01	0.01993	2.49E-03	1.04889	1.25498	0.07699	2.14E-01	5.24E-01
15447161	27	2013	12	23	13	39	25.974	36.14198	-118.05878	7.411	4.30	1.00	0.00782	2.37E-03	0.95990	1.99000	0.03267	7.34E-01	1.66E-01	0.01703	2.90E-03	0.98511	1.56281	0.02951	7.64E-01	4.68E-01
11413954	23	2014	1	15	9	35	18.575	34.14917	-117.44353	3.823	4.43	0.40	0.00352	1.32E-04	0.92732	1.99000	0.31187	2.09E-01	2.46E-01	0.01715	2.50E-04	0.95210	1.17567	0.23850	4.20E-01	2.76E-01
15475329	32	2014	3	13	2	11	4.178	36.11971	-118.04991	1.769	4.39	1.00	0.00780	2.19E-03	0.95758	1.99000	0.03305	1.70E-01	5.12E-01	0.01743	2.73E-03	0.98262	1.54951	0.02862	2.52E-01	4.58E-01
15476961	10	2014	3	17	13	25	36.386	34.13826	-118.48701	9.073	4.40	0.40	0.00262	3.61E-04	0.81720	1.99000	0.03928	4.98E-03	1.85E-01	0.00582	6.10E-04	0.83491	1.71636	0.03351	1.81E-02	1.37E-01
15481673	4	2014	3	29	4	9	41.470	33.90461	-117.95333	6.005	5.09	0.50	0.00463	1.23E-02	1.11723	1.99000	0.02567	1.66E-01	1.05E-02	0.00684	1.06E-02	1.12080	1.85580	0.02416	2.37E-01	6.72E-02
37214496	25	2014	4	19	12	15	13.208	35.46663	-118.52184	4.918	4.24	1.00	0.00140	2.93E-04	1.00362	1.99000	0.02842	1.51E-01	4.18E-01	0.01584	3.06E-04	0.94866	0.73964	0.02332	1.84E-01	3.58E-01
15520985	22	2014	7	5	16	59	33.740	34.28072	-117.02666	7.257	4.58	0.20	0.00706	5.31E-04	0.98350	1.99000	0.10376	4.92E-01	3.02E-01	0.02988	8.05E-04	1.04422	1.04045	0.08996	6.84E-01	2.16E-01
37298672	52	2014	12	24	5	51	51.030	33.18247	-115.58426	1.764	4.19	0.50	0.00516	6.85E-04	1.27924	1.99000	0.82656	9.98E-01	9.98E-01	0.02412	5.14E-04	1.23659	0.66124	0.55990	9.79E-01	9.80E-01
37301704	11	2015	1	4	3	18	9.145	34.60709	-118.63591	9.210	4.25	0.50	0.00538	3.96E-04	0.87739	1.99000	0.01506	9.15E-02	2.47E-01	0.01544	6.04E-04	0.90558	1.53191	0.01194	1.73E-01	2.00E-01
37352384	45	2015	3	30	9	21	56.296	34.79334	-116.26973	6.748	4.04	1.20	0.00586	5.27E-03	1.05760	1.99000	0.03790	1.00E+00	5.75E-01	0.02362	5.45E-03	1.04491	1.15492	0.02790	1.00E+00	4.54E-01
37243591	15	2015	9	16	16	10	47.062	34.14925	-116.85215	10.706	4.00	0.00	0.00322	1.60E-04	0.87453	1.99000	0.19602	2.24E-02	9.28E-02	0.03939	4.91E-04	0.93035	0.27041	0.14324	2.88E-01	2.81E-01
37506472	2	2015	12	27	18	31	17.864	35.20731	-117.27849	8.289	4.25	1.00	0.00169	1.29E-02	1.01820	2.01000	0.00788	8.04E-02	1.43E-01	0.00047	1.39E-02	1.01696	2.46604	0.00798	6.34E-02	1.11E-02
37507576	36	2015	12	30	1	48	57.190	34.19651	-117.41762	8.329	4.40	0.40	0.00295	9.77E-05	0.92297	1.99000	0.31753	4.73E-01	6.04E-01	0.01409	1.70E-04	0.94061	1.24814	0.24341	6.93E-01	5.12E-01
37510616	29	2016	1	6	14	42	34.652	33.96615	-116.88068	17.066	4.39	0.00	0.00324	3.81E-05	0.93663	1.99000	1.14901	2.78E-01	3.62E-01	0.01725	6.26E-05	0.94468	0.95840	0.90229	4.24E-01	3.78E-01
37299263	3	2016	1	24	15	32	16.340	34.69768	-116.24407	4.479	4.11	1.20	0.00644	3.29E-03	1.08278	1.99000	0.07844	3.86E-05	7.16E-03	0.01937	2.59E-03	1.04626	1.30084	0.05956	2.06E-04	3.93E-02
37526424	13	2016	2	20	6	13	20.070	34.60461	-116.63484	9.941	4.31	1.00	0.00135	1.42E-03	1.26156	1.99000	0.04878	2.62E-02	8.07E-02	0.00428	1.12E-03	1.19502	1.43107	0.04726	3.68E-02	7.42E-02
37374687	24	2016	6	10	8	4	38.638	33.43693	-116.44620	12.136	5.19	-0.30	0.00512	2.41E-04	0.98318	1.99000	6.89956	1.02E-06	2.94E-02	0.02212	6.06E-04	1.10183	1.13309	5.21855	3.63E-01	3.55E-01
37644544	17	2016	7	31	16	21	5.325	32.96068	-115.74706	1.113	4.03	1.00	0.00072	8.24E-04	1.46829	1.99000	0.03600	3.09E-01	1.71E-01	0.00059	2.92E-03	2.00000	0.54726	0.03626	1.26E-01	1.72E-01
37700296	37	2016	9	26	14	31	8.129	33.29397	-115.70733	7.497	4.32	0.60	0.00583	3.66E-03	1.32225	1.99000	0.07126	1.71E-04	4.43E-01	0.02090	1.20E-03	1.31922	0.82789	0.06675	2.16E-02	4.06E-01
37701544	34	2016	9	27	3	23	57.446	33.29242	-115.71007	5.893	4.33	0.60	0.00576	3.69E-03	1.32214	1.99000	0.07020	2.45E-02	4.35E-01	0.02072	1.22E-03	1.32039	0.83180	0.06697	4.35E-03	4.08E-01
14623804	40	2010	4	7	5	21	25.720	32.72137	-115.88230	4.403	4.27	0.50	0.02049	2.53E-01	1.44102	1.99000	0.11534	1.00E+00	6.30E-01	0.04115	2.07E-02	1.34453	0.99439	0.10291	1.00E+00	4.90E-01
30461759	42	2010	4	7	5	21	41.680	32.70908	-115.88179	4.176	4.28	0.50	0.02049	2.51E-01	1.44258	1.99000	0.11586	1.00E+00	6.37E-01	0.04103	2.04E-02	1.34429	0.99240	0.10379	1.00E+00	5.01E-01

TABLE 2.S.2: This study's mainshock selection in the QTM 12.5 dev Southern Californian catalog and their respective two set of ETAS inverted parameters (A,c,p,α,μ) for α free or $\alpha = 2$ (Each mainshock is related to a local catalog defined as all the seismicity within a 20 by 20 km^2 box around the mainshock and above the local magnitude of completeness M_c). For each ETAS parameter estimates we present the 20-day foreshock window p-value evaluated with the ETAS expected 20-day seismicity and the declustering approach.

Chapter 3

Evidence of a transient aseismic slip driving the 2017 Valparaiso earthquake sequence, from foreshocks to aftershocks

Preliminary words

After investigating the statistical significance of several foreshock sequences over Southern California, I now propose a detailed analysis of a single foreshock sequence in Chile, including additional geophysical observations to track an aseismic slip transient. The identification of aseismic slow slip before a mainshock is often interpreted as a nucleation phase or the occurrence of a slow-slip event triggering the mainshock sequence. However, these two alternative interpretations are frequently not rigorously examined. The inherently statistical nature of the ETAS analysis limits its capacity for a deeper exploration of the tectonic processes that may drive unusual increases in foreshock seismicity rates. When our ETAS analysis rejects the cascade hypothesis, it does not provide further insights into the underlying fault processes. Therefore, after the purely statistical analysis of a large set of foreshock sequences in the first chapter, I propose here to incorporate multiple types of measurements to investigate a specific foreshock sequence.

I focus on the 2017 Valparaiso earthquake sequence and its $M_w = 6.9$ mainshock, that was preceded by a 2-day intense foreshock sequence. Previous studies (Ruiz et al., 2017; Caballero et al., 2021) have highlighted the occurrence of aseismic slip during the foreshock sequence that was interpreted as the a nucleation phase of the mainshock. This Valparaiso sequence offers an ideal case for examining the interplay between aseismic slip and foreshock seismicity.

To conduct a comprehensive investigation into the foreshock process, this work relies on a high-resolution seismicity catalog that includes low magnitude earthquakes. With this purpose, we build our own earthquake catalog using cutting-edge detection tools. This strategy enables a comprehensive understanding of the seismicity, from the initial detection to the statistical analysis and repeater identification, while accounting for possible catalog uncertainties (e.g., missed events, location and magnitude accuracy, ...)

This study was conducted with my 2 advisors Olivier Lengliné and Zacharie Duputel and in collaboration with Yuji Itoh and Anne Socquet from ISTerre. This work is published in *Journal of Geophysical Research: Solid Earth*.

3.1 Abstract

Following laboratory experiments and friction theory, slow slip events and seismicity rate accelerations observed before mainshocks are sometimes interpreted as evidence of a nucleation phase. However, such precursory observations still remain scarce and are associated with different time and length scales, raising doubts about their actual preparatory nature. We study the 2017 Valparaiso $M_w = 6.9$ earthquake, which was preceded by aseismic slip accompanied by an intense seismicity, suspected to reflect its nucleation phase. We complement previous observations, which have focused only on precursory activity, with a continuous investigation of seismic and aseismic processes from the foreshock sequence to the post-mainshock phase. By building a high-resolution earthquake catalog and searching for anomalous seismicity rate increases compared to aftershock triggering models, we highlight an over-productive seismicity starting within the foreshock sequence and persisting several days after the mainshock. Using repeating earthquakes and high-rate GPS observations, we highlight a transient aseismic perturbation starting 1-day before the first foreshock and continuing after the mainshock. The estimated slip rate over time is lightly impacted by large magnitude earthquakes and does not accelerate towards the mainshock. Therefore, the unusual seismic and aseismic activity observed during the 2017 Valparaiso sequence might be interpreted as the result of a slow slip event starting before the mainshock and continuing beyond it. Rather than pointing to a possible nucleation phase of the 2017 Valparaiso mainshock, the identified slow slip event acts as an aseismic loading of nearby faults, increasing the seismic activity, and thus the likelihood of a large rupture.

3.2 Introduction

Both laboratory experiments and friction theory show that earthquake ruptures do not begin abruptly but are preceded by a slow slip phase accelerating over a finite nucleation zone (Das & Scholz, 1981; Dieterich, 1992; Rubin & Ampuero, 2005; Latour et al., 2013; McLaskey, 2019). However, extrapolating the results of these models to natural faults is not straightforward, as some parameters entering the model definition are not known for large-scale systems (Ampuero & Rubin, 2008; Kaneko & Ampuero, 2011). In particular, the size of the nucleation zone predicted by such models is not well constrained. If the nucleation length is large, the slow, quasi-static, predicted crack-like expansion could be observed on natural faults. On the other hand, an accelerating pulse in a small nucleation zone could be more difficult to detect in practice. The existence and detectability of such nucleation phases before actual earthquakes is thus an important question with direct implications for earthquake prediction and seismic hazard assessment (Brodsky & Lay, 2014).

Recently, with geodetic measurements, several aseismic slip transients (also called slow-slip event) have been reported before the occurrence of large earthquakes (Mavrommatis et al., 2014; Ruiz et al., 2014; Socquet et al., 2017; Ruiz et al., 2017; Voss et al., 2018; Durand et al., 2020; Marill et al., 2021). In addition to geodetic observations, other observations such as repeating earthquakes are frequently used to support the detection of these aseismic processes (Nadeau & Johnson, 1998; Igarashi et al., 2003; Kato et al., 2012; Mavrommatis et al., 2015; Kato et al., 2016a; Uchida, 2019). Because of their timing, preceding large events, these transient aseismic slips are sometimes interpreted as an evidence of the mainshock nucleation phase as depicted by theory and laboratory experiments. However, despite the densification of geodetic and seismic networks around active faults, precursory aseismic slip observations still remain scarce in comparison with the number of instrumentally recorded large earthquakes. The reported examples often have large uncertainties in both their location and temporal evolution, making it difficult to infer any acceleration trend as the mainshock approaches. Moreover, there are significant discrepancies in the duration of reported preparatory slip, ranging from a few tens of seconds (Tape et al., 2018) to decades before the main rupture (Mavrommatis et al., 2014; Marill et al., 2021). While these different durations could potentially reflect differences in nucleation zone size or frictional parameters, they also raise doubts about whether these observations are actually reflecting the same unique geophysical process.

On the other hand, many large earthquakes are also preceded by seismicity rate increases, which may be additional evidence of a slow preparatory process before large earthquakes (Dodge et al., 1995, 1996; Bouchon et al., 2011, 2013; Seif et al., 2019). In the framework of a slow nucleation phase, such foreshock activity is interpreted as rupture of locked small asperities driven by background aseismic slip acceleration. (Ohnaka, 1992; Dodge et al., 1996; McLaskey, 2019) However, analyzing solely the seismicity rate to infer preparatory process before large earthquake is a difficult task (Ross et al., 2019b; Ende & Ampuero, 2020; Moutote et al., 2021). Indeed, earthquakes are strongly spatiotemporally clustered (Helmstetter & Sornette, 2003; Marsan & Lengliné, 2008), mainly because they interact with each other, making their probability of occurrence dependent on the past seismic activity. Therefore, the successive occurrence of earthquakes and their interactions can lead to seismicity rate increases, even without any external loading process (Helmstetter & Sornette, 2003; Felzer et al., 2004; Marsan & Enescu, 2012). Therefore, determining if the rise of foreshock earthquake sequence results uniquely from earthquake interactions or could in some occasion represent a true signal associated with an underlying aseismic transient remains actively debated (Llenos et al., 2009; Mignan, 2015; Kato et al., 2016a; Tape et al., 2018; Ellsworth & Bulut, 2018; Gomberg, 2018).

It is worth mentioning that detecting both a transient aseismic slip and an enhanced earthquake activity before large earthquakes may not appear as sufficient evidence of nucleation phase. There are indeed multiple evidence of earthquake swarms that have been linked to a slow slip transient without culminating into a large rupture (Lohman & McGuire, 2007; Vallée et al., 2013; Nishikawa et al., 2021) and we know that transient aseismic slip can occur independently from any significant seismicity (Rogers & Dragert, 2003; Radiguet et al., 2012). The observation of transient aseismic slip before large earthquakes is also sometimes shown to rather be independent fault process that happen to trigger subsequent large earthquakes by stress transfer (Radiguet et al., 2016; Voss et al., 2018; Klein et al., 2018, 2021, 2023). An interesting example was reported near the Guerrero gap, Mexico, where at least 4 episodic and co-located slow slip events have been successively detected over 10 years without being followed by any significant earthquake. Yet, in 2014, a slow slip event on the same portion of the interface was followed by the $M_w = 7.3$ Papanoa earthquake (Radiguet et al., 2016). Such an example shows that detecting both a transient aseismic slip and an unusually high seismicity before a large earthquake may not necessarily represent a deterministic nucleation process of a mainshock. Therefore, questions subsist on the interpretation of the seismic and aseismic processes observed before large earthquakes and on the estimation of their predictive power for the subsequent large rupture.

In this study, we analyze in detail seismic and aseismic processes before and after the April 2017 Valparaiso $M_w = 6.9$ earthquake (Chile; Figure 3.3.1). This mainshock was preceded by an intense 2-day long foreshock sequence with magnitudes up to $M_w = 6$ and was followed by an abundant aftershock activity. In addition, an aseismic precursory fault slip has been reported during the foreshock sequence (Ruiz et al., 2017; Caballero et al., 2021). This aseismic pre-slip may have initiated before the first foreshock and persisted, at least, up to the mainshock

(Caballero et al., 2021). However, its onset timing and detailed time evolution are still unclear due to the sampling intervals of the GPS data previously used (6 hours and 1 day in Ruiz et al., 2017 and Caballero et al., 2021, respectively). Furthermore, aseismic processes following the mainshock have not been investigated. The seismicity rate during the foreshock-mainshock-aftershock sequence was not yet tested against earthquakes interaction model to confirm previously suggested unusual increases. Hence, we, first, build a high-resolution seismic catalog from 2016 to 2021. Then, we compare the seismicity in the vicinity of the mainshock with aftershock triggering models to highlight unusual variations in seismicity rates. In the second part, we investigate the aseismic slip transient during the entire earthquake sequence using repeating earthquake and high-rate GPS observation. We, finally, discuss whether the aseismic slip transient is part of the nucleation of the mainshock or if it just mediates the whole Valparaiso seismic sequence.

3.3 ValEqt: A high resolution catalog

In order to carry out a detailed analysis of the micro-seismic activity near the mainshock, we build a high resolution catalog using recently developed detection methods. We use 13 broadband stations from the National Seismological Center (CSN) of the University of Chile (Barrientos & National Seismological Center (CSN) Team, 2018) in the vicinity of the mainshock from 1 January 2016 to 1 January 2021 (see Figure 3.3.1). Only a few stations were available earlier than 2016, which does not allow us to carry out a reliable seismicity analysis before that date.

3.3.1 Detection, location and magnitude estimation

We pick P- and S- wave arrivals of earthquakes on daily raw waveforms using EQTransformer, an automatic deep learning phase picker trained on a worldwide earthquake database (Mousavi et al., 2020). We associate phases picks into events with REAL (Zhang et al., 2019), performed over a 3° by 3° grid. We only consider events for which both P and S phases are associated on at least 3 stations. We locate events using NonLinLoc (Lomax et al., 2000) in a 3D velocity model of Chile (Ruiz et al., 2017). We discard events with a NonLinLoc RMS residual above 1s to avoid false detections.

We then estimate a local magnitude following the original Richter approach on Wood-Anderson seismometers. For that purpose, we correct the recorded waveforms from their instrument response and convolve them with a Wood-Anderson response. For all stations and horizontal components, we convert the maximum zero to peak S waves amplitude, A_{WA}, into a magnitude, M, using the Richter empirical formula (Richter, 1935, 1958; Shearer, 2019):

$$M = \log_{10}(A_{WA}) - 2.21 + 2.56 \log_{10}(\Delta) \tag{3.1}$$

where A_{WA}, is in mm and Δ is the hypocentral distance in km. The event magnitude is taken as the median of all estimations over stations/components. Given its proximity to the ocean, the Valparaiso region is prone to oceanic microseismic noise that dominates the S wave amplitude of small events. To reduce the noise level, we thus first filter all waveforms between 1 and 20 Hz prior to the magnitude estimation. If an event is estimated with a magnitude $M > 3$, we re-estimate its magnitude accounting for lower frequencies with a 0.05-20 Hz bandpass filtering.

The resultant catalog consists of more than 75 000 events from 2016 to 2021 within a 3 by 3 degree region centered on the Valparaiso mainshock. Over the same region and period, the official Chilean catalog (Centro Seismologico National, CSN) reported only $\sim$7000 events. Figure 3.3.1 shows the spatial and temporal distribution of earthquakes according to this catalog.

3.3.2 Event selection and comparison with the CSN catalog

To study the seismic activity in the vicinity of the mainshock, we extract all the earthquakes in a sub-region within $-33.5° \leq Latitude \leq -32.8°$ and $-72.5° \leq Longitude \leq -71.5°$ with no depth cutoff (Plain red rectangle in Figure 3.3.1.a). This sub-catalog (hereafter, referred to ValEqt catalog) gathers more than 10000 events. Our goal here is to focus on seismicity in the vicinity of the mainshock that is not affected by other nearby large earthquakes. From Figure 3.3.1.b we see several temporally clustered seismic activity. The largest one related to the 2017 $M_w = 6.9$ Valparaiso mainshock. We see that none of the earthquakes outside our selection range seems to significantly affect the seismic activity within the sub-region. The depth distribution of earthquakes along longitude clearly highlights the subduction surface (Figure 3.3.1.c). The 2017 activity is located on the shallowest part of the subduction surface with no direct connection with deeper

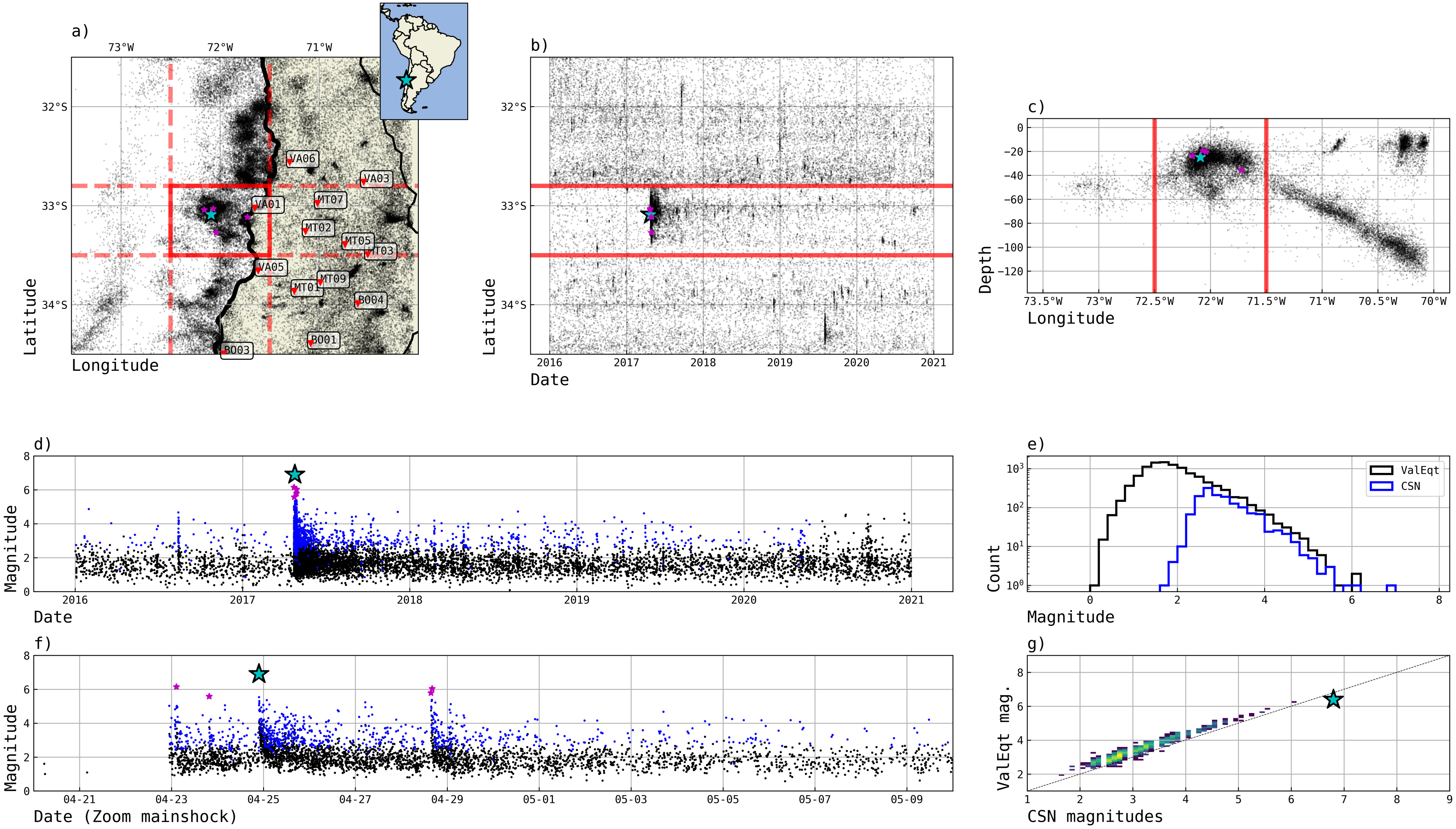

FIGURE 3.3.1: Time, location and magnitude of earthquakes detected in this study between 2016 and 2021. a) Horizontal location of earthquakes. The thick red line shows the extent of the ValEqt catalog analyzed in this study. The red triangles show the location of the 13 broadband stations used to build the catalog. b) Time evolution of the latitude of earthquakes between the two vertical red-dashed lines in a). c) Depth and longitude of earthquakes between the two horizontal red-dashed lines in a). Magenta stars indicate $M \geq 6$ earthquakes. d) Time and magnitude of earthquakes within the ValEqt sub-region (thick red rectangle in a)). Black dots are our catalog. Blue dots (in the foreground) are the CSN catalog used as reference. e) Gutenberg-Richter magnitude frequency distribution of our ValEqt (blue) and CSN (blue) catalogs . f) Same as d) but zoomed in time in the vicinity of the mainshock. g) Comparison of magnitude estimations for common earthquakes in the CSN and the ValEqt catalogs. The light blue star indicates the $M_w = 6.9$ mainshock.

activities.

We compare our ValEqt catalog with the CSN catalog (Figures 3.3.1.d and .f) in the same sub-region. The frequency-magnitude distribution in Figure 3.3.1.e shows that the ValEqt catalog includes much more small magnitude earthquakes than the CSN catalog, lowering the local magnitude of completeness from $M_c^{CSN} = 3$ to $M_c^{ValEqt} = 2$. Our detection procedure identified almost all earthquakes on CSN catalog. We only miss 12 CSN earthquakes all with a magnitude below 3, either because the data of the 13 stations used in our study were unavailable at that time or these earthquakes were interlaced with the waveform of a preceding earthquake, making it difficult to pick their P and S phases even after a careful review. On the other hand, thanks to EQTransformer, we detected many earthquakes with a magnitude above 3 not listed in CSN catalog. These newly identified earthquakes mainly occurred immediately after a larger earthquake, making them difficult to detect by standard methods (i.e., STA/LTA or visual inspection) because of the amplitude ratio. Figure 3.3.1.g shows the differences in magnitude for earthquakes recorded in both catalogs. Overall, the ValEqt magnitudes are consistent with the CSN estimations, but with a constant bias of about $+0.2$ units. This shift could result from the use of a different relation to compute earthquakes magnitude between both catalogs. Because local magnitude saturates for large magnitude earthquakes, the mainshock magnitude was originally underestimated as $M = 6.2$ by our procedure. We, therefore, fix manually its value based on its moment magnitude $M_w = 6.9$. Locations from the ValEqt catalog are similar to those reported by CSN (See Figure 3.S.1). Latitude, longitude and depth $1 - \sigma$ uncertainties are estimated to 0.02°, 0.06° and 6.3 km, respectively. The larger uncertainties in longitude and depth are likely due to the offshore locations of earthquakes constrained by onland stations. From Figure 3.3.1.c, we see that earthquakes within the sub-region are widely dispersed at depth, with events sometimes located below the subduction interface. Events at large depth are associated with a small number of phase picks, resulting in a large depth uncertainty (see Figure 3.S.2 and 3.S.3). The mainshock and other $M_w > 4$ earthquakes in the region are most likely located on the megathrust interface according to their location and shallow thrusting mechanism (Caballero et al., 2021). Given the large depth uncertainties, it is thus reasonable to assume that most seismic events in the area are located on the subduction interface.

3.4 Seismicity analysis

The high resolution ValEqt catalog (Figure 3.3.1.d,f) allows us to obtain a refined view of the seismicity rate variations observed in the region before and after the $M_w = 6.9$ Valparaiso mainshock. The two largest foreshocks are recorded with $M = 6.1$ and $M = 5.5$, approximately 2 days and 1 days before the mainshock, respectively. The largest aftershock occurred 4 days after the mainshock with a magnitude $M = 6.1$.

Because of its space and time correlation with the mainshock, a previously reported slow slip event during the foreshock sequence (Ruiz et al., 2017; Caballero et al., 2021) is suspected to reflect the nucleation process of the $M_w = 6.9$ earthquake and may possibly drive part of the foreshock seismicity. However, sharp increase of the seismicity rate following the two largest foreshocks in Figure 3.4.1.a suggests that a large part of the seismicity may be explained only by aftershock triggering and do not require any slow-slip as their background driver. Therefore, we test the hypothesis that the detected seismicity can be explained by models that account only for earthquake interactions. We use two temporal models of aftershock triggering: the Epidemic Type Aftershock Sequence (ETAS) model (Ogata, 1988; Zhuang et al., 2012) and a Model Independent Stochastic Declustering approach (Marsan & Lengliné, 2008). We ignore the spatial variation of seismicity and focus only on its temporal variations because the studied region is sufficiently small and isolated from any seismicty rate variations from surrounding regions.

3.4.1 ETAS and short-term incompleteness

The ETAS model has been widely used to generate synthetic earthquake catalogs (Zhuang & Touati, 2015). It can serve as a basis for establishing a reference earthquake catalog and testing any deviation from it (Ogata, 1989, 1992; Marsan et al., 2014; Moutote et al., 2021; Seif et al., 2019). It is also used to forecast seismicity (Zhuang, 2012; Taroni et al., 2018). The ETAS model is a superposition of a stationary background seismicity term and an aftershock triggering scaled in intensity by the magnitude of the triggering event. The conditional intensity $\lambda_0(t)$ (i.e., the expected seismicity rate at t) given by the ETAS model can be written as:

$$\lambda_0(t) = \mu + \sum_{i|t_i<t} A e^{\alpha(M_i - M_c)}(t - t_i + c)^{-p}, \tag{3.2}$$

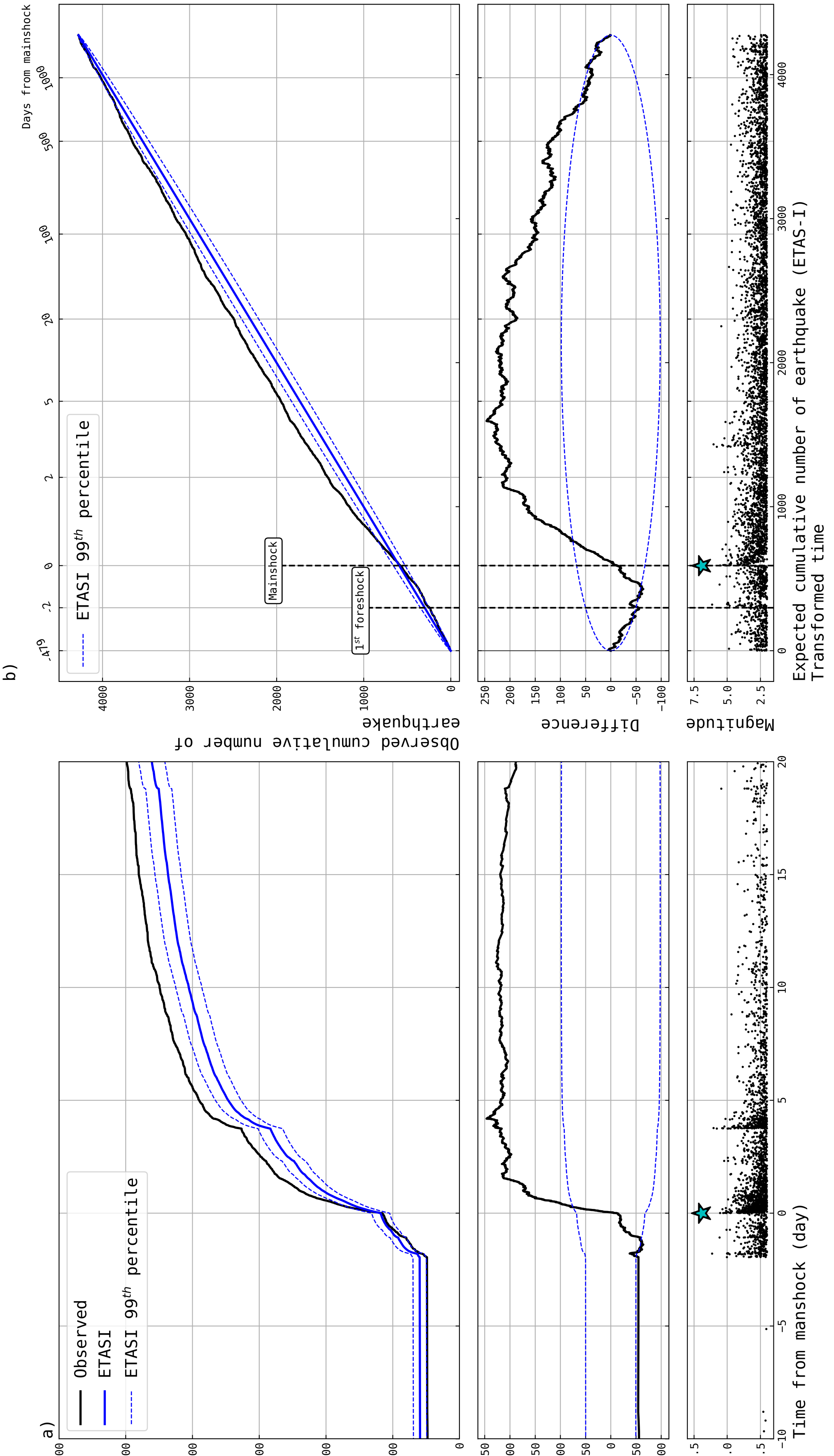

FIGURE 3.4.1: (a) Time-evolution of the cumulative number of earthquakes observed in the ValEqt catalog (black) and predicted by the best fitting ETASI model (blue) around the mainshock time. The blue dotted line shows the ETASI 99th percentile confidence interval. The middle subplot is the difference between the blue and black lines. Black dots in the bottom subplot indicate the time-magnitude evolution of the ValEqt catalog. (b) same as (a) but for the full 5-years period and with the transformed-time domain axis (Ogata, 1988). The blue star indicates the mainshock. Note how the transformed time domain allows an efficient analysis of the full 5-years seismicity with respect to the ETASI model.

where μ is the stationary background seismicity rate. The sum on the right hand side of this equation describes the expected aftershock seismicity rate at time t, triggered by all the preceding events. The parameters c and p describe the time-decay in the aftershock seismicity rate (Omori, 1895; Utsu et al., 1995). The intensity of the triggering is scaled by A and α, the global aftershock productivity of the region and the magnitude dependency in the number of triggered events, respectively. M_c is the magnitude of completeness of the catalog. In the ETAS model, magnitudes are assumed to be independent and distribute according to Gutenberg-Richter's law (G-R). We can write the G-R probability density function as:

$$f_0(M) = \beta \mathrm{e}^{-\beta(M-M_c)}, \tag{3.3}$$

$\beta = b\ln(10)$ with b the b-value of the G-R law. The G-R law and the ETAS model are only defined above the magnitude of completeness M_c that is supposed to be constant over time. However, in actual seismicity catalogs, we frequently observe temporal variations of M_c (Kagan, 2004; de Arcangelis et al., 2018; Hainzl, 2016). Such variations of M_c are usually attributed to deterioration of the detection performance of low magnitude earthquakes during network maintenance or during period of high seismic activity. The latter is our main concern for the ValEqt catalog since the data availability is quite constant over the studied time-period. When the seismicity rate is high, records of seismic wave of low magnitude earthquakes are likely to be hidden by larger magnitude events. As shown in Figure 3.3.1.e, we estimate an average magnitude of completeness $M_c = 2$ for the ValEqt catalog over 5 years. However, M_c can increase just after large earthquakes because of the numerous aftershocks they trigger. Figure 3.4.2 shows a deficiency in small magnitude earthquakes in the first hour following the $M_w = 6.9$ mainshock and the magnitude of completeness rose up to $M_c \sim 3.5$ immediately after it. The observed $M \geq 2$ earthquake rate is, therefore, underestimated just after the mainshock, which may bias the estimation of an ETAS magnitude-dependent triggering process. This bias is often referred to as Short-Term Incompleteness because it is visible just after large earthquakes (Kagan, 2004; de Arcangelis et al., 2018; Hainzl, 2016). However, it can be generalized to a Rate-dependent incompleteness (Hainzl, 2021) since missing low magnitude events can affect any time-window with a sufficiently high seismicity rate.

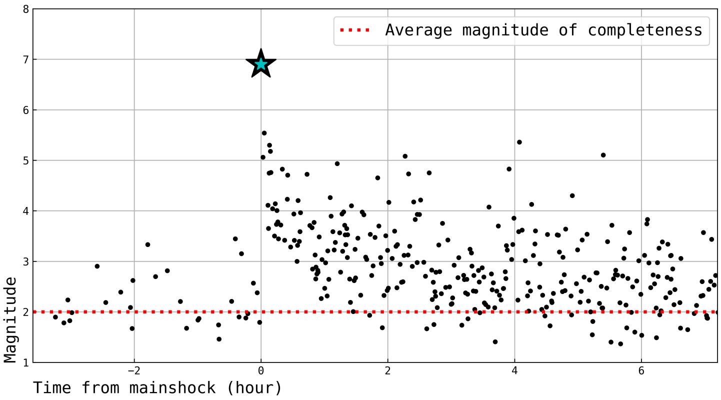

FIGURE 3.4.2: Short-term incompleteness after the Valparaiso mainshock. The red horizontal line is the average magnitude of completeness (M_c) estimated from the G-R distribution of the entire ValEqt catalog. Note the lack of low magnitude earthquakes above M_c during the earliest aftershock times. The light blue star indicate the mainshock.

To accommodate our seismicity analysis with $M_c = 2$ while taking into account the rate-dependent incompleteness, we use the ETASI model (i.e., ETAS-Incomplete; Hainzl, 2016, 2021) instead of the ETAS model. This new formulation takes into account a rate-dependent incompleteness by adding one parameter T_b, defined as a blind time; for a duration T_b following an earthquake of magnitude M, any event of magnitude less than M cannot be detected. In practice, the ETASI model acts as an apparent rate at every t, considering the likelihood of observing large magnitude events in $[t - T_b, t]$. The ETASI apparent seismicity rate function is (Hainzl, 2021):

$$\lambda(t) \approx \frac{1}{T_b}(1 - \mathrm{e}^{-T_b \lambda_0(t)}). \tag{3.4}$$

From equation (3.4), we see that the ETASI rate $\lambda(t)$ is simply the original ETAS rate $\lambda_0(t)$ of Equation (3.2) modulated by the blind time T_b during high seismicity rate periods. Likewise, the G-R distribution is affected by the rate-dependent incompleteness because some low magnitude earthquakes are undetected. The apparent Gutenberg-Richter distribution at t is (Hainzl, 2021):

$$f(m,t) \approx \beta T_b \lambda_0(t) \frac{\mathrm{e}^{-\beta(M-M_c)} \mathrm{e}^{T_b \lambda_0(t) \mathrm{e}^{-\beta(M-M_c)}}}{1 - \mathrm{e}^{-T_b \lambda_0(t)}} \tag{3.5}$$

From a given catalog $(t_i \in [T_1, T_2], m_i \geq M_c)$, we extract the best fitting ETASI parameters by maximizing the following Log-Likelihood function (Hainzl, 2021):

$$\mathcal{LL} = \sum_{i=1}^{N} \ln[f(m_i, t_i)] + \sum_{i=1}^{N} \ln[\lambda(t_i)] - \int_{T_1}^{T_2} \lambda(t)\,\mathrm{d}t \tag{3.6}$$

For the ValEqt catalog, we extract the best fitting parameters for magnitudes above the magnitude of completeness $M_c = 2$. Moreover, following Davidsen & Baiesi (2016), we impose self-similarity in the aftershock triggering process by fixing $\alpha = \beta$ during the maximization of the likelihood function. With this self similarity constraint, the probability for a $M = 8$ to trigger $M = 6$ earthquakes is assumed same as the probability for a $M = 4$ to trigger $M = 2$ earthquakes, for example. We tested a case without this self-similarity constraint at the earlier stage of this study, but the resultant branching rate inverted from the ValEqt catalog was much larger than 1, leading to a non-stationary synthetic ETAS catalog with an infinite number of aftershocks and increasingly large magnitudes. This constraint also reduces the number of free parameters to 6 as for the classic ETAS model. The best fitting ETASI parameters extracted from the ValEqt catalog are presented on Table 3.4.1.

To test the reliability of the ETASI Log-Likelihood maximization, we invert the ETASI parameters for 100 synthetics ETASI catalogs (Figure 3.S.4). We use the ETASI parameters extracted from ValEqt (Table 3.4.1) as the true parameters to generate the synthetic catalogs (Zhuang & Touati, 2015). Results indicate that $A, p, \alpha = \beta$, μ and T_b are well constrained by the parameter estimation and c slightly overestimated but with a reasonably close value. This tendency agrees with the conclusions of Hainzl (2021). They have found a similar bias for c and suggested that it may be explained by the lack of earthquakes during rate-dependent incompleteness. Such incomplete data breaks the triggering links between earthquakes and complicates the estimation of an Omori-Utsu rate decay for individual aftershock sequences. Moreover, after large magnitude earthquakes, the early aftershock rate is mainly controlled by the rate-dependent incompleteness for a period greater than c. It delays the apparent start of the Omori-Utsu rate decay and likely bias the c-value estimation toward higher values. In any case, as suggested by Hainzl (2021), the c-value estimated with the ETASI model is less biased than estimated with the classic ETAS model over incomplete catalogs.

TABLE 3.4.1: Best fitting ETASI parameters extracted from the ValEqt catalog

Parameter	A	c (Minutes)	p	$\alpha = \beta$	μ (events/day)	T_b (seconds)
Value	9.9e−3	11.74	1.18	1.71	0.27	116.57

3.4.2 Testing ValEqt against the ETASI model

With the best-fitting parameters (Table 3.4.1) and Equation (3.4), we compute the seismicity rate expected from ETASI at any time t in the studied time-period. Integrating this expected seismicity rate over time gives an expected number of earthquakes. We define the cumulative number of earthquakes expected from the best fitting ETASI model, $\tau(t)$, as:

$$\tau(t) = \int_{T_1}^{t} \lambda(u)\, \mathrm{d}u, \tag{3.7}$$

where, λ is the ETASI rate given by Equation (3.4) and T_1 is the start time of the catalog. We compare $\tau(t)$ with the observed cumulative number of earthquakes at t, $N_{obs}(t)$. If the best fitting ETASI model explains perfectly the observed seismicity, $\tau(t)$ and $N_{obs}(t)$ must be equal over time. In such a scenario, it implies that we cannot reject the hypothesis that the earthquake sequence can be modeled with a constant background rate and aftershock triggering. Any strong differences between $\tau(t)$ and $N_{obs}(t)$ highlight an anomalous activity with respect to the ETASI model. Representing the predicted seismic activity, $\tau(t)$ as a function of the observed seismic activity, $N_{obs}(t)$ is known as the transformed time analysis introduced by Ogata (1988).

The evolution of $\tau(t)$ and $N_{obs}(t)$ around the mainshock occurrence time is displayed in Figure 3.4.1.a. On Figure 3.4.1.b, we display the entire period in the transformed time domain. This transformed time representation enables a simplified comparison of the seismicity over the full duration of the catalog, by gathering periods of low and high seismicity in a single figure. In the transformed time domain, if the seismicity is perfectly explained by the best-fitting ETASI process, $\tau(t)$ and $N_{obs}(t)$ should be equal and thus exhibit a straight line with a slope of 1 (i.e., a unit Poisson rate) with a normal standard deviation of $\sigma(t) = \sqrt{\tau(t)(1 - \frac{\tau(t)}{\tau(T_2)})}$ (Ogata, 1992). If the curve significantly diverges from this straight line, we can interpret the local slope as a seismicity deficit (slope < 1) or excess (slope > 1) compared to the ETASI model. They are better illustrated by the difference $N_{obs}(t) - \tau(t)$ (Figure 3.4.1), in which the seismicity deficit and excess correspond to negative and positive slopes, respectively. Our results highlight that the seismicity surrounding the Valparaiso mainshock diverges from the ETASI prediction by more than 3σ. We observe three main regimes of seismicity with respect to the best-fitting ETASI model. From the starting time of the catalog and up to the first foreshock, we observe a low negative slope that indicates a small deficit of earthquakes compared to ETASI model. We then observe a significant change toward a positive slope (step $\geq 3\sigma$) highlighting an excess of seismicity, starting within the foreshock sequence and persisting at least 5 days after the mainshock. After that time, the slope slowly returns to its initial low deficit regime. These results indicate that the best fitting ETASI model cannot successfully reproduce the 5-year seismicity variations observed in the area of the 2017 Valparaiso mainshock. Specifically, they suggest that the anomalously high seismic activity observed from -1 day up to at least +2 (possibly up to +5 days) days after the mainshock is driven by another process that is not captured by our stationary ETAS model. Similar variations of $N_{obs}(t)$ - $\tau(t)$ as reported in Figure 3.4.1 are actually observed in synthetic catalogs with a finite duration transient background seismicity over the stationary background rate (see Text 3.S.1 and Figure 3.S.5). Such a transient increase of the seismicity in a synthetic catalog produce a similar positive anomaly as in Figure 3.4.1 when analyzed with the ETASI model with a constant background rate. Moreover, it also shows that the two periods of low seismic productivity can be explained by the enhanced earthquake activity around the mainshock, because the transient biases the estimation of ETASI parameters towards higher productivity values (i.e., larger values for A in Equation 3.2).

In order to interpret the observed seismicity excess, we performed additional ETASI inversions that include additional triggering terms during the Valparaiso sequence, modeling a transient triggering. This allows us to quantitatively capture the part of the seismicity that cannot be attributed to background and aftershocks triggering. We first add a transient constant rate, μ_2, starting at the time of the first foreshock and lasting for an unknowns duration T_e days, incremented each +0.5 days. We find that, including such a transient background rate can significantly reduce the Akaike Information Criterion (AIC), and thus better explain the seismicity. The AIC allows to compare different models with different parameters by correcting the likelihood (Equation 3.6) by the number of model parameters k used: $AIC = 2k - 2\mathcal{LL}$ (Akaike, 1974; Ogata, 1989). The best model, with the lowest AIC is obtained when $T_e = 3.5$ days with a rate $\mu_2 = 87.3$ (i.e., $\sim$305 events; Figure 3.S.6.a and Table 3.S.1). However, even with this transient constant rate, a part of the seismicity excess observed after the mainshock is still not well captured. Because the remaining seismicity excess seems causal to the mainshock, we choose to freely invert the magnitude of the mainshock in addition to the transient constant rate. We find (Figure 3.S.6.b and Table 3.S.1) that including both the transient and a free mainshock magnitude in the model can further reduce the AIC and can explain all the seismicity excess. The transient constant term is lasting $T_e = 3.5$ days with a rate $\mu_2 = 76.1$ (i.e., $\sim$266 events) and the mainshock magnitude is evaluated to $M_{mainshock} = 8.2$. This shows that the seismicity excess can be modeled by a transient rate starting at the time of the foreshock sequence and lasting for 1.5 days following the mainshock time and with an unusually high aftershock productivity for the mainshock. It further supports that the seismicity before and after the mainshock is unusually enhanced with respect to typical magnitude-dependent aftershock triggering and requires external triggering process to be well captured.

3.4.3 Declustering approach

To confirm whether the anomalously high seismic activity around the mainshock is a real and significant feature, we employ another declustering approach, which is a modified version of the model-independent stochastic declustering (MISD) algorithm of Marsan & Lengliné (2008). Our method differs from the original MISD in two aspects: First, as did for the ETAS model, we focus on the temporal variations of the seismicity rate by ignoring the spatial dependence. Second, in addition to the magnitude-dependent aftershock seismicity and the stationary background seismicity, we consider an external forcing process that can trigger an additional seismicity around the mainshock. It models seismicity unrelated to earthquake interaction, such as slow slip driven seismicity. Neglecting any spatial dependence in the original method, the earthquake rate at time t can be expressed as

$$\phi(t) = \phi_0 + \sum_{i,t_i<t} g(m_i, t - t_i) \tag{3.8}$$

where ϕ_0 is a constant background rate over the whole duration of the catalog T; m_i and t_i are the magnitude and occurrence time of earthquake i, respectively, and g is a triggering kernel. The method assumes no shape for g but simply considers a piecewise constant discretization in time and magnitude of the kernel such that

$$g_{kl} = g\left(M_k < m < M_{k+1}, T_l < t < T_{l+1}\right) \tag{3.9}$$

where T_l, and M_k are the time and magnitude intervals used for discretization, respectively. Based on equation (3.8) and an initial guess of g, we can compute the earthquake rate $\phi(t)$ and then the weights ω_{ij} of earthquake i triggering earthquake j and the background weight ω_{0j}. These weights are defined as

$$\omega_{ij} = \frac{g(m_i, t_j - t_i)}{\phi(t_j)}; \, \omega_{0j} = \frac{\phi_0}{\phi(t_j)}, \tag{3.10}$$

$$\sum_{i=1}^{j-1} \omega_{ij} + \omega_{0j} = 1. \tag{3.11}$$

where the last equation is used for normalization and actually transforms these weights into probabilities. These weights are then used to compute a new estimate of the triggering kernel and the background rate. The process is repeated until reaching the convergence. A detailed description of the algorithm is available in Marsan & Lengliné (2010).

Then, we account for a possible additional seismicity driven by an external process. Similarly to the ETASI analysis, we assume that this external forcing process starts at a time, t_e and lasts for a unknown duration T_e and that this contribution can be modeled with a constant rate, ϕ_e such that the seismicity rate is now described as

$$\phi(t) = \phi_0 + \sum_{i, t_i < t} g(m_i, t - t_i) + \phi_e \left(\mathcal{H}(t - t_e) - \mathcal{H}(t - t_e - T_e)\right) \tag{3.12}$$

where $\mathcal{H}$ is the Heaviside step function. We do not attempt to model the shape of this external triggering process but rather keep a simplified model with a constant rate. Therefore, we introduce the weights $\omega_{ej} = \phi_e / \phi(t_j)$ if $t_e < t_j < t_e + T_e$ and 0 otherwise. The normalization condition becomes $\sum_{i=1}^{j-1} \omega_{ij} + \omega_{0j} + \omega_{ej} = 1$. This additional triggering modifies the log-likelihood function associated with the original algorithm such that we have now:

$$L = -\phi_0 T - \phi_e T_e + n_0 \ln \phi_0 + n_e \ln \phi_e - \sum_{ij} n_i g_{ij} \delta t_j + \sum_{ij} n_{ij} \ln \left(g_{ij}\right), \tag{3.13}$$

with, n_0 the number of background earthquakes, $n_0 = \sum_i \omega_{0i}$ and $n_e = \sum_i \omega_{ei}$ the number of earthquakes triggered by the external forcing process. The number of earthquakes with magnitude in the interval $[m_i, m_{i+1}]$ is noted n_i, while n_{ij} is the number of earthquakes triggered by a magnitude i earthquake in the time interval $[t_j, t_{j+1}]$ of duration δt_j. Based on this approach, we compute the background rate ϕ_0, the kernel g and the external forcing rate, ϕ_e. As the duration of this external forcing T_e is unknown, we simply estimate it by grid search ranging from 0.01 day up to 30 days. The best parameters are obtained by maximizing L. In order to test the method, we perform a series of synthetic tests to check the ability of the proposed algorithm to recover a transient episode of seismicity (See Text 3.S.2 and Figure 3.S.7).

We apply the declustering algorithm described above to the ValEqt catalog with t_e = 47 hours before the occurrence of the Valparaiso mainshock (i.e., the origin time of the first foreshock). We also take into account the time-evolution of the magnitude of completeness following large earthquakes using the approach of Peng et al. (2007) in which a transient magnitude of completeness $m_c(t) = \overline{m}(t) - 1/(b\ln(10))$ is computed with $\overline{m}(t)$ an average magnitude computed over the next N_e earthquakes in time. It follows that an earthquake at time t counts as $n(t) = 10^{b(m_c(t)-m_c)}$. Here, we set $b = 0.74$ as inverted from the ETASI procedure, $m_c = 2$ and we choose $N_e = 10$ as in Marsan & Lengliné (2010). The maximum of L is obtained with a value of T_e = 10 days, corresponding to an inverted value of ϕ_e= 41 earthquake per day. Such large values of transient duration and rate indicate that a substantial part of the seismicity is not well explained by magnitude-dependent triggering kernels alone. Figure 3.4.3 shows the background events and those triggered by the external process (i.e., events that do not result from earthquake interactions). This confirms the previous ETASI analysis that an additional triggering, starting before the Valparaiso mainshock and lasting several days after its occurrence is needed in order to correctly represent the seismicity.

3.5 Repeater activity

A slowly creeping subducting interface loads embedded asperities that repeatedly fail over time, producing repeating earthquakes, which are characterized with similar source location and waveforms (Uchida, 2019; Kato et al., 2012; Kato et al., 2016a). Such repeater events can then be used to track aseismic slip rates surrounding the ruptured asperities.

To search for repeating events in the vicinity of the 2017 Valparaiso earthquake, we evaluate the similarity of waveforms for all earthquake pairs within the ValEqt catalog. We compute an average cross-correlation coefficient (CC) over the 7 stations that are associated with the largest number of P and S picks (i.e.,

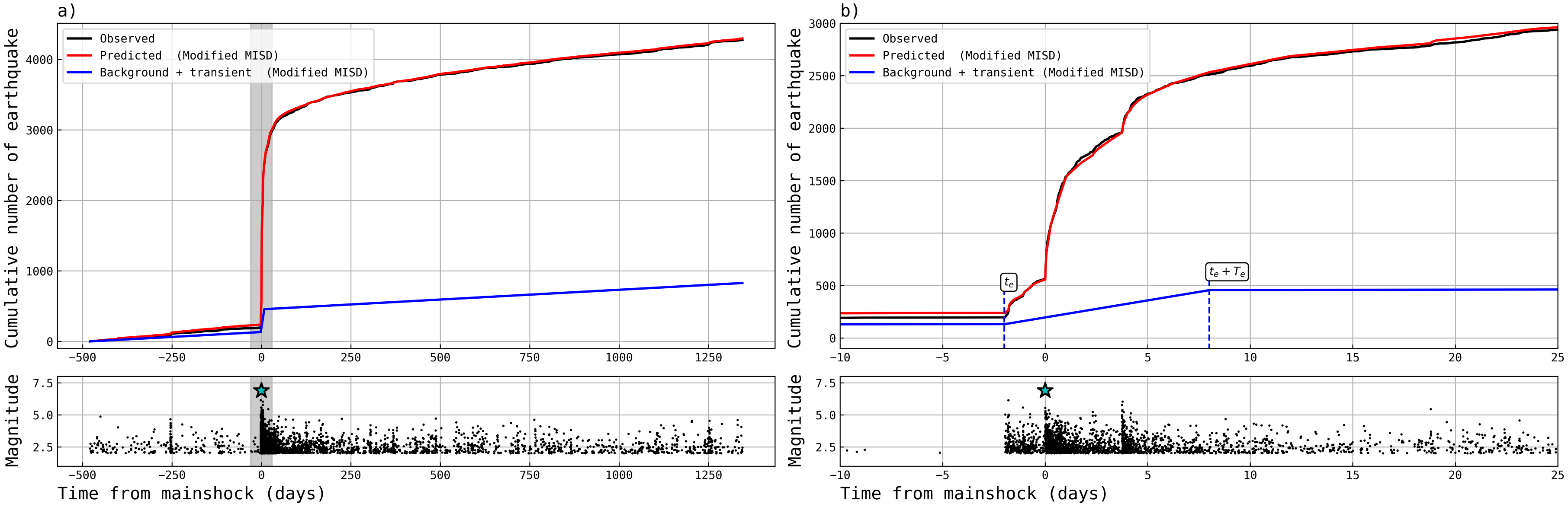

FIGURE 3.4.3: a) Cumulative count of earthquakes of the ValEqt catalog (black) and their prediction by the best fitting modified MISD (red). (blue) Cumulative count of earthquake declustered by the modified MISD analysis. This include background events and those triggered by the external process ($\sum_i \omega_{0i} + \omega_{ei}$). Bottom subplot (black dots) shows times and magnitudes of the ValEqt catalog. b) Same as a) but zoomed in the Grey area. t_e and T_e are respectively the start time and the duration of the external process of our modified MISD model.

MT01, MT09, MT02, VA03, VA06, MT07 and VA05). At every station, the cross-correlation coefficient is defined as the maximum value of the cross-correlation function between the two waveforms of the earthquake pair. This cross-correlation function is computed in a 40-second time window starting 5 seconds before the P arrival in the 2 to 20 Hz band. This large time window allows us to include both P and S arrivals and to maximize the signal to noise ratio. The final CC value of the earthquake pair is defined as the average of the CC values computed at available stations. Pairs of events that share less than 3 stations are automatically discarded. Then, we gather earthquakes with similar waveforms into families based on a hierarchical clustering algorithm using a complete linkage over the CC value. We retain families of earthquakes with a high waveform similarity (i.e., $CC > 0.80$) as a first sub-set of potential repeating earthquakes. Then, we ensure that events within a family are all co-located on the same asperity using the HypoDD double-difference relocation algorithm (Waldhauser & Ellsworth, 2000). For every pair of events, we estimate travel time differences between both P and S phases at all the available stations. Travel time difference between 2 phases of each event pair is estimated by cross-correlation. For P phase, we use a 5 second window that starts 1.5 seconds before the pick. For S phase, we use a 10 second window starting 3 seconds before the pick. Those traces were previously band-pass filtered with a band width of 2-20 Hz. To evaluate the relocation uncertainties, we relocate events within each family using the SVD solving method of HypoDD, using the CC values as a weight of differential travel-time measurements. On average, a pair of event is relocated with 13 differential travel-time measurements. During the relocation process, we discard events with a inter-event distance greater than 1 km or with an RMS residual greater than 6 times the standard deviation. After the relocation, we estimate a rupture radius for each event by assuming a circular crack model with a stress drop of 3 MPa (Hanks & Bakun, 2002). From relocated hypocenters and their circular rupture radii, we compute the 3D distance between rupture patches for every earthquake pairs within families. Taking hypocenter location uncertainties into account, we further discard events that have less than 80% of chance to intersect with all the other rupture areas of the family. Finally, we discard events within a family with a magnitude difference $\Delta M \geq 1$. With these multiple criteria, high waveform similarity, collocation, and a similar magnitude of all the events in each family can safely be interpreted as actual repeating earthquakes.

Following this approach, we detected 342 repeater families consisting of at least 2 events (Figures 3.5.1 and 3.5.2). Across all the families, we identified 1171 repeating earthquakes. In order to test the robustness of our repeating earthquake analysis, we changed the various thresholds for forming the repeater sequences. It yielded moderate variation in the number of repeaters and number of families, but it does not alter the conclusions presented below, regarding the temporal evolution of the repeater activity. An intense repeater activity initiated during the 2-day foreshock sequence with the highest rate over the whole catalog period. After the mainshock occurrence, the repeater rate decays continuously over the whole analyzed period, but never returns to the initial rate observed before the foreshock sequence. Unlike the seismicity of the ValEqt catalog, the repeaters rate is not strongly impacted by the occurrences of large magnitude earthquakes.

Compared to the earthquakes in the ValEqt catalog, the repeater activity is confined to a small region (Figure 3.5.2). The main repeater activity is located in the vicinity of the mainshock hypocenter and a secondary activity is observed to the south before and after the largest aftershock. During the foreshock sequence, the repeater activity and the seismicity are almost perfectly co-located. After the mainshock, the repeater activity remains exclusively located at the initial foreshock location, unlike the seismicity that spreads to a wider area.

The aforementioned observations indicate that the repeater activity does not behave as a random subset of the seismicity. Repeaters seem to be driven by a specific process that initiates before the mainshock and extend after it, within a specific area delimited by the foreshock activity. Moreover, the repeater activity appears to decay continuously over time and is not strongly affected by the occurrence of large earthquakes, nor the mainshock. The intense repeater activity observed during the foreshock sequence recalls the occurrence of the pre-mainshock aseismic transient slip detected by Ruiz et al. (2017) and (Caballero et al., 2021). Using these repeaters, we estimate time-evolution of aseismic slip on the subduction interface over the entire earthquake sequence. We follow the approach of Kato et al. (2012) and Kato et al. (2016a) using a circular crack model with a constant stress drop of 3 MPa to estimate the individual repeater slip amplitudes (Hanks & Bakun, 2002; Uchida, 2019). Then, individual slip amplitudes are summed over time and averaged by the number of repeater families to estimate cumulative slip evolution (Figure 3.5.1). To the first order, the obtained slip rate is maximum at the beginning of the foreshock sequence and slowly decays with time over days to months until the end of the studied time-period. Impacts of large earthquakes to this steady decay appears very limited (Figure

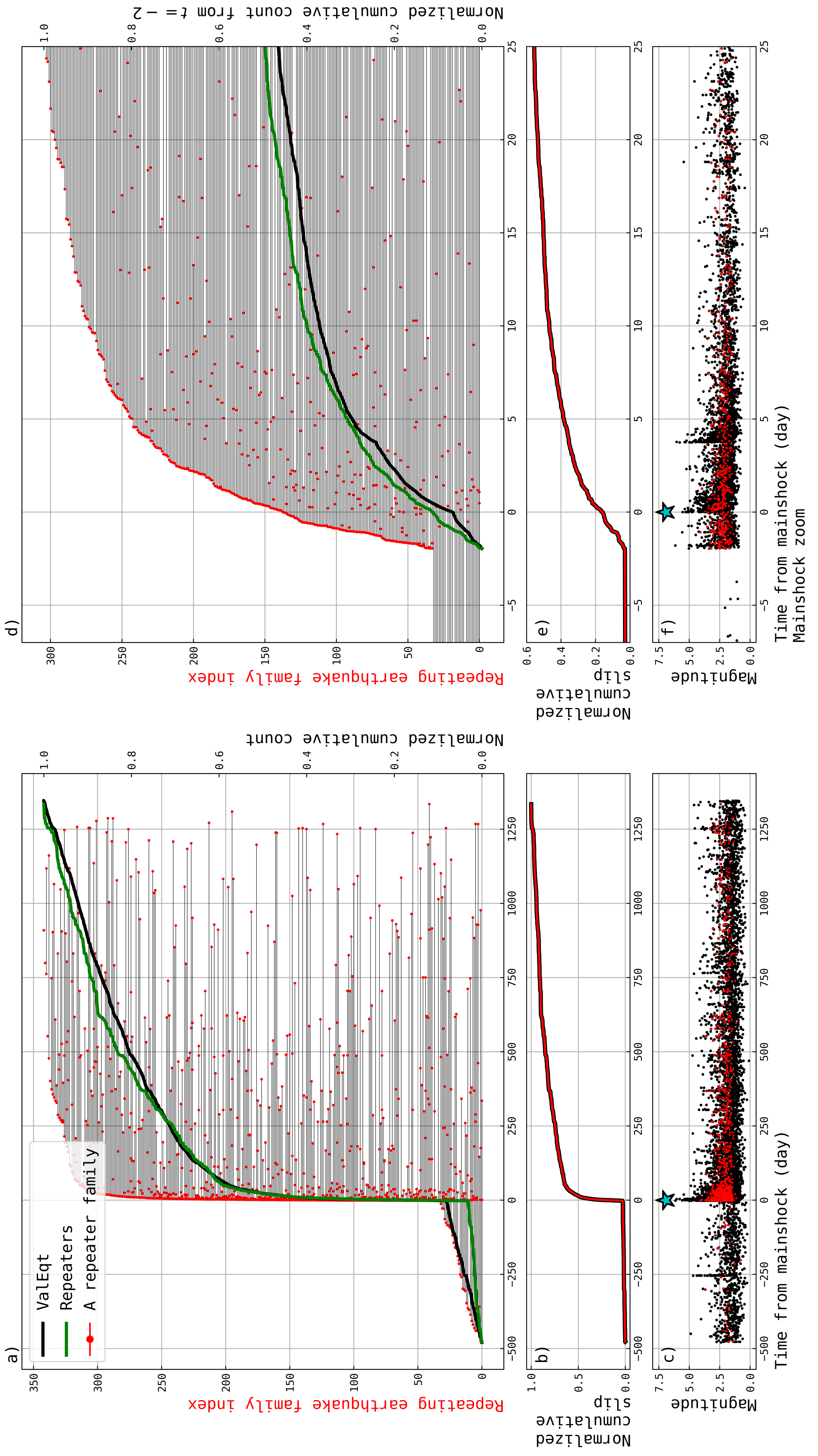

FIGURE 3.5.1: (a) Families of repeating earthquake detected in the ValEqt catalog. A horizontal black line represents one family by connecting the repeating earthquake (red dots). The green and black curves are the normalized cumulative number of repeaters and ValEqt earthquakes respectively. (b) Normalized cumulative slip estimated from repeating earthquakes. (c) Times and magnitudes of ValEqt earthquakes (black dot) and repeating earthquakes (red dot). The blue star indicates the mainshock. (d, e and f) Same as (a, b and c) but zoomed in the vicinity of the mainshock time. Note that the normalized cumulative count of repeaters and ValEqt earthquakes starts at t=-2 days in (d).

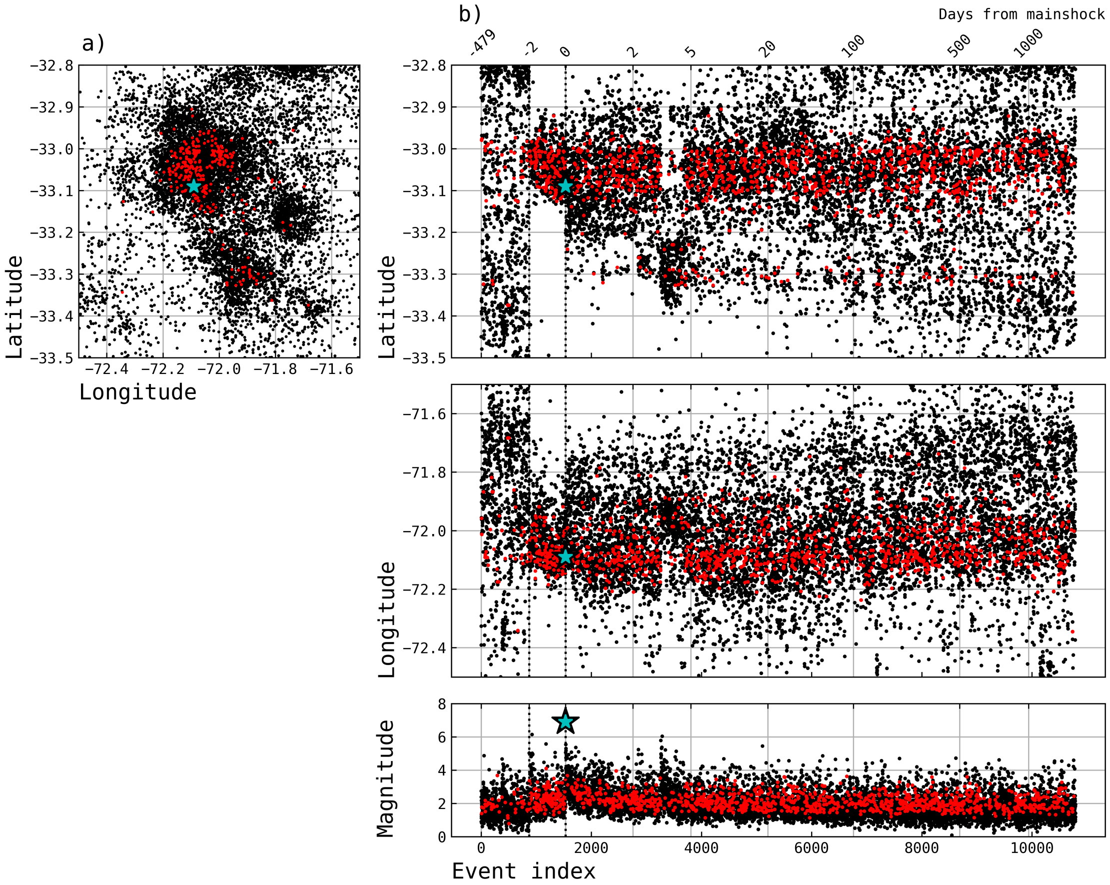

FIGURE 3.5.2: Space and time evolution of the ValEqt seismicity (black dots) and repeating earthquakes (red dots). The light blue star indicates the mainshock. a) Horizontal distribution of the seismicity. b) Latitudes, longitudes and magnitudes against the chronological index of the ValEqt seismicity. The chronological index shown by the bottom horizontal axis ticks for each subplot. The corresponding time (days from mainshock) is shown with the top horizontal axis ticks. The two vertical dotted lines highlight the indices/timings of the first foreshock and the mainshock.

3.5.1). Overall, these results suggest that the transient aseismic slip initiated during the foreshock sequence persists after the mainshock, following a steady rate decay.

3.6 Aseismic slip before and after the mainshock by high-rate GPS

The inferred unusual seismic activity (Figure 3.4.1, 3.4.3) suggests the presence of a specific triggering process before and after the mainshock. The repeater-based slip rate (Figure 3.5.1, 3.5.2) suggests that this triggering process is a transient aseismic slip. Indeed, a transient aseismic slip is reported for the pre-mainshock stage (Ruiz et al., 2017; Caballero et al., 2021), but temporal relationship between the aseismic preslip and the foreshock sequence has remained unclear, which is key to understanding mechanical processes. For the post-mainshock stage, no studies have yet investigated very early postseismic deformation and rapid afterslip associated with the 2017 Valparaiso mainshock. Therefore, to fill the gap between the two stages, we use high-rate GPS (hereafter, HRGPS) to investigate transient slip during the whole 2017 sequence as independent observable from the seismicity analysis. We directly interpret pre- and post-seismic HRGPS time series as proxy of slow slip in this study; Viscoelastic relaxation is the other dominant mechanism responsible for postseismic deformation in subduction zones, but their contribution would be negligible given the mainshock magnitude and time scale considered in this study (Periollat et al., 2022; Sun & Wang, 2015; Wang et al., 2012).

We employ 5-minute coordinates between 30 days before and after the day of the mainshock at 6 sites near the epicenter (Figure 3.S.8) (Caballero et al., 2021), processed by Nevada Geodetic Laboratory (Blewitt et al., 2018). Nominal errors of these coordinates are $\sim$ 7 mm and $\sim$ 9 mm for east and north components, respectively. These coordinates are estimated by a Kalman filter and smoother with 17 m of the scale of random-walk process (Blewitt et al., 2018), so forward and backward propagations of the sudden coseismic offsets unlikely happened. We do not use sites VALN and CUVI (Figure 3.S.8) because 5-min coordinates of the former are too noisy and those of the latter are not available. The original coordinates are affected by a high noise level, so we post-process the series to alleviate the fluctuations (Figure 3.S.9). We first fix the coordinates into the South American plate reference frame by using its Euler pole with respect to ITRF2014

(Altamimi et al., 2017) (black dots in Figure 3.S.9). Then, we remove the fluctuations associated with multipath (Choi et al., 2004; Itoh & Aoki, 2022; Larson et al., 2007; Ragheb et al., 2007), which is estimated as a seasonal component of "Seasonal-Trend decomposition using LOESS (STL)" (Cleveland et al., 1990; Pedregosa et al., 2011) with a period of 86100 seconds. This period is the closest integer multiple of the sampling interval to a typical repeat period of multipath signature (86154 seconds; Ragheb et al., 2007). Then, the multipath free time series (red in Figure 3.S.9) is corrected for a diurnal variation component following the same procedure as the multipath removal but with a repeat period of 86400 seconds in order to obtain diurnal fluctuations free series (purple in Figure 3.S.9).

Next, we remove common mode fluctuation at all the sites, which are primarily due to fluctuation of reference frame and uncertainty of satellite orbits (Wdowinski et al., 1997). We extract common mode fluctuation (orange in Figure 3.S.9) by stacking coordinate time series at distant sites from the source area (Figure 3.S.8). Before stacking, we remove some outliers and the linear trend. Here, outliers are defined as epochs satisfying Equation (3.14) (Itoh et al., 2022).

$$\left| x_i - \frac{q_1 + q_3}{2} \right| > n * \frac{q_3 - q_1}{2} \tag{3.14}$$

where, x_i is displacement at the i-th epoch, q_1 and q_3 are the 25 and 75 percentile values of the position time series, respectively, and n is a threshold which was set to 8 in this study. The linear trend is estimated from the time series without outliers. The extracted common mode fluctuation is subsequently subtracted from the time series at the 6 sites of interest (blue in Figure 3.S.9).

Then, we remove the pre-mainshock trend from the common mode free time series. The linear trend is estimated from the data between 30 and 10 days before the mainshock. The trend is extrapolated to the subsequent period. Finally, we stack the cleaned time series at BN05 and TRPD, which are only $\sim$ 5 km apart, to further reduce the noise level (Figures 3.S.10 and 3.S.11). For stacking, the two time series are weighted according to the inverse of the square of quartile deviation of time series from 30 to 10 days before the mainshock. Hereafter, we assign a pseudo-name of site STAC to the stacked time series for the ease of writing and discussion.

Finally, we remove mainshock coseismic offsets from the time series at all sites (Figures 3.6.1, 3.S.12, and 3.S.13). We also remove the offset caused by the largest aftershock that is visible on the time series at QTAY (Figure 3.6.1). We calculate the mainshock offsets as a difference between pre- and post-event positions, which were defined as average positions during 1 and 0.5 days before and after the event, respectively. The same procedure is applied to the largest aftershock except for the post-event window length set to be 1 day. Interestingly, at the coastal sites (QTAY and STAC consisting of BN05 and TRPD), the steep trend following the mainshock coseismic step (red in Figure 3.6.1) was not significantly discernible after the step removal. Investigating their origin is beyond the scope of this study, but we speculate that they are just occasional deviation of GPS time series which are divided by the mainshock step happening somewhat during this deviation.

The stacked time series at STAC, closest to the mainshock epicenter, clearly exhibits a westward motion before, during, and after the mainshock (Figure 3.6.1). The pre-mainshock transient motion started $\sim$3 days before the mainshock and $\sim$1 day before the first foreshock. No acceleration of displacements is discernible before the mainshock, which can be interpreted as no acceleration of aseismic slip toward the mainshock. Coseismic displacement associated with the largest foreshock is not resolved and possibly buried in the remaining noise given the expected amplitude (Caballero et al., 2021). Interestingly, the transient trenchward motion continues smoothly before and after the mainshock and lasted $\sim$20 days (green in Figure 3.6.1). In other words, there is no notable acceleration of motion following the mainshock. Such an apparent lack of mainshock-induced acceleration is also seen in the daily GPS coordinates across the mainshock time (Ruiz et al., 2017). Furthermore, the site motion did not change its direction across the mainshock occurrence time (Figure 3.S.14) and the coseismic displacement also points in the same direction. Similarly, continuous transient westward motion before and after the mainshock is visible with smaller amplitudes at QTAY, $\sim$20 km south of STAC (Figure 3.6.1). At the other 3 sites, namely, CTPC, RCSD, and ROB1, the transient motion before the first foreshock is less convincing but the moving median curve demonstrate slight deviation from the trend. The non-uniform but coherent trenchward pattern of postseismic motion several days before and after the mainshock excludes the possibility that they represent local artifacts (Figures 3.S.10 and 3.S.14). The north component of GPS coordinate time series does not exhibit discernible pre-mainshock motion but post-mainshock motion is visible at CTPC, RCSD, and ROB1 (Figure 3.S.11). Based on these predominantly trenchward motions at the multiple sites in the same direction across the mainshock occurrence time (Figure 3.S.14) and without abrupt changes in their direction and rate, we conclude that the HRGPS observations indicate the occurrence of a continuous aseismic slip transient along the megathrust.

3.7 Discussion and conclusions

In this study, we have investigated the seismic and aseismic processes during the 2017 Valparaiso earthquake sequence, from the time of the first foreshocks to the end of the post-seismic sequence. We have built a high resolution catalog of the seismicity from 2016 to 2021, improving the completeness by 1 magnitude unit compared to the local CSN catalog. Thanks to this catalog, we have tested whether the seismicity can be explained by a stationary background term, that may describe a constant tectonic loading, and aftershock triggering. We showed that the stationary hypothesis cannot accurately describe the observed seismicity, particularly before and after the mainshock. Two different temporal magnitude-dependent aftershock triggering models (i.e., ETASI and MISD models) have shown that the seismicity from the foreshock sequence up to several days after the mainshock (2 and 8 days, respectively) is more abundant than predicted. This result suggests the presence of an additional forcing superimposed to the stationary background and magnitude-dependent aftershock triggering. Such a transient forcing term may be linked to an increase of the slip rate on the interface which has been already suggested for the pre-seismic period of the Valparaiso sequence (Ruiz et al., 2017; Caballero et al., 2021). To better document a potential increase in slip rate on the interface and its temporal variation, we have used repeating earthquake and HRGPS positions during the entire sequence, including during the days following the mainshock. Assuming that the repeater rate is directly linked to the slip rate, our results indicate that a transient perturbation of the slip rate begins with the start of the foreshock sequence and decays over days to months without a clear termination. At the first order, the steady decay of the estimated slip rate during the Valparaiso sequence indicates that the mainshock and other large earthquakes have a limited impact on its temporal evolution. Using HRGPS data, we have confirmed the previously reported slow slip during the foreshock sequence and found that it started $\sim$1 day before the first foreshock occurrence. The HRGPS data also indicate a quite steady decelerating westward motion since its emergence before the first foreshock up to 20 days after mainshock (Figure 3.6.1). This steady westward displacement, preceding the mainshock and persisting after it, is broadly consistent with the slip rate inferred from repeaters. This finding supports the idea that the post-mainshock aseismic slip transient may be the continuation of the pre-mainshock slip. Finally,

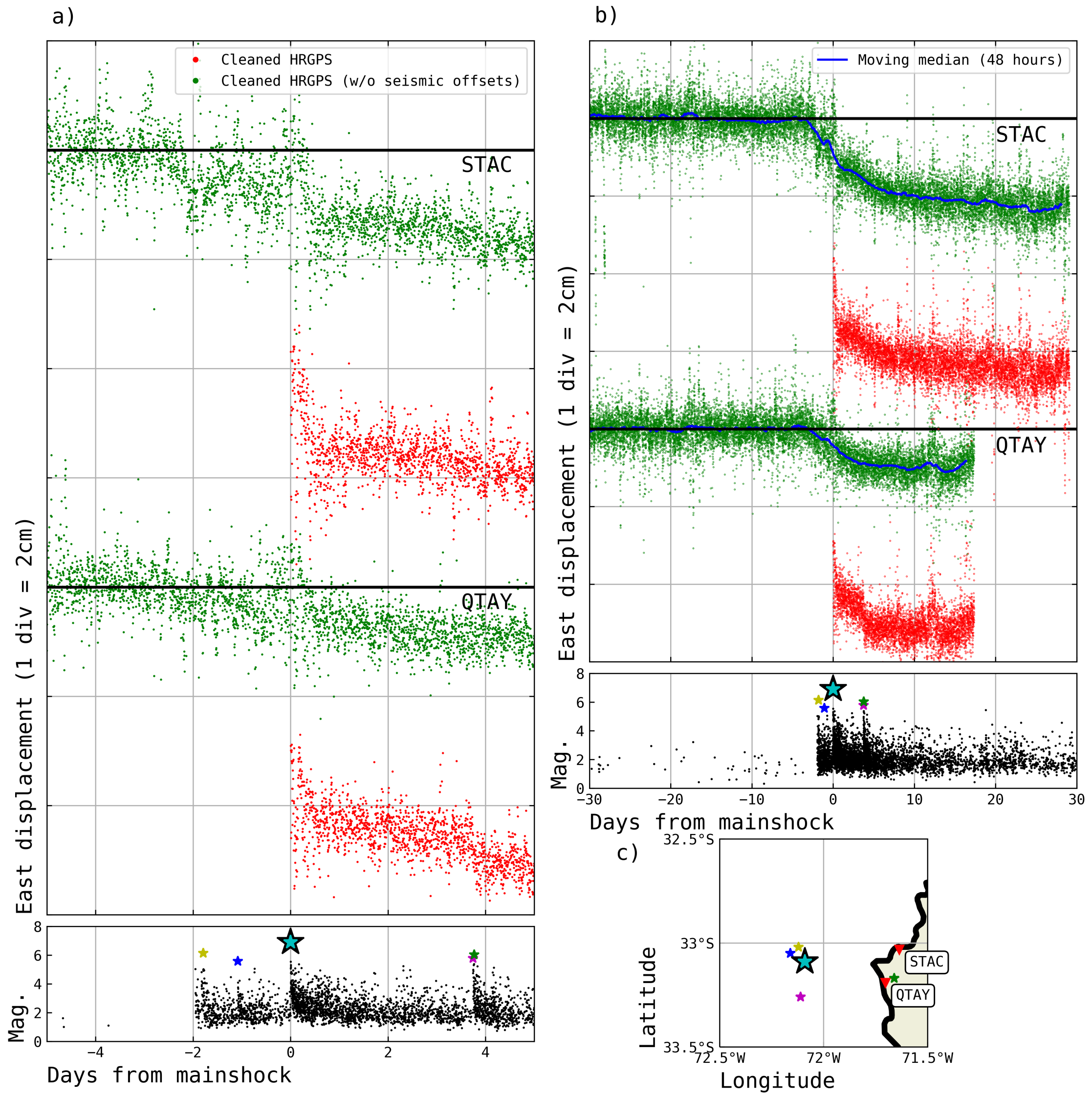

FIGURE 3.6.1: Comparison of high-rate GPS displacements and seismicity evolution before and after the 2017 Valparaiso mainshock. a) Red and green dots indicate cleaned east positions between 5 days before and after the mainshock with and without seismic offsets, respectively, at the two closest sites QTAY and STAC (location shown in c)). Note that STAC is a pseudo-site name assigned to stacked time series of TRPD and BN05 (See text and Figure 3.S.8 for details). Black dots at the bottom panel indicate magnitude of detected seismicity. Notable large earthquakes are marked with stars, epicenters of which are shown in c). b) Same as a) but with data between 30 days before and after the mainshock. A moving median with a window length of 48 hours, calculated from the data without coseismic offsets, is shown in blue for each site. c) Site location (red inverted triangles) and epicenters (stars with corresponding colors with a) and b)). The same figure but for all available HRGPS sites is shown in Figure 3.S.10 for east displacement and 3.S.11 for north displacement.

both the seismicity and the HRGPS observations show no evidence of slip acceleration prior to the mainshock.

In order to compare our different observations, we summarize the results of our 4 analyses in Figure 3.7.1. We observe that the analyzed signals do not perfectly agree with each other and indicate different start and end times of the identified transient. Setting the mainshock time as $t = 0$, the seismicity excess is evidenced from -1.5 to at least 2 days for the ETASI analysis and from -2 to 8 days for the MISD analysis. The repeating earthquakes track a transient aseismic slip since the occurrence time of first foreshock (-2 days) up to months after the mainshock while the HRGPS suggests that the transient aseismic slip initiates at about -3 days (i.e., $\sim$1 day before the first foreshock) and persists at least for 20 days after the mainshock. Such differences originate from different sensitivity of geodetic and seismic observations to interface slip. Our land-based geodetic measurements reflect slip along a large area of the subduction interface. On the other hand, the statistical seismicity analysis is representative of the process taking place only at the location of each earthquake. Repeating earthquakes provide localized, but sparse in-situ measurements of the slip rate on a limited area of the interface (Figure 3.5.2). Defining the exact interplay between all of these observations is challenging. Still, all these signals consistently demonstrate the same sliding behavior on the interface, with an enhanced slip rate extending over several days both before and after the mainshock.

The difference of slip behavior inferred from our various observations may also partly result from uncertainties and hypotheses inherent to each analysis. As earthquakes interact in space, the ETAS and MISD models are often used with a spatial kernel to weight inter-event distances in the aftershock triggering scheme (Zhuang et al., 2011). However, in this study, we focus only on the temporal variations of seismicity, as spatial considerations would likely complicate the aftershock triggering association in a small study area like ours. Because of earthquake location uncertainties due to the geometry of our network, the inter-event distance is not well constrained and may lead to unrealistic event association. Yet, thanks to our spatial selection, the ValEqt seismicity is sufficiently isolated and clustered around the mainshock to be analyzed temporally (see Section 3.3; Figure 3.3.1). We also acknowledge that the repeating earthquake detection and the inferred slip rate is prone to multiple uncertainties. First, the repeating earthquake detection is also impacted by the rate dependent incompleteness mentioned in Section 3.4. As we cannot detect a lot of low magnitude

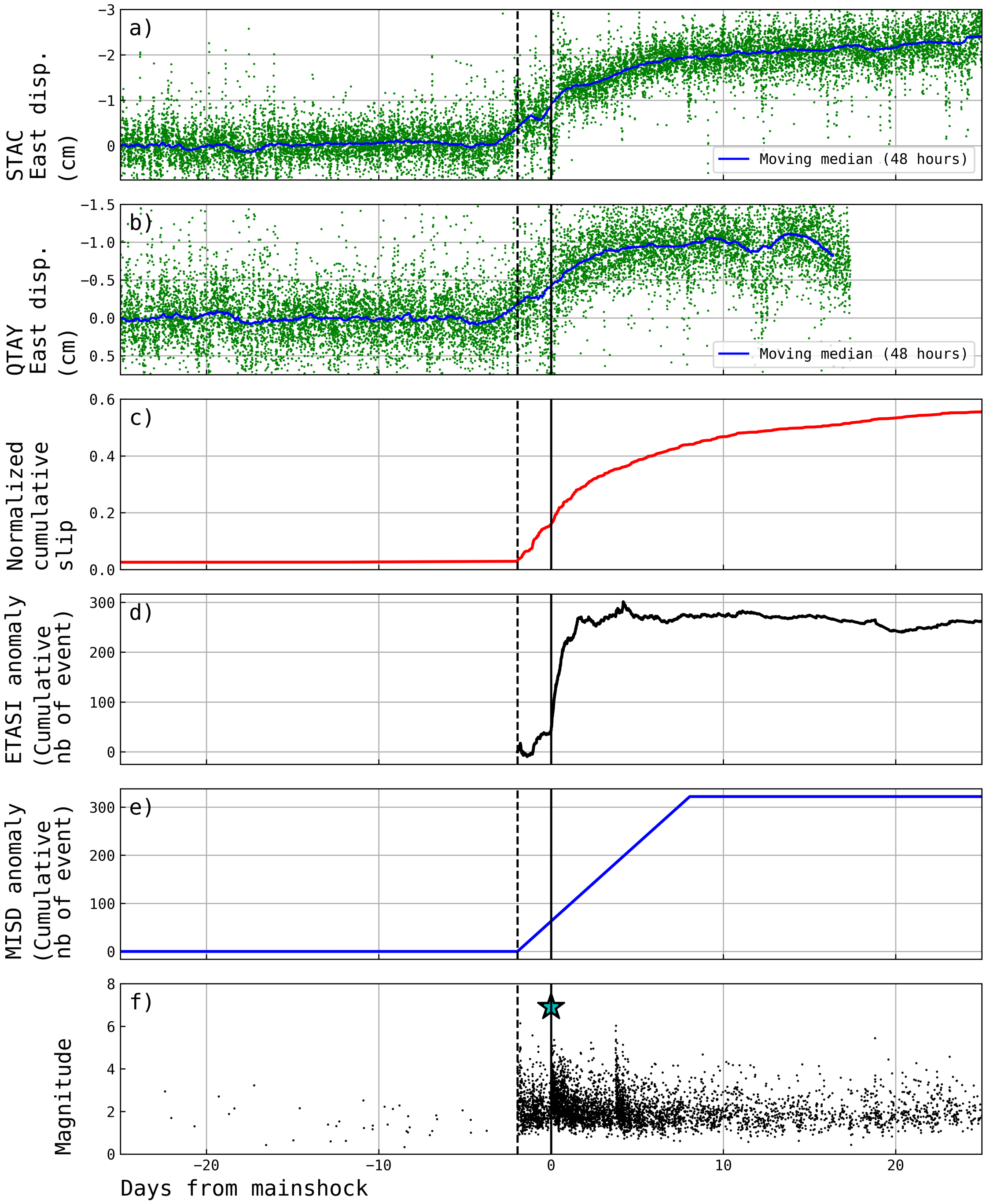

FIGURE 3.7.1: Summary of the seismic and geodetic measurements presented in this study. a-b) Cleaned HRGPS east positions at sites QTAY and STAC with the co-seismic steps removed (see Figure 3.6.1). c) Normalized cumulative slip estimated from repeating earthquake. (see Figure 3.5.1). d) Cumulative number of event unexplained by the ETASI model since the time of the first foreshock (Figure 3.4.1). e) Cumulative number of event triggered by the external forcing in the MISD analysis (see Figure 3.4.3). f) Times and magnitudes of ValEqt earthquakes. The blue star indicates the mainshock.

earthquakes when the seismicity rate is high, we also miss possible repeaters. Such incompleteness may impact the slip rate inferred just after the mainshock and other large earthquakes. Moreover, when the seismicity rate is high, the 40 second cross-correlation window is likely to screen several successive waveforms and further blur the detection of potential repeaters. To evaluate the influence of the window length, we also performed the repeater detection using a smaller cross-correlation windows centered only on the P phases. We obtained more repeater families for the same CC threshold, but with similar conclusions as the ones presented here (see Figure 3.S.15). Second, the repeater rupture sizes and slips are estimated with the standard scaling laws and apriori values (i.e., stress-drop, shear modulus). Using a different scaling law or stress drop (Uchida, 2019; Nadeau & Johnson, 1998; Hanks & Bakun, 2002) yield slightly different repeater families and absolute slip estimates, but still we can draw similar conclusions (see Table 3.S.2 and Figure 3.S.16). In order to minimize the influence of these choices, we focus our analysis of slip only on its temporal evolution pattern and not on its absolute amount. Finally, to support our current selection criteria for the co-location of our repeaters (i.e., 80% chance of intersecting rupture front, taking into account relocation uncertainties), we also performed a more selective screening process based on the percentage of rupture overlap between repeaters. Because the relocation uncertainties from HypoDD are found to be significantly smaller than the average circular fracture radii of our repeaters (see Figure 3.S.17), we neglect here relocation uncertainties. From the relocated hypocenters and their circular rupture area, we calculate the percentage of overlap between rupture patches for each earthquake pair within families and discard events that have less than 80% overlap with all other rupture areas in the family. The resulting repeater selection and aseismic slip estimate are almost unchanged and lead to similar conclusions (see Figure 3.S.18), which support our initial selection criterion. The HRGPS data contains noise inherent to the processing strategy, which were not completely removed in this study. The remaining noise limits the possibility to capture second order features of the slab interface processes, such as an accelerated slip just before the mainshock. Moreover, our HRGPS displacements can contain seismic slip contributions (Caballero et al., 2021). However, Caballero et al. (2021) found that the contribution of $M<6$ earthquakes to GNSS displacements is very limited, even when accounting for the cumulative moment induced by micro-earthquakes. Therefore, after removing the co-seismic offset of the mainshock and the offsets induced by other large earthquakes, it is reasonable to assume that our HRGPS displacements predominantly represent the contribution of aseismic slip.

In spite of the aforementioned limitations, our observations bring new insights on the possible mechanisms that have driven the 2017 Valparaiso seismic sequence. We show that both the transient aseismic slip and the seismicity excess are not restricted to the foreshock sequence but persist after the mainshock for several days. Repeating earthquakes along with HRGPS time series indicate a continuous aseismic slip transient before and after the mainshock with no significant jump in the slip rate and direction at the time of the mainshock (Figures 3.7.1.a-b), although an acceleration related to afterslip would have been expected after earthquakes with M$\sim$7 or greater (Marone et al., 1991; Miura et al., 2006; Periollat et al., 2022). Although Figure 3.7.1.c depicts slip and displacement variations associated with large earthquakes in the Valparaiso sequence, these temporal changes are small compared with the long-term transient starting before and persisting after the mainshock. This relative continuity of the aseismic transient raises the question of whether the pre- and post-mainshock processes should be interpreted as a single process or as two distinct fault processes that are separated by the mainshock. The commencement of an afterslip with a similar slip rate as the slow slip rate observed immediately before the mainshock seems quite unlikely. In addition, if the post-mainshock aseismic slip is only an afterslip triggered by the mainshock and distinct from the pre-mainshock aseismic slip, we may expect it to approximately scale with the mainshock magnitude (Alwahedi & Hawthorne, 2019; Churchill et al., 2022) and with the aftershocks activity (Hsu et al., 2006; Perfettini & Avouac, 2007; Perfettini et al., 2018). Therefore, it does not explain why we still observe a seismicity excess after the Valparaiso mainshock, that is quite over-productive given the mainshock magnitude (see Section 3.4). Our observations may rather suggest a unique transient aseismic process persisting during the whole sequence, with very little slip-rate fluctuation induced by large earthquakes. This interpretation of persisting slow slip event is consistent with observations of a continuously enhanced foreshock and post-mainshock seismicity previously reported by Marsan et al. (2014). They showed that worldwide mainshocks preceded by an enhanced foreshock seismicity are also associated with an over-productive aftershock activity and likely requiring an external triggering process such as aseismic slip transient or/and fluid migrations that occur before and after the mainshock occurrence.

Observed precursory aseismic slip is sometimes interpreted as a nucleation phase of the mainshock slowly accelerating toward dynamic rupture by referring to experimental and numerical simulation studies (Das & Scholz, 1981; Dieterich, 1992; Ampuero & Rubin, 2008; Ohnaka, 1992; Latour et al., 2013). In this model, monitoring foreshocks (small asperities loaded by the slipping interface) and the aseismic slip may help to track the ongoing rupture and carry a strong predictive power on the subsequent mainshock occurrence. In the case of the 2017 Valparaiso earthquake, however, there is no clear evidence that pre-mainshock seismic and aseismic processes culminate with the mainshock but rather seems to persist after it. Therefore, they probably cannot be interpreted as a tracer of an accelerating pre-slip nucleation phase. Our results rather indicate that the transient aseismic slip is not directly linked to the occurrence of the mainshock rupture, but acts as an aseismic loading of locked asperities on the fault, and potentially triggering them (Meng & Duan, 2022). Large earthquakes triggered by aseismic loading processes have already been observed in several regions that are frequently associated with slow slip events. Radiguet et al. (2016) showed that recurrent slow slip events with no subsequent large earthquakes was observed on the same interface for years, just next to a large locked asperities, but it finally triggered the 2014 $M_w = 7.3$ Papanoa earthquake. Interestingly, the results of Radiguet et al. (2016) show a slight acceleration of displacements following the Papanoa mainshock, which remain small compared to the overall amplitude of the SSE. Similar recurrent slow-slip observations were associated with the triggering of the 2012 $M_w = 7.6$ earthquake in Costa Rica (Voss et al., 2018) or the 2020 $M_w = 6.9$ mainshock in the Atacama region in Chile (Klein et al., 2023), that was also followed with unusually large post-seismic displacements. There are also numerous examples of slow slip events that have been associated with seismicity swarms but not followed by a large mainshock (Lohman & McGuire, 2007; Vallée et al., 2013; Nishikawa et al., 2021). The complex interactions between slow slip and large earthquakes, as evidenced by all these observations, indicate that a transient aseismic slip alone cannot reliably serve as an indicator of an impending mainshock. For the Valparaiso 2017 sequence, the aseismic slip transient initiated just before the first foreshock, may have loaded asperities of the fault plane, triggering seismicity until several days after the mainshock. It suggests that the Valparaiso mainshock behaves as any other seismic asperities, with a probability of occurrence simply mediated by the transient aseismic slip loading. Therefore, to properly address the precursory nature of unusual aseismic and seismic activities, our results suggest that earthquake sequences need to be continuously analyzed, including both foreshock to post-mainshock observations. Although this model may not appears as deterministic as the nucleation phase model, the real-time monitoring of transient aseismic slip and enhanced seismicity can still provide useful additional information about the state of seismic hazard on aseismically slipping faults.

3.S Supporting Information for "Evidence of a transient aseismic slip driving the 2017 Valparaiso earthquake sequence, from foreshocks to aftershocks"

3.S.1 ETAS-I Synthetic tests

To support the significance of the transient seismicity observed in the vicinity of the mainshock in section 3.4, we perform the same analysis over synthetic catalogs. Synthetic catalogs follow the ETASI model (as defined in the main text), but contain a transient background seismicity somewhere in time in addition to the stationary background rate μ. We generate a synthetic catalogs as follow:

1. We first draw true background events over 5-years from a stationary Poisson process of rate μ.
2. In addition to this stationary background seismicity, we add a transient background seismicity comprising 300 events after a start time T_0. The 300 waiting times after T_0 are drawn from an exponential distribution with an expected value $\lambda = 5$ days.
3. We draw all magnitudes independently from the G-R law.
4. We generate cascade of aftershock sequences for all background events following the ETAS model (Zhuang & Touati, 2015).
5. We build the short-term incompleteness by removing events hidden by T_b (Hainzl, 2021).

The resulting catalog contains magnitude-dependent aftershocks and stationary background events consistent with our ETASI model but also 300 transient background events after T_0. The ETASI parameters $(A, c, p, \alpha, \mu, b, T_b)$ used for the simulation of the stationary background rate and aftershock sequences are the one extracted from the ValEqt catalog. We present an example of a synthetic catalog on figure 3.S.5.

We perform the same seismicity analysis described in section 3.4 but with synthetic catalogs previously generated and try to recover the transient background signal we added. As for ValEqt, we first extract from the synthetic catalogs, the best-fitting parameters of the ETASI model fixing $\alpha = \beta$. Then, thanks to the transformed time analysis, the synthetic seismicity is tested with respect to predictions. Figure 3.S.5.c-d shows that we recover a significant difference between the synthetic seismicity and the best-fitting ETASI prediction, exactly at the time of the transient background rate. We observe the same three regimes of seismicity as observed in the ValEqt analysis: A slight deficit of seismicity for the two time-periods outside of the transient and a significant excess of seismicity within the transient. Note that the number of earthquakes in excess is consistent with the 300 transient events added during the simulation. This support the hypothesis that a non-stationary transient background rate can be detected by identifying breaking point in the transformed time analysis. It also shows that a transient background seismicity bias the parameter estimation of the ETASI model. The seismicity outside the transient is in deficit compared to the best-fitting ETASI parameters, even if during these ranges earthquakes can be fully explain the ETASI parameters extracted from ValEqt. We find that the parameter estimation of A is biased toward a higher value than the one used for the simulation. This is because the model is trying to include a maximum of the non-stationary transient events in the aftershock triggering scheme to reduce at best the seismicity excess. It increases the aftershock productivity of the best-fitting ETASI parameters at the cost of stationary times.

3.S.2 MISD synthetic tests

Our modified MISD model contain an additional triggering kernel expected to capture earthquakes not explained by a magnitude-dependent triggering scheme. To support our modified MISD model and test its ability to capture the transient non-stationary seismicity at proximity to the mainshock, we perform the same analysis over synthetic catalogs. We use two sets of synthetic catalogs generated according to the ETAS model:

1. 100 synthetic catalogs containing a transient background seismicity in addition to the stationary background rate.
2. 100 synthetic catalogs with no transient seismicity.

The synthetic catalogs are generated following the method described in ETASI synthetic test section, with or without the transient after T_0. Here, (1) tests the ability of the external triggering kernel to recover a non-stationary transient. (2) ensure that the external kernel don't capture any seismicity when there is no anomaly. For the ValEqt catalog, the start point of the external triggering kernel of the MISD model was a-priory pinned with the start of foreshock sequence to further study the transient seismicity previously highlighted the ETASI analysis. For synthetic catalogs we a-priory pin the transient start point as follow: For (1), the start point of the MISD external triggering kernel is set at the beginning of the transient, as if it was previously detected by an ETASI analysis (see ETASI synthetics test). For (2), as their is no transient, we pin the kernel start 2 days before the largest magnitude of the catalog, to mimic the settings of the Valparaiso foreshock sequence.

We present in Figure 3.S.7 the cumulative count of earthquake declustered by the MISD analysis for the 2 test sets . Declustered events include background events and those associated with the external triggering process. MISD results of the two synthetic case (1) and (2) are present in Figure 3.S.7.a and b, respectively. For (1), we shows that the declustering is recovering both stationary background events and the 300 transient background events. For (2), the external kernel do not gather any earthquakes and we only recover the stationary background rate. It shows that the external triggering kernel is only able to extract a seismicity that is not explained by a magnitude-dependent triggering process or a stationary background rate. If the catalog is fully explained by a magnitude-dependent triggering process, the external kernel rate and length reduce to zero.

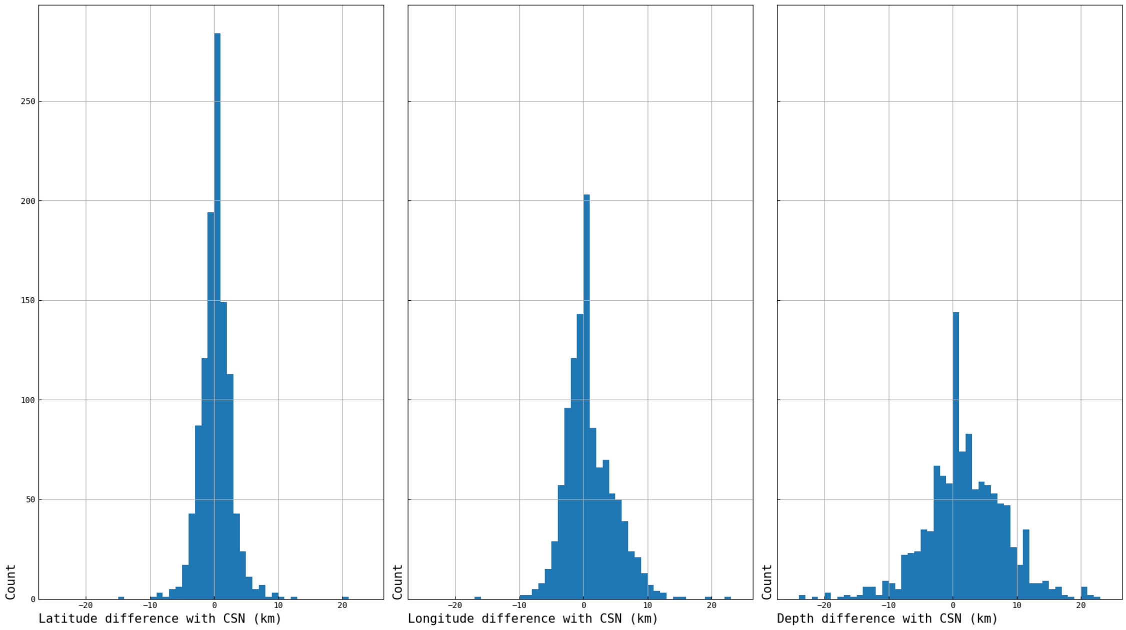

FIGURE 3.S.1: Differences in earthquake locations between the ValEqt catalog and the CSN catalog.

TABLE 3.S.1: Parameters and AIC estimates of ETASI inversions

Model	T_{end} (days)	μ_2 (event/day)	Magnitude mainshock	AIC
ETASI	–	–	6.9 (fixed)	-13249.6
ETASI + μ_2	480.85314	76.12	6.9 (fixed)	-13309.3
ETASI + μ_2 + Free mainshock	480.85314	87.3	8.2 (free)	-13461.7

TABLE 3.S.2: Repeater detection as function of the stress drop used in the circular crack model

Stress Drop $\Delta\sigma$	Number of repeater families	Total number of repeaters
1 MPa	347	1190
3 MPa	343	1171
10 MPa	333	1131

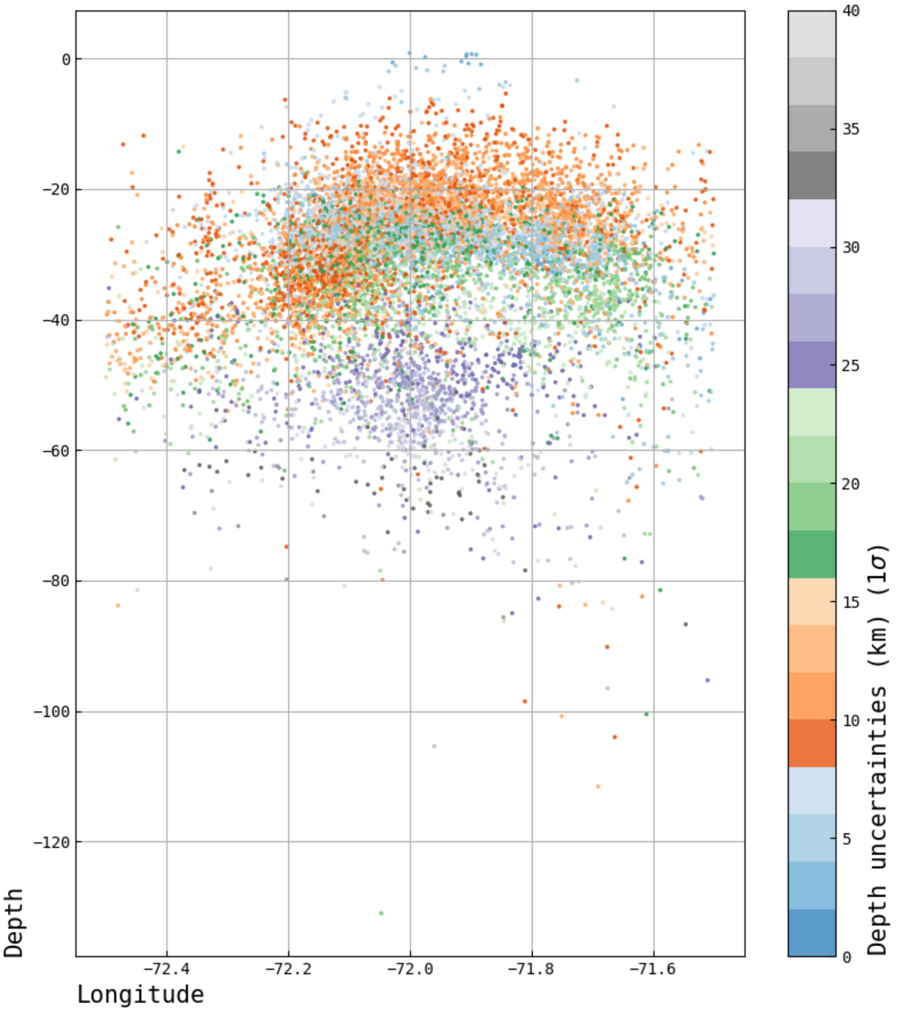

FIGURE 3.S.2: Vertical dispersion of earthquakes of the ValEqt catalog against depth location uncertainties.

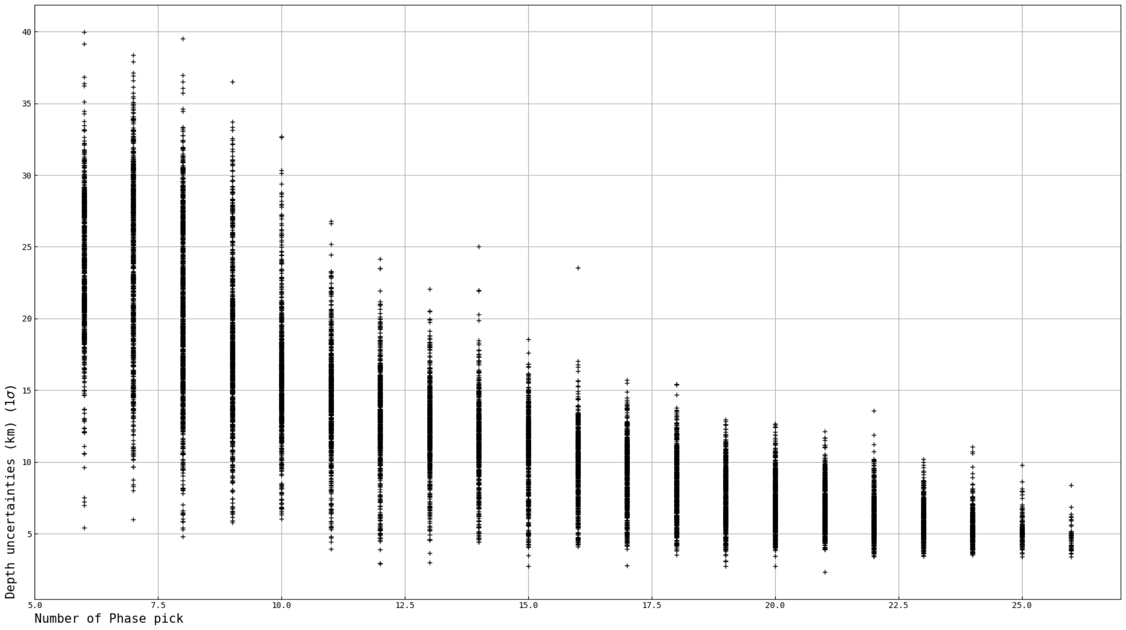

FIGURE 3.S.3: Depth location uncertainties against the number of phase picks

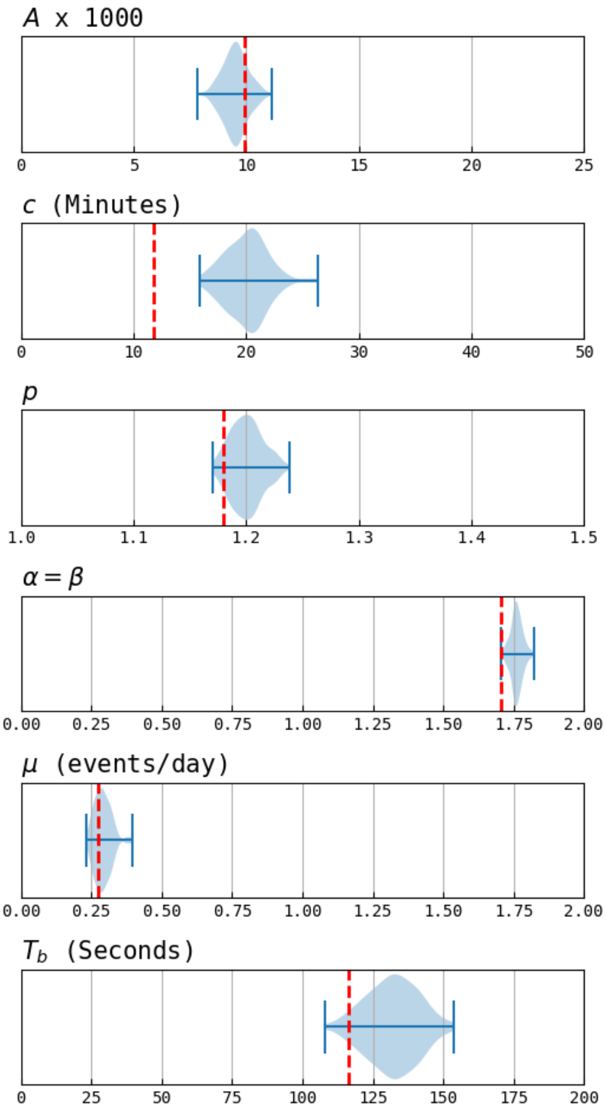

FIGURE 3.S.4: Maximum likelihood estimation of the parameters of 100 synthetic catalogs following the ETASI model. Red vertical dotted lines are the true ETASI parameters used for the generation of the synthetics catalogs.

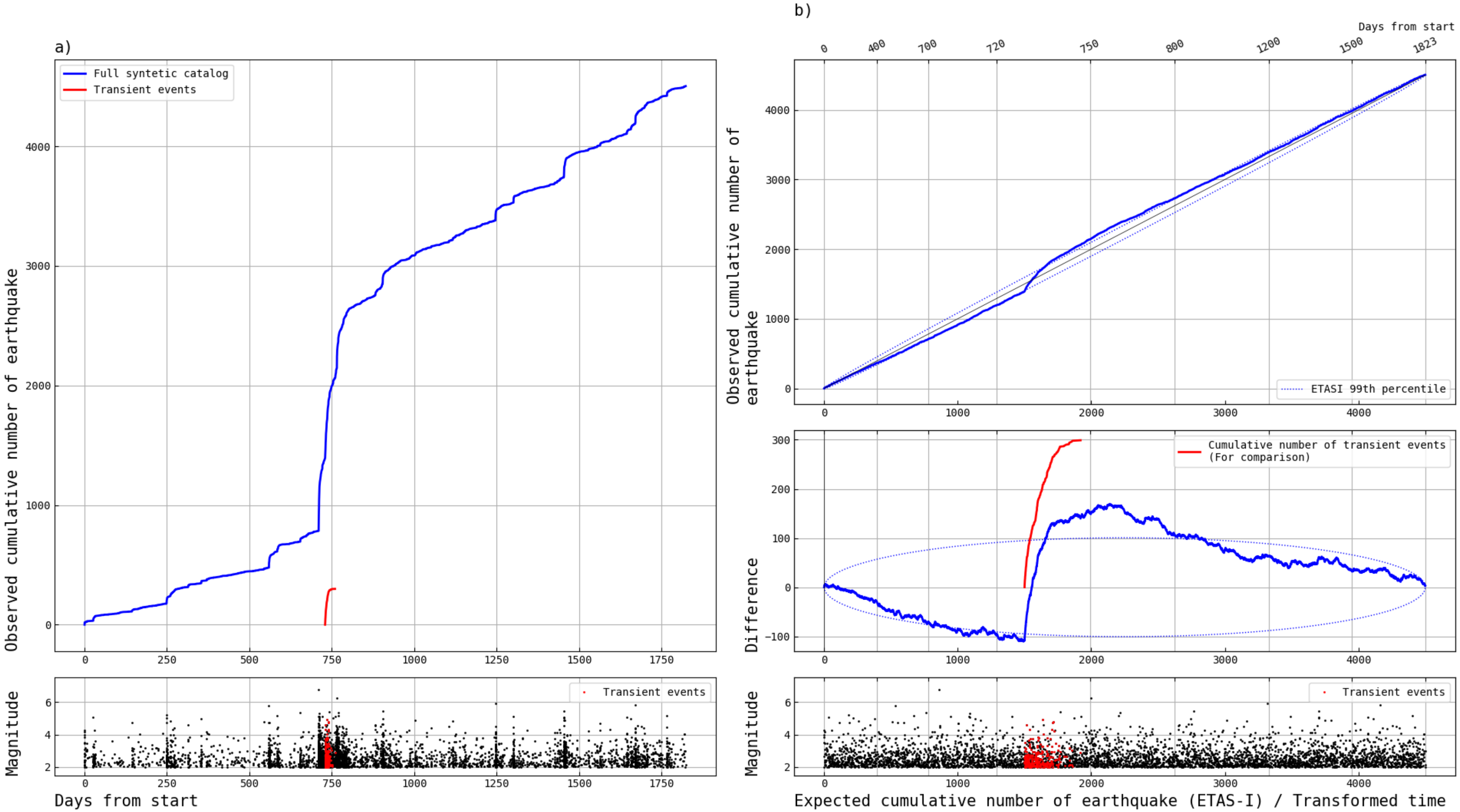

FIGURE 3.S.5: ETASI seismicity analysis over a synthetics catalog following the ETASI model but including a transient non-stationary background rate. (a) (Blue) Time-evolution of the cumulative number of earthquakes in the synthetic catalog. (Red) Cumulative number of the non-stationary background event in the synthetic catalog. Bottom subplot is the time and magnitude of the synthetic catalog. The bottom subplot (black dots) is the time-magnitude evolution of the ValEqt catalog. (b) Cumulative number of earthquakes observed in the synthetic catalog against the cumulative number of earthquakes predicted by the best fitting ETASI model. Blue dotted lines shows the ETASI 99^{th} percentile confidence interval. This x-axis representation of time is knows as the transformed time analysis Ogata, 1988. The middle subplot is the difference between the observed and expected cumulative number of earthquake in the transformed time domain. (Red) Cumulative number of the non-stationary background event in the transformed time domain. We observe a significant seismicity excess compared to the best fitting ETASI model exactly where we added the transient non-stationary background event. Bottom subplot show the magnitudes of the synthetic catalog in the transformed time domain.

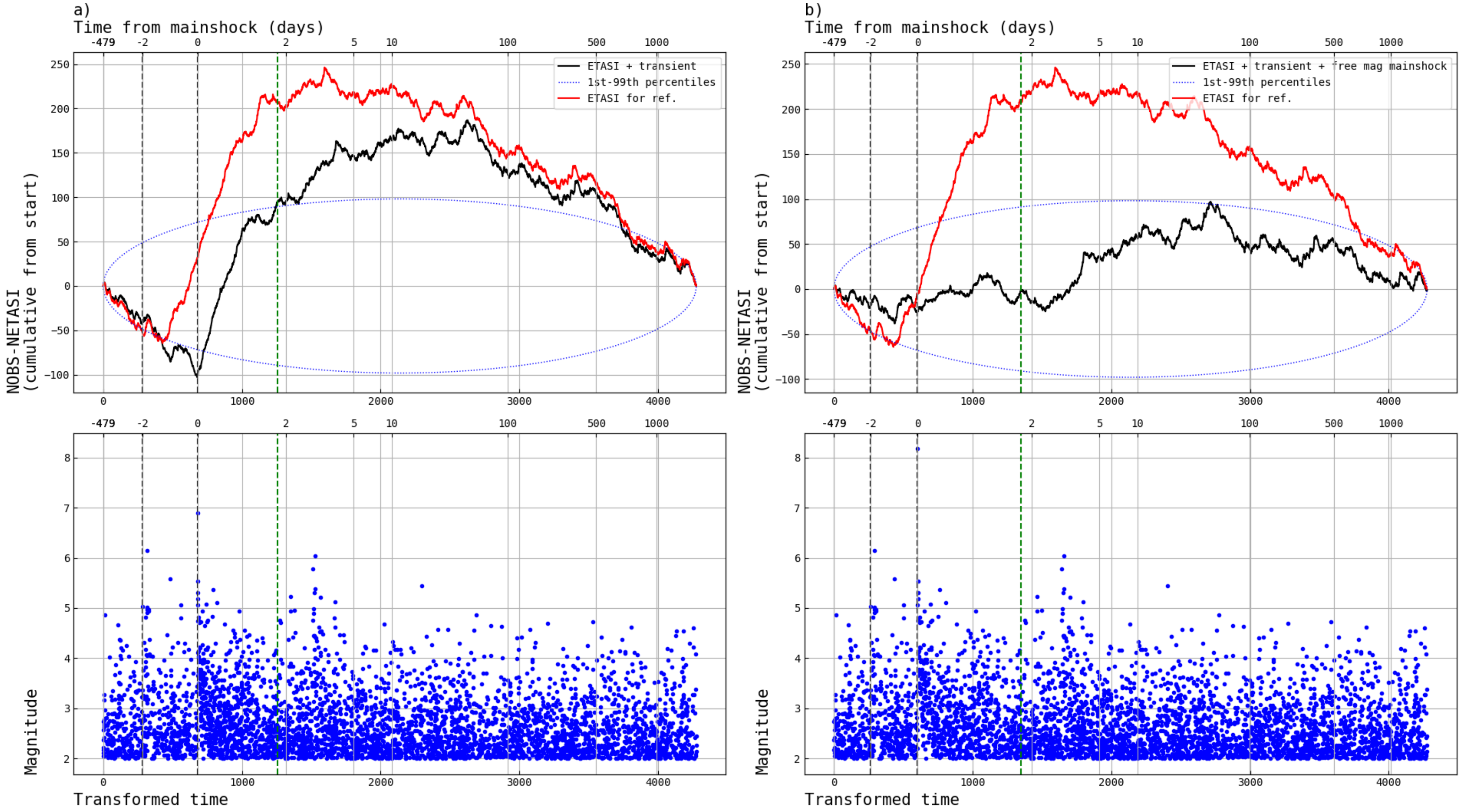

FIGURE 3.S.6: (a) Transformed-time analysis with a modified ETASI model that include an additional constant rate from the first foreshock up to T=480.8 days. (b) Transformed-time analysis with a modified ETASI model that include an additional transient constant rate from the first foreshock up to T=480.8 days and a free magnitude for the mainshock. The top subplot is the difference between the observed and expected cumulative number of earthquake in the transformed time domain. The bottom subplot is transformed time vs magnitudes. Vertical black dotted line are the first foreshock and the mainshock respectively. Vertical green dotted line is the end of the transient constant rate from the first foreshock.

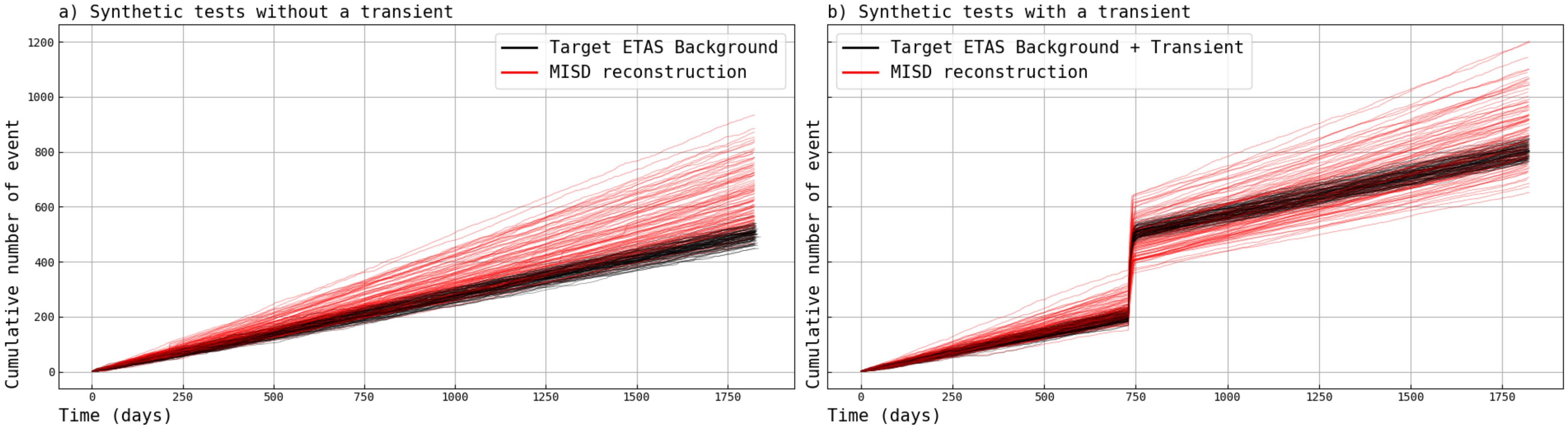

FIGURE 3.S.7: MISD seismicity analysis over 100 synthetics catalog following the ETASI model but including a transient non-stationary background rate. (a) Cumulative number of background earthquake declustered by the MISD procedure over 100 synthetic catalog with no transient. (b) Cumulative number of background earthquake declustered by the MISD procedure over 100 synthetic catalog containing a transient background seismicity. When there is a transient, our MISD model is able to recover both stationary background events and the transient background events. When there is no transient, MISD model is only recover the stationary background events.

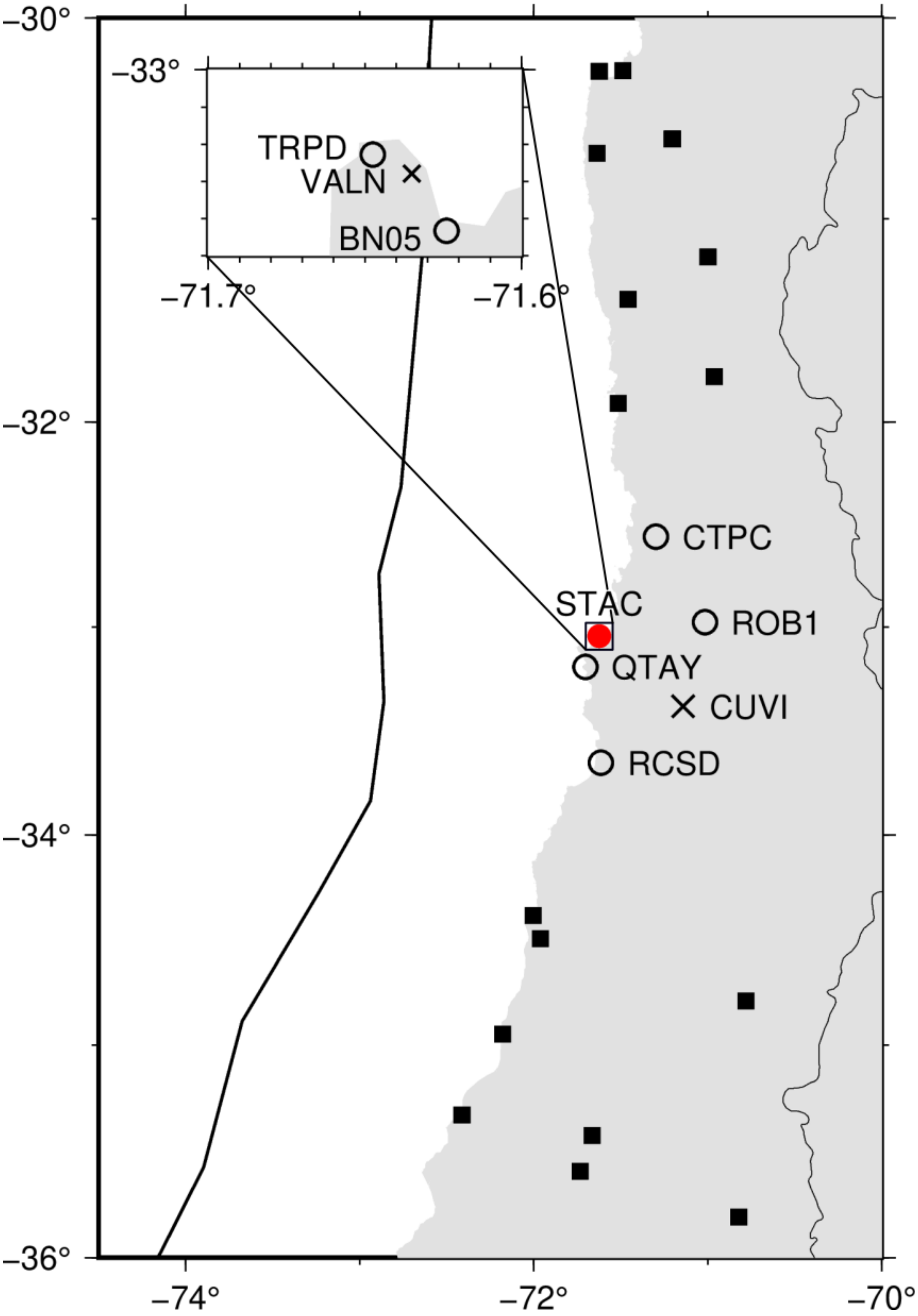

FIGURE 3.S.8: GPS site location (site names labeled). Open circles and crosses indicate sites used and not used for this study, respectively. A red dot indicates a site STAC which is a pseudo-site to represent stacked time series of TRPD and BN05 shown in the inset (See main text and Figures 3.6.1, 3.S.10, and 3.S.11 for details). Solid squares indicate sites used for common mode filter construction.

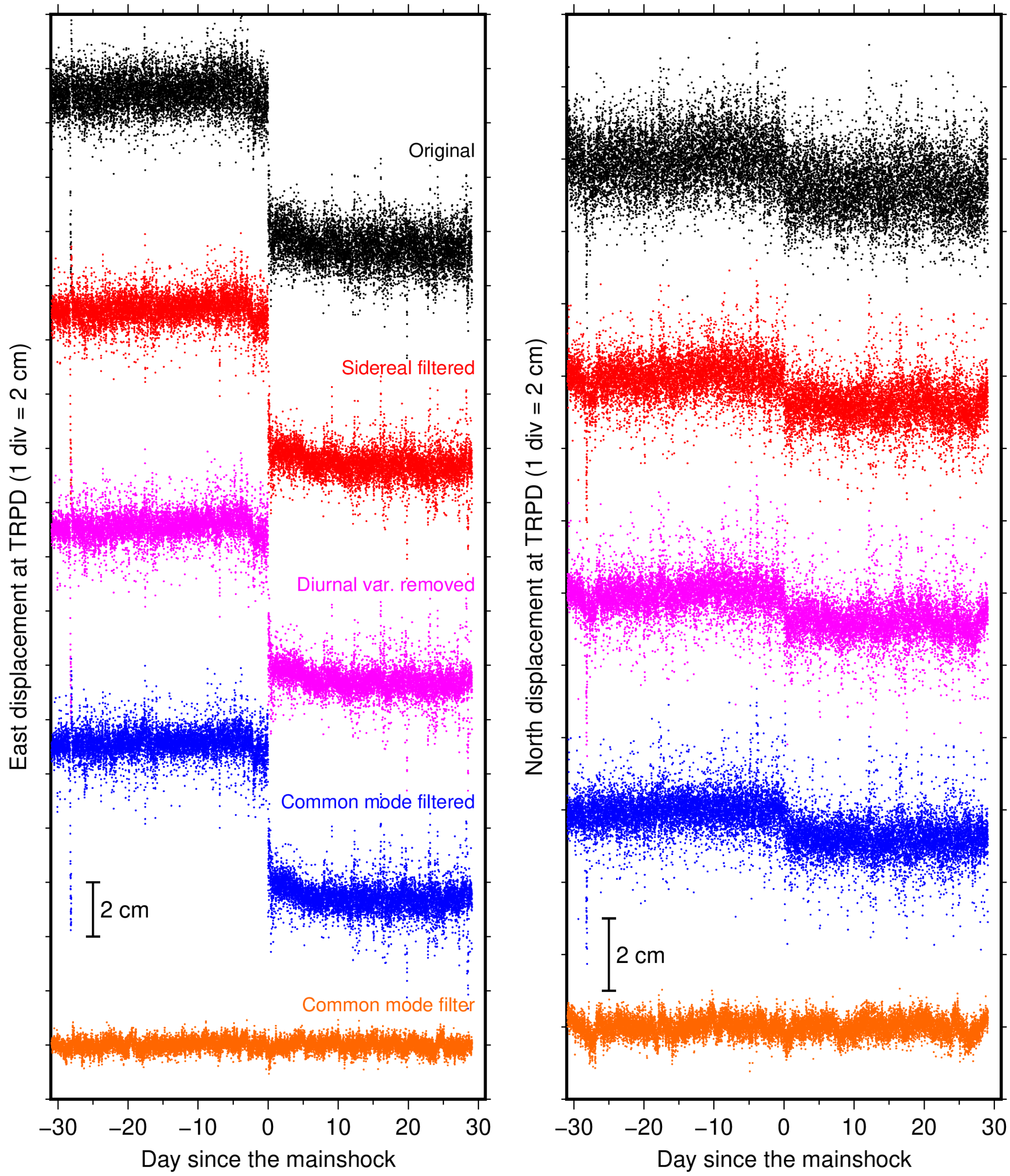

FIGURE 3.S.9: Example of high-rate GPS post-processing at site TRPD (Figure 3.S.8) for east (left) and north (right) components. Black dots indicate high-rate GPS coordinates fixed to South American plate reference system. Red, purple, and blue dots indicate those after multipath effects, diurnal variation, and common mode fluctuation removals, respectively (See main text for details). Orange dots indicate a common mode filter.

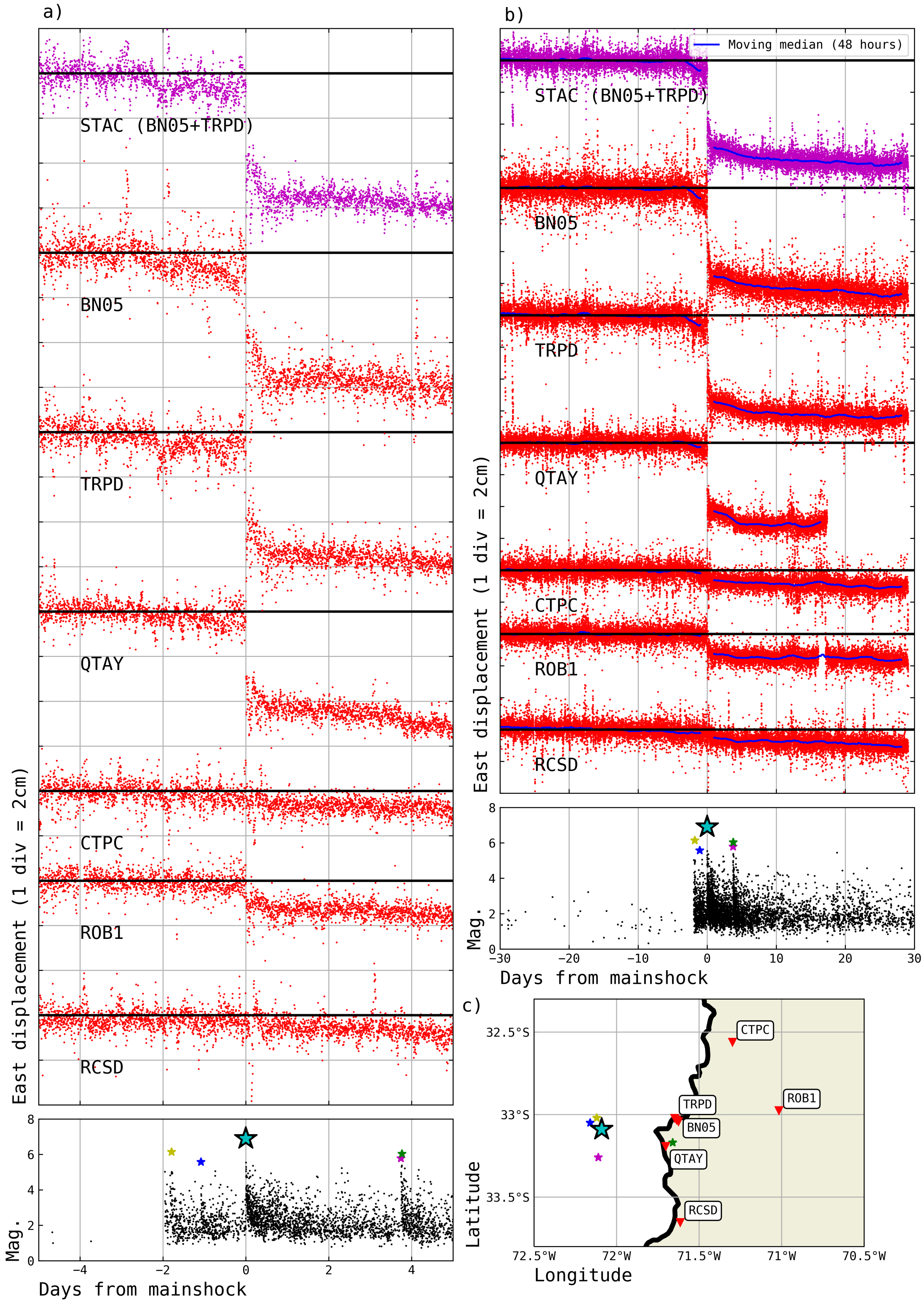

FIGURE 3.S.10: Comparison of high-rate GPS displacements and seismicity evolution before and after the 2017 Valparaiso mainshock. a) Red dots show cleaned east positions between 5 days before and after the mainshock at the two closest sites QTAY and STAC (location shown in c)). Note that STAC is a pseudo-site name assigned to stacked time series of TRPD and BN05 (See text and Figure 3.S.8 for details). Black dots at the bottom panel indicate magnitude of detected seismicity. Notable large earthquakes are marked with stars, epicenters of which are shown in c). b) Same as a) but with data between 30 days before and after the mainshock. A moving median with a window length of 24 hours is shown in blue for each site. c) Site location (red inverted triangles) and epicenters (stars with corresponding colors with a) and b)).

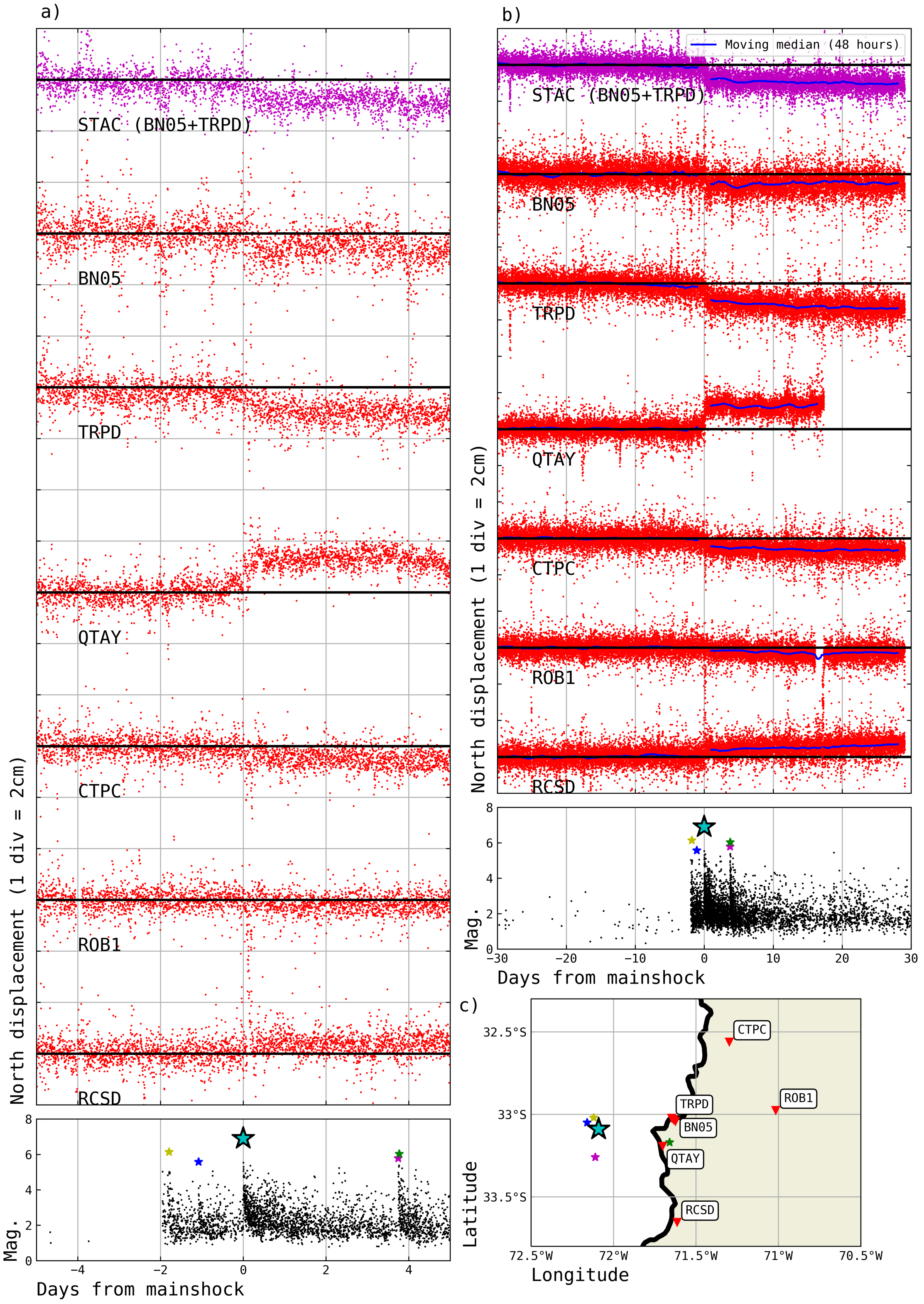

FIGURE 3.S.11: Same as Figure 3.S.10 but for north displacements.

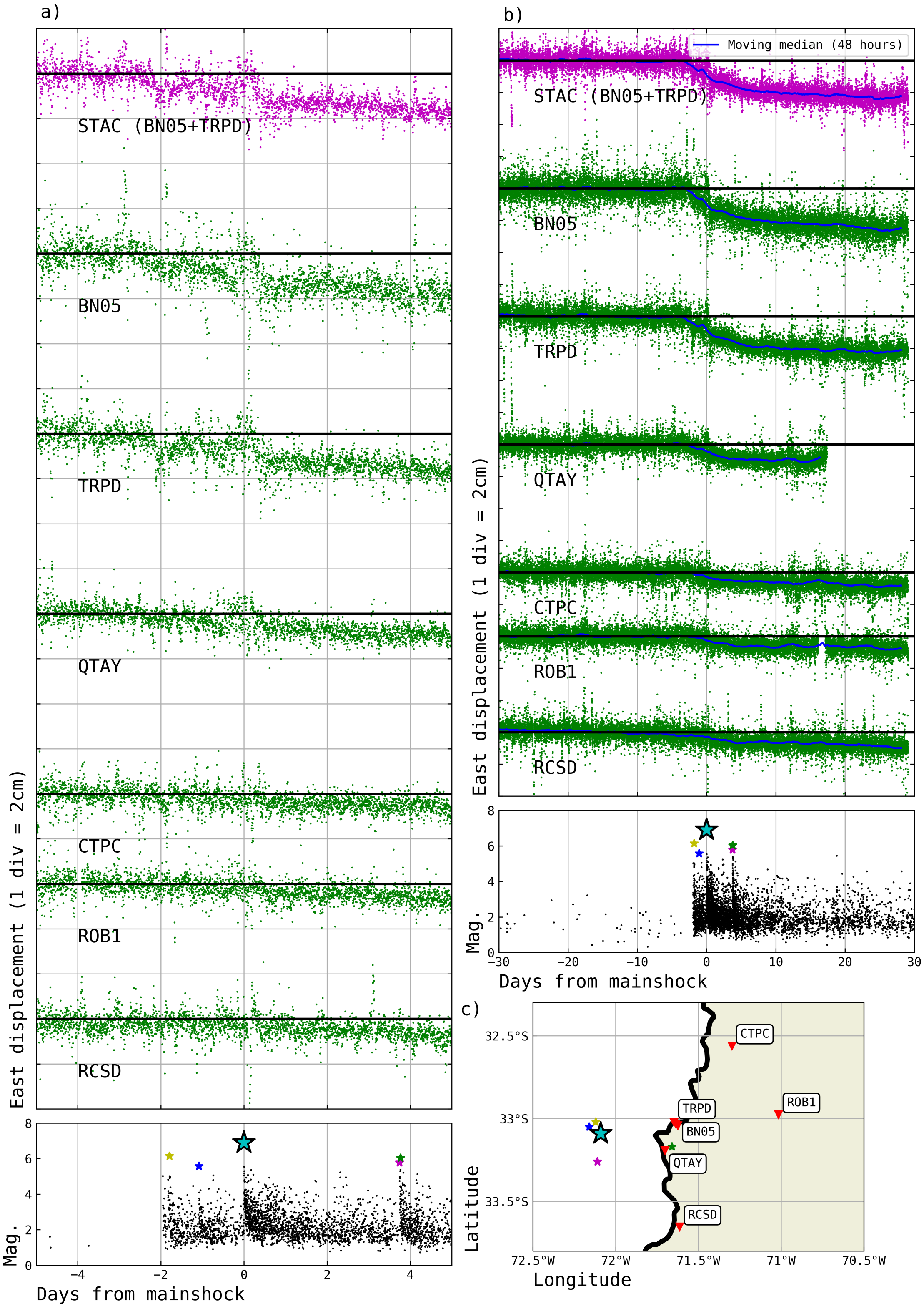

FIGURE 3.S.12: Same as Figure 3.S.10 but without co-seismic steps.

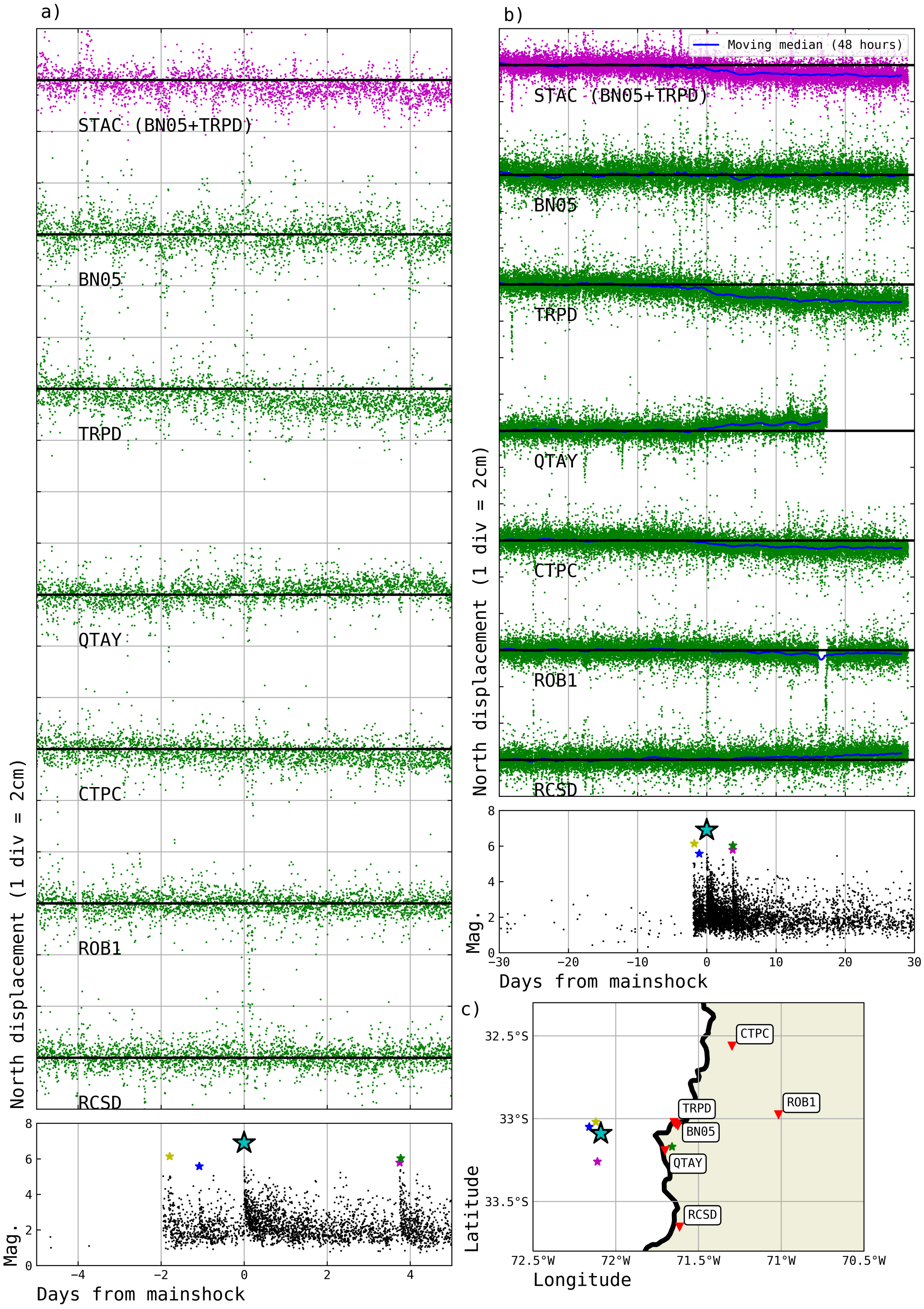

FIGURE 3.S.13: Same as Figure 3.S.11 but without co-seismic steps.

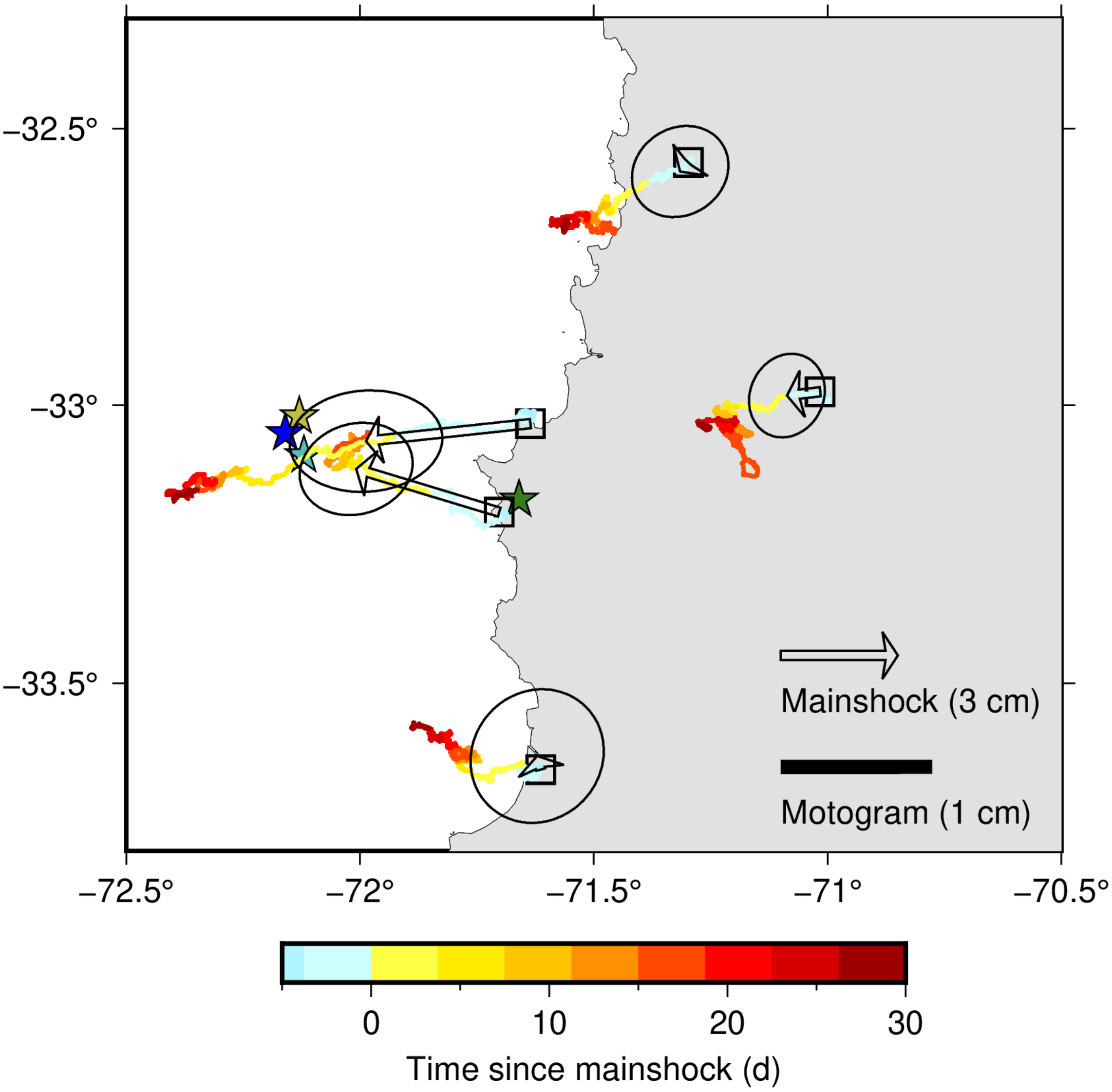

FIGURE 3.S.14: Motogram of GPS site motions during the Valparaiso sequence (color dots). Open arrows indicate the mainshock coseismic displacements.

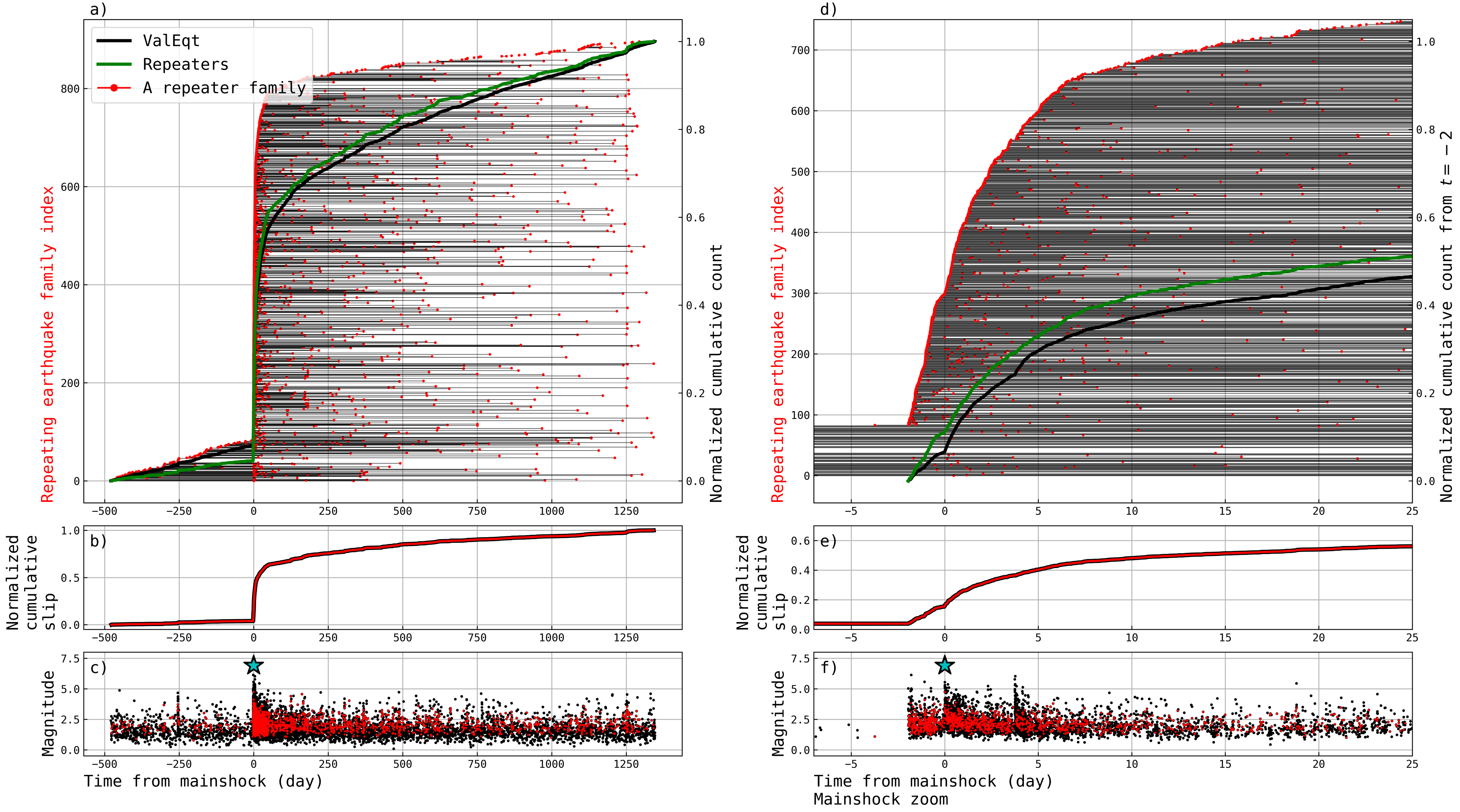

FIGURE 3.S.15: (a) Families of repeating earthquake detected in the ValEqt catalog but using a cross-correlation window centered only on the P phase. A horizontal black line represent one family by connecting the repeating earthquake (red dots). The green and black curves is the normalized cumulative number of repeaters and ValEqt earthquakes respectively. (b) Normalized cumulative slip estimated from repeating earthquakes. (c) Times and magnitudes of ValEqt earthquakes (black dot) and repeating earthquakes (red dot). The blue star indicate the mainshock. (d, e and f) Same as (a, b and c) but zoomed in the vicinity of the mainshock time. Note that the normalized cumulative count of repeaters and ValEqt earthquake start at t=-2 days in (d).

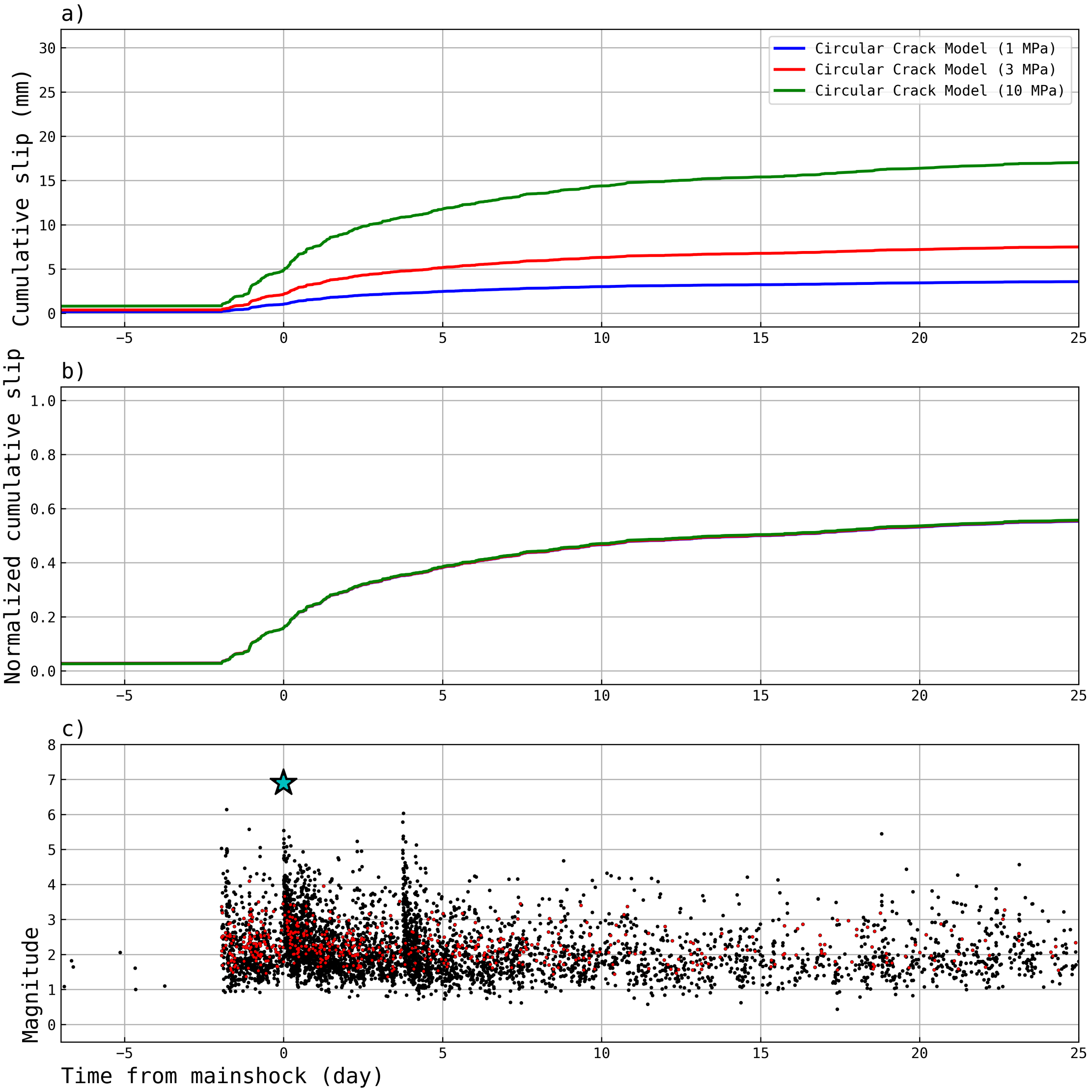

FIGURE 3.S.16: Aseismic slip estimate from repeating earthquakes as function of Stress Drop (Circular Crack model). (a) Absolute slip estimate. (b) Normalized slip estimate. (c) Times and magnitudes of ValEqt earthquakes (black dot) and repeating earthquakes (red dot). The blue star indicate the mainshock.

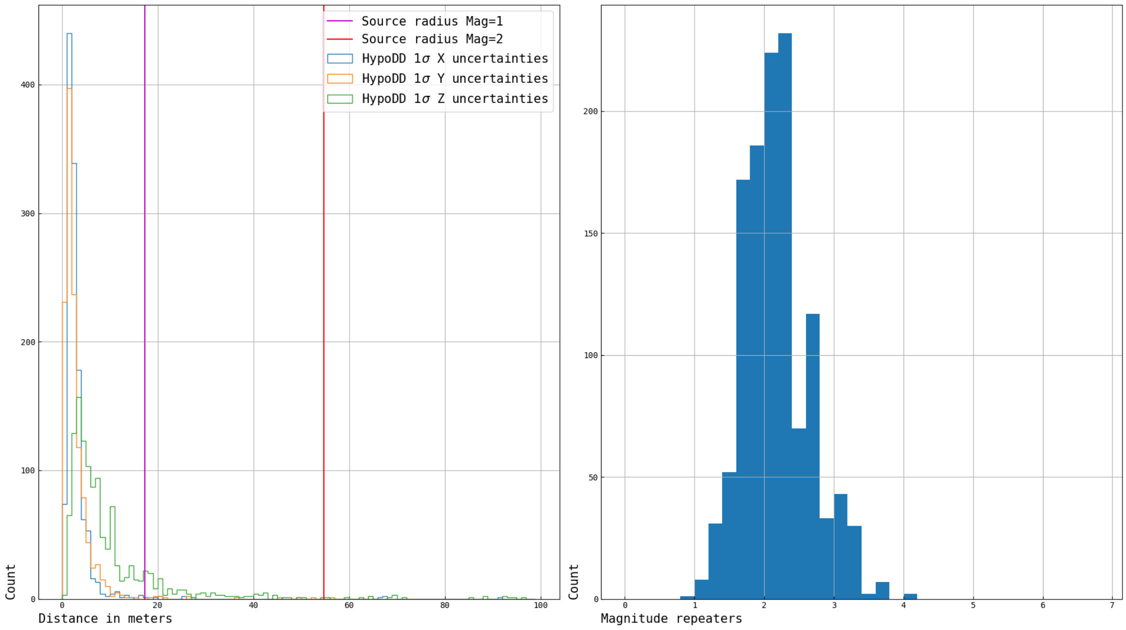

FIGURE 3.S.17: HypoDD relocation uncertainties (left) and magnitude distribution of the repeaters (right). For reference, we show on the left the typical source radius of M=1 (purple) and M=2 (red) earthquakes for a stress drop of 3MPa

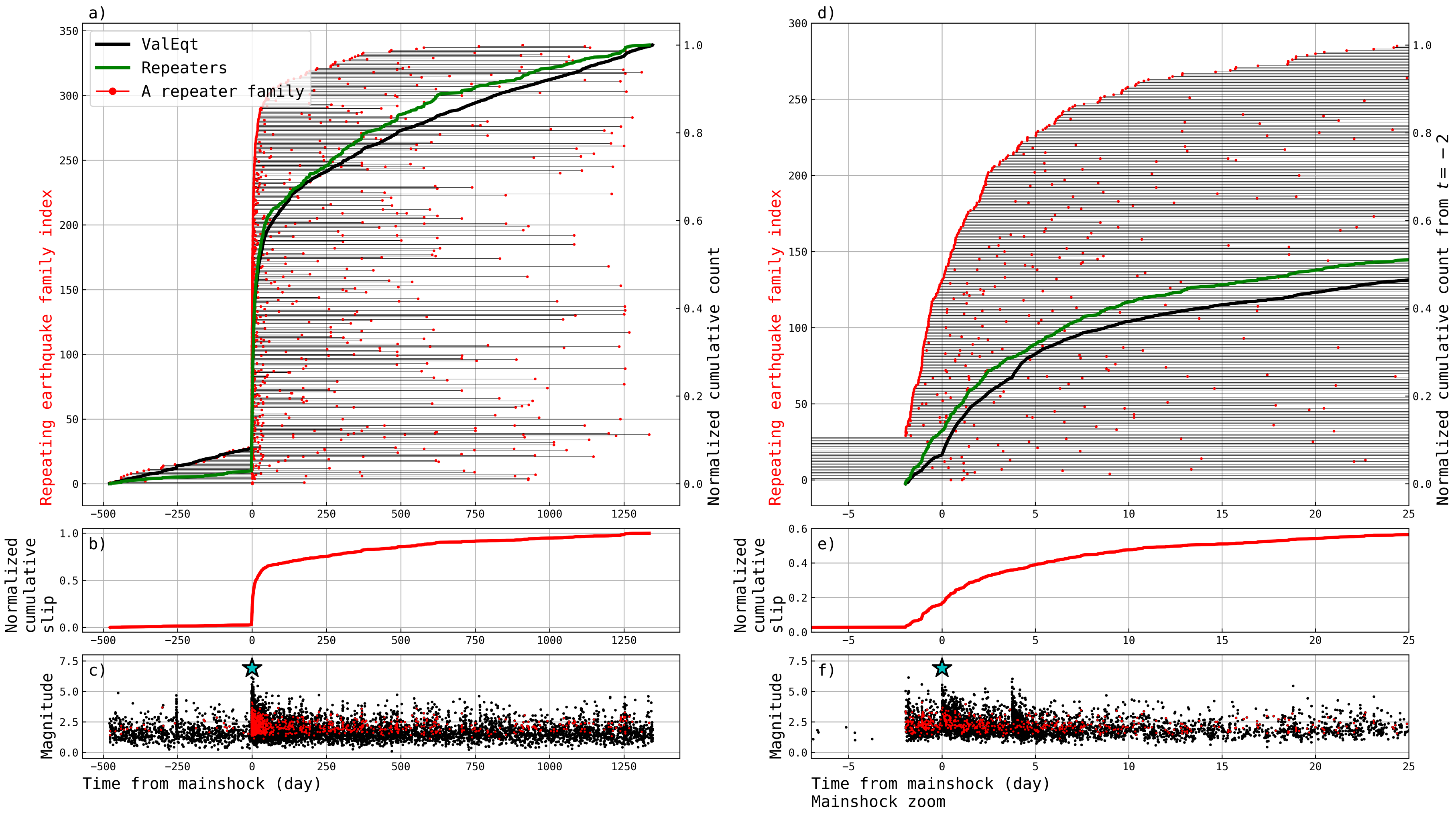

FIGURE 3.S.18: (a) Families of repeating earthquake detected in the ValEqt catalog but using a minimum rupture patches overlap of at least 80%. A horizontal black line represent one family by connecting the repeating earthquake (red dots). The green and black curves is the normalized cumulative number of repeaters and ValEqt earthquakes respectively. (b) Normalized cumulative slip estimated from repeating earthquakes. (c) Times and magnitudes of ValEqt earthquakes (black dot) and repeating earthquakes (red dot). The blue star indicate the mainshock. (d, e and f) Same as (a, b and c) but zoomed in the vicinity of the mainshock time. Note that the normalized cumulative count of repeaters and ValEqt earthquake start at t=-2 days in (d).

Chapter 4

Conclusions

4.1 General conclusions

Understanding how large earthquakes start is one of the major goal of seismology today. A better understanding of the faulting mechanisms that precede these large ruptures is essential to understand whether observations can be used to better anticipate them.

Many mainshocks are preceded by foreshocks, which are sometimes considered to be precursors, reflecting a preparatory process for the main rupture. However, circumstances under which they occur and whether they have any predictive power is still an open question. Contrasting conceptual models have been proposed to explain their generation: In a first model, foreshocks are generated by a cascade of earthquake triggering (Ellsworth & Beroza, 1995; Helmstetter & Sornette, 2003; Mignan, 2015), propagating through local fault asperities thanks to successive stress variations (possibly mediated by aseismic afterslip). Such a cascade of earthquakes eventually triggers a large rupture, that is later interpreted as the mainshock. In this case, the triggering of the mainshock is unlikely to be anticipated with foreshocks because all earthquakes obey to the same triggering mechanism, independently from their size. In a second model, foreshocks are passive tracers of the aseismic nucleation phase of the mainshock (Das & Scholz, 1981; Dieterich, 1992; Ohnaka, 2000; Bouchon et al., 2011; McLaskey, 2019). During the nucleation, a precursory aseismic slip grows slowly on the fault before accelerating towards a large-scale dynamic rupture. Within the nucleation zone, small embedded seismic asperities can be triggered by aseismic pre-slip, generating foreshocks. Here the foreshocks have a strong predictive power for the mainshock. Finally, we can consider a third model in which a slow-slip event and a cascade of earthquake triggering coexist (Marsan et al., 2014; Radiguet et al., 2016; Voss et al., 2018). Here, the earthquake sequence (its mainshock and foreshocks) is a by-product of a cascade of earthquakes driven by a slow-slip event. The slow-slip event causes an increase of the background seismic activity. This increased activity is amplified and completed by earthquake triggering, which in turn can enhance the likelihood of a large earthquake. Here, as in the cascade model, the triggering of a large earthquake is possible depending on the state of stress of the fault. Foreshocks and aseismic slip are not deterministic of the mainshock, but can still indicate a perturbed fault where triggering a large earthquake is more likely.

Trough this thesis I have studied in detail several foreshock sequences and investigated whether they can be explained by one of these models. The investigation of foreshocks benefits from the creation of high resolution seismicity catalogs that have been built with modern detection tools. Such high-resolution catalogs are expected to help detect unusual foreshock seismicity that may be driven by an underlying aseismic process (Mignan, 2015). For the analysis, I have made extensive use of a statistical modeling of the seismicity and aftershocks to test the cascade model hypothesis and to confront the foreshock seismic activity against aseismic slip observations.

In a first study, we re-evaluated the significance of 53 individual foreshock sequences within a template matching catalog of Southern California (Ross et al., 2019b). We have tested the statistical significance of enhanced foreshock activities, taking into account earthquake triggering, using the temporal Epidemic Type Aftershock Sequences (ETAS) model. According to our analyses, more than 80% of mainshocks are preceded in the last 20 days by seismicity rates consistent with those predicted by ETAS, even when the magnitude of completeness is as low as $m_c = 0$. Therefore, a cascade of earthquakes is a good candidate to explain most of the Southern California foreshock generation. The remaining mainshocks (10/53) are preceded by a high seismic activity, which is significantly different from ETAS cascades. These cases are therefore likely to be controlled by a process other than usual earthquake triggering processes. Among those 10 cases, we distinguish 3 cases that exhibit an anomalous seismic activity that is specifically related to the mainshock. Such deviation of the foreshock seismicity from ETAS is often interpreted as tracer of a nucleation phase of the mainshock (Mignan, 2015; Gomberg, 2018; Seif et al., 2019; Lippiello et al., 2019). The other 7/10 cases show recurrent anomalies over time and may rather reflect other transient forcing phenomena not directly related to the occurrence of a mainshock (i.e., slow-slip event, geothermal activities, ...). However, the statistical seismicity analysis can't infer the triggering mechanism in place. Additional investigations are needed to decipher if the high seismic activity is actually driven by a nucleation phase or another forcing.

In a second study, we have focused on an individual foreshock sequence and performed additional analyses to track aseismic processes in addition to the statistical analysis. We have investigated the 2017 Valparaiso earthquake sequence, which includes a $M_w = 6.9$ mainshock, preceded by an intense foreshock seismicity and for which an aseismic pre-slip has been reported (Ruiz et al., 2017;

Caballero et al., 2021). We generated a high-resolution seismicity catalog using the deep learning phase picker EQTransformer (Mousavi et al., 2020), a recent phase associator (Zhang et al., 2019, REAL) and the location algorithm NonLinLoc (Lomax et al., 2000). This catalog reveals an unusually high seismic activity within the foreshock sequence and persisting for several days after the mainshock. Using repeating earthquakes and high-rate GPS, our study highlights a transient aseismic slip, starting just before the first foreshock and persisting days after the mainshock. Therefore, it is unlikely that the cascade model could have fully generated the foreshock seismicity. Because seismic and aseismic signals persist after the mainshock, with no acceleration trend towards the mainshock, these signals do not seem to indicate a nucleation phase, contrarily to what has been reported before (Ruiz et al., 2014; Caballero et al., 2021). Observations rather suggest the occurrence of a slow-slip event driving an intense seismic activity from foreshocks to aftershocks.

These results suggest that the low magnitude of completeness of the catalog does not warrant the systematic detection of underlying aseismic process through foreshocks. In Figure 4.1.1, I present an updated figure of the meta-analysis of Mignan (2015) that incorporates the results of this thesis. We show that the claim of a detection threshold $m_{min} = M - 3.0$ is not enough to systematically highlight an unusual foreshock activity. The vast majority foreshock sequences do not show a deviation from ETAS, supporting the cascade model even when including low magnitude earthquakes. If specific seismic activities driven by nucleation phases were systematically present before each mainshock, lowering the completeness level should have improved their overall detection. Instead, we only observe occasional deviations with no apparent dependence on the completeness level. Therefore, observations does not support the systematic generation of foreshock sequences by nucleation phases.

It is possible that a nucleation phase exists, but that it may remain undetectable given the current resolution of our catalogs or given the seismicity rate variations induced by other forcing phenomena not necessarily associated with the occurrence of a mainshock. For example, in Southern California, 7/53 catalogs detected with a foreshock anomalies also observe recurrent anomalies over time without being associated with a mainshock. Such a result is likely to require independent transient forcing throughout the catalog, which could be explained, for example, by episodic slow-slip events. Other transient processes related to high heat flow and/or geothermal activities may also be good candidates for specific areas of Southern California (Enescu et al., 2009; Manganiello et al., 2023). Conversely, in Valparaiso, the 'precursory' aseismic slip and high seismic activity persists after the mainshock, which also contradicts the mainshock-oriented nature of a possible nucleation phase. The occurrence of a slow-slip event forcing, from foreshocks to aftershocks, is better suited to explain the sequence. From these examples, we suggest that unusually active foreshock sequences may simply reflect the rare cases where an additional forcing do exist (slow-slip event, geothermal activity, ect..) rather than a pervasive nucleation phase signature.

Therefore, the results of this thesis suggest that, on average, earthquake interactions are the main process driving seismicity and foreshocks, but that a change in forcing, such as a slow-slip event for example, can occasionally enhance the background seismic activity. Such transient forcing phenomena is better suited to explain our results and to explain why certain mainshocks are sometimes preceded by very active foreshocks and sometimes not. Statistically, a non-stationary ETAS model can explain such a seismic process well. Seismicity is controlled by earthquake interactions and a non-stationary background rate, which may reflect a transient forcing. First, when the tectonic forcing is constant (e.g., a locked or continuously creeping fault), the background rate is constant and the variations in the seismicity rate are completely controlled by earthquake interactions as in the cascade model. Magnitudes are independent and randomly sampled from the Gutenberg-Richter distribution. Second, when a transient forcing is observed (e.g., a slow-slip event), the background rate locally increase, enhancing the average earthquake interaction rates compared to a constant forcing. More earthquakes are triggered and the likelihood of a large magnitude event is increased compared to the stationary ETAS model. In other word, during such transient forcing, the probability of observing a large magnitude is increased, but a large event might not necessarily occur. The largest magnitude earthquake of the sequence is retrospectively interpreted as a mainshock and earthquakes preceding it as foreshocks. Such model can explain both why certain mainshocks are sometimes (but not always) preceded by highly active foreshocks, and why it is impossible to identify foreshocks and mainshocks in real time. Foreshocks and mainshocks are arbitrary definitions, not based on any actual physical characteristic of the seismic activity. The predictive power of foreshocks is therefore low. However, during such a transient forcing of the seismic activity, a large magnitude has, on average, a greater chance of occurring than during a constant forcing. Therefore, tracking evidence of transient forcing and aseismic slips may

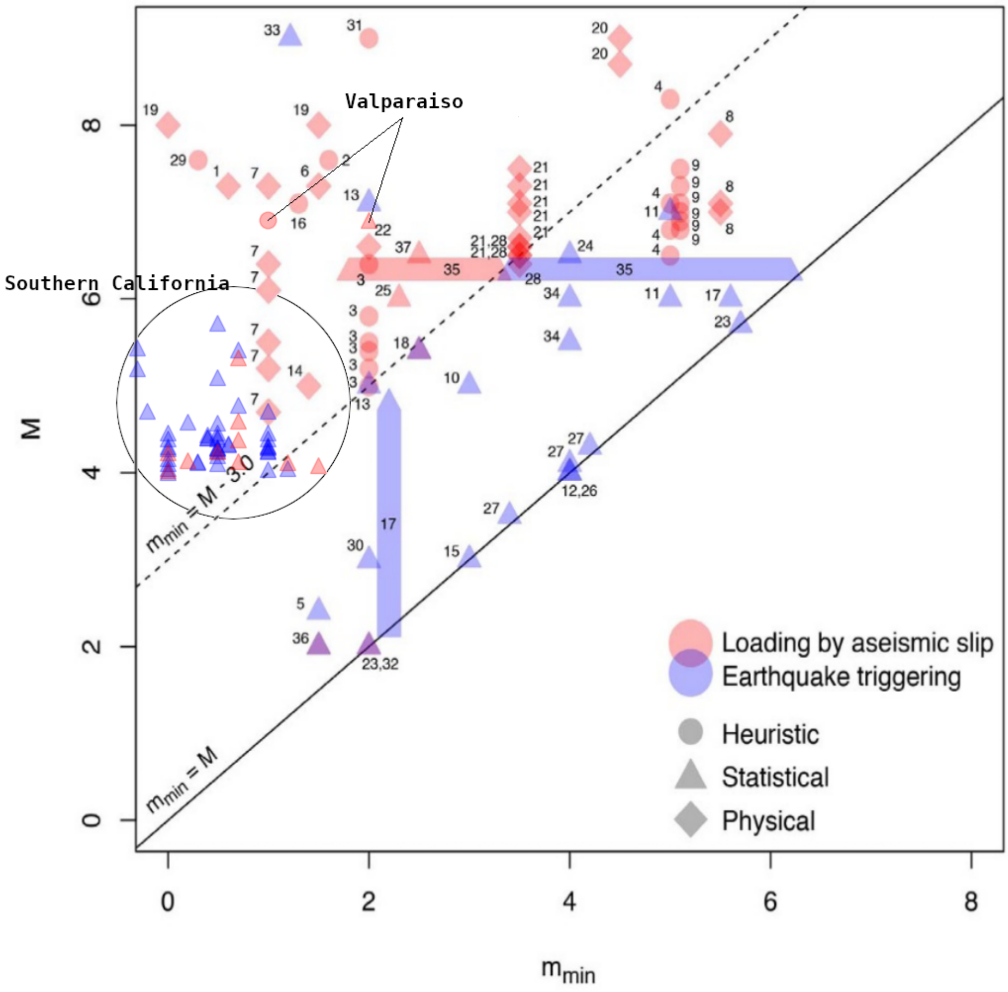

FIGURE 4.1.1: Same as Figure 1.17, but with the Southern California foreshock sequences analysed in chapter 2 and the foreshock sequence of the Valparaiso mainshock analyzed in chapter 3. For southern California, anomalous foreshock sequences unexplained by the ETAS model are labeled "Loaded by aseismic slip", as this is suggested as a corollary when earthquake triggering is rejected in Mignan (2015). We note that our statistical analysis does not infer the actual physical triggering mechanism, and we provide no further evidence for a nucleation phase or slow-slip event triggering in Southern California. For Valparaiso, we provide two points for the same foreshock sequence, one from the statistical analysis and one from the repeating earthquake and HRGPS analysis (heuristic).

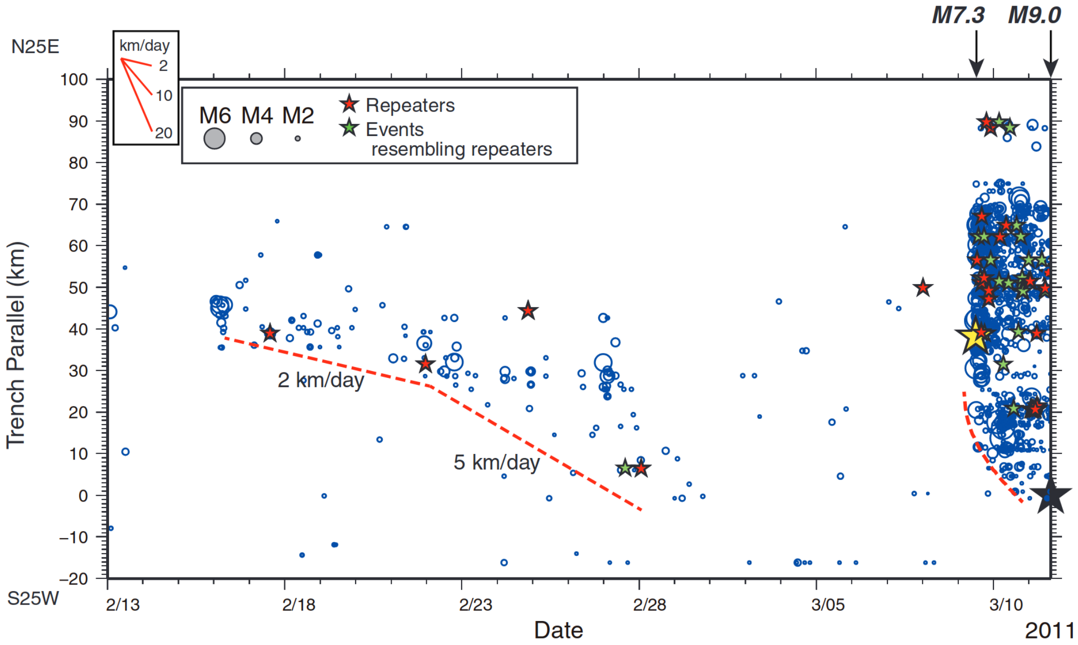

FIGURE 4.2.1: An example of a foreshock migration pattern before the 2011 Tohoku earthquake (Modified from Kato et al., 2012). Blue circles are earthquakes detected between 13 February and the mainshock origin time, along trench distance and time. Blue circles are scaled to magnitudes. Red dashed lines, approximate locations of the earthquake migration fronts. Red stars are repeating earthquakes. Green stars are events that were found to resemble those repeating events. Black star is the $M_w = 9.0$ mainshock. Yellow star is the $M_w = 7.3$ largest foreshock.

help improve real-time assessments of seismic hazard.

4.2 Perspectives

In this concluding section, I propose to explore perspectives and potential future research ideas that have emerged during this thesis journey to understand foreshock earthquakes. The discussion includes aspects of unfinished work and addresses recommendations for future studies of foreshock seismicity.

4.2.1 Ongoing work

Throughout this thesis, we have focused on the temporal evolution of seismicity, neglecting the spatial distribution of earthquakes. However, a spatial migration of foreshocks is often claimed to be an additional evidence of an underlying aseismic process, overtaking basic earthquake triggering spatial ranges. For example, Kato et al. (2012) and Kato et al. (2016a) pointed out a migration of the foreshock activity towards the mainshock epicenter and interpreted it as the consequence of a nucleation phase (see Figure 4.2.1). Usually, migrating patterns in seismicity are highlighted through 2D plots that depict trench distance or along trench distance against time. These plots often show linear migration fronts that encapsulate dispersive seismicity originating from an initial earthquake (Kato et al., 2012; Chen & Shearer, 2013; Kato & Nakagawa, 2014; Kato et al., 2016b). However, the significance of an earthquake migration pattern projected in such distance vs time plot may appear very qualitative. It generally does not take into account the natural migration that may result from earthquake triggering. Therefore, a reliable statistical tool is needed to test whether a migratory pattern can be explained by earthquake interactions or by an additional forcing process. We have performed preliminary tests using 2D space-time ETAS simulations that include a migration pattern within background earthquakes (i.e., a non-stationary background rate). One of our attempts was to use a declustering method (Zaliapin & Ben-Zion, 2020) to separate aftershocks from background earthquakes (see Figure 4.2.2). The declustered background events can then be tested against a stationary Poisson hypothesis to possibly highlight the non-stationary migration zone. However, our preliminary tests encounter difficulties in properly declustering background earthquakes and are often contaminated by tails of large aftershock sequences, making it difficult to identify migrating background earthquakes from aftershocks (i.e., bottom panels of Figure 4.2.2).

Future works also require a better understanding of the spatial and temporal variability of aftershock triggering. The number of triggered aftershocks is usually considered to be similar for triggering events of the same magnitude. Aftershock rates are commonly described using the general Omori-Utsu decay, where intensity is simply scaled with the magnitude of the triggering event (i.e., Equation 1.9). However, while magnitude (moment) is a good estimate of the energy released by an earthquake, seismic events of the same magnitude can have different source properties (e.g., stress drop, slip distribution, etc.) that may impact the aftershock generation. Advancing the understanding of what controls aftershock productivity may help to better constrain seismicity rate variations and whether it can be related to earthquake triggering or a background rate change driven by a transient forcing. Previous studies have investigated the aftershock productivity and observed a variability within magnitudes greater than the expected Poisson variations (Marsan & Helmstetter, 2017; Dascher-Cousineau et al., 2020). It was found that some source properties (stress-drop, source width and

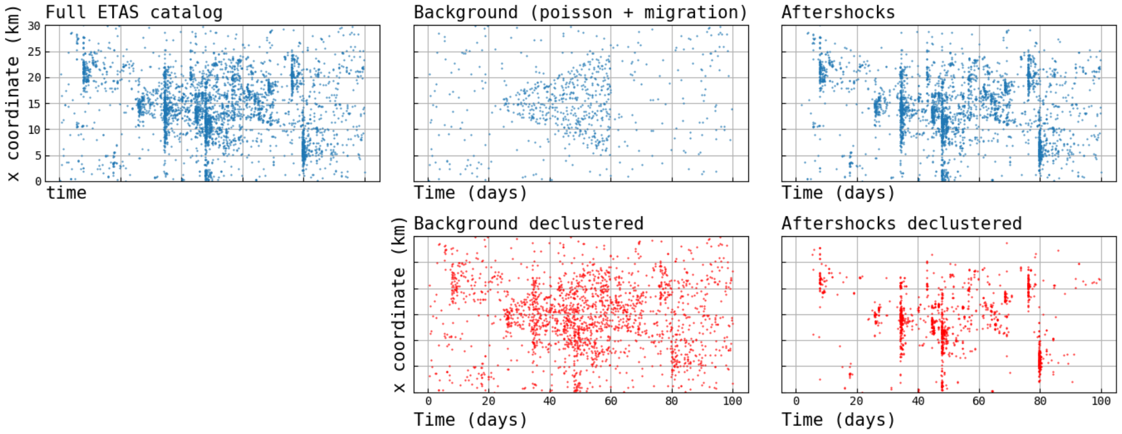

FIGURE 4.2.2: An example of a synthetic ETAS catalog with a migrating background rate. The 3 top panels show a synthetic ETAS catalog with it's background part and aftershock part. Background events are non-stationary and include a migration pattern between $t = 20$ and $t = 60$. The background rate is of $\mu = 0.1$ and $\mu = 1$ inside and outside the migration ranges, respectively. Bottom panel show an attempt of declustering background and aftershock earthquake with a method inspired from Zaliapin & Ben-Zion (2020).

aspect ratio) do correlate well with aftershock productivity (Zaliapin & Ben-Zion, 2016; Dascher-Cousineau et al., 2020). At the end of my Ph.D. research, I started to further investigate the variability of aftershock productivity using earthquake source time functions of the catalog SCARDEC (Vallée & Douet, 2016). We have reproduced aftershock variability and its deviation from Poisson variations using our own selection of mainshocks and aftershocks (see figure 4.2.3). As previously reported, we see that the variability in the number of triggered aftershocks is much greater that what is expected from the theoretical magnitude scaling of the Omori-Utsu law (i.e., Equation 1.9). We propose to further investigate the effect of the length and complexity of the source time function on aftershock productivity. Source time functions can sometimes be smooth with a unique mode or be very complex with multiple modes. As a consequence, complex source time functions are sometimes difficult to interpret as a unique earthquake and rather reflect successive ruptures (Jia et al., 2022, for example). Such variability of the moment release for a given magnitude estimate suggest that it may affect differently the subsequent aftershock productivity.

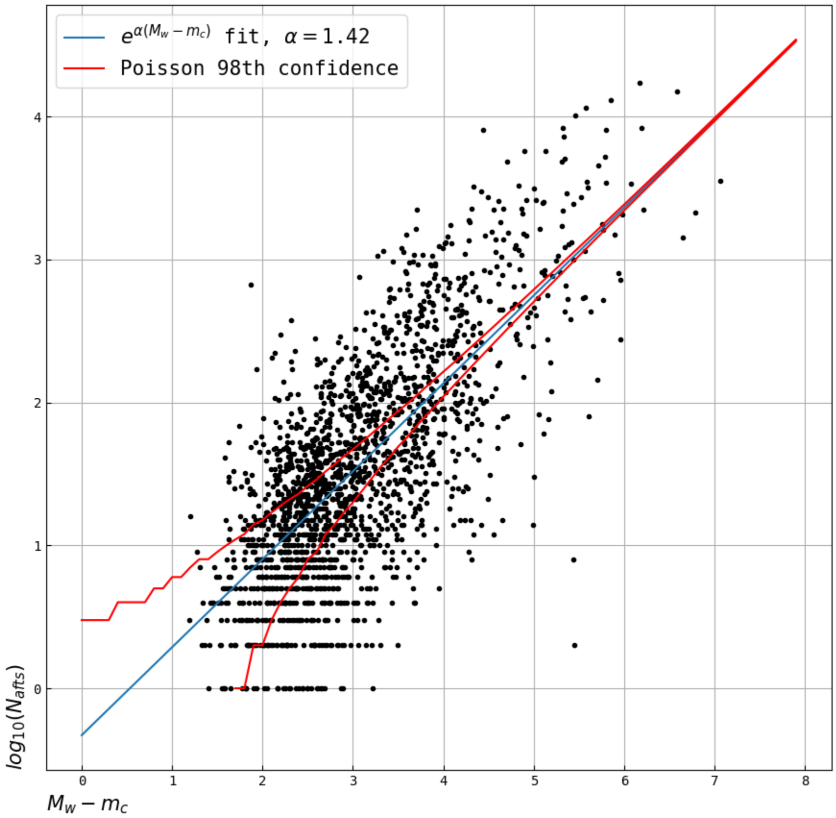

FIGURE 4.2.3: Variability in the number of aftershocks observed after mainshocks in the SCARDEC catalog (Vallée & Douet, 2016). Aftershocks are defined as all events observed 100 days after the mainshock within a circular radius corresponding to the theoretical source radius (Wells & Coppersmith, 1994). Earthquakes from the SCARDEC catalog are selected as mainshocks if they correspond to the largest earthquake observed in 2 years within the same radius. The blue line is the least squares fit of the theoretical aftershock productivity by magnitude (i.e., equation 1.9), while the red lines are the 98th Poisson confidence intervals.

4.2.2 Guidelines for future foreshock seismicity analysis

This thesis has explored and analyzed various aspects of foreshock activity, shedding light on its significance and providing valuable insights into understanding the generation of large earthquakes. Nevertheless, it is clear that a complete understanding of foreshock generation is still out of reach.

Although the results of this thesis above tend to reject the nucleation phase model for the generation of foreshocks, other analysis within high-resolution catalogs are needed to properly assess the role of earthquake triggering and aseismic slip in the triggering of mainshocks. The Southern California and Valparaiso sequences do not necessarily reflect the global behavior of seismicity and other analysis of additional foreshock sequences would probably allow more robust conclusions to be drawn. Furthermore, our results suggest that a better understanding the foreshock process requires the analysis of entire sequences, including both foreshock and post-mainshock activity. Indeed, any unusual seismic or aseismic patterns detected in a window that abruptly stop with the mainshock are likely to be interpreted as mainshock-directed and reflect a preparatory phase. Therefore, the continuity of the pattern before and after the mainshock occurrence must be investigated before concluding on the preparatory nature of a signal. In the same way, it is probably more appropriate to systematically analyze complete seismic sequences; defined for example as all seismicity that deviates from the background rate; without selecting (possibly arbitrarily) a mainshock/foreshock. One might then investigate how seismic and aseismic patterns possibly mediates the occurrence of the largest magnitude events within entire earthquake sequences.

In any case, it appears clear that high quality earthquake datasets, including both small magnitude events and dense geodetic observations are required to better understand foreshock sequences. This will allow a better understanding and quantification of the interplay between seismic activity and aseismic slip to estimate the aseismic slip-driven part of foreshocks. The availability of large datasets over a long period of time will also allow an increase in the number of potential mainshocks to be analyzed, thus allowing more robust conclusions to be drawn. In this sense, high-resolution seismicity catalogs and geodetic measurements covering multiple earthquake cycles and mainshocks are particularly needed to constrain any singularity in foreshock processes.

Bibliography

Abercrombie, R. E. & J. Mori (May 1996). "Occurrence patterns of foreshocks to large earthquakes in the western United States". In: *Nature* 381.6580, pp. 303–307. ISSN: 1476-4687. DOI: `10.1038/381303a0`.

Akaike, H. (Dec. 1974). "A new look at the statistical model identification". In: *IEEE Transactions on Automatic Control* 19.6, pp. 716–723. ISSN: 1558-2523. DOI: `10.1109/TAC.1974.1100705`.

Aki, K. (Sept. 1965). "Maximum likelihood estimate of b in the formula log N = a - bM and its confidence limits". In: *Bulletin of the Earthquake Research Institute* 43.2, pp. 237–239.

Aki, K. & P. G. Richards (2009). *Quantitative seismology*. 2. ed., corr. print. Mill Valley, Calif: Univ. Science Books. ISBN: 978-1-891389-63-4.

Allen, R. V. (Oct. 1978). "Automatic earthquake recognition and timing from single traces". In: *Bulletin of the Seismological Society of America* 68.5, pp. 1521–1532. ISSN: 0037-1106. DOI: `10.1785/BSSA0680051521`.

Altamimi, Z. et al. (June 2017). "ITRF2014 plate motion model". In: *Geophysical Journal International* 209.3, pp. 1906–1912. ISSN: 0956-540X. DOI: `10.1093/gji/ggx136`.

Alwahedi, M. A. & J. C. Hawthorne (2019). "Intermediate-Magnitude Postseismic Slip Follows Intermediate-Magnitude (M 4 to 5) Earthquakes in California". In: *Geophysical Research Letters* 46.7, pp. 3676–3687. ISSN: 1944-8007. DOI: `10.1029/2018GL081001`.

Ampuero, J.-P. & A. M. Rubin (2008). "Earthquake nucleation on rate and state faults – Aging and slip laws". In: *Journal of Geophysical Research: Solid Earth* 113.B1. ISSN: 2156-2202. DOI: `10.1029/2007JB005082`.

Arrowsmith, S. J. et al. (2022). "Big Data Seismology". In: *Reviews of Geophysics* 60.2, e2021RG000769. ISSN: 1944-9208. DOI: `10.1029/2021RG000769`.

Baer, M. & U. Kradolfer (Aug. 1987). "An automatic phase picker for local and teleseismic events". In: *Bulletin of the Seismological Society of America* 77.4, pp. 1437–1445. ISSN: 0037-1106. DOI: `10.1785/BSSA0770041437`.

Barrientos, S. & National Seismological Center (CSN) Team (Mar. 2018). "The Seismic Network of Chile". In: *Seismological Research Letters* 89.2A, pp. 467–474. ISSN: 0895-0695, 1938-2057. DOI: `10.1785/0220160195`.

Bedford, J. et al. (May 2015). “Investigating the final seismic swarm before the Iquique-Pisagua 2014 Mw 8.1 by comparison of continuous GPS and seismic foreshock data”. In: *Geophysical Research Letters* 42.10, pp. 3820–3828. ISSN: 1944-8007. DOI: `10.1002/2015GL063953`.

Berg, E. (Sept. 1968). “Relation between Earthquake Foreshocks, Stress and Mainshocks”. In: *Nature* 219.5159, pp. 1141–1143. ISSN: 1476-4687. DOI: `10.1038/2191141a0`.

Beroza, G. C. & S. Ide (2011). “Slow Earthquakes and Nonvolcanic Tremor”. In: *Annual Review of Earth and Planetary Sciences* 39.1, pp. 271–296. DOI: `10.1146/annurev-earth-040809-152531`.

Blewitt, G., W. C. Hammond & C. Kreemer (Sept. 2018). *Harnessing the GPS Data Explosion for Interdisciplinary Science*. http://eos.org/science-updates/harnessing-the-gps-data-explosion-for-interdisciplinary-science.

Bouchon, M. et al. (Feb. 2011). “Extended nucleation of the 1999 mw 7.6 izmit Earthquake”. In: *Science* 331.6019, pp. 877–880. ISSN: 0036-8075, 1095-9203. DOI: `10.1126/science.1197341`.

Bouchon, M. et al. (Apr. 2013). “The long precursory phase of most large interplate earthquakes”. In: *Nature Geoscience* 6.4, pp. 299–302. ISSN: 1752-0894, 1752-0908. DOI: `10.1038/ngeo1770`.

Brodsky, E. E. & T. Lay (May 2014). “Recognizing Foreshocks from the 1 April 2014 Chile Earthquake”. In: *Science* 344.6185, pp. 700–702. DOI: `10.1126/science.1255202`.

Caballero, E. et al. (Mar. 2021). “Seismic and aseismic fault slip during the initiation phase of the 2017 $m_{w} = 6.9$ valparaíso earthquake”. In: *Geophysical Research Letters* 48.6. ISSN: 0094-8276, 1944-8007. DOI: `10.1029/2020GL091916`.

Chen, X. & P. M. Shearer (2013). “California foreshock sequences suggest aseismic triggering process”. In: *Geophysical Research Letters* 40.11, pp. 2602–2607. ISSN: 1944-8007. DOI: `10.1002/grl.50444`.

Choi, K. et al. (2004). “Modified sidereal filtering: Implications for high-rate GPS positioning”. In: *Geophysical Research Letters* 31.22. ISSN: 1944-8007. DOI: `10.1029/2004GL021621`.

Christophersen, A. & E. G. C. Smith (Oct. 2008). “Foreshock Rates from Aftershock Abundance”. In: *Bulletin of the Seismological Society of America* 98.5, pp. 2133–2148. ISSN: 0037-1106. DOI: `10.1785/0120060143`.

Churchill, R. M. et al. (2022). “Afterslip Moment Scaling and Variability From a Global Compilation of Estimates”. In: *Journal of Geophysical Research: Solid Earth* 127.4, e2021JB023897. ISSN: 2169-9356. DOI: `10.1029/2021JB023897`.

Cleveland, R. B., W. S. Cleveland & I. Terpenning (Mar. 1990). "STL: A Seasonal-Trend Decomposition Procedure Based on Loess". In: *Journal of Official Statistics* 6.1, p. 3. ISSN: 0282423X.

Cocco, M. & J. R. Rice (2002). "Pore pressure and poroelasticity effects in Coulomb stress analysis of earthquake interactions". In: *Journal of Geophysical Research: Solid Earth* 107.B2, ESE 2–1–ESE 2–17. ISSN: 2156-2202. DOI: `10.1029/2000JB000138`.

Dal Zilio, L. & J.-P. Ampuero (Mar. 2023). "Earthquake doublet in Turkey and Syria". In: *Communications Earth & Environment* 4.1, pp. 1–4. ISSN: 2662-4435. DOI: `10.1038/s43247-023-00747-z`.

Daley, D. J. & D. Vere-Jones (2003). *An introduction to the theory of point processes*. 2nd ed. New York: Springer. ISBN: 978-0-387-95541-4 978-0-387-21337-8 978-0-387-49835-5.

Das, S. & C. H. Scholz (1981). "Theory of time-dependent rupture in the Earth". In: *Journal of Geophysical Research: Solid Earth* 86.B7, pp. 6039–6051. ISSN: 2156-2202. DOI: `10.1029/JB086iB07p06039`.

Dascher-Cousineau, K. et al. (2020). "What Controls Variations in Aftershock Productivity?" In: *Journal of Geophysical Research: Solid Earth* 125.2, e2019JB018111. ISSN: 2169-9356. DOI: `10.1029/2019JB018111`.

Davidsen, J., C. Gu & M. Baiesi (May 2015). "Generalized Omori–Utsu law for aftershock sequences in southern California". In: *Geophysical Journal International* 201.2, pp. 965–978. ISSN: 0956-540X. DOI: `10.1093/gji/ggv061`.

Davidsen, J. & M. Baiesi (2016). "Self-similar aftershock rates". In: *Physical Review E* 94.2. ISSN: 2470-0045, 2470-0053. DOI: `10.1103/PhysRevE.94.022314`.

de Arcangelis, L., C. Godano & E. Lippiello (2018). "The Overlap of Aftershock Coda Waves and Short-Term Postseismic Forecasting". In: *Journal of Geophysical Research: Solid Earth* 123.7, pp. 5661–5674. ISSN: 2169-9356. DOI: `10.1029/2018JB015518`.

Dieterich, J. (1994). "A constitutive law for rate of earthquake production and its application to earthquake clustering". In: *Journal of Geophysical Research: Solid Earth* 99.B2, pp. 2601–2618. ISSN: 2156-2202. DOI: `10.1029/93JB02581`.

Dieterich, J. H. (Sept. 1992). "Earthquake nucleation on faults with rate-and state-dependent strength". In: *Tectonophysics* 211.1, pp. 115–134. ISSN: 0040-1951. DOI: `10.1016/0040-1951(92)90055-B`.

Dodge, D. A., G. C. Beroza & W. L. Ellsworth (1995). "Foreshock sequence of the 1992 Landers, California, earthquake and its implications for earthquake nucleation". In: *Journal of Geophysical Research: Solid Earth* 100.B6, pp. 9865–9880. DOI: `10.1029/95JB00871`.

Dodge, D. A., G. C. Beroza & W. L. Ellsworth (1996). "Detailed observations of California foreshock sequences: Implications for the earthquake initiation process". In: *Journal of Geophysical Research: Solid Earth* 101.B10, pp. 22371–22392. ISSN: 2156-2202. DOI: `10.1029/96JB02269`.

Durand, V. et al. (Sept. 2020). "A Two-Scale Preparation Phase Preceded an Mw 5.8 Earthquake in the Sea of Marmara Offshore Istanbul, Turkey". In: *Seismological Research Letters* 91.6, pp. 3139–3147. ISSN: 0895-0695. DOI: `10.1785/0220200110`.

Ekström, G., M. Nettles & A. M. Dziewoński (June 2012). "The global CMT project 2004–2010: Centroid-moment tensors for 13,017 earthquakes". In: *Physics of the Earth and Planetary Interiors* 200–201, pp. 1–9. ISSN: 0031-9201. DOI: `10.1016/j.pepi.2012.04.002`.

El-Isa, Z. H. & D. W. Eaton (Mar. 2014). "Spatiotemporal variations in the b-value of earthquake magnitude–frequency distributions: Classification and causes". In: *Tectonophysics* 615–616, pp. 1–11. ISSN: 0040-1951. DOI: `10.1016/j.tecto.2013.12.001`.

Ellsworth, W. L. & G. C. Beroza (1995). "Seismic evidence for an earthquake nucleation phase". In: *Science* 268, p. 6.

Ellsworth, W. L. & F. Bulut (July 2018). "Nucleation of the 1999 Izmit earthquake by a triggered cascade of foreshocks". In: *Nature Geoscience* 11.7, pp. 531–535. ISSN: 1752-0908. DOI: `10.1038/s41561-018-0145-1`.

Ende, M. P. A. & J.-P. Ampuero (Feb. 2020). "On the Statistical Significance of Foreshock Sequences in Southern California". In: *Geophys. Res. Lett.* 47.3. ISSN: 0094-8276, 1944-8007. DOI: `10.1029/2019GL086224`.

Enescu, B., S. Hainzl & Y. Ben-Zion (Dec. 2009). "Correlations of Seismicity Patterns in Southern California with Surface Heat Flow Data". In: *Bulletin of the Seismological Society of America* 99.6, pp. 3114–3123. ISSN: 0037-1106. DOI: `10.1785/0120080038`.

Fang, Z., J. H. Dieterich & G. Xu (2010). "Effect of initial conditions and loading path on earthquake nucleation". In: *Journal of Geophysical Research: Solid Earth* 115.B6. ISSN: 2156-2202. DOI: `10.1029/2009JB006558`.

Felzer, K. R., R. E. Abercrombie & G. Ekström (2004). "A Common Origin for Aftershocks, Foreshocks, and Multiplets". In: *Bulletin of the Seismological Society of America* 94.1, pp. 88–98. DOI: `10.1785/0120030069`.

Felzer, K. R., M. T. Page & A. J. Michael (Feb. 2015). "Artificial seismic acceleration". In: *Nature Geoscience* 8.2, pp. 82–83. ISSN: 1752-0908. DOI: `10.1038/ngeo2358`.

Felzer, K. R. et al. (2002). "Triggering of the 1999 Mw 7.1 Hector Mine earthquake by aftershocks of the 1992 Mw 7.3 Landers earthquake". In: *J. Geophys. Res.* 107.B9, ESE 6–1–ESE 6–13. DOI: `10.1029/2001JB000911`.

Gao, D., H. Kao & B. Wang (2021). "Misconception of Waveform Similarity in the Identification of Repeating Earthquakes". In: *Geophysical Research Letters* 48.13, e2021GL092815. ISSN: 1944-8007. DOI: `10.1029/2021GL092815`.

Gardner, J. K. & L. Knopoff (Oct. 1974). "Is the sequence of earthquakes in Southern California, with aftershocks removed, Poissonian?" In: *Bulletin of the Seismological Society of America* 64.5, pp. 1363–1367. ISSN: 0037-1106. DOI: `10.1785/BSSA0640051363`.

Ghosh, D., A. Deb & R. Sengupta (Oct. 2009). "Anomalous radon emission as precursor of earthquake". In: *Journal of Applied Geophysics* 69.2, pp. 67–81. DOI: `10.1016/j.jappgeo.2009.06.001`.

Gibbons, S. J. & F. Ringdal (Apr. 2006). "The detection of low magnitude seismic events using array-based waveform correlation". In: *Geophysical Journal International* 165.1, pp. 149–166. ISSN: 0956-540X. DOI: `10.1111/j.1365-246X.2006.02865.x`.

Gomberg, J. (July 2018). "Unsettled earthquake nucleation". In: *Nature Geoscience* 11.7, pp. 463–464. ISSN: 1752-0908. DOI: `10.1038/s41561-018-0149-x`.

Gomberg, J. & the Cascadia 2007 and Beyond Working Group (July 2010). "Slow-slip phenomena in Cascadia from 2007 and beyond: A review". In: *GSA Bulletin* 122.7-8, pp. 963–978. ISSN: 0016-7606. DOI: `10.1130/B30287.1`.

Gong, J., W. Fan & R. Parnell-Turner (2022). "Microseismicity Indicates Atypical Small-Scale Plate Rotation at the Quebrada Transform Fault System, East Pacific Rise". In: *Geophysical Research Letters* 49.3, e2021GL097000. ISSN: 1944-8007. DOI: `10.1029/2021GL097000`.

Gutenberg, B. & C. F. Richter (Oct. 1944). "Frequency of earthquakes in California*". In: *Bulletin of the Seismological Society of America* 34.4, pp. 185–188. ISSN: 0037-1106. DOI: `10.1785/BSSA0340040185`.

— (Nov. 1956). "Magnitude and energy of earthquakes". In: *Annals of Geophysics* 9.1, pp. 1–15. ISSN: 2037-416X. DOI: `10.4401/ag-5590`.

Hainzl, S., A. Christophersen & B. Enescu (Aug. 2008). "Impact of Earthquake Rupture Extensions on Parameter Estimations of Point-Process Models". In: *Bulletin of the Seismological Society of America* 98.4, pp. 2066–2072. ISSN: 0037-1106. DOI: `10.1785/0120070256`.

Hainzl, S. & D. Marsan (2008). "Dependence of the Omori-Utsu law parameters on main shock magnitude: Observations and modeling". In: *Journal of Geophysical Research: Solid Earth* 113.B10. ISSN: 2156-2202. DOI: `10.1029/2007JB005492`.

Hainzl, S. (Sept. 2016). “Apparent triggering function of aftershocks resulting from rate-dependent incompleteness of earthquake catalogs”. In: *Journal of Geophysical Research: Solid Earth* 121.9, pp. 6499–6509. ISSN: 21699313. DOI: `10.1002/2016JB013319`.

— (Sept. 2021). “ETAS-Approach Accounting for Short-Term Incompleteness of Earthquake Catalogs”. In: *Bulletin of the Seismological Society of America*. ISSN: 0037-1106, 1943-3573. DOI: `10.1785/0120210146`.

Hainzl, S. & Y. Ogata (2005). “Detecting fluid signals in seismicity data through statistical earthquake modeling”. In: *Journal of Geophysical Research: Solid Earth* 110.B5. ISSN: 2156-2202. DOI: `10.1029/2004JB003247`.

Hainzl, S., F. Scherbaum & C. Beauval (Feb. 2006). “Estimating Background Activity Based on Interevent-Time Distribution”. In: *Bulletin of the Seismological Society of America* 96.1, pp. 313–320. ISSN: 0037-1106. DOI: `10.1785/0120050053`.

Hainzl, S., O. Zakharova & D. Marsan (June 2013). “Impact of Aseismic Transients on the Estimation of Aftershock Productivity Parameters”. In: *Bulletin of the Seismological Society of America* 103.3, pp. 1723–1732. ISSN: 0037-1106. DOI: `10.1785/0120120247`.

Hanks, T. C. & D. L. Anderson (Apr. 1969). “The early thermal history of the earth”. In: *Physics of the Earth and Planetary Interiors* 2.1, pp. 19–29. ISSN: 0031-9201. DOI: `10.1016/0031-9201(69)90015-6`.

Hanks, T. C. & W. H. Bakun (June 2002). “A Bilinear Source-Scaling Model for M-log A Observations of Continental Earthquakes”. In: *Bulletin of the Seismological Society of America* 92.5, pp. 1841–1846. ISSN: 0037-1106. DOI: `10.1785/0120010148`.

Harris, R. A. (1998). “Introduction to Special Section: Stress Triggers, Stress Shadows, and Implications for Seismic Hazard”. In: *Journal of Geophysical Research: Solid Earth* 103.B10, pp. 24347–24358. ISSN: 2156-2202. DOI: `10.1029/98JB01576`.

Helmstetter, A., Y. Y. Kagan & D. D. Jackson (2005). “Importance of small earthquakes for stress transfers and earthquake triggering”. In: *Journal of Geophysical Research: Solid Earth* 110.B5. ISSN: 2156-2202. DOI: `10.1029/2004JB003286`.

Helmstetter, A. & D. Sornette (2003). “Foreshocks explained by cascades of triggered seismicity”. In: *Journal of Geophysical Research: Solid Earth* 108.B10. ISSN: 2156-2202. DOI: `10.1029/2003JB002409`.

Hsu, Y.-J. et al. (June 2006). “Frictional Afterslip Following the 2005 Nias-Simeulue Earthquake, Sumatra”. In: *Science* 312.5782, pp. 1921–1926. DOI: `10.1126/science.1126960`.

Igarashi, T., T. Matsuzawa & A. Hasegawa (2003). "Repeating earthquakes and interplate aseismic slip in the northeastern Japan subduction zone". In: *Journal of Geophysical Research: Solid Earth* 108.B5. ISSN: 2156-2202. DOI: `10.1029/2002JB001920`.

Im, K. & J.-P. Avouac (Oct. 2023). "Cascading foreshocks, aftershocks and earthquake swarms in a discrete fault network". In: *Geophysical Journal International* 235.1, pp. 831–852. ISSN: 0956-540X. DOI: `10.1093/gji/ggad278`.

Ito, Y. et al. (July 2013). "Episodic slow slip events in the Japan subduction zone before the 2011 Tohoku-Oki earthquake". In: *Tectonophysics*. Great Earthquakes along Subduction Zones 600, pp. 14–26. ISSN: 0040-1951. DOI: `10.1016/j.tecto.2012.08.022`.

Itoh, Y. & Y. Aoki (Feb. 2022). "On the performance of position-domain sidereal filter for 30-s kinematic GPS to mitigate multipath errors". In: *Earth, Planets and Space* 74.1, p. 23. ISSN: 1880-5981. DOI: `10.1186/s40623-022-01584-8`.

Itoh, Y., Y. Aoki & J. Fukuda (May 2022). "Imaging evolution of Cascadia slow-slip event using high-rate GPS". In: *Scientific Reports* 12.1, p. 7179. ISSN: 2045-2322. DOI: `10.1038/s41598-022-10957-8`.

Jia, Z., Z. Zhan & H. Kanamori (Feb. 2022). "The 2021 South Sandwich Island M_w 8.2 Earthquake: A Slow Event Sandwiched Between Regular Ruptures". In: *Geophysical Research Letters* 49.3. ISSN: 0094-8276, 1944-8007. DOI: `10.1029/2021GL097104`.

Jones, L. & P. Molnar (Aug. 1976). "Frequency of foreshocks". In: *Nature* 262.5570, pp. 677–679. ISSN: 1476-4687. DOI: `10.1038/262677a0`.

— (1979). "Some characteristics of foreshocks and their possible relationship to earthquake prediction and premonitory slip on faults". In: *Journal of Geophysical Research: Solid Earth* 84.B7, pp. 3596–3608. ISSN: 2156-2202. DOI: `10.1029/JB084iB07p03596`.

Kagan, Y. Y. & L. Knopoff (1981). "Stochastic synthesis of earthquake catalogs". In: *Journal of Geophysical Research: Solid Earth* 86.B4, pp. 2853–2862. ISSN: 2156-2202. DOI: `10.1029/JB086iB04p02853`.

— (June 1987). "Statistical Short-Term Earthquake Prediction". In: *Science* 236.4808, pp. 1563–1567. ISSN: 0036-8075, 1095-9203. DOI: `10.1126/science.236.4808.1563`.

Kagan, Y. Y. (Aug. 2004). "Short-Term Properties of Earthquake Catalogs and Models of Earthquake Source". In: *Bulletin of the Seismological Society of America* 94.4, pp. 1207–1228. ISSN: 0037-1106. DOI: `10.1785/012003098`.

Kanamori, H. & D. L. Anderson (1975). "Theoreritical basis of some empirical relations in seismology". In: *Bulletin of the Seismological Society of America* 65.5, pp. 1073–1095.

Kanamori, H. (1977). "The energy release in great earthquakes". In: *Journal of Geophysical Research (1896-1977)* 82.20, pp. 2981–2987. ISSN: 2156-2202. DOI: `10.1029/JB082i020p02981`.

Kanamori, H. & L. Rivera (2006). "Energy partitioning during an earthquake". In: *Geophysical Monograph Series*. Ed. by R. Abercrombie et al. Vol. 170. Washington, D. C.: American Geophysical Union, pp. 3–13. ISBN: 978-0-87590-435-1. DOI: `10.1029/170GM03`.

Kaneko, Y. & J.-P. Ampuero (2011). "A mechanism for preseismic steady rupture fronts observed in laboratory experiments". In: *Geophysical Research Letters* 38.21. ISSN: 1944-8007. DOI: `10.1029/2011GL049953`.

Kato, A. et al. (Feb. 2012). "Propagation of Slow Slip Leading Up to the 2011 Mw 9.0 Tohoku-Oki Earthquake". In: *Science* 335.6069, pp. 705–708. ISSN: 0036-8075, 1095-9203. DOI: `10.1126/science.1215141`.

Kato, A. & S. Nakagawa (2014). "Multiple slow-slip events during a foreshock sequence of the 2014 Iquique, Chile Mw 8.1 earthquake". In: *Geophysical Research Letters* 41.15, pp. 5420–5427. ISSN: 1944-8007. DOI: `10.1002/2014GL061138`.

Kato, A. et al. (Apr. 2016a). "Accelerated nucleation of the 2014 Iquique, Chile Mw 8.2 Earthquake". In: *Scientific Reports* 6.1, p. 24792. ISSN: 2045-2322. DOI: `10.1038/srep24792`.

Kato, A. et al. (2016b). "Foreshock migration preceding the 2016 Mw 7.0 Kumamoto earthquake, Japan". In: *Geophysical Research Letters* 43.17, pp. 8945–8953. ISSN: 1944-8007. DOI: `10.1002/2016GL070079`.

Kattamanchi, S., R. K. Tiwari & D. S. Ramesh (Nov. 2017). "Non-stationary ETAS to model earthquake occurrences affected by episodic aseismic transients". In: *Earth, Planets and Space* 69.1, p. 157. ISSN: 1880-5981. DOI: `10.1186/s40623-017-0741-0`.

Kay, S. M. (Feb. 1993). *Fundamentals of statistical signal processing: estimation theory*. USA: Prentice-Hall, Inc. ISBN: 978-0-13-345711-7.

Keiiti, A. (July 1966). "Generation and Propagation of G Waves from the Niigata Earthquake of June 16, 1964. : Part 2. Estimation of earthquake moment, released energy, and stress-strain drop from the G wave spectrum". In: *Bulletin of the Earthquake Research Institute* 44.1, pp. 73–88. DOI: `10.15083/0000033586`.

Klein, E. et al. (2018). "Deep Transient Slow Slip Detected by Survey GPS in the Region of Atacama, Chile". In: *Geophysical Research Letters* 45.22, pp. 12,263–12,273. ISSN: 1944-8007. DOI: `10.1029/2018GL080613`.

Klein, E. et al. (Sept. 2021). “Interplay of seismic and a-seismic deformation during the 2020 sequence of Atacama, Chile”. In: *Earth and Planetary Science Letters* 570, p. 117081. ISSN: 0012-821X. DOI: `10.1016/j.epsl.2021.117081`.

Klein, E. et al. (Jan. 2023). “Return of the Atacama deep Slow Slip Event: The 5-year recurrence confirmed by continuous GPS”. In: *Physics of the Earth and Planetary Interiors* 334, p. 106970. ISSN: 0031-9201. DOI: `10.1016/j.pepi.2022.106970`.

Kwiatek, G., T. H. W. Goebel & G. Dresen (2014). “Seismic moment tensor and b value variations over successive seismic cycles in laboratory stick-slip experiments”. In: *Geophysical Research Letters* 41.16, pp. 5838–5846. ISSN: 1944-8007. DOI: `10.1002/2014GL060159`.

Lapusta, N. & J. R. Rice (2003). “Nucleation and early seismic propagation of small and large events in a crustal earthquake model”. In: *Journal of Geophysical Research: Solid Earth* 108.B4. ISSN: 2156-2202. DOI: `10.1029/2001JB000793`.

Larson, K. M., A. Bilich & P. Axelrad (2007). “Improving the precision of high-rate GPS”. In: *Journal of Geophysical Research: Solid Earth* 112.B5. ISSN: 2156-2202. DOI: `10.1029/2006JB004367`.

Latour, S. et al. (Oct. 2013). “Characterization of nucleation during laboratory earthquakes”. In: *Geophys. Res. Lett.* 40.19, pp. 5064–5069. ISSN: 0094-8276, 1944-8007. DOI: `10.1002/grl.50974`.

Le Pichon, X. (1968). “Sea-floor spreading and continental drift”. In: *Journal of Geophysical Research (1896-1977)* 73.12, pp. 3661–3697. ISSN: 2156-2202. DOI: `10.1029/JB073i012p03661`.

Lee, H.-Y. & R. Douilly (Dec. 2022). “Earthquake Swarms in Southern Hispaniola Revealed by Spatiotemporal Evolution of Seismicity from Multi-Station Template Matching”. In: *Bulletin of the Seismological Society of America* 113.1, pp. 115–130. ISSN: 0037-1106. DOI: `10.1785/0120220125`.

Lengliné, O., Z. Duputel & V. Ferrazzini (May 2016). “Uncovering the hidden signature of a magmatic recharge at Piton de la Fournaise volcano using small earthquakes”. In: *Geophysical Research Letters* 43.9, pp. 4255–4262. ISSN: 00948276. DOI: `10.1002/2016GL068383`.

Lengliné, O. & D. Marsan (2009). “Inferring the coseismic and postseismic stress changes caused by the 2004 Mw = 6 Parkfield earthquake from variations of recurrence times of microearthquakes”. In: *Journal of Geophysical Research: Solid Earth* 114.B10. ISSN: 2156-2202. DOI: `10.1029/2008JB006118`.

Lengliné, O. et al. (2012). “Decay and expansion of the early aftershock activity following the 2011, Mw9.0 Tohoku earthquake”. In: *Geophysical Research Letters* 39.18. ISSN: 1944-8007. DOI: `10.1029/2012GL052797`.

Lippiello, E. et al. (Nov. 2012). “Spatial organization of foreshocks as a tool to forecast large earthquakes”. In: *Scientific Reports* 2.1, p. 846. ISSN: 2045-2322. DOI: `10.1038/srep00846`.

Lippiello, E., C. Godano & L. de Arcangelis (2019). “The Relevance of Foreshocks in Earthquake Triggering: A Statistical Study”. In: *Entropy* 21.173, p. 13. DOI: `10.3390/e21020173`.

Liu, M. et al. (2020). “Rapid Characterization of the July 2019 Ridgecrest, California, Earthquake Sequence From Raw Seismic Data Using Machine-Learning Phase Picker”. In: *Geophysical Research Letters* 47.4, e2019GL086189. ISSN: 1944-8007. DOI: `10.1029/2019GL086189`.

Llenos, A. L., J. J. McGuire & Y. Ogata (Apr. 2009). “Modeling seismic swarms triggered by aseismic transients”. In: *Earth and Planetary Science Letters* 281.1, pp. 59–69. ISSN: 0012-821X. DOI: `10.1016/j.epsl.2009.02.011`.

Lohman, R. B. & J. J. McGuire (2007). “Earthquake swarms driven by aseismic creep in the Salton Trough, California”. In: *Journal of Geophysical Research: Solid Earth* 112.B4. ISSN: 2156-2202. DOI: `10.1029/2006JB004596`.

Lomax, A. et al. (2000). “Probabilistic Earthquake Location in 3D and Layered Models”. In: *Advances in Seismic Event Location*. Ed. by G. Nolet, C. H. Thurber & N. Rabinowitz. Vol. 18. Dordrecht: Springer Netherlands, pp. 101–134. ISBN: 978-90-481-5498-2 978-94-015-9536-0. DOI: `10.1007/978-94-015-9536-0_5`.

Mallet, R. (1862). *Great Neapolitan earthquake of 1857 : the first principles of observational seismology as developed in the report to the Royal Society of London of the expedition made by command of the Society into the interior of the Kingdom of Naples, to investigate the circumstances of the great earthquake of December 1857*. London : Chapman and Hall.

Manganiello, E., M. Herrmann & W. Marzocchi (2023). “New Physical Implications From Revisiting Foreshock Activity in Southern California”. In: *Geophysical Research Letters* 50.1, e2022GL098737. ISSN: 1944-8007. DOI: `10.1029/2022GL098737`.

Marill, L. et al. (2021). “Fourteen-Year Acceleration Along the Japan Trench”. In: *Journal of Geophysical Research: Solid Earth* 126.11, e2020JB021226. ISSN: 2169-9356. DOI: `10.1029/2020JB021226`.

Marone, C. J., C. H. Scholtz & R. Bilham (1991). “On the mechanics of earthquake afterslip”. In: *Journal of Geophysical Research: Solid Earth* 96.B5, pp. 8441–8452. ISSN: 2156-2202. DOI: `10.1029/91JB00275`.

Marsan, D. & B. Enescu (2012). “Modeling the foreshock sequence prior to the 2011, MW9.0 Tohoku, Japan, earthquake”. In: *Journal of Geophysical Research: Solid Earth* 117.B6. ISSN: 2156-2202. DOI: `10.1029/2011JB009039`.

Marsan, D. & A. Helmstetter (2017). “How variable is the number of triggered aftershocks?” In: *Journal of Geophysical Research: Solid Earth* 122.7, pp. 5544–5560. ISSN: 2169-9356. DOI: `10.1002/2016JB013807`.

Marsan, D. & O. Lengliné (2010). “A new estimation of the decay of aftershock density with distance to the mainshock”. In: *Journal of Geophysical Research: Solid Earth* 115.B9. ISSN: 2156-2202. DOI: `10.1029/2009JB007119`.

Marsan, D. et al. (Oct. 2014). “Foreshock activity related to enhanced aftershock production: Foreshock and aftershock activities”. In: *Geophysical Research Letters* 41.19, pp. 6652–6658. ISSN: 00948276. DOI: `10.1002/2014GL061219`.

Marsan, D. & O. Lengliné (Feb. 2008). “Extending Earthquakes’ Reach Through Cascading”. In: *Science* 319.5866, pp. 1076–1079. DOI: `10.1126/science.1148783`.

Marsan, D., E. Prono & A. Helmstetter (Feb. 2013). “Monitoring Aseismic Forcing in Fault Zones Using Earthquake Time Series”. In: *Bulletin of the Seismological Society of America* 103.1, pp. 169–179. ISSN: 0037-1106. DOI: `10.1785/0120110304`.

Marty, S. et al. (2023). “Nucleation of Laboratory Earthquakes: Quantitative Analysis and Scalings”. In: *Journal of Geophysical Research: Solid Earth* 128.3, e2022JB026294. ISSN: 2169-9356. DOI: `10.1029/2022JB026294`.

Marzocchi, W. & J. Zhuang (2011). “Statistics between mainshocks and foreshocks in Italy and Southern California”. In: *Geophysical Research Letters* 38.9, n/a–n/a. ISSN: 00948276. DOI: `10.1029/2011GL047165`.

Mavrommatis, A. P., P. Segall & K. M. Johnson (July 2014). “A decadal-scale deformation transient prior to the 2011 Mw 9.0 Tohoku-oki earthquake”. In: *Geophys. Res. Lett.* 41.13, pp. 4486–4494. ISSN: 00948276. DOI: `10.1002/2014GL060139`.

Mavrommatis, A. P. et al. (2015). “Long-term acceleration of aseismic slip preceding the Mw 9 Tohoku-oki earthquake: Constraints from repeating earthquakes”. In: *Geophysical Research Letters* 42.22, pp. 9717–9725. ISSN: 1944-8007. DOI: `10.1002/2015GL066069`.

McLaskey, G. C. (2019). “Earthquake Initiation From Laboratory Observations and Implications for Foreshocks”. In: *Journal of Geophysical Research: Solid Earth* 124.12, pp. 12882–12904. ISSN: 2169-9356. DOI: `10.1029/2019JB018363`.

McLaskey, G. C. & B. D. Kilgore (2013). “Foreshocks during the nucleation of stick-slip instability”. In: *Journal of Geophysical Research: Solid Earth* 118.6, pp. 2982–2997. ISSN: 2169-9356. DOI: `10.1002/jgrb.50232`.

McLaskey, G. C. & D. A. Lockner (2014). “Preslip and cascade processes initiating laboratory stick slip”. In: *Journal of Geophysical Research: Solid Earth* 119.8, pp. 6323–6336. ISSN: 2169-9356. DOI: `10.1002/2014JB011220`.

Meng, L. et al. (Feb. 2015). “Dual megathrust slip behaviors of the 2014 Iquique earthquake sequence”. In: *Earth and Planetary Science Letters* 411, pp. 177–187. ISSN: 0012-821X. DOI: `10.1016/j.epsl.2014.11.041`.

Meng, Q. & B. Duan (Oct. 2022). “Dynamic Modeling of Interactions between Shallow Slow-Slip Events and Subduction Earthquakes”. In: *Seismological Research Letters*. ISSN: 0895-0695. DOI: `10.1785/0220220138`.

Mignan, A. (2015). “The debate on the prognostic value of earthquake foreshocks: A meta-analysis”. In: *Scientific Reports* 4.1, p. 4099. ISSN: 2045-2322. DOI: `10.1038/srep04099`.

Miura, S. et al. (Dec. 2006). “Co- and post-seismic slip associated with the 2005 Miyagi-oki earthquake (M7.2) as inferred from GPS data”. In: *Earth, Planets and Space* 58.12, pp. 1567–1572. ISSN: 1880-5981. DOI: `10.1186/BF03352662`.

Mizrahi, L., S. Nandan & S. Wiemer (2021). “Embracing Data Incompleteness for Better Earthquake Forecasting”. In: *Journal of Geophysical Research: Solid Earth* 126.12, e2021JB022379. ISSN: 2169-9356. DOI: `10.1029/2021JB022379`.

Mogi, K. (Sept. 1963a). “Some Discussions on Aftershocks, Foreshocks and Earthquake Swarms : the Fracture of a Semi-infinite Body Caused by an Inner Stress Origin and Its Relation to the Earthquake Phenomena (Third Paper)”. In: *Bulletin of the Earthquake Research Institute* 41.3, pp. 615–658. ISSN: 00408972.

— (Sept. 1963b). “The Fracture of a Semi-infinite Body Caused by an Inner Stress Origin and Its Relation to the Earthquake Phenomena (Second Paper) : The Case of the Materials Having Some Heterogeneous Structures”. In: *Bulletin of the Earthquake Research Institute* 41.3, pp. 595–614. ISSN: 00408972.

Moradpour, J., S. Hainzl & J. Davidsen (2014). “Nontrivial decay of aftershock density with distance in Southern California”. In: *Journal of Geophysical Research: Solid Earth* 119.7, pp. 5518–5535. DOI: `10.1002/2014JB010940`.

Mousavi, S. M. et al. (July 2019a). “CRED: A Deep Residual Network of Convolutional and Recurrent Units for Earthquake Signal Detection”. In: *Scientific Reports* 9.1, p. 10267. ISSN: 2045-2322. DOI: `10.1038/s41598-019-45748-1`.

Mousavi, S. M. et al. (2019b). “STanford EArthquake Dataset (STEAD): A Global Data Set of Seismic Signals for AI”. In: *IEEE Access* 7, pp. 179464–179476. ISSN: 2169-3536. DOI: `10.1109/ACCESS.2019.2947848`.

Mousavi, S. M. et al. (Aug. 2020). “Earthquake transformer—an attentive deep-learning model for simultaneous earthquake detection and phase picking”. In: *Nature Communications* 11.1, p. 3952. ISSN: 2041-1723. DOI: `10.1038/s41467-020-17591-w`.

Moutote, L. et al. (Apr. 2021). "Rare occurrences of non-cascading foreshock activity in Southern California". In: *Geophysical Research Letters* 48.7, e2020GL091757. ISSN: 0094-8276, 1944-8007. DOI: `10.1029/2020GL091757`.

Münchmeyer, J. et al. (2022). "Which Picker Fits My Data? A Quantitative Evaluation of Deep Learning Based Seismic Pickers". In: *Journal of Geophysical Research: Solid Earth* 127.1, e2021JB023499. ISSN: 2169-9356. DOI: `10.1029/2021JB023499`.

Nadeau, R. M. & L. R. Johnson (June 1998). "Seismological studies at Parkfield VI: Moment release rates and estimates of source parameters for small repeating earthquakes". In: *Bulletin of the Seismological Society of America* 88.3, pp. 790–814. ISSN: 0037-1106. DOI: `10.1785/BSSA0880030790`.

Nadeau, R. M. & T. V. McEvilly (July 1999). "Fault Slip Rates at Depth from Recurrence Intervals of Repeating Microearthquakes". In: *Science* 285.5428, pp. 718–721. DOI: `10.1126/science.285.5428.718`.

Nakatani, M. (Mar. 2020). "Evaluation of Phenomena Preceding Earthquakes and Earthquake Predictability". In: *Journal of Disaster Research* 15.2, pp. 112–143. DOI: `10.20965/jdr.2020.p0112`.

Nandan, S. et al. (2017). "Objective estimation of spatially variable parameters of epidemic type aftershock sequence model: Application to California". In: *Journal of Geophysical Research: Solid Earth* 122.7, pp. 5118–5143. ISSN: 2169-9356. DOI: `10.1002/2016JB013266`.

Narteau, C. et al. (Dec. 2009). "Common dependence on stress for the two fundamental laws of statistical seismology". In: *Nature* 462.7273, pp. 642–645. ISSN: 1476-4687. DOI: `10.1038/nature08553`.

Nishikawa, T. & S. Ide (Dec. 2014). "Earthquake size distribution in subduction zones linked to slab buoyancy". In: *Nature Geoscience* 7.12, pp. 904–908. ISSN: 1752-0908. DOI: `10.1038/ngeo2279`.

Nishikawa, T., T. Nishimura & Y. Okada (2021). "Earthquake Swarm Detection Along the Hikurangi Trench, New Zealand: Insights Into the Relationship Between Seismicity and Slow Slip Events". In: *Journal of Geophysical Research: Solid Earth* 126.4, e2020JB020618. ISSN: 2169-9356. DOI: `10.1029/2020JB020618`.

Ogata, Y. (1988). "Statistical Models for Earthquake Occurrences and Residual Analysis for Point Processes". In: *Journal of the American Statistical Association* 83.401, pp. 9–27. ISSN: 0162-1459, 1537-274X. DOI: `10.1080/01621459.1988.10478560`.

— (Nov. 1989). "Statistical model for standard seismicity and detection of anomalies by residual analysis". In: *Tectonophysics* 169.1, pp. 159–174. ISSN: 0040-1951. DOI: `10.1016/0040-1951(89)90191-1`.

Ogata, Y. (1992). "Detection of precursory relative quiescence before great earthquakes through a statistical model". In: *Journal of Geophysical Research* 97.B13, p. 19845. DOI: `10.1029/92JB00708`.

Ogata, Y. & K. Katsura (2014). "Comparing foreshock characteristics and foreshock forecasting in observed and simulated earthquake catalogs". In: *Journal of Geophysical Research: Solid Earth* 119.11, pp. 8457–8477. ISSN: 2169-9356. DOI: `10.1002/2014JB011250`.

Ogata, Y., K. Katsura & M. Tanemura (Oct. 2003). "Modelling heterogeneous space-time occurrences of earthquakes and its residual analysis". In: *Journal of the Royal Statistical Society: Series C (Applied Statistics)* 52.4, pp. 499–509. DOI: `10.1111/1467-9876.00420`.

Ohnaka, M. (Dec. 2000). "A Physical Scaling Relation Between the Size of an Earthquake and its Nucleation Zone Size". In: *pure and applied geophysics* 157.11, pp. 2259–2282. ISSN: 1420-9136. DOI: `10.1007/PL00001084`.

Ohnaka, M. (Sept. 1992). "Earthquake source nucleation: A physical model for short-term precursors". In: *Tectonophysics* 211.1, pp. 149–178. ISSN: 0040-1951. DOI: `10.1016/0040-1951(92)90057-D`.

— (2003). "A constitutive scaling law and a unified comprehension for frictional slip failure, shear fracture of intact rock, and earthquake rupture". In: *Journal of Geophysical Research: Solid Earth* 108.B2. ISSN: 2156-2202. DOI: `10.1029/2000JB000123`.

Ojala, I. O., I. G. Main & B. T. Ngwenya (2004). "Strain rate and temperature dependence of Omori law scaling constants of AE data: Implications for earthquake foreshock-aftershock sequences". In: *Geophysical Research Letters* 31.24. ISSN: 1944-8007. DOI: `10.1029/2004GL020781`.

Omori, F. (1895). "On the After-shocks of Earthquakes". In: *The journal of the College of Science, Imperial University* 7.2, pp. 111–200. DOI: `10.15083/00037562`.

Papazachos, B. C. (Nov. 1975). "Foreshocks and earthquake prediction". In: *Tectonophysics* 28.4, pp. 213–226. ISSN: 0040-1951. DOI: `10.1016/0040-1951(75)90038-4`.

Pedregosa, F. et al. (2011). "Scikit-learn: Machine Learning in Python". In: *Journal of Machine Learning Research* 12.85, pp. 2825–2830. ISSN: 1533-7928.

Peng, Z. & J. Gomberg (Sept. 2010). "An integrated perspective of the continuum between earthquakes and slow-slip phenomena". In: *Nature Geoscience* 3.9, pp. 599–607. ISSN: 1752-0908. DOI: `10.1038/ngeo940`.

Peng, Z. & P. Zhao (Dec. 2009). "Migration of early aftershocks following the 2004 Parkfield earthquake". In: *Nature Geoscience* 2.12, pp. 877–881. ISSN: 1752-0908. DOI: `10.1038/ngeo697`.

Peng, Z. et al. (2007). "Seismicity rate immediately before and after main shock rupture from high-frequency waveforms in Japan". In: *Journal of Geophysical Research: Solid Earth* 112.B3. ISSN: 2156-2202. DOI: `10.1029/2006JB004386`.

Perfettini, H. & J.-P. Avouac (2007). "Modeling afterslip and aftershocks following the 1992 Landers earthquake". In: *Journal of Geophysical Research: Solid Earth* 112.B7. ISSN: 2156-2202. DOI: `10.1029/2006JB004399`.

Perfettini, H. et al. (2018). "A Model of Aftershock Migration Driven by Afterslip". In: *Geophysical Research Letters* 45.5, pp. 2283–2293. ISSN: 1944-8007. DOI: `10.1002/2017GL076287`.

Periollat, A. et al. (2022). "Transient brittle creep mechanism explains early postseismic phase of the 2011 tohoku-oki megathrust earthquake: observations by high-rate GPS solutions". In: *Journal of Geophysical Research: Solid Earth* 127.8, e2022JB024005. ISSN: 2169-9356. DOI: `10.1029/2022JB024005`.

Radiguet, M. et al. (2012). "Slow slip events and strain accumulation in the Guerrero gap, Mexico". In: *Journal of Geophysical Research: Solid Earth* 117.B4. ISSN: 2156-2202. DOI: `10.1029/2011JB008801`.

Radiguet, M. et al. (Nov. 2016). "Triggering of the 2014 Mw7.3 Papanoa earthquake by a slow slip event in Guerrero, Mexico". In: *Nature Geoscience* 9.11, pp. 829–833. ISSN: 1752-0908. DOI: `10.1038/ngeo2817`.

Ragheb, A. E., P. J. Clarke & S. J. Edwards (May 2007). "GPS sidereal filtering: coordinate- and carrier-phase-level strategies". In: *Journal of Geodesy* 81.5, pp. 325–335. ISSN: 1432-1394. DOI: `10.1007/s00190-006-0113-1`.

Reasenberg, P. A. (1999). "Foreshock occurrence before large earthquakes". In: *Journal of Geophysical Research: Solid Earth* 104.B3, pp. 4755–4768. DOI: `10.1029/1998JB900089`.

Reid, H. F. (1910). "The California earthquake of April 18, 1906". In: *Canergie Institution fo Washington* 2.

Richter, C. F. (Jan. 1935). "An instrumental earthquake magnitude scale". In: *Bulletin of the Seismological Society of America* 25.1, pp. 2–32. ISSN: 0037-1106. DOI: `10.1785/BSSA0250010001`.

— (1958). *Elementary Seismology*. W H Freeman & Co.

Roeloffs, E. A. (June 1988). "Hydrologic precursors to earthquakes: A review". In: *Pure and Applied Geophysics* 126.2-4, pp. 177–209. DOI: `10.1007/BF00878996`.

— (May 2006). "Evidence for aseismic deformation rate changes prior to earthquakes". In: *Annual Review of Earth and Planetary Sciences* 34.1, pp. 591–627. DOI: `10.1146/annurev.earth.34.031405.124947`.

Rogers, G. & H. Dragert (June 2003). "Episodic Tremor and Slip on the Cascadia Subduction Zone: The Chatter of Silent Slip". In: *Science* 300.5627, pp. 1942–1943. DOI: `10.1126/science.1084783`.

Ross, Z. E. et al. (July 2016). "An Improved Algorithm for Real-Time S-Wave Picking with Application to the (Augmented) ANZA Network in Southern California". In: *Bulletin of the Seismological Society of America* 106.5, pp. 2013–2022. ISSN: 0037-1106. DOI: `10.1785/0120150230`.

Ross, Z. E. et al. (Aug. 2018). "Generalized Seismic Phase Detection with Deep Learning". In: *Bulletin of the Seismological Society of America* 108.5A, pp. 2894–2901. ISSN: 0037-1106. DOI: `10.1785/0120180080`.

Ross, Z. E. et al. (Oct. 2019a). "Hierarchical interlocked orthogonal faulting in the 2019 Ridgecrest earthquake sequence". In: *Science* 366.6463, pp. 346–351. DOI: `10.1126/science.aaz0109`.

Ross, Z. E. et al. (2019b). "Searching for hidden earthquakes in Southern California". In: *Science* 364.6442, pp. 767–771. ISSN: 0036-8075, 1095-9203. DOI: `10.1126/science.aaw6888`.

Rubin, A. M. & J.-P. Ampuero (2005). "Earthquake nucleation on (aging) rate and state faults". In: *Journal of Geophysical Research: Solid Earth* 110.B11. ISSN: 2156-2202. DOI: `10.1029/2005JB003686`.

Ruiz, S et al. (2014). "Intense foreshocks and a slow slip event preceded the 2014 Iquique Mw 8.1 earthquake". In: *Science* 345.6201, pp. 1165–1169.

Ruiz, S. et al. (Oct. 2017). "Nucleation Phase and Dynamic Inversion of the Mw 6.9 Valparaíso 2017 Earthquake in Central Chile". In: *Geophys. Res. Lett.* 44.20, pp. 10,290–10,297. ISSN: 00948276. DOI: `10.1002/2017GL075675`.

Saichev, A. & D. Sornette (2007). "Theory of earthquake recurrence times". In: *Journal of Geophysical Research: Solid Earth* 112.B4. ISSN: 2156-2202. DOI: `10.1029/2006JB004536`.

Saragiotis, C., L. Hadjileontiadis & S. Panas (June 2002). "PAI-S/K: A robust automatic seismic P phase arrival identification scheme". In: *IEEE Transactions on Geoscience and Remote Sensing* 40.6, pp. 1395–1404. ISSN: 1558-0644. DOI: `10.1109/TGRS.2002.800438`.

Scholz, C. H. (1968). "Microfracturing and the inelastic deformation of rock in compression". In: *Journal of Geophysical Research (1896-1977)* 73.4, pp. 1417–1432. ISSN: 2156-2202. DOI: `10.1029/JB073i004p01417`.

Scholz, C. H. (Jan. 1998). "Earthquakes and friction laws". In: *Nature* 391.6662, pp. 37–42. ISSN: 1476-4687. DOI: `10.1038/34097`.

— (2015). "On the stress dependence of the earthquake b value". In: *Geophysical Research Letters* 42.5, pp. 1399–1402. ISSN: 1944-8007. DOI: `10.1002/2014GL062863`.

Schurr, B. et al. (Aug. 2014). “Gradual unlocking of plate boundary controlled initiation of the 2014 Iquique earthquake”. In: *Nature* 512.7514, pp. 299–302. ISSN: 0028-0836, 1476-4687. DOI: `10.1038/nature13681`.

Seif, S. et al. (2017). “Estimating ETAS: The effects of truncation, missing data, and model assumptions”. In: *Journal of Geophysical Research: Solid Earth* 122.1, pp. 449–469. ISSN: 2169-9356. DOI: `10.1002/2016JB012809`.

Seif, S. et al. (2019). “Foreshocks and their potential deviation from general seismicity”. In: *Bulletin of the Seismological Society of America* 109.1, pp. 1–18. DOI: `10.1785/0120170188`.

Shearer, P. M. (Oct. 2012a). “Space-time clustering of seismicity in California and the distance dependence of earthquake triggering”. In: *Journal of Geophysical Research: Solid Earth* 117.B10. ISSN: 01480227. DOI: `10.1029/2012JB009471`.

Shearer, P. M. (2012b). “Self-similar earthquake triggering, Båth’s law, and foreshock/aftershock magnitudes: Simulations, theory, and results for southern California”. In: *Journal of Geophysical Research: Solid Earth* 117.B6. ISSN: 2156-2202. DOI: `10.1029/2011JB008957`.

— (July 2019). *Introduction to Seismology*. 3rd edition. Cambridge ; New York, NY: Cambridge University Press. ISBN: 978-1-107-18447-3.

Skoumal, R. J. et al. (Nov. 2014). “Optimizing multi-station earthquake template matching through re-examination of the Youngstown, Ohio, sequence”. In: *Earth and Planetary Science Letters* 405, pp. 274–280. ISSN: 0012-821X. DOI: `10.1016/j.epsl.2014.08.033`.

Sleeman, R. & T. van Eck (June 1999). “Robust automatic P-phase picking: an online implementation in the analysis of broadband seismogram recordings”. In: *Physics of the Earth and Planetary Interiors* 113.1, pp. 265–275. ISSN: 0031-9201. DOI: `10.1016/S0031-9201(99)00007-2`.

Socquet, A. et al. (2017). “An 8 month slow slip event triggers progressive nucleation of the 2014 Chile megathrust”. In: *Geophysical Research Letters* 44.9, pp. 4046–4053. DOI: `10.1002/2017GL073023`.

Sornette, D. & M. J. Werner (2005). “Apparent clustering and apparent background earthquakes biased by undetected seismicity”. In: *Journal of Geophysical Research: Solid Earth* 110.B9. ISSN: 2156-2202. DOI: `10.1029/2005JB003621`.

Soto, H. & B. Schurr (Nov. 2021). “DeepPhasePick: a method for detecting and picking seismic phases from local earthquakes based on highly optimized convolutional and recurrent deep neural networks”. In: *Geophysical Journal International* 227.2, pp. 1268–1294. ISSN: 0956-540X. DOI: `10.1093/gji/ggab266`.

Stein, S. & M. Wysession (2008). *An Introduction to Seismology, Earthquakes, and Earth Structure*. 1er édition. Wiley-Blackwell.

Sun, T. & K. Wang (2015). "Viscoelastic relaxation following subduction earthquakes and its effects on afterslip determination". In: *Journal of Geophysical Research: Solid Earth* 120.2, pp. 1329–1344. ISSN: 2169-9356. DOI: `10.1002/2014JB011707`.

Tape, C. et al. (July 2018). "Earthquake nucleation and fault slip complexity in the lower crust of central Alaska". In: *Nature Geoscience* 11.7, pp. 536–541. ISSN: 1752-0908. DOI: `10.1038/s41561-018-0144-2`.

Taroni, M. et al. (July 2018). "Prospective CSEP Evaluation of 1-Day, 3-Month, and 5-Yr Earthquake Forecasts for Italy". In: *Seismological Research Letters* 89.4, pp. 1251–1261. ISSN: 0895-0695. DOI: `10.1785/0220180031`.

Trugman, D. T. & Z. E. Ross (Aug. 2019). "Pervasive Foreshock Activity Across Southern California". In: *Geophys. Res. Lett.* 46.15, pp. 8772–8781. ISSN: 0094-8276, 1944-8007. DOI: `10.1029/2019GL083725`.

Twardzik, C. et al. (Dec. 2022). "Bayesian inference on the initiation phase of the 2014 Iquique, Chile, earthquake". In: *Earth and Planetary Science Letters* 600, p. 117835. ISSN: 0012-821X. DOI: `10.1016/j.epsl.2022.117835`.

Uchida, N. (Dec. 2019). "Detection of repeating earthquakes and their application in characterizing slow fault slip". In: *Progress in Earth and Planetary Science* 6.1, p. 40. ISSN: 2197-4284. DOI: `10.1186/s40645-019-0284-z`.

Uchida, N. & R. Bürgmann (May 2019). "Repeating Earthquakes". In: *Annual Review of Earth and Planetary Sciences* 47.1, pp. 305–332. ISSN: 0084-6597, 1545-4495. DOI: `10.1146/annurev-earth-053018-060119`.

Uchida, N. & T. Matsuzawa (July 2013). "Pre- and postseismic slow slip surrounding the 2011 Tohoku-oki earthquake rupture". In: *Earth and Planetary Science Letters* 374, pp. 81–91. ISSN: 0012-821X. DOI: `10.1016/j.epsl.2013.05.021`.

Uchida, N. et al. (July 2004). "Pre- and post-seismic slow slip on the plate boundary off Sanriku, NE Japan associated with three interplate earthquakes as estimated from small repeating earthquake data". In: *Tectonophysics* 385.1, pp. 1–15. ISSN: 0040-1951. DOI: `10.1016/j.tecto.2004.04.015`.

Utsu, T. (Mar. 1971). "Aftershocks and Earthquake Statistics(2) : Further Investigation of Aftershocks and Other Earthquake Sequences Based on a New Classification of Earthquake Sequences". In: *Journal of the Faculty of Science, Hokkaido University. Series 7, Geophysics* 3.4, pp. 197–266.

Utsu, T. et al. (1995). "The Centenary of the Omori Formula for a Decay Law of Aftershock Activity." In: *Journal of Physics of the Earth* 43.1, pp. 1–33. ISSN: 1884-2305, 0022-3743. DOI: `10.4294/jpe1952.43.1`.

Vallée, M. & V. Douet (Aug. 2016). "A new database of source time functions (STFs) extracted from the SCARDEC method". In: *Physics of the Earth and Planetary Interiors* 257, pp. 149–157. ISSN: 0031-9201. DOI: `10.1016/j.pepi.2016.05.012`.

Vallée, M. et al. (2013). "Intense interface seismicity triggered by a shallow slow slip event in the Central Ecuador subduction zone". In: *Journal of Geophysical Research: Solid Earth* 118.6, pp. 2965–2981. ISSN: 2169-9356. DOI: `10.1002/jgrb.50216`.

Veen, A. & F. P. Schoenberg (June 2008). "Estimation of Space–Time Branching Process Models in Seismology Using an EM–Type Algorithm". In: *Journal of the American Statistical Association* 103.482, pp. 614–624. ISSN: 0162-1459, 1537-274X. DOI: `10.1198/016214508000000148`.

von Seggern, D. H. & J. G. Anderson (May 2017). "Velocity change in the zone of a moderate Mw 5.0 earthquake revealed by autocorrelations of ambient noise and by event spectra". In: *Pure and Applied Geophysics* 174.5, pp. 1923–1935. DOI: `10.1007/s00024-017-1521-2`.

Voss, N. et al. (Oct. 2018). "Do slow slip events trigger large and great megathrust earthquakes?" In: *Science Advances* 4.10, eaat8472. DOI: `10.1126/sciadv.aat8472`.

Vuan, A. et al. (2017). "Loading Rate Variations Along a Midcrustal Shear Zone Preceding the Mw6.0 Earthquake of 24 August 2016 in Central Italy". In: *Geophysical Research Letters* 44.24, pp. 12,170–12,180. ISSN: 1944-8007. DOI: `10.1002/2017GL076223`.

Waldhauser, F. & W. L. Ellsworth (Dec. 2000). "A Double-Difference Earthquake Location Algorithm: Method and Application to the Northern Hayward Fault, California". In: *Bulletin of the Seismological Society of America* 90.6, pp. 1353–1368. ISSN: 0037-1106. DOI: `10.1785/0120000006`.

Wang, K., Y. Hu & J. He (Apr. 2012). "Deformation cycles of subduction earthquakes in a viscoelastic Earth". In: *Nature* 484.7394, pp. 327–332. ISSN: 1476-4687. DOI: `10.1038/nature11032`.

Wang, R. et al. (2020). "Injection-Induced Earthquakes on Complex Fault Zones of the Raton Basin Illuminated by Machine-Learning Phase Picker and Dense Nodal Array". In: *Geophysical Research Letters* 47.14, e2020GL088168. ISSN: 1944-8007. DOI: `10.1029/2020GL088168`.

Wdowinski, S. et al. (1997). "Southern California permanent GPS geodetic array: Spatial filtering of daily positions for estimating coseismic and postseismic displacements induced by the 1992 Landers earthquake". In: *Journal of Geophysical Research: Solid Earth* 102.B8, pp. 18057–18070. ISSN: 2156-2202. DOI: `10.1029/97JB01378`.

Wells, D. L. & K. J. Coppersmith (Aug. 1994). "New empirical relationships among magnitude, rupture length, rupture width, rupture area, and surface displacement". In: *Bulletin of the Seismological Society of America* 84.4, pp. 974–1002. ISSN: 0037-1106. DOI: `10.1785/BSSA0840040974`.

Wiemer, S., S. McNutt & M. Wyss (1998). "Temporal and three-dimensional spatial analyses of the frequency-magnitude distribution near Long Valley Caldera, California". In: *Geophysical Journal International* 134.2, pp. 409–421. ISSN: 0956-540X. DOI: `10.1046/j.1365-246X.1998.00561.x`.

Woollam, J. et al. (Jan. 2019). "Convolutional Neural Network for Seismic Phase Classification, Performance Demonstration over a Local Seismic Network". In: *Seismological Research Letters* 90.2A, pp. 491–502. ISSN: 0895-0695. DOI: `10.1785/0220180312`.

Yamashita, F. et al. (July 2021). "Two end-member earthquake preparations illuminated by foreshock activity on a meter-scale laboratory fault". In: *Nature Communications* 12.1, p. 4302. ISSN: 2041-1723. DOI: `10.1038/s41467-021-24625-4`.

Zaliapin, I. & Y. Ben-Zion (Oct. 2016). "A global classification and characterization of earthquake clusters". In: *Geophysical Journal International* 207.1, pp. 608–634. ISSN: 0956-540X. DOI: `10.1093/gji/ggw300`.

— (2020). "Earthquake Declustering Using the Nearest-Neighbor Approach in Space-Time-Magnitude Domain". In: *Journal of Geophysical Research: Solid Earth* 125.4, e2018JB017120. ISSN: 2169-9356. DOI: `10.1029/2018JB017120`.

Zhang, M., W. L. Ellsworth & G. C. Beroza (2019). "Rapid earthquake association and location". In: *Seismological Research Letters* 90.6, pp. 2276–2284. ISSN: 0895-0695, 1938-2057. DOI: `10.1785/0220190052`.

Zhu, W. & G. C. Beroza (Oct. 2018). "PhaseNet: A Deep-Neural-Network-Based Seismic Arrival Time Picking Method". In: *Geophysical Journal International*. ISSN: 0956-540X, 1365-246X. DOI: `10.1093/gji/ggy423`.

Zhuang, J. (July 2012). "Long-term earthquake forecasts based on the epidemic-type aftershock sequence (ETAS) model for short-term clustering". In: *Research in Geophysics* 2.1, e8–e8. ISSN: 2038-9663. DOI: `10.4081/rg.2012.e8`.

Zhuang, J. & S. Touati (2015). "Stochastic simulation of earthquake catalogs". In: *Community Online Resource for Statistical Seismicity Analysis* Theme V.1, p. 34.

Zhuang, J. et al. (2011). "Basic models of seismicity: spatiotemporal models". In: DOI: `10.5078/CORSSA-07487583`.

Zhuang, J. et al. (2012). "Basic models of seismicity: temporal models". In: DOI: `10.5078/CORSSA-79905851`.

Luc Moutote

Foreshock earthquake sequences: Earthquake cascades or aseismic triggering

Abstract

Understanding how large earthquakes begin remains one of the major challenge in seismology. This question is central to our understanding of earthquakes, including the long controversial issue of their predictability. Many large earthquakes are preceded by foreshocks, which are sometime considered to be precursors, reflecting a nucleation process of the main rupture. However, we are still unable to fully understand under which circumstances they occur and if they have any predictive power. In this Ph.D. thesis I use high resolution seismicity catalogs to study foreshock sequences and their connection with the preparation phase of mainshocks. First, based on a highly complete earthquake catalog, I studied 53 foreshock sequences observed in Southern California. I found that 10 out of 53 mainshocks are preceded by a significantly elevated seismic activity when accounting for usual aftershock clustering. This shows that anomalous foreshock activity in Southern California is relatively uncommon. Then I investigated the 2017 Valparaiso Mw= 6.9 earthquake sequence. Using seismicity rate analysis, repeating earthquakes and HR-GPS observations, I highlighted a transient aseismic perturbation starting before the first foreshock and extending after the mainshock. Rather than pointing to a possible preparatory phase of the mainshock, the identified signal seems to highlight a transient aseismic perturbation, from foreshock to aftershock, not specifically targeted toward the occurrence of the $M_w = 6.9$ mainshock. My observations suggest that a mainshock preparatory phase is unlikely to be detectable in foreshock activity. Nevertheless, a better understanding of the interplay between seismicity and aseismic slip is likely to improve our understanding of the fault processes that lead to large magnitudes.

Keywords:
Foreshocks ; Seismicity analysis ; Aseismic slip ; Nucleation of earthquake

Résumé

Comprendre comment les grands tremblements de terre se déclenchent et comment mieux les anticiper reste de nos jours un des défis majeur de la sismologie. De nombreux grands tremblements de terre sont précédés de plus petits séismes, souvent interprétés comme des précurseurs reflétant un processus de nucléation de la future grande rupture. Toutefois, nous ne sommes toujours pas en mesure de comprendre pleinement dans quelles circonstances ils se produisent et s'ils ont un quelconque pouvoir prédictif. Dans cette thèse de doctorat, j'utilise des catalogues de sismicité haute-résolution pour étudier des séquences de pré-chocs et leurs possibles liens avec une phase de préparation des grands séismes. Tout d'abord, j'ai étudié 53 séquences pré-chocs en Californie du Sud. Je montre que seulement 10 des 53 séquences observent une activité sismique anormalement élevée lorsque l'on prend en compte les variations habituelles de la sismicité. Donc, une activité anormale des séismes pré-chocs en Californie du Sud est relativement rare. J'ai ensuite étudié en détail une séquence sismique à Valparaiso en 2017. En analysant les variations du taux de sismicité, les séismes répétitifs et des mesures HR-GPS, j'ai mis en évidence un glissement asismique transitoire commençant avant le premier pré-choc et se prolongeant après le choc principal. Les séismes pré-chocs semblent ainsi être contrôlé par une perturbation asismique transitoire plus longue, de la séquence pré-choc à post- choc principal, plutôt que d'indiquer une possible phase préparatoire. Mes observations suggèrent qu'il est peu probable qu'une phase préparatoire des chocs principaux soit systématiquement détectable avec l'activité des séismes pré-chocs. Néanmoins, il apparaît qu'une meilleure compréhension de l'interaction entre la sismicité et le glissement asismique pourrait améliorer notre compréhension des processus de failles qui déclenchent les grandes magnitudes.

Mots-clés :
Séismes pré-chocs ; Analyse de sismicité ; Glissement asismique ; Nucléation des séismes